Harmonics in Offshore Wind Power Plants Employing Power Electronic Devices in the Transmission System

Glasdam, Jakob Bærholm

Publication date:
2015

Document Version
Publisher's PDF, also known as Version of record

Harmonics in Offshore Wind Power Plants Employing Power Electronic Devices in the Transmission System

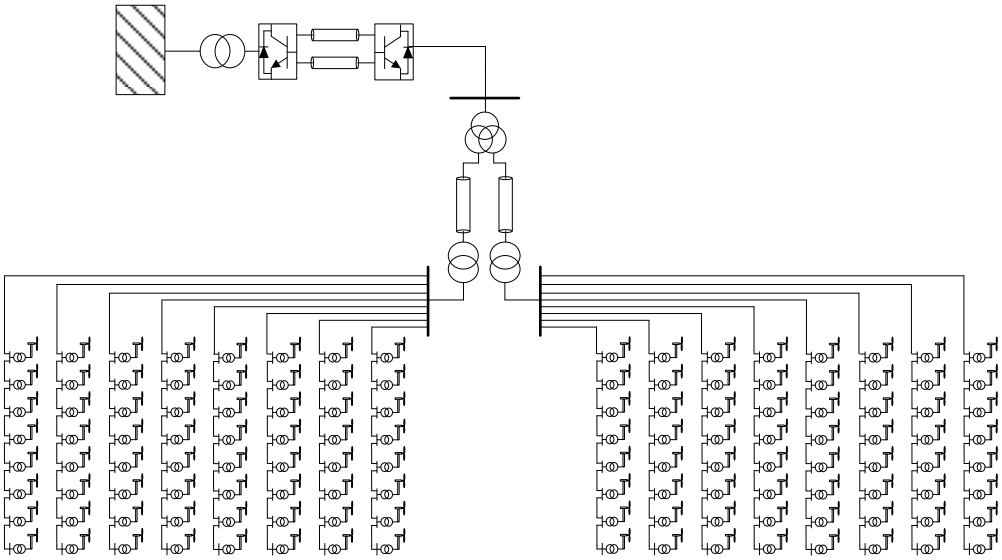

Jakob Glasdam

Harmonics in Offshore Wind Power Plants Employing Power Electronic Devices in the Transmission System

By

Jakob Glasdam

Dissertation submitted to the Faculty of Engineering, Science and Medicine at Aalborg University in partial fulfillment of the requirements for the degree of Doctor of Philosophy in Electrical Engineering.

This version is made by the Doctoral School especially for PhD theses at VBN.

Assessment committee

Professor Frede Blaabjerg (chairman)
Department of Energy Technology, Aalborg University

Adjunct Professor Lennart Harnefors
KTH, ABB Corporate Research

Professor Carlo Alberto Nucci
Department of Electrical, Electronic and Information Engineering, School of Engineering and Architecture University of Bologna

Supervisors

Prof. Claus Leth Bak
Department of Energy Technology, Aalborg University

Dr. Jesper Hjerrild
DONG Energy Wind Power

Dr. Łukasz Hubert Kocewiak
DONG Energy Wind Power

Department of Energy Technology
Aalborg University, Denmark
March 2015

PhD Thesis

Harmonics in Offshore Wind Power Plants Employing Power Electronic Devices in the Transmission System

JAKGL@dongenergy.dk

Printed in Denmark

ISBN: 978-87-92846-63-1

Aalborg University

Department of Energy Technology

Pontoppidanstræde 101

DK-9220 Aalborg East, Denmark.

http://www.et.aau.dk/

Preface

This PhD dissertation was submitted to the Faculty of Engineering, Science and Medicine at Aalborg University in partial fulfilment of the requirements for the PhD degree in Electrical Engineering. The research was conducted in the Department of Energy Technology at Aalborg University as well as in DONG Energy Wind Power (DEWP). The project was industry-oriented, which created a unique opportunity to carry out research gathering benefits from both the industry and academia.

The project has been followed by Prof. Claus Leth Bak who is with Department of Energy Technology, Aalborg University and Dr. Jesper Hjerrild and Dr. Łukasz Hubert Kocewiak who are with DEWP.

The project has been financed by DEWP with support from Danish Ministry of Science, Innovation and Higher Education.

The author has had the pleasure of being a guest researcher at The National Renewable Energy Laboratory (NREL) in Colorado, US. NREL commissioned an advanced multi-megawatt sized power electronic grid simulator test system during the author's stay-abroad. Obtained test results are used to develop and evaluate time domain models of the grid simulator and a commercial type 4 wind generator turbine.

One master project has been supervised within the confines of this project.

The thesis comprises three main parts. A reference list can be found at the end of the main report at page 169. The references are shown as [i], where i is the number of the literature in the reference list. Tables, figures and equations are shown as C-N, where C is the chapter number and N is a unique number for the particular figure, table or equation.

A list of the publications realised within the project is found in section 14.5.

Supervisor's Foreword

I have had the great pleasure of following Jakob during parts of his studies for his Master's in Energy Engineering, both as his lecturer and as his supervisor in his final MSc thesis project. Nowadays I mainly work as head of the Energy Technology PhD program with more than 100 PhD students working in various topics of Energy Engineering, but the lecturing in key Power System courses in our Energy Engineering education makes it possible for me note particularly skilled and motivated students and propose them to continue their studies as a PhD student.

When I first met Jakob it became inevitably clear rather quickly that he certainly belonged to this category of students and at the same time I enjoyed working with him. Together we agreed upon a suitable Master's thesis project for his final project. Jakob choose to work with a so-called "long thesis", which covers 60 ECTS and extends over two full semesters, i.e. one full academic year. The expectations to such MSc theses are much higher than the ordinary 30 ECTS thesis and the candidate actually can work like in some way resembling a mini-PhD.

Jakob choose to work with a very challenging topic in cooperation with Danish power generation company DONG Energy. Dong Energy is a market leader in offshore wind power and they proposed to study the modeling and validation of vacuum circuit breakers in time domain with the purpose of being able to simulate precisely switching transients in a large offshore wind farm. The topic is highly complicated and demands for strong skills, both related to high voltage gaseous physics as well as time domain modeling theories and mathematical skills and including real offshore system measurements for validation. Jakob worked in a highly independent manner through this topic and finalized his MSc with the highest possible grade for the project "Development, Validation and Application of a Vacuum Circuit Breaker Model for Time Domain Analysis in Large Offshore Wind Farms", having more than 250 pages of work.

In another occasion Jakob and I met with an internationally highly renowned professor, who read his thesis and declared that it could have been submitted to achieve the PhD degree. He proposed that we made a joint paper, which has been published in 'Electric Power Systems Research' journal.

So it was highly evident to both me and the company supervisor from Dong Energy that we in Jakob had an obvious candidate for an industrial PhD study. Jakob's industrial PhD study was funded partly by the Danish Ministry of science and DONG Energy and he was supervised by me in the PhD project entitled "Harmonics in Offshore Wind Power Plants Employing Power Electronic Devices in the Transmission System", which is in the hand of the reader of this foreword.

In order to understand the motivation of this project and its usefulness some background information is necessary. Denmark is a frontrunner in wind power and especially offshore wind power, which is in a very rapid growth, both in Denmark and other Countries. Dong Energy installs and operates such large scale wind power plants consisting of maybe hundred individual wind turbines and with a total rating of several hundred megawatts. The wind turbines of today all employ power electronic interfaces to the electric collection grid, consisting of a widespread, somewhat meshed submarine cable network connecting to an offshore transformer, which connects to the onshore transmission system.

The reliability of this remote, not easily accessible electrical device (as a total) is of the utmost importance for the overall economy of an offshore wind power plant. One of the factors affecting reliability is harmonic interactions between wind turbine control and network harmonic impedance, which varies significantly for various conditions. Harmonic instabilities ultimately can stop an offshore wind power plant in being able to operate so the problem is serious and must be thoroughly studied in the design phase of an offshore wind power plant.

Jakob's overall task was to make and validate a time domain simulation model and method, which can be used to analyze the harmonic stability interactions in a large offshore wind power plant. He

accomplished this by a very rigorous power system modelling and validation approach, which included real life measurements both in the London Array wind power plant as well as in NREL (national renewable energy laboratory, Colorado, US). He used the detailed models for setting up realistic system study cases in order to analyze possible harmonic interaction problems and propose methods to mitigate such.

His work is supported by 9 peer-reviewed publications (2 journals and 7 conferences) in esteemed publications such as Cigré and IEEE. Additionally, his research work has been published as a book in "Springer Theses - Recognizing Outstanding Ph.D. Research".
Jakob's PhD thesis was assessed by highly esteemed Professors Frede Blaabjerg (chairman), Lennart Harnefors and Carlo Alberto Nucci with the designation "he is an excellent researcher", a conclusion I as his supervisor is very proud of on behalf of Jakob.

If I should look back over the years and point out one outstanding feature of Jakob it has to be his ability to work very independently in very complex matters and at the same time being able not to lose the grip and deliver the expected results in a well-worked through and useful quality. On the more personal level I have enjoyed working with Jakob through these years and I hope that we can continue our cooperation in some way in the future. This is likely as Jakob today works in DONG Energy with whom I have the pleasure to continue cooperation with.

The book in front of you presents Jakob's fine work during his PhD and I sincerely hope you will find it valuable and enjoy reading it.

Aalborg, July 2015 Claus Leth Bak, Professor

Acknowledgements

I would like to express my deepest thanks to my supervisors, Prof. Claus Leth Bak from Aalborg University, Dr. Jesper Hjerrild and Dr. Łukasz Hubert Kocewiak from DONG Energy Wind Power (DEWP) for all their support and help in the project development. The feedback from the academia as well as from the industry was especially fruitful in order to create a good collaboration between both units, which is reflected in this report.

This research project is a continuation of Dr. Kocewiak's PhD project, entitled 'Harmonics in Large Offshore Wind Farms". Substantial amount of measurement data was collected within the previous project from various offshore wind power plants (OWPPs). The previous project focused primarily on the harmonic characterization of the commercial wind turbine generators (WTGs). This project has utilised not only the measurement system and post processing tools developed within the previous project but also drawn significantly on Dr. Kocewiak's experience. It is to the author's belief that the outcome of the measurement campaigns both at the National Renewable Energy Laboratory (NREL) and at London Array OWPP would not have been as successful as they are considered to be, without the support of Dr. Kocewiak, which is greatly appreciated. The continuous research activities also illustrate DEWP's continuous concern about power quality in their systems and DEWP's desire to be at the frontier of the state-of-the-art knowledge and technology.

My grateful thanks go my two Industrial PhD colleagues at DEWP, Lorenzo Zeni and Mikkel Gryning for the many good discussions and exchanges of experience. Four joint publications have been some of the many good outcome of our collaboration. I would especially like to thank Dr. Zeni for the many discussions regarding the control of the multi-level cascaded converters.

I'd like to give special thanks to all my colleagues NREL for their hospitality, especially Dr. Vahan Gevorgian and Mr. Robb Wallen.

Great thanks go to the staff at London Array for their valuable aid during the planning, installation of the measurement system and for maintaining the internet connection to the measurement equipment, which was very troublesome due to the remote location of the onshore substation. I would have had to travel from Denmark to the U.K more than the six times, if the staff did not show so much patience and provided their much-appreciated help.

I have had the pleasure of being a supervisor for a Master project at Aalborg University. The master student, Mr. Egill Thorbergsson, provided assistance in the high-voltage laboratory at Aalborg University in the calibration of the voltage probes used in the measurement campaign at London Array OWPP. The calibration was done at a late stage of Mr. Thorbergsson's master project, but he still found the time to help. This is much appreciated.

On a more personal note, I would like to thank my patient and understanding girlfriend, my friends and family for their valuable support and understanding.

Jakob Glasdam

January 2015, Skærbæk, Denmark

Abstract

Introduction

The trend in power generation is to partly replace conventional power plants with renewable energy sources. Offshore wind power has been selected to take up a significant proportion of the renewable energy production. The grid codes have been updated to accommodate the rising share of wind power. The onshore as well as offshore wind power plants (OWPPs) therefore have to meet the same stringent requirement as the conventional power plants. This can be accommodated by employment of flexible alternating current transmission system (FACTS) devices, such as the static compensator (STATCOM).

Nowadays, OWPPs are connected through a widespread medium-voltage submarine cable system and grid connected using long high-voltage alternating current (HVAC) cables, representing challenges related to e.g. harmonics resonances. The trend is to locate the OWPPs even further from shore, which gives rise to a number of challenges to the wind power industry with regard to construction, installation as well as transmission of the generated energy. The STATCOM and the voltage-sourced converter high-voltage direct current (VSC-HVDC) are attractive solutions for grid connection of remotely located OWPPs.

The new system configuration requires in-depth knowledge of all relevant technical aspects, including e.g. the involved control systems performance and robustness for all possible operating conditions. The transmission system operator might impose new control requirements when the VSC-HVDC is going to be widely used for OWPP grid connection and the dynamic compliance specifications might change. This sets up a need to develop new strategies for ensuring robustness and adaptability, considering aspects such as fault-handling, ancillary services, congestion management, harmonics etc. It is therefore important to analyse and assess all possible control aspects related to the interaction between the OWPP and the power electronic devices (PEDs) in the transmission system (e.g. the STATCOM and the HVDC system).

OWPPs are susceptible to the harmonic instability, where the extensive sub-marine cabling and possible low available short-circuit power at the grid connection point may create resonance(s) within the bandwidth of the wind turbine generator (WTG) controller. The interaction between the controller and the electrical system external to the WTG may result in an unacceptable high harmonic distortion level. This reduces the efficiency of the generation and transmission of the electrical energy in the OWPP along with increasing the thermal stress of the PEDs and passive components such as the WTG transformer, causing accelerated component aging and may cause malfunctioning of the OWPP protection system. In addition, the harmonic instability may lead to excessive overvoltages, which will cause disconnection of the WTG(s) leading to loss of production, which, due to the size of nowadays OWPPs, will have a serious impact of the revenue to the owners.

The harmonic stability studies of grid-connected converters with the power system (i.e. the examination of the PED current controller's susceptibility to resonances in the power system) have received academic focus in recent years due to the rapidly increasing penetration of renewable energy and distributed generation resources. Additionally, harmonic stability studies have also become an important part of the system design studies of a HVAC grid connected OWPP. Similarly, harmonic stability studies are needed for the planned VSC-HVDC grid connected OWPPs. Since the offshore electrical environment is significantly altered compared to the offshore network in an HVAC connected OWPP, there is a need to define the harmonic stability assessment procedure and its application for the HVDC grid connected OWPPs.

By achieving a better understanding of the complexity of how such systems (e.g. the WTG and the HVDC station) interact with each other, seen from a harmonic perspective; it will be possible to make a better and more cost-efficient design of e.g. harmonic filters and reactive compensation. Furthermore,

it will also enable the OWPP developer, such as DONG Energy Wind Power (DEWP), to provide relevant input for the grid code compliance of an OWPP as well as define technical requirements to potential suppliers.

Purpose of the Industrial PhD Project

The purpose of this Industrial PhD project has been to investigate and address the interaction (from a harmonic perspective) between the OWPP, and the associated control systems in the WTGs and other PEDs in the transmission system with focus on the VSC-HVDC and the STATCOM. The main scope has been on the assessment of the frequency domain evaluation approach, commonly applied in the OWPP design phase. This has been accomplished by comparing results obtained from conventional and linearized frequency domain analysis methods such as the Nyquist stability criterion against the detailed electromagnetic transient (EMT) based model realised in PSCAD/EMTDC.

Measurement Campaigns

Detailed, yet generic models of the involved PEDs have been developed in order to meet the project requirements of analysing the harmonic stability phenomena. The generic EMT models of the PEDs have been validated based on comparison of measurement data, in order to ensure their trustworthiness. Test and field measurements have therefore been conducted on commercial PEDs such as ±50 MVar Siemens SVC Plus, the 7 MW ABB SVC Light (modified back-to-back configuration) and a commercial multi-megawatt sized type 4 WTG.

Measurements constitute a core part in industry-oriented research. Due to this fact, the research project owes its uniqueness and contributes new insight to the academia. A long term harmonic measurement campaign has therefore been prepared and conducted within the PhD project at Clevehill substation, UK, where four STATCOMs are installed. The Cleveill substation serves as grid connection for the 600 MW sized London Array OWPP. The STATCOMs employ the modular multi-levels cascaded converter (MMCC) technology, which is considered state-of-the-art within the industry. The measurement data obtained on the STATCOM has allowed the author to acquire detailed information preferred in order to develop a generic, yet detailed, EMT based model of the MMCC STATCOM, including the switching devices and distributed sub-module (SM) dynamics.

Additionally, the author has, together with colleagues at DEWP, established a Cooperative Research and Development Agreement (CRADA) between DEWP and the National Renewable Energy Laboratory (NREL) in Boulder, Colorado, USA. NREL has recently commissioned an advanced multi-megawatt sized power electronic grid simulator test system. Test results obtained during the author's stay at NREL are used to develop and evaluate generic, yet detailed EMT models of the grid simulator (referred to as controllable grid interface, CGI) and a commercial multi-megawatt sized type 4 WTG.

PED Modelling and Validation

The relatively high number of non-linear semi-conductors in the MMCCs possesses some challenges in the EMT programs, such as PSCAD/EMTDC, as the semi-conductors are triggered by relatively high-frequency signals and as the electrical system's admittance matrix is altered at each switching instant. A significant computational effort is required for re-triangularisation of the electrical network subsystem's admittance matrix. The computational burden is considerably increased for the large number of semi-conductors, making the simulation of the MMCC in some occasions impractical when using a conventional modelling approach. Previously, a detailed equivalent model of the MMCC VSC-HVDC has been devised based on the "Nested Fast and Simultaneous Solution" procedure. However, there are some limitations to the previous model as it is specifically intended for the MMCC employing half-bridge converters in the SMs. The somewhat more complex structure of the full-bridge converter employed in the MMCC STATCOM makes it complex to apply the existing modelling approach for the STATCOM. A universal modelling technique is proposed, which is able to represent both the half- and full-bridge based SMs. The modelling technique is simple as the derivation of the SM's Norton equivalent is merely based on circuit inspection. The measurement data from the London Array OWPP measurement campaign has successfully been applied in the evaluation of the generic model of the

STATCOM implemented in PSCAD/EMTDC. In general it can be said that the proposed generic model is highly capable of replicating the measured waveforms even with no information available of the control and modulation technique applied in the commercial STATCOM.

The evaluated STATCOM model has enabled the development of a trustworthy, full model of the MMCC HVDC, which has been implemented in PSCAD/EMTDC. Simulation studies on the HVDC system has demonstrated the converter's ability to successfully control the distributed SM voltages, dynamically and for steady-state operating conditions.

The model evaluation of the commercial WTG and the CGI has been done for both normal and abnormal operating conditions, such as fast and slow balanced and unbalanced faults realised at the test facility at NREL. The evaluation demonstrated that it is possible to accurately simulate the measured waveforms with little or even no information available applied PED control methodology as well as the control system parameters, which are influencing the characteristics of both the CGI and the WTG. The successful validation gives credibility to the time domain modelling of the involved PEDs for the harmonic stability assessment in OWPPs.

System Studies

Harmonic stability studies have been realised in OWPPs employing PEDs in the transmission system. The harmonic stability in an HVDC grid connected OWPP has been investigated in both the frequency and time domain using the validated models of the PEDs. The application of the frequency domain in the stability analysis raises the conceptual challenge of recognising the source and the load (i.e. the plant), as either the WTG or the HVDC system can be treated as the source in the analysis, yielding different results. In this case both the load and the source are actively controlled power system devices. The time domain approach on the other hand provides a holistic approach, without the need to assign the source in the analysis.
Based on a number of study cases, it is demonstrated that a good correlation exists between the time and frequency domain methods for the stability analysis. However, limitations of the frequency domain were observed when resonances at higher frequencies exist (i.e. near the switching frequency and above the bandwidth of the current controller). Therefore, it is proposed to conduct the analysis primarily in the frequency domain. Once all the considered operating scenarios are covered (typically in the excess of 1000) a few cases should be selected and repeated in the time domain, which is both more challenging and more time consuming than the frequency domain method.

Time domain studies in an HVAC grid connected OWPP with a STATCOM located at the grid connection point have shown that the undesirable controller interaction between the WTGs and the STATCOM deteriorates the controllability of the internal dynamics of the MMCC STATCOM.

It was found that the total inter-harmonic distortion index according to IEC Standard 61000-4-7 is useful to assess possible and undesired control interaction between the PEDs in OWPPs. The total harmonic distortion index, on the other hand, is found to contain very little information on possible PED controller interaction.

It was shown that an application of active filtering in the WTGs by means of a band rejection filter (i.e. notch filter) in the main control chain can potentially reduce the harmonic emission and improve the overall stability in OWPPs without interfering with the OWPP overall design. This can be achieved by providing additional damping or shifting the resonance frequencies. Improving the PED's controllers' rejection capability called active damping is a certain type of active filtering. The converter may be controlled adaptively or tuned to suppress selected harmonic components. The application of active filtering was demonstrated for OWPPs with a STATCOM or an HVDC located in the transmission system. The active filtering was found to improve the internal dynamics of the MMCC STATCOM.

Based on the findings of the research project, a best practice for the evaluation of the harmonic stability in OWPPs employing PEDs in the transmission system has been formulated and is enclosed in the dissertation.

Dansk Resumé (Danish Abstract)

Introduktion

Trenden inden for energiproduktion er, at delvis udskifte konventionelle kraftværker med vedvarende energikilder. Energi fra havvind er udvalgt til at bidrage med en stor andel af den producerede vedvarende energi. De tekniske forskrifter for design og drift af elsystemerne er blevet opdateret for at kunne adaptere den stigende andel af vindenergi i elnettet. Land- såvel som havvindmølleparker skal derfor fremadrettet opfylde samme strenge krav, som der i dag stilles til de konventionelle kraftværker. Dette kan imødegås ved anvendelse af aktivt styret effektelektronik såsom FACTS (flexible alternating current transmission system) komponenter såsom den statiske kompensator (static compensator, STATCOM).

Vindmøllerne i de store havvindmølleparker er tilsluttet et stort, distribueret havkabelsystem. Den samlede genererede vindenergi transporteres til land via lange højspændingskabler. Kombinationen af de mange aktivt styrede effektelektronik komponenter i f.eks. vindmøllerne og den udbredte anvendelse af kabler repræsenterer et antal af udfordringer ift. f.eks. harmoniske resonanser. De planlagte vindmølleparker lokaliseres endnu længere fra land end hvad er tilfældet i dag. Dette medfører flere udfordringer for vindenergiindustrien, i form a konstruktion, drift samt eksport af den genererede vindenergi. STATCOM'en såvel som anvendelse af en jævnstrømsforbindelse (HVDC, der står for high-voltage direct current) i tilslutningssystemet af vindmølleparken til elnettet er attraktive løsninger ift. at transportere energien til land.

Den nye systemkonfiguration, hvor der anvendes aktivt styret effektelektronik i transmissionssystemet, nødvendiggør et mere dybdegående kendskab til alle relevante tekniske aspekter, såsom hvorledes kontrolsystemerne i effekteletronik systemerne interagerer med hinanden og med det elektriske system, set fra et harmonisk synspunkt. Elnetoperatøren opstiller muligvis nye krav til vindmølleparkerne den dag hvor nettilslutningen af vindmølleparkerne i højere grad sker ved brug af HVDC.

Dette fordrer et behov for at opstille nye strategier for at sikre robust og fleksibel drift af vindmølleparken eksempelvis ift. parkens respons overfor fejl i elsystemet, supplerende services såsom spændingskontrol, elsystemets evne til at aftage den producerede energi samt kontrol af udbredelse af harmoniske strømme. Det er derfor vigtigt at analysere samtlige potentielle forekomster denne harmoniske interaktionen mellem vindmølleparken og effektelektronikken, der anvendes i transmissionssystemet, såsom STATCOM'en og HVDC systemet.

Havvindmølleparkerne er sårbare overfor harmonisk ustabilitetet, hvor det udbredte søkabelsystem og muligt lavt kort kortslutningsniveau i nettilslutningspunktet skaber et antal resonanser inden for båndbredden af det aktive kontrolsystem, der anvendes i vindmøllerne, samt i STATCOM'en og i HVDC anlægget. Forekomsten af harmonisk ustabilitet medfører et utilladeligt højt niveau af harmonisk støj, der reducerer effektiviteten af den generede energi samt eksporten af denne. Yderligere, den harmoniske ustabilitet øger den termiske stress, der påføres både de aktive komponenter i effektelektronik systemerne samt i de passive komponenter såsom vindmølletransformere og i kabelsystemet. Dette medfører accelereret ældning af komponenterne, samt fejlbehæftet drift af beskyttelsessystemerne i vindmølleparken. Desuden kan den harmoniske ustabilitet føre til uacceptable overspændinger, som vil medføre udkobling af vindmøllerne indtil fejlen er fundet og rettet, hvilket ikke er ligefrem grundet kompleksiteten af problemstillingen. Vejrforholdene til havs udgør en yderligere usikkerhed, der muligvis forhindrer adgang til parken i længere perioder. Dette fører til tab af produktion i den lange periode før fejlen er udbedret. Dette kan medføre alvorlige økonomiske tab for ejerne, grundet størrelserne på havvindmølleparkerne.

Udfordringerne ifb. med harmonisk stabilitet af nettilsluttet effektelektronik har modtaget akademisk fokus i de senere år på grundlag af den hastigt stigende udbredelse af vedvarende energi og decentrale

produktionsenheder. Derudover er de harmoniske stabilitetsundersøgelser også blevet en væsentlig del af designet af nettilslutningen af havvindmølleparker ved brug af konventionel vekselstrømsteknologi. Der er ligeledes et behov for harmoniske stabilitetsundersøgelser for de planlagte HVDC tilsluttede vindmølleparker, da det elektriske system ændrer karakteristika ved indførsel af et HVDC anlæg. Der er endvidere et behov for at definere den harmoniske stabilitet analyseprocedure og dens anvendelse for HVDC tilsluttede havvindmølleparker.

Opnåelsen af en bedre forståelse af kompleksiteten af, hvorledes sådanne systemer (f.eks. vindmøllerne og HVDC anlægget) interagerer med hinanden, set fra en harmonisk perspektiv, vil muliggøre en mere omkostningseffektiv konstruktion af eksempelvis harmoniske filtre og reaktiv effektkompensation. Desuden vil det også sætte vindmølleparkdesigneren, såsom DONG Energy Wind Power (DEWP), i stand til at give relevante input i forbindelse med vurderingen af, hvorvidt vindmølleparken overholder de tekniske forskrifter. Endvidere sætter den øgede viden DEWP i stand til i højere grad at udforme relevante og detaljerede tekniske krav til potentielle leverandører af eksempelvis HVDC anlægget.

Formålet med ErhvervsPhD-Projektet

Formålet med dette ErhvervsPhD-projektet har været at undersøge og behandle interaktionen (fra et harmonisk perspektiv) mellem vindmølleparken, og de tilhørende kontrolsystemer i vindmøllerne og andre aktivt styret effektelektronik i transmissionssystemet med fokus på jævnstrømsforbindelsen og STATCOM'en.

Det primære fokus har været vurderingen af brugbarheden af evalueringsmetoden for harmonisk stabilitet i frekvensdomænet, der almindeligvis anvendes i designfasen af en vindmøllepark. Dette er foretaget ved at sammenligne resultaterne fra konventionelle og lineariserede frekvensdomæne analysemetoder såsom Nyquist stabilitetskriterium mod detaljerede elektromagnetisk transient (EMT) baseret modeller realiseret i PSCAD/EMTDC.

Målekampagner

Detaljerede, generiske EMT modeller af effektelektronik komponenterne typisk anvendt i havvindmølleparker er blevet opstillet og valideret på grundlag af sammenligning af måledata, for at sikre modellernes troværdighed og anvendelighed ift. harmonisk stabilitetsstudier. Måledata er blevet opsamlet på kommercielle effektelektronikkomponenter såsom den ±50 MVar store Siemens SVC Plus (STATCOM), ABB's 7 MW SVC Light (modificeret back-to-back-konfiguration) og en kommerciel type 4 vindmølle i multimegawatt størrelsen for både normal drift og under dynamiske forhold herunder emulerede kortslutningsfejl. Måledata som disse udgør en central del i industri-orienterede forskningsprojekter og bidrager med ny indsigt, relevant for den akademiske verden. En målekampagne på 1 måneds varighed er derfor gennemført i PhD-projektet på Clevehill Substation, UK, hvor fire STATCOMs er installeret. CleveHill Substation tjener som nettilslutning for den 600 MW store London Array havvindmøllepark. STATCOM'en hvorpå målingerne er foretaget er udstyret med modulære multiniveauer kaskade-koblede konvertere (MMKK), der anses som værende nyeste teknologi indenfor effektelektronik branchen. Analysen af opsamlede måledata har tilvejebragt erhvervelsen af detaljerede oplysninger, der er vurderet værdifulde for at udvikle en generisk, dog detaljeret EMT baseret model af STATCOM'en, inklusive STATCOM'ens indre dynamiske forhold, der gør sig kendetegnet ved MMKK teknologien.

Derudover har forfatteren af denne afhandling i fællesskab med kollegaer i DEWP etableret en forsknings- og udviklingsaftale mellem DEWP og National Renewable Energy Laboratory (NREL) i Boulder, Colorado, USA. NREL har for nylig idriftsat en avanceret 7 MW effektelektronik baseret testsystem. Testresultater opnået under forfatterens ophold ved NREL anvendes til at udvikle og evaluere generiske, men alligevel detaljerede EMT basserede modeller af netsimulatoren (kaldet kontrollerbar net-interface, KNI) og en kommerciel type 4 vindmølle i multimegawatt størrelsen.

Modellering og Validering af Effektelektronik Komponenterne

Det forholdsvis høje antal af ikke-lineære halvledere i MMKK'erne afstedkommer udfordringer i EMT simuleringsværktøjerne, såsom PSCAD/EMTDC, da de involverede halvledere er styret af relativt højfrekvente signaler. Endvidere ændres det elektriske systems' admittansmatrice hver gang en af disse halvledere tændes eller slukkes, hvilket forekommer på mikrosekund niveau. Der kræves en betydelig beregningsmæssige indsats for at re-triangulere admittansmatricen.

Den beregningsmæssige byrde forøges væsentligt når antallet af halvledere forøges, hvilket gør simulering af effektelektronik komponenter udstyret med MMKK i nogle tilfælde upraktisk, når der anvendes konventionelle modelleringsmetoder.

En detaljeret ækvivalent model af en HVDC station udstyret med MMKK teknologien er tidligere blevet opstillet på baggrund af den såkaldte "Nested Fast and Simultaneous Solution" procedure. Der forekommer dog visse begrænsninger for denne forrige model, som er udtrykkeligt tiltænkt MMKK'er, hvor der anvendes halvbro-konverteren som byggeklods, hvilket er tilfældet i f.eks. Siemens' og ABBs HVDC produkter baseret på spændingskildekonverter teknologien (VSC-HVDC, hvor VSC står for voltage-sourced converter).

Den noget mere komplekse struktur af fuldbro-konvertere, der anvendes i MMKK STATCOM'erne og visse VSC-HVDC systemer og visse andre aktive effektelektronik komponenter komplicerer anvendelsen af den eksisterende modelleringsteknik for disse konvertere. Der opstilles og foreslås i denne afhandling en universel modelleringsteknik, som er i stand til at repræsentere både halv- og fuldbro baseret MMKK'er i EMT værktøjer. Modelleringsteknikken er ligefrem, da den beror på opstillingen af en Norton ækvivalent af enten halv- eller fuldbro konverteren. Opstillingen af denne ækvivalent er baseret på simpel inspektion af de opstillede kredsløbsækvivalenter for henholdsvis halv- og fuldbro konverteren. Resultater fra målekampagnen ved London Array havvindmøllepark har med succes været anvendt i evalueringen af den generiske model af Siemens SVC Plus STATCOM, implementeret i PSCAD/EMTDC. Generelt kan det siges, at den foreslåede generiske model er i stand til at replicere de målte udgangs strømme og spændinger, selv med ingen oplysninger tilgængelige ift. hvorledes den kommercielle STATCOM er styret.

Den evaluerede model af STATCOM'en har gjort det muligt at udvikle en troværdig, komplet model af VSC-HVDC systemet, der ligeledes er blevet opstillet i PSCAD/EMTDC. Undersøgelser foretaget på baggrund af simuleringer foretaget på HVDC modellen har påvist konverterens evne til at styre de interne, distribuerede spændingskilder, både dynamisk og for stationære driftsforhold.

Detaljerede, generiske modeller af KNI'en og den kommercielle type 4 vindmølle installeret i testfaciliteterne hos NREL er blevet opstillet i PSCAD/EMTDC. Modellerne af disse er blevet valideret på baggrund af sammenligning med testresultater for både normale og unormale driftsforhold, såsom kortvarige og langsomt restaurerende over- og underspændingsfejl, af både balanceret og ubalanceret karakter, realiseret i forsøgslaboratoriet hos NREL. Evalueringen har vist, at det er muligt med høj præcision at simulere de målte elektriske variabler med ringe eller slet ingen oplysninger om hvorledes disse kommercielle effektelektronik komponenter er styret, ligesom det er tilfældet for STATCOM'en, nævnt i det ovenstående. Den vellykkede validering giver troværdighed til tidsdomænemodellerne af de involverede effektelektronik komponenter for harmoniske stabilitets studier i havvindmølleparker.

System Studier

Harmonisk stabilitetsundersøgelser er blevet realiseret i havvindmølleparker, hvor der anvendes effektelektronik i transmissionssystemet.

De harmoniske stabilitetsforhold i en HVDC nettilsluttet vindmøllepark er blevet undersøgt i både frekvens- og tidsdomænet ved brug af validerede modeller af effektelektronik komponenterne, nævnt i det forrige afsnit. Anvendelsen af frekvensdomænet i stabilitetsanalysen fordrer konceptuelle udfordringer ift. specifikation af "regulatoren" og "reguleringsobjektet", da både de aktivt styrede vindmøller samt HVDC anlægget kan betragtes som enten regulatoren eller reguleringsobjektet i analysen. Forskellige resultater kan forventes i tilfælde af, at vindmøllerne anses som regulatoren frem for HVDC anlægget. Tidsdomæneanalysen fordrer en mere holistisk tilgang, da behovet for specifikation af reguleringsobjektet ikke er tilstede. Baseret på en række studier er det påvist, at der findes en god korrelation mellem tids- og frekvensdomæne metoder til stabilitetsanalyser i havvindmølleparker. Begrænsninger er dog observeret for frekvensdomænetilgangen, når der forekommer resonanser i den højere ende af det betragtede frekvensområde (dvs. i nærheden af switch frekvensen og over regulatorens båndbredde). Derfor foreslås det at udføre analysen primært i frekvensdomænet, da beregningsomkostningerne er minimale ift. i tidsdomænet. Når alle specificerede driftsscenarier er dækket (typisk over 1000) i frekvensdomænet er det tilrådeligt at udvælge enkelte driftsscenarier og gentage stabilitetsanalysen i tidsdomænet, hvilket dog er både mere udfordrende og mere tidskrævende end frekvensdomænemetoden. Den harmoniske evaluering i tidsdomænet kan derved med fordel anvendes som second opinion, hvilket vil øge reliabiliteten af stabilitetsevalueringen.

En undersøgelse af de harmoniske stabilitetsforhold i en havvindmøllepark, der er nettilsluttet ved anvendelse af en STATCOM har vist at den uhensigtsmæssige harmoniske interaktion mellem vindmøllerne, det passive elektriske system samt STATCOM'en forringer STATCOM'ens evne til at kontrollere de interne dynamiske forhold.

Det blev konstateret og påvist, at det totale inter-harmoniske forvrængningsindeks, beregnet i henhold til standarden IEC 61000-4-7 er brugbar til at vurdere forekomsten af harmonisk stabilitet i tidsdomæne evalueringen. Det totale harmoniske forvrængningsindeks er på den anden side, vurderet til at indeholde meget få oplysninger om eventuel harmonisk stabilitet i havvindmølleparker.

Det blev vist, at en anvendelse af aktivt styret filtrering i den direkte kontrolkæde i vindmøllerne kan potentielt reducere de harmoniske emissioner fra vindmøllerne og effektelektronikken i transmissionssystemet. Aktiv filtrering kan, set fra et harmonisk perspektiv, forbedre den generelle stabilitet i havvindmølleparker, uden at interferere med det overordnede design af parken. Dette foretages ved, enten at tilvejebringe yderligere dæmpning eller forskyde resonansfrekvenser, eller en kombination af begge.

På grundlag af resultaterne af forskningsprojektet er der blevet formuleret en anbefaling til, hvorledes evalueringen af den harmoniske stabilitet kan foretages i havvindmølleparker, hvor der anvendes effektelektronik i transmissionssystemet.

Table of Content

Acronyms

Table I - List of used acronyms.

Acronym	Meaning
DEWP	DONG Energy Wind Power
AAU	Aalborg University, Denmark
NREL	National Renewable Energy Laboratory, Colorado, US
NWTC	National Wind Technology Center
IEEE	Institute of Electrical and Electronics Engineers
CRADA	Cooperative Research and Development Agreement
ECTS	European Credit Transfer System
TSO	Transmission system operator
WPP	Wind power plant
OWPP	Offshore WPP
LAOWPP	London Array OWPP
CPP	Conventional power plants
PCC	Point of common coupling
PED	Power electronic device
IGBT	Insulated gate bipolar transistor
GTO	gate turn-off thyristor
CGI	Controllable grid interface
FSC	Full-scale converter
NPC	Neutral-point clamping
ANPC	Active NPC
DSHB	Double star half-bridge (converter)
DSFB	Double star full-bridge
SSFB	Single star full-bridge
SDFB	Single delta full-bridge
WTG	Wind turbine generator
GSC	Grid side converter
MV	Medium-voltage
HV	High-voltage
HVAC	High-voltage alternating current
HVDC	High-voltage direct current
DC	Direct current
AC	Alternating current
VSC	Voltage-sourced converter
LCC	Line commutated converter
FACTS	Flexible AC transmission system
STATCOM	Static compensator
MMCC	Modular multi-level cascaded converter
TSC	Thyristor Switched Capacitor/Test side converter
TCR	Thyristor Controlled Reactor
SVC	Static var compensator
SM	Sub-module
SRF	Stationary reference frame
RRF	Rotating reference frame

Table I (continued) List of used acronyms.

Acronym	Meaning
ARMA	auto regressive moving average (model)
FDNE	Frequency dependent network equivalent
PI	Proportional-integral OR used as a cable model designation
FRT	Fault ride-through
LVRT	LV ride-through
HVRT	HV ride-through
BRF	Band rejection filter
ASCP	Available short circuit power
MSR	Mechanically switched reactor
CT	Current transducer
VT	Voltage transducer
DUT	Device under test
PMG	Permanent magnet generator
IG	Induction generator
THD	Total harmonic distortion
TIHD	Total interharmonic distortion
HSG	Harmonic subgroup
IHG	Inter-harmonic subgroup
FFT	Fast Fourrier transformation
GM	Gain margin
VGM	Vector gain margin
PM	Phase margin
POD	Phase opposition disposition
APOD	Alternative POD
PWM	Pulse-width modulation
PSPWM	Phase shifted PWM
OPWM	Optimised PWM
ICC	Inner current controller
PLL	Phase-locked loop
OFTO	Offshore transmission system ownership
DPL	DigSILENT Programming Language
FDPM	Frequency dependent phase (cable) model
TDM	Time domain model
FDM	Frequency domain model
DEM	Detailed equivalent model
EMT	Electromagnetic transient
EMTP	EMT program
AVM	Average model
WSC	Waveshaping circuit

PART I
Introduction and Problem Analysis

Part I of this dissertation presents the introduction, background, scope and expected deliverables from this Industrial PhD project. This part furthermore defines the research approach taken and the thesis outline.

Chapter 1 Introduction

This chapter presents a description of nowadays large offshore wind power plants (OWPPs) with widespread usage of power electronic devices (PEDs). Selected challenges and opportunities, related to this Industrial PhD project will be described.

The overview given in this chapter provides the information needed for defining the scope and expected deliverables from the PhD project, which will be presented in the following chapter.

1.1 Nowadays Offshore Wind Power Plants

The trend in power generation is to partly replace conventional power plants (CPPs) with renewable energy sources. Offshore wind power has been selected to take up a significant proportion of renewable energy [1-3]. Figure 1-1 shows the global wind capacity growth [4,5]. Offshore as well as onshore wind power plants (WPPs) have different characteristics from the CPPs, especially due to the fluctuating wind and in case the WPP is connected to a weak system [6-9] The grid codes have been updated to accommodate the rising share of wind power [6,10]. The WPP therefore has to meet the same stringent requirement as the CPPs, which can be accommodated by employment of flexible alternating current (AC) transmission system (FACTS) devices such as the static compensator (STATCOM) [11,12].

Nowadays, OWPPs are connected through a widespread medium-voltage cable system and grid connected using long high-voltage (HV) cables, representing challenges related to e.g. harmonics [13,14].

The trend is to locate the OWPPs even further from shore, which gives rise to a number of challenges to the wind power industry with regard to construction, installation as well as transmission of the generated energy [15-17].

The STATCOM and the voltage-sourced converter high-voltage direct current (VSC-HVDC) are attractive solutions for grid connection of remotely located OWPPs, as will be described in more details in section 1.2. A review of the state-of-the-art STATCOM and VSC-HVDC is provided in chapter 3.

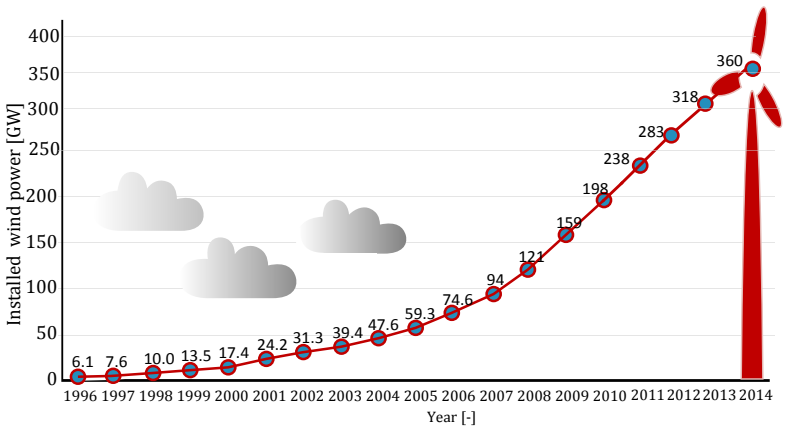

Figure 1-1 Global wind capacity.

1.1.1 Wind Turbine Generator

Wind turbine generators (WTGs) with back-to-back full-scale converters (FSCs) (i.e. type 4 [18]) are typically used in OWPPs [1,19]. The FSC enables independent control of the frequency of the generator and thereby operating the WTG in variable speed mode, which leads to higher efficiency, reduced loading on the gear box and drive train [20]. Furthermore, the type 4 WTGs can provide good reactive power support, and fault ride-through capability [18].

The WTGs are grid friendly power system components in most power quality aspects. However, due to the previously mentioned characteristics of OWPPs (i.e. the extensive sub-marine cabling), the application of actively controlled WTGs significantly increases the complexity of the OWPP structure [21] This is especially true for the OWPP's harmonic stability, as described in section 1.3.

1.2 OWPP Grid Connection Employing Power Electronic Devices

The application of the VSC-HVDC and the STATCOM for grid connection of OWPPs will briefly be described in this section.

1.2.1 HVDC for OWPPs

The VSC-HVDC technology seems to be a potential solution to the challenges related to grid connection of remotely located OWPPs. The VSC-HVDC technology has therefore become the preferred choice for grid connection of a large number of the planned OWPPs in e.g. the United Kingdom Round 3 projects and in Germany [16, 22, 23].

HVDC Technologies

There exist fundamentally two HVDC technologies: (*i*) the conventional thyristor-based line commutated converter (LCC)-HVDC, which is a well-proven technology, with the first application in 1954 in Gotland [24]. (*ii*) VSC-HVDC, which is a relatively new technology under development [25-27]. The VSC technology was initially developed for drive technologies [28]. Due to significant increase in voltage and power ratings of semi-conductors such as the insulated gate bipolar transistor (IGBT), the VSC-HVDC scheme started to find applications in the late 1990s, especially when the interconnected AC networks had low short circuit levels or where a small footprint was required [29-32].The maturity of the LCC- and the VSC-HVDC systems is illustrated in Figure 1-2 in terms of publications in a popular electrical engineering database. The Institute of Electrical and Electronics Engineers (IEEE) is considered by many as the biggest professional association gathering electrical and electronics engineers from many fields and is thus considered here. From Figure 1-2 it can be seen that the research on the LCC-HVDC is more matured and the growth rate is still comparable with that of the VSC-HVDC, although the latter is becoming more and more popular.

The VSC offers several advantages over the LCC-HVDC scheme, as the IGBT can be turned on/off using an electronic gate signal [29]. This offers a number of advantages including: Less sensitivity to the strength of the AC network, black start capability of the converter, fast and decoupled control of bi-directional active and reactive power flow [30-35]. Furthermore, the VSC-HVDC's DC link voltage is not required to invert polarity in case of power flow reversal as in the LCC scheme. This uni-polarity makes it possible to use extruded polymer cables, which offer the advantages of lower weight and cost compared to the mass-impregnated cables used in the LCC-HVDC scheme [24, 36]

Due to its higher power rating, the LLC scheme is the preferred choice for grid connection of remote located onshore wind power plants (WPPs) in e.g. China [37]. As the onshore footprint requirements are less strict compared to offshore installations, it is possible to install large filters associated with the LCC scheme and an additional STATCOM. The STATCOM will in this situation offer similar capabilities in terms of e.g. reactive power control and voltage support, required for LCC converter commutation [38].

VSC-HVDC grid connection of onshore and offshore WPPs is to some extend electrically similar (the sub-marine cables have a more complex structure due to e.g. armouring), but offshore installation is associated with higher cost and risks as well as stricter footprint requirements. It might therefore be more feasible to employ the LCC scheme onshore, as outlined in the above. For onshore WPPs it might be possible to use overhead lines in the DC system, depending on local conditions.

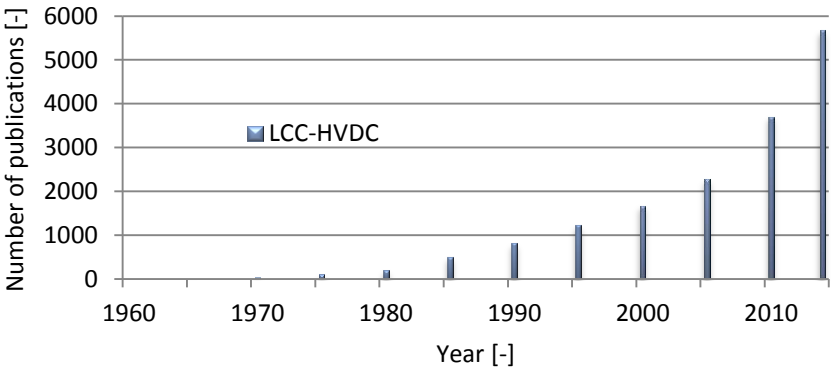

a) Literature on LLC-HVDC in the IEEE Explorer database. (5 year interval).

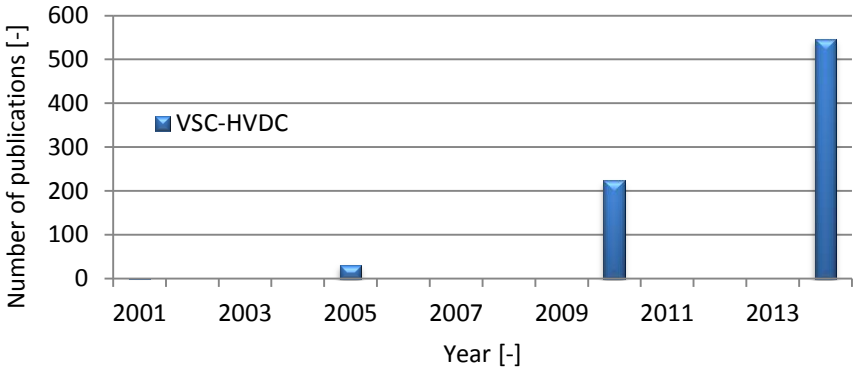

b) Literature on VSC-HVDC in the IEEE Explorer database. (5 year interval).

Figure 1-2 Literature on the LCC- and VSC-HVDC in the IEEE Explorer database. (The number of publications in the first few years for both technologies is so low that it is not visible on the applied scale. These are still included in order to map the first occurrence of a publication).

VSC-HVDC for OWPP Grid Connection

For high power VSC-HVDC transmission system applications, the three main topologies utilized so far are the two-level, three-level converters and the relatively new modular multi-level cascaded converter (MMCC) [30, 39, 40]. Whereas only the Trans Bay Cable project utilizes the merging MMCC technique [23], the two- and three-level topologies have found their application in a number of installations, as outlined in Table 1-1 [24, 41, 42]. A review of the three main topologies (and some of their variants) is briefly given in chapter 3.

Seven projects using the VSC-HVDC for grid connection of an OWPP are listed in Table 1-1, where BorWin1 is the only commissioned at the time of writing. Hence, it is evident that there is very limited experience using the VSC-HVDC technology for both OWPP grid connection and for more conventional interconnection of two power systems. A large number of future OWPPs, which are not listed in Table 1-1, are considered in e.g. the UK, but a VSC-HVDC vendor has not yet been decided [22].

Table 1-1 Overview of selected VSC-HVDC projects.

Installation	Installed	Manufacturer	P_{rated} [MW]	Converter topology
Gotland	1999	ABB	50	2-level (1st gen.)
Murraylink	2002	ABB	220	3-level (2nd gen.)
Estlink	2006	ABB	350	2-level (3rd gen.)
BorWin1 (OWPP)	2009	ABB	400	2-level (3rd gen.)
Trans Bay Cable Project	2010	Siemens	400	MMCC
BorWin2 (OWPP)	2013	Siemens	800	MMCC
HelWin1 (OWPP)	2013	Siemens	576	MMCC
DolWin1 (OWPP)	2013	ABB	800	MMCC (4th gen.)
SylWin1 (OWPP)	2014	Siemens	864	MMCC
South-West Link	2014	Alstom	1440	MMCC
HelWin2 (OWPP)	2015	Siemens	800	MMCC
Dolwin2 (OWPP)	2015	ABB	900	MMCC

The VSC-HVDC system is associated with a high initial cost, but the marginal cost per MV is relative low, making it advantageous to connect multiple OWPPs (or clusters) to a common offshore HVDC hub [16, 17, 42]. Figure 1-3 shows three candidate configurations for grid connection of OWPPs using VSC-HVDC. Whereas BorWin1 in Germany is the only operating VSC-HVDC connected OWPP using the point-to-point in Figure 1-3a, it is expected that future grid connections will be made by connecting the offshore HVDC terminal either on the AC and/or on the DC side of the converter (Figure 1-3a and b) [15,16]. As large OWPP clusters are distributed over a large physical area with different wind conditions it is possible to optimise the utilisation and loading of the VSC-HVDC converters using these configurations. As an example, VSC-HVDC 1 can be used to transmit the produced power in case of low wind at OWPP 1 and full production from OWPP 2 in Figure 1-3b, while VSC-HVDC 2 is out of service for maintenance purposes etc.

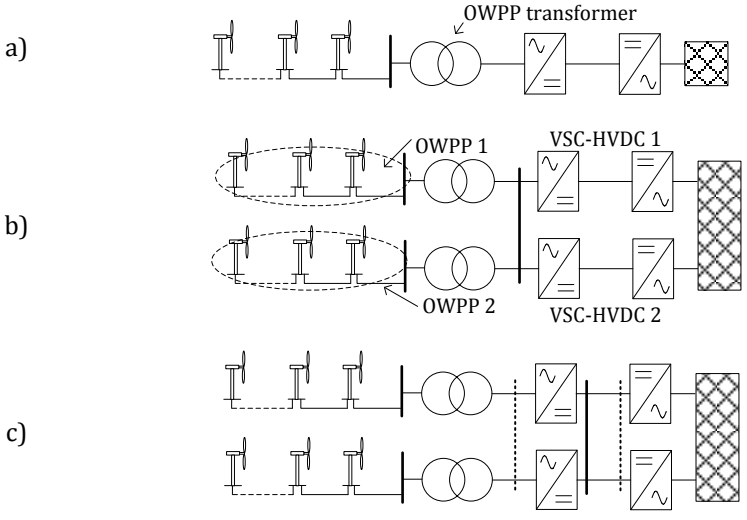

Figure 1-3 Simplified single line diagrams of grid connection of OWPP(s) using a) point-to-point VSC-HVDC b) parallel point-to-point connected on the offshore AC side, fed by multiple OWPPs c) multi-terminal. HVDC converter transformers (if any) have not been included in the figures.

In the following are listed some of the main advantages of VSC-HVDC for OWPP grid connection: [17, 29, 42]:

- Most economically/technically feasible grid connection solution for longer transmission distances. (The actual break-even distance is a complex figure, which is affected by factors such as the rating of the OWPP, the limited experience with HVDC grid connected OWPPs and the limited number of VSC-HVDC vendors etc. The feasibility of employing the HVDC in the OWPP grid connection should be done for a specific case).
- Can be connected to a weak grid and hence does not suffer from commutation failures.
- Does not require reactive power compensation as the LCC-HVDC, which alleviates the need for e.g. a synchronous machine at the offshore platform.
- Low (or no) filter requirements.
- Lower space-requirement compared to the LCC-scheme, which is a major factor for offshore applications.
- Able to transmit power from zero to full rating in both directions, which enables OWPP start-up (black start capability) and low wind speeds operating capabilities. (For OWPP applications, the bi-directional power capability could be advantageous in multi-terminal grids).
- The VSC-HVDC system decouples the onshore and offshore AC grids; hence a fault in e.g. the onshore grid is not transferred to the offshore grid, which can lower the fault ride through requirements of the WTGs (depending on local regulations).
- The AC decoupling makes it possible to use different frequencies in the offshore (i.e. within the OWPP) and onshore grid.

Figure 1-4 illustrates the research interest in the HVDC grid connected OWPPs. The number of publications is significantly increased in the few recent years. Comparing with Figure 1-2b it can be seen that the majority of the VSC-HVDC research has been in connection with grid connection of OWPPs.

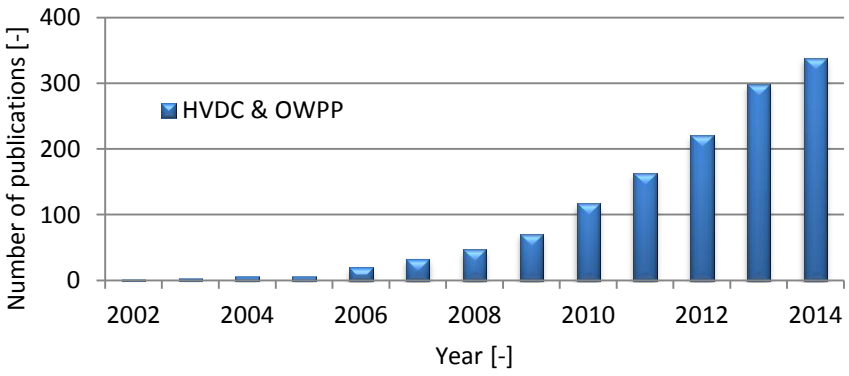

Figure 1-4 Number of publications in the IEEE database using the keywords “HVDC” and “offshore wind farms.”

1.2.2 Selected Challenges Associated with VSC-HVDC for OWPP Grid Connection

The new system configuration requires in-depth knowledge of all relevant technical aspects, including e.g. the involved control systems performance and robustness for all possible operating conditions. The transmission system operator (TSO) might impose new control requirements when VSC-HVDC is going to be used for OWPP grid connection and the dynamic compliance specifications might change. This sets up a need to develop new strategies for ensuring robustness and adaptability, considering aspects such as fault-handling, ancillary services, congestion management, harmonics etc. It is therefore important to analyse and assess all possible control aspects related to the interaction between the OWPP and the PED in the transmission system.

The harmonic stability is considered a core concern within the industry [21] and will be addressed in this research project. A description of the harmonic stability phenomena is given in section 1.3. The research project does not only consider the VSC-HVDC grid connected OWPPs, but also OWPPs with STATCOMs at the grid connection point, as this grid connection methodology is widely used for grid connection of OWPPs in e.g. the UK [12, 43, 44]. A description of the STATCOM is thus given in the following section.

1.2.3 FACTS for OWPPs

The wind energy integration into the power system on such a large scale as shown in Figure 1-1 is not straightforward [17]. Previously, due to the low wind penetration level, the grid codes did not consider the effect of the OWPP [6, 10]. The power system and its operation was designed and developed with CPP as the cornerstone [45]. OWPPs have different characteristics from the CPPs [17] and the effect of the OWPP on the connected power system can no longer be neglected [46].

The rising share of wind energy (and renewable energy sources in general) will inevitably affect the power system's performance and stability [47] The TSOs are aware of these challenges and have outlined rights and responsibilities for the connection of the WTGs and OWPPs to the electrical power system [6, 10, 48]. Current grid codes require OWPPs, in a similar way as CPPs, not only to ride through numerous power system disturbances, but also to contribute to network stability support and the provision of ancillary services [49]

In order to accommodate the above mentioned challenges and meet with relevant grid code "add-on" equipment such the STATCOM may be considered [11]. As previously mentioned, the STATCOM is part of the FACTS family. FACTS devices have been used for some decades in order to improve system stability, voltage regulation and for other purposes as described in [44, 45].

The thyristor based Static Var Compensator (SVC) has historically been the most popular choice to meet these requirements [43, 44]. The Thyristor Switched Capacitor (TSC) supplies the SVC's capacitive reactive power and a Thyristor Controlled Reactor (TCR) supplies the inductive reactive power. The output of the TSC is either zero or full reactive power, whereas the TCR can be continuously controlled to output zero to rated inductive reactive power by controlling the switching angle. Continuous control in the capacitive range is made by controlling the TCR to cancel the current of the TSC.

The FACTS family was extended by the introduction of the two-level static compensator (STATCOM), employing self-commutated elements such as the gate turn-off thyristor (GTO), which was introduced in the nineties [50]. The STATCOM has a much better dynamic performance compared to the SVC, as the change in reactive power supply/absorption is done merely by adjusting the magnitude of the output voltage. Another advantage of the STATCOM over the SVC is that it can provide rated reactive power at very low voltage level [51].

The main drawbacks of the two-level STATCOM include (but are not limited to) high switching losses at relatively high switching frequency and large filters [25]. A GTO based MMCC STATCOM was introduced in 1998 to alleviate these drawbacks [52, 53]. The state-of-the-art MMCC STATCOM

employs IGBTs rather than GTOs and consists of a number of distributed DC voltages, which are incrementally inserted or by-passed in order to synthesise a high quality sinusoidal voltage waveform. The MMCC technology was extended to the VSC-HVDC system in [54] and the MMCC is now considered state-of-the-art for both the VSC-HVDC and the STACOM (as can be observed from Table 1-1 and Table 1-2) [17].

Table 1-2 shows an overview of selected STATCOM projects based on the MMCC topology.

Table 1-2 Overview of selected STATCOM projects based on the MMCC topology [52, 55].

Installation	Installed	Manufacturer	Q_{rated} [MVAr]	Number of STATCOMS [-]
East Claydon	2001	Areva	150	2
Glenbrook	2003	Areva	150	2
Thanet (OWPP)	2009	Siemens	100	2
Greater Gabbard (OWPP)	2010	Siemens	150	2
Kikiwa	2010	Siemens	70	2
London Array (OWPP)	2011	Siemens	200	4
LINCS (OWPP)	2011	Siemens	100	2
Wycarbah	2012	Siemens	300	3
Gwynt y Môr (OWPP)	2012	Siemens	100	2
West of Duddon Sands (OWPP)	2014	Siemens	100	2

1.3 Harmonics in OWPPs

Harmonics are a core concern in the offshore wind industry, due to the converter rich grid with extensive sub-marine cabling. Based on the working experience at DONG Energy Wind Power, the author distinguishes between three harmonic categories as described in the following.

Harmonic Emission from the PEDs

Some of the many advantages of using the type 4 WTG were given in section 1.1.1. As a side effect, the PEDs act as harmonic sources.

The harmonics emitted by the individual WTG contribute to the overall harmonic generation of the entire OWPP [56]. Some the harmonic components may be correlated to the fundamental frequency, some may be correlated to the PED modulation strategy [57]. Furthermore, harmonics can be attenuated internally within the OWPP using either passive or active filtering [58].

Due to the passive components, such as the capacitance of the extensive cabling and the inductance of the transformers, series and parallel resonances will occur. These resonances may either increase or decrease a given voltage or current harmonic component.

OWPP Acting as a Harmonic Sink

The extensive cabling in the export system of an HVAC grid connected OWPP may act as a sink to back-ground harmonics present in the external grid.

Harmonic Stability

OWPPs are susceptible to the harmonic instability, where the extensive sub-marine cabling and possible low available short-circuit power (ASCP) at the point of common coupling may create resonance(s) within the bandwidth of the WTG controller [7, 21, 58].

High grid impedance is commonly considered to be the main factor in the destabilisation of the converter [7, 9, 59]. However, due to the OWPP characteristics previously mentioned not only the possible low available short-circuit power at the point of common connection but also the extensive sub-marine cabling will inevitably create resonance(s) within the WTG converter's controller bandwidth [7, 21, 58]. The interaction may result in an unacceptable high harmonic distortion level [12], which will reduce the efficiency of the generation and transmission of the electrical energy in the OWPP. Furthermore, the increased harmonic distortion level will increase the thermal stresses of the PEDs and passive components such as the WTG transformer and the inter-turbine cables in the internal OWPP collecting grid, causing accelerated component ageing and may cause malfunctioning of the OWPP protection system. In addition, harmonic instability may lead to excessive overvoltages, which will cause the disconnection of the WTG(s) leading to loss of production, which, due to the size of nowadays OWPPs, will have a serious impact on the revenue. Harmonic stability studies of grid-connected converters with the power system (i.e. the investigation of the converter's current controller's susceptibility to resonances in the power system) have received academic focus in recent years due to the rapidly increasing penetration of renewable energy and distributed generation resources e.g. [8,9,12,17,21,58-63] as well as railway networks [64, 65]. Harmonic stability studies have also become an important part of the system design studies of an HVAC grid connected OWPP. Similarly, harmonic stability studies are needed for the planned VSC-HVDC grid connected OWPPs. Since the offshore electrical environment is significantly altered compared to the offshore network in an HVAC connected OWPP, there is a need to define the harmonic stability assessment procedure and its application for the HVDC grid connected OWPPs. Similarly, there is a need to assess the modelling requirements of the HVDC system.

Currently, the harmonic stability studies for HVAC connected OWPPs are mainly done in the frequency domain [7, 21, 58], since the electrical system can be analytically described and conventional indices such as e.g. the Nyquist stability criterion can be applied [21]. As outlined in [12], there are limitations to frequency domain analysis, as linearization is done on both the non-linear switching devices as well as the control system. Furthermore, saturation effects of e.g. transformers and the integrator part of the PED proportional-integral (PI) controller are neglected. These effects can (depending on the modelling detail) be included in the time domain model description. Limitations of the time domain approach include both time-consuming model implementation and initialisation of the developed model. Furthermore, the time domain approach does not directly indicate the stability margins of the system. Based on frequency and time domain harmonic stability studies in [21] and [12], respectively, it was shown that the harmonic impedance in the HVAC connected OWPP is highly affected by the number of WTGs in service. It is therefore necessary to perform in the range of thousands of study cases to cover all possible operating points of the OWPP and the external network. Similarly, a very high number of cases need to be covered in the harmonic stability studies of an HVDC connected OWPP. This is somewhat straightforward in the frequency domain, whereas it will be more challenging in the time domain, due to the limitations mentioned in the above and more detailed in [12].

The application of the frequency domain in the stability analysis rises the conceptual challenge of recognising the source and the load (i.e. the plant), as either the grid (in HVAC grid connected OWPPs) or the WTG converters can be treated as the source in the analysis, yielding different results [9] The challenges become even more relevant in case of HVDC grid connected OWPPs. In this case both the load and the source are actively controlled power system devices. The time domain approach on the other hand provides a holistic approach, without the need to assign the source in the analysis.

Typically, the stability of grid connected converters are tested using an average converter model in the time domain, which is considered valid up to a frequency significantly lower than the switching frequency [8]. The application of an average converter model in the time domain is essentially the dual to the frequency domain representation (with the exception of e.g. saturation effect of transformers and the PI controller's

integrator), and thus do not provide more information on the current controller's susceptibility, which is not readily available from the frequency domain model. Detailed time domain models taken into consideration the switching devices of both the WTGs, the STATCOM and the HVDC system is considered in this work in order to provide a more realistic evaluation of the frequency domain and its application in the design phase of HVDC or STATCOM grid connected OWPPs.

Figure 1-5 shows a visualisation of the three OWPP grid connected methodologies considered in this project (HVAC grid connected OWPP without and with PED in the transmission system and VSC-HVDC grid connected OWPP, figure a, b and c, respectively). The highly simplified single line diagrams in the figure also indicate possible resonance paths, as seen from the PED terminals (red for the individual/grouped WTG(s) and blue for the STATCOM and VSC-HVDC). As indicated in figure b, the external system contains background harmonics, which may be amplified due to the capacitance presented by the OWPP. As indicated in figure a, the external system also contains a number of resonances. The frequency characteristics of the external grid are highly affected by the operating conditions of the system. In general all of these conditions should be considered in all harmonic studies for HVAC grid connected OWPPs. In reality, this is impractical (especially in the time domain). Typically, the grid impedance is provided by the TSO to the OWPP developer in the form of an impedance area for the harmonic emission analysis and a few discrete points on the boundary of the area should be considered [56].

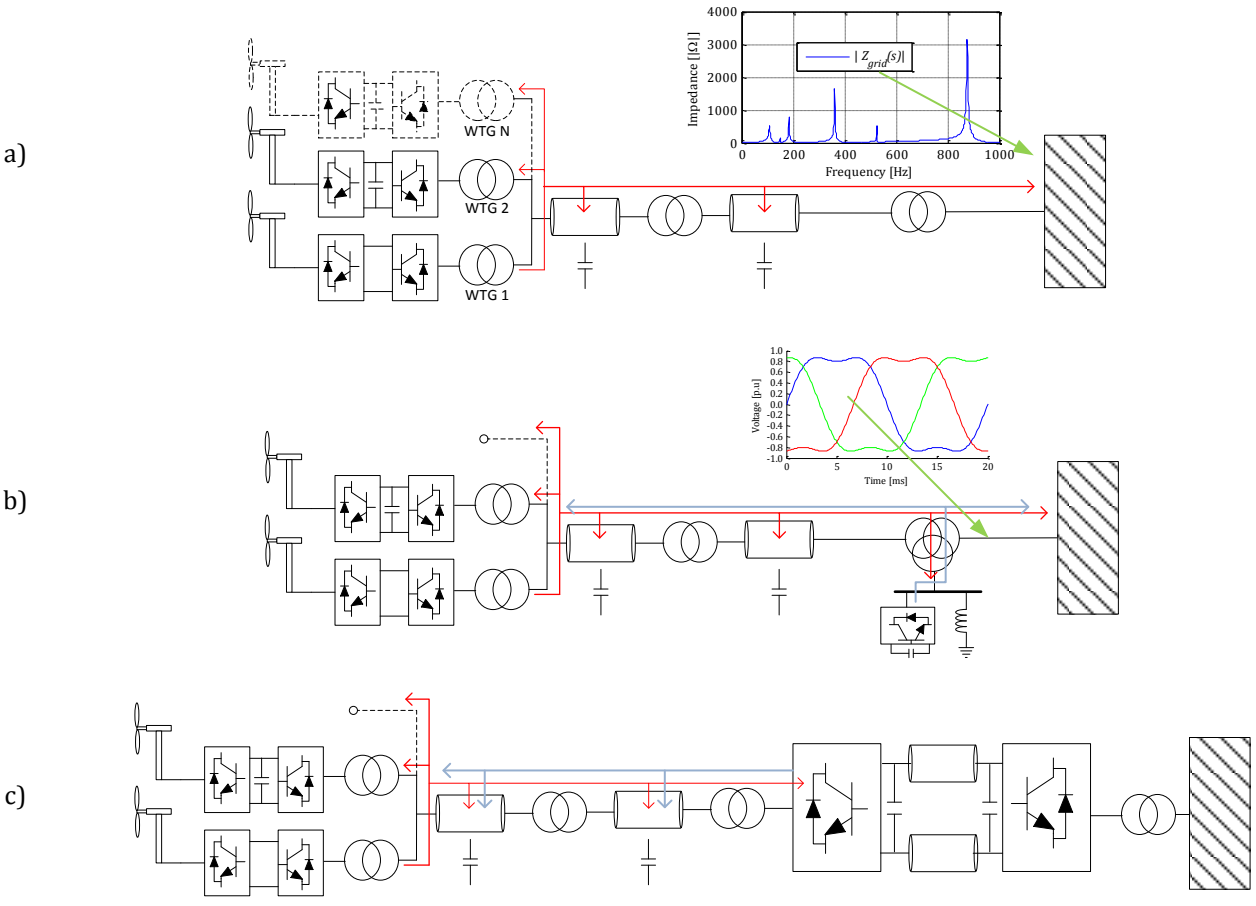

Figure 1-5 Simplified single line diagram of three candidate OWPP grid connections. a) Conventional grid connection without PED in the transmission system. b) A STATCOM located at the onshore substation. c) Grid connection empoying an HVDC link. The figures are highly simplified, possible shunt filter and passive reactive power compensation are not included etc.

1.4 Chapter Summary

An overview of possible grid connection of remotely located OWPPs has been given. Challenges related to harmonics in OWPPs have been described with main emphasis on the harmonic stability, as this is the topic of this Industrial PhD project.

Based on the overview given in this chapter it is possible to define the motivation and scope of the PhD project as will be done in the following chapter.

Chapter 2 Problem Definition

An overview of grid connection methodologies of offshore wind power plants (OWPPs) and harmonic challenges related hereto were given in the preceding chapter. The scope and deliverables from this Industrial PhD project are presented in this chapter, based on the overview in chapter 1. This chapter furthermore defines the approach, limitations and thesis outline.

2.1 Background

OWPPs can be characterized as a power electronic device (PED) rich grid, as described in the preceding chapter. The PhD project is expected to develop a deeper understanding on how the PEDs and associated control systems interact (from a harmonic perspective) with each other and with the passive electrical components in the OWPPs, such as the extensive submarine cabling.

The purpose is to meet a necessary need to develop and strengthen DONG Energy Wind Power's (DEWP's) in-house competencies with regard to electrical system modelling and analysis of large OWPPs employing PEDs in the transmission system, such as the Static Compensator (STATCOM) and the voltage-sourced converter high-voltage direct current (VSC-HVDC, hereafter denoted HVDC for brevity).

By achieving a better understanding of the complexity of how such actively controlled systems interact with each other, seen from a harmonic perspective, it will be possible to make a better and more cost-efficient design of e.g. harmonic filters, reactive compensation etc. This will eventually enable DEWP to optimise the overall electrical infrastructure in modern OWPP incorporating a number of power electronic devices (PEDs), which is of key importance for timely grid connection of the OWPP.

Furthermore, the attained knowledge enables DEWP to give relevant input during the grid code compliance process of an OWPP. The project will enable DEWP to get the right information for e.g. the HVDC system in due time during the design of an OWPP and will lead to lowering the risks in each of DEWP's OWPP projects. Additionally, the project aids DEWP define technical requirements to potential suppliers and increase the in-house competencies required for optimised OWPP design,

2.2 Research Objectives

This Industrial PhD project will mainly focus on investigating the best possible way(s) to perform harmonic stability studies in HVAC and HVDC grid connected OWPPs. The project aims at gaining new insight, methods and models, which will contribute to achieve a better understanding of the harmonic stability phenomena in OWPPs. Eventually, the knowledge and applicable models expected to be derived within the project will enable the involved parties (e.g. the OWPP developer and the power electronic device (PED) vendors) to improve e.g. the filter design and in general ensure a high degree of reliability of future OWPPs where PEDs are widely applied.

In order to achieve the above-mentioned goals, the following main objectives are defined as:

- To obtain knowledge of the modular multi-level cascaded converters (MMCCs) for wind power integration (HVDC and STATCOM).
- **Develop and validate appropriate models of the PEDs, including the MMCCs.**
    - In time and frequency domain, where found applicable.
    - Conduct field measurement campaign for model validations.
- **Investigate OWPP harmonic stability issues** for frequencies above the fundamental frequency with widespread use of active PEDs.
    - Compare different stability assessment methods **in time and frequency domain.**
- **Develop a best practice for harmonic stability assessment in OWPPs.**

2.2.1 Formulation of Specific Research Questions

In order to meet the main objectives stated in the above, the following research questions have been formulated:

1. What is the state-of-the-art for the MMCC technology for HVDC and STATCOM systems?
2. Is it possible to develop generic yet detailed models of the WTGs, HVDC and STATCOM systems for harmonic studies in OWPPs?
    a. What are the required modelling details?
    b. How are PEDs typically controlled?
    c. How can the developed models be evaluated?
3. How is the harmonic stability in OWPPs currently evaluated?
4. What is the state-of-the-art harmonic instability mitigation means applied in the OWPPs nowadays?
    a. Can these mitigation means be applied in OWPPs with PEDs in the transmission system?
5. What are the advantages/limitations of using a time or frequency domain approach in the evaluation of harmonic stability in OWPPs?
    a. What are the pros/cons using the two domains?
    b. Is there a correlation between the results obtained in the two domains?
    c. Is it possible to utilise the advantages of each of the domains in the stability assessment?
    d. Taking into account the above questions, is it possible to derive a procedure for evaluation of the harmonic stability in OWPPs with PEDs in the transmission system, which can be applied in the design phase of future OWPPs?

2.3 Approach and Methodology

The methods which will primarily be applied in this Industrial PhD project include literature study and theoretical analysis, measurement data acquisition and post-processing, component modelling and validation and finally power system simulations and analysis based on the developed models.

2.3.1 Literature study and Theoretical Analysis

Theoretical analysis is a suitable method during the study of the PEDs used in the WTGs and in the transmission system. The study will include the working principle of the state-of-the-art type 4 WTGs, the MMCC HVDC and the MMCC STATCOM, on their topology and control methodology. The state-of-the-art review on the MMCC technology includes both previous work in academia and especially what is offered by relevant vendors, as this is relevance to OWPP developers such as DEWP. The review will focus on the topology of relevant converter systems and on the structure of the applied control system.

A fundamental understanding of the time and frequency domains must be obtained in order to assess their application for harmonic stability studies in OWPPs. This will be achieved by reviewing the existing methods used in the industry as well as academic contributions.

A review on the typical modelling of the internal OWPP cable collecting grid and the external power system (in HVAC grid connected OWPPs) enables the PhD student to develop and implement a suitable model in the simulation tool(s).

2.3.2 Measurement Data Acquisition and Processing

One of the main advantages of being an Industrial PhD project is the possibility to conduct field measurements on commercial power system components.

Two measurement campaigns have been conducted within the current project as described in the following.

MMCC STATCOM located at the grid connection point of London Array OWPP

A long term harmonic measurement campaign has been conducted at the CleveHill onshore substation, connecting London Array OWPP to the transmission system. Four STATCOMs are located at CleveHill substation, and measurements were made on one of these. The purpose of the measurement data is foremost to obtain real life knowledge of the STATCOM and for model development and evaluation.

The STATCOM measurement could furthermore be used to gain in-depth knowledge on how such a MMCC based PED acts a harmonic source. This could then be transferred into a harmonic emission model of the STATCOM. The one month duration of the campaign was therefore selected in order capture a large number of operating conditions of the STATCOM, the OWPP and the external grid, as each of these will have an impact on the harmonic emission of the STATCOM.

As described in section 2.1, the main scope of this project is the evaluation of the harmonic stability phenomena in OWPPs; hence the evaluation of the harmonic emission is suggested for future work, see section 14.6.

The obtained measurements are considered a significant contribution from this work, as there is no previously public available high-resolution measurements data on an actual STATCOM. The measurements have also been utilised in improving the author's knowledge on MMCCs, which is needed for detailed STATCOM modelling as well as for evaluation of the model.

Measurements at National Renewable Energy Laboratory (NREL), Colorado, US

The author has had the pleasure of being employed as a guest researcher at the National Wind Technology Center (NWTC) at NREL as part of the PhD project. The NWTC commissioned an advanced grid simulated test system during the author's stay at the research facility. The grid simulator (referred to as Controllable Grid Interface, CGI) is capable of supporting multiple types of grid compliance tests, including low and high-voltage fault ride-through (LVRT and HVRT, respectively), frequency response, and voltage support for WTGs and other types of renewable energy sources and storage units (a system description is given in chapter 7).

According to the author's knowledge, the CGI shown in Figure 7-3 on page 84 is a modified version of ABB's SVC Light (PCS 6000) [66].

Tests on a commercial multi-megawatt sized type 4 WTG connected to the CGI for both normal and abnormal operating conditions (e.g. LVRTs of various types and durations) were realised during the author's three stays at NREL. The test results were found to provide a useful source of information on how commercial PEDs are controlled and how they respond to e.g. a full single-phase fault at their terminals. The test data was furthermore used to develop suitable generic models of the PEDs for harmonic stability studies as described in the following.

2.3.3 Component Modelling and Validation

When the relevant knowledge of the above mentioned PEDs is defined and described in the theoretical analysis, it will be transferred into simulation models intended for harmonic stability studies in OWPPs. The models will be validated by comparison of simulation results with measurement data in the time domain.

The acquisition of detailed generic models of the PEDs (especially the STATCOM and the HVDC) enables one to gain further insight on e.g. the MMCC's working principles, which might not have been possible by the literature study alone. Having these models is deemed valuable to DEWP, as it enables the company to acquire relevant information and specify relevant requirements related to harmonic stability in the early stages of the negotiations with possible PED vendors.

Active Component Modelling in the Time Domain

Generic, yet detailed electromagnetic transient (EMT) models of the following actively controlled PEDs have been developed and implemented in the simulation tool PSCAD/EMTDC:

- WTG (normal as well as abnormal operating conditions).
- CGI (normal as well as abnormal operating conditions).
- MMCC STATCOM.
- MMCC HVDC.

The measurement data obtained within the project will be used to evaluate the developed models of the WTG, the CGI and the STATCOM. Based on the reflections presented in Chapter 3 to 6 it is considered that the validated model of the MMCC STATCOM can be transferred to the generic MMCC HVDC.

Harmonics in power systems are considered a steady-state operating condition [67]. The model evaluation of the WTG and the CGI during abnormal operating conditions might therefore appear to be unnecessary in relation to this research project. However, the evaluation has been included in the work presented in this report due to the following considerations:

- Provides in-depth insight of the operating characteristics of commercial PEDs, which was proven very useful in the modelling and further evaluation of the PEDs.
- Active filtering is typically used in the direct chain of the WTG's current control system, as described in chapter 10. Hence, the active filtering might impede the dynamic response of the WTG during e.g. faults. Having validated generic models of the WTG (without any active harmonic filtering) during faults enables the researcher to evaluate the dynamic impact of these filters by simply adding the active filtering described in Chapter 10 into the already validated model and compare the results. This is suggested for future work.
- A Cooperative Research and Development Agreement (CRADA) was signed between NREL and DEWP in order for the author to be employed as a guest researcher at NREL. Deliverables from the CRADA include both modelling and evaluation of the PED models. Thus, the modelling and validation of the abnormal operating conditions was a prerequisite for the establishment of the CRADA.

Active Component Modelling in the Frequency Domain

As defined in section 2.1, the main focus of this research project will be on the evaluation of the frequency domain with regard to the time domain method. Linearized models of the PEDs therefore need to be developed and implemented in a suitable simulation tool (in this work DigSILENT PowerFactory and MatLab).

Passive Component Modelling

The relatively complex structure of converter rich OWPPs with extensive submarine cabling possesses modelling challenges (especially for time domain simulations using EMT programs (EMTPs). Therefore, suitable methods for representation of the OWPP and the external power system (in HVAC connected OWPPs) must be devised.

2.3.4 Power System Simulations

Simulations studies are useful in order to investigate and understand possible phenomena related to harmonic distortion in an OWPP with the possible employment of PEDs in the transmission system. The investigation at system level will be done on basis of the validated models and will be carried out in both time and frequency domain. As defined in section 2.1, the main focus will be on the evaluation of the frequency domain with regard to the time domain. The electrical system considered in this work is presented in Figure 2-1. Figure 2-1a shows a generic overview of an aggregated OWPP. An export cable connects the OWPP to one of the three external systems shown in Figure 2-1b.

a)

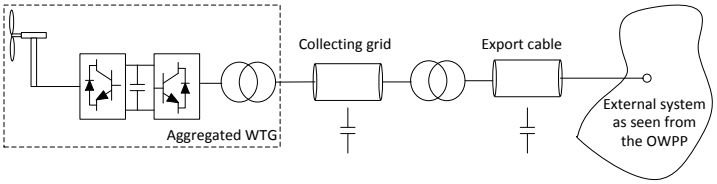

b)

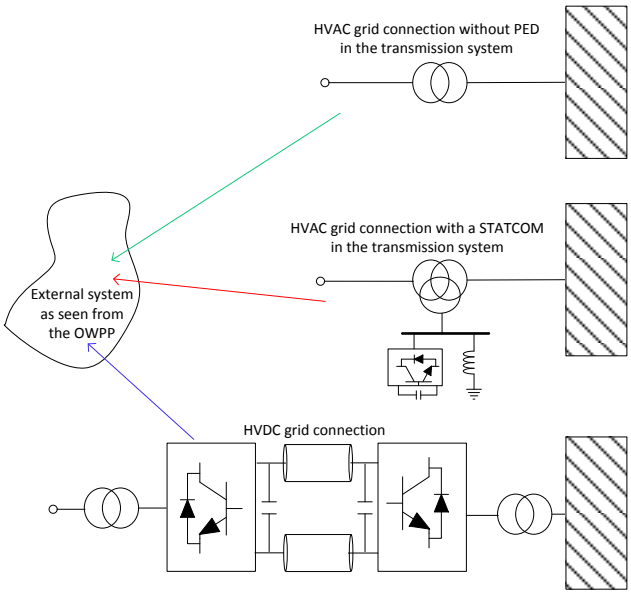

Figure 2-1 a) Simplified single line diagram of generic OWPP. b) HVAC grid connections without and with PEDs in the external system.

2.3.5 Project Flowchart

The approach defined in section 2.3.1 to 2.3.4 can be visualised using a flowchart, as presented in Figure 2-2, which provides a good overview of the different processes. It should be noted that the applied approach in this work does not exactly follow the flow indicated in Figure 2-2, as e.g. the theoretical analysis of the PEDs and the harmonic stability was done throughout the project time frame. Furthermore, the experience gained during e.g. the WTG and the CGI modelling was transferred to the already developed STATCOM and HVDC models, which were then optimised and updated. Similarly, if any of the models were found insufficient in the model application process (the "blue process" in Figure 2-2) they would be updated in the component modelling process. For example, if

the STATCOM model was found insufficient in the model application process it would be updated in the modelling process. Then, the updated model would be directly transferred back and applied in the model application process. Including all of these iterations would significantly increase the complexity of Figure 2-2.

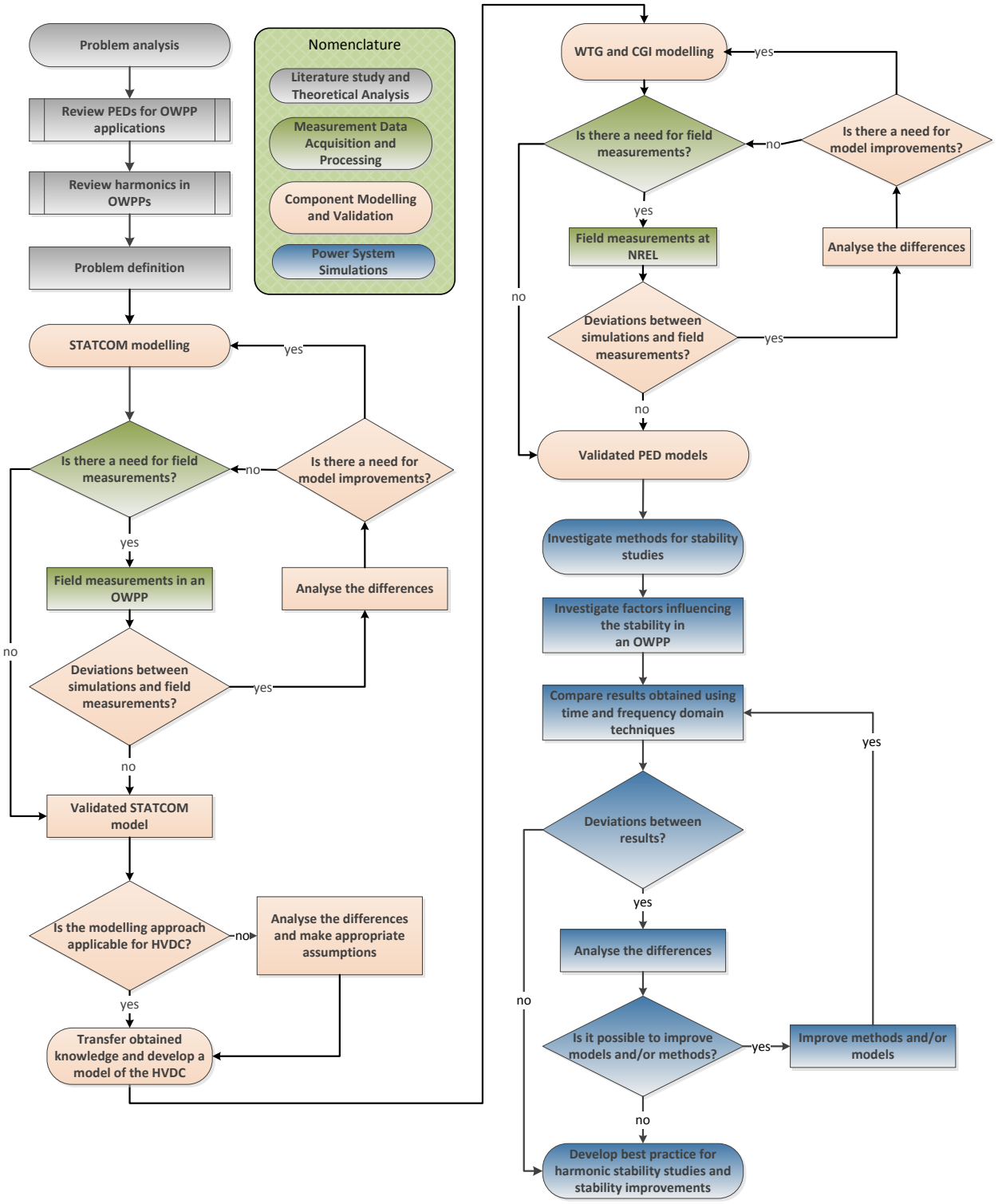

Figure 2-2 Generalised project flowchart.

The generalised flowchart in Figure 2-2 is by the author and supervisors considered to provide a simplified, yet realistic overview of how the project was executed.

2.4 Limitations

A relatively thorough description of the limitations made within the three year research project is given in this section. The purpose of the description is:

- To demonstrate the author's awareness of the limitations made and their impact on the outcome of the project.
- To provide the reader with a framework to evaluate the soundness of the results obtained within the project (both on a scientific level and for industrial applications).
- To strengthen the foundations of future, related research projects which can take into account some of the limitations made here.
- To provide inspiration for future, related research projects with inspiration on what could be additionally included in their scope (in combination with the future work in section 14.6.

The conscious specified limitations are:

- **London Array measurement campaign** (campaign description is given in Chapter 5)
    - Measurement data was only collected at the tertiary winding of the onshore transformer (i.e. only at the STATCOM). Measurement data could have been collected offshore, in a few selected WTGs and/or at the offshore park transformer.
        - This was not done as offshore measurement campaigns are associated with high costs, required significantly more planning and execution time than was available. Furthermore, there are uncertainties regarding access to the WTGs due to weather conditions.
        - Extensive offshore field measurement campaigns have previously been conducted and post-processed in the previous Industrial PhD project "Harmonics in Large Offshore Wind Farms" in DEWP [58].
    - The application of the one month measurement campaign in this project was limited to validation of the developed EMT-like MMCC models. A more thorough evaluation of the STATCOM operating as a harmonic source is proposed as future work, using the measurement data.
- **Passive power system component modelling**
    - An aggregated representation of the OWPP is used in this work, as it simplifies the modelling work.
        - OWPP aggregation is the standard approach in the industry for harmonic stability studies.
        - EMT-like simulations with detailed modelling of the full-scale converter (FSC) models in a converter rich grid such as an OWPP is by the author considered impractical due to significant time and calculation burden consumption.
        - A preliminary assessment of this approach was carried out using a full (real-life) OWPP model in DigSILENT PowerFactory.
            - The preliminary assessment indicates a good correlation between the impedance seen from the terminals of a specific WTG in the full model and to that of the aggregated WTG.
            - Results are not included since the applied models is for a real-life OWPP project.
            - The main scope of this work is the evaluation of the frequency domain approach related to the time domain.

        - Sensible to do the evaluation based on state-of-the-art harmonic stability procedure.
    - Possible resonances in the external power system in the HVAC grid connected OWPP has been included using a frequency dependent network equivalent (FDNE). A look-up table of the grid impedance ($Z_{th}(f)$) provided by a TSO was used in the analysis. The exact implementation of the FDNE in the current version of PSCAD/EMTDC (v4.5) is not straightforward.
        - Could be achieved by using an auto regressive moving average (ARMA) model [68].
            - Requires a rational function description of $Z_{th}(f)$, which can be obtained using a system identification technique.
            - The next version of PSCAD/EMTDC (i.e. v4.6) includes an FDNE model in the main library.
            - The ARMA modelling requires a certain amount of coding in e.g. the FORTRAN language.
                - The author has in this work developed detailed equivalent models of the MMCCs using similar coding, and hence demonstrated the skills needed to model the ARMA.
        - A simplified FDNE is derived using a number of parallel RLC branches, which provides a relatively good correlation with the actual $Z_{th}(f)$ provided by a TSO.
            - This is considered appropriate as the main scope of this work is the comparison of the frequency and time domain harmonic stability methods using generic models.
    - The inherent background harmonics in the HVAC grid connected OWPP has been omitted in the time domain model for simplicity.
        - The inclusion would have added to the overall harmonic distortion but it is presumed not to have an impact of the occurrence of instability. The evaluation of the background harmonics influence on the OWPP stability is proposed for future work.
- **PED modelling**
    - The applied current control of the PEDs is realised in the rotating reference frame (RRF) only.
        - Additional harmonic controllers of e.g. the 5th and 7th in e.g. a nested structure or in separate RRFs have been omitted.
            - They will add additional challenges related to the harmonic stability [8].
    - The voltage balancing of the sub-module (SM) voltages of the MMCCs is achieved using control strategies presented in the literature (see Chapter 6)
        - The control parameters were tuned by trial-and-error.
            - Complex analysis is needed to define the transfer function needed to analytically tune the controllers.

2.5 Thesis Outline

Table 2-1 on the following page shows an overview of the thesis, described more carefully in the following:

Part I Introduction and Problem Analysis

Part I has presented the background, motivation and scope of the Industrial PhD project.

An overview of possible grid connection of remotely located OWPPs has been given in Chapter 1. Challenges related to harmonics in OWPPs have been also been described with main emphasis on the harmonic stability, as this is the topic of this Industrial PhD project.

This chapter has presented the scope and deliverables from this Industrial PhD project. Furthermore, the chapter has described the applied methodology, limitations and the thesis outline.

Part II Power System Component Modelling and Evaluation

Part II of the thesis focuses on the modelling of the PEDs, the two measurement campaigns and evaluation of the developed models.

Chapter 3 presents and describes some of the various MMCC systems, which are commercially available and considered within the research project. The chapter presents a brief overview of the previous two- and three-level VSC-HVDC technologies.

Chapter 4 presents the detailed equivalent EMT based modelling technique developed within this project, which is capable to model the commercial MMCC STATCOM and MMCC HVDC systems considered in this work.

Chapter 5 describes the measurement campaign realised at the STATCOM, located at the onshore grid connection point of London Array OWPP.

Chapter 6 presents the time domain models of the MMCCs implemented in PSCAD/EMTDC. The low level control, ensuring the stabilisation of the distributed SM voltages in the MMCCs will be described and implemented in the STATCOM and the HVDC models. The evaluation of the STATCOM is presented based on comparison with the measurement data obtained from London Array OWPP in Chapter 5.

The system description of the CGI and the commercial multi-megawatt sized type 4 WTG installed at the National Renewable Energy Laboratory (NREL) is presented in Chapter 7.

Detailed, generic EMT models of the CGI and the WTG are developed and implemented in PSCAD/EMTDC in Chapter 8.

The models are evaluated based on comparison with test measurement in Chapter 9.

Chapter 10 presents the frequency domain modelling of the PEDs.

Chapter 11 presented the methods used in this work for modelling the passive OWPP components (such as the cables etc.) in the time and frequency domains.

Part III System Studies and Conclusion

Part III of the thesis presents power system studies realised based on the developed models in Part II.

Chapter 12 presents the harmonic stability evaluation in OWPPs employing PEDs in the transmission system.

Chapter 13 presents a discussion of the findings and how to relate these to industrial applications.

Chapter 14 presents the concluding remarks and the list of publications realised within the confines of this Industrial PhD project. Suggested future work is also outlined in Chapter 14.

The list of references is given on page 169.

Table 2-1 Overview of the thesis.

2.6 Chapter Summary

This chapter has presented the scope and deliverables from this Industrial PhD project. Furthermore, the chapter has described the applied methodology, limitations and thesis outline.

The scope of this project is to make a review of the state-of-the-art PEDs in OWPPs, to develop generic models of the PEDs in time and frequency domain, to conduct field measurement and apply the measurement data to validate the time domain models. Furthermore, the main scope is to conduct harmonic stability simulation studies in both the time and frequency domain and evaluate the results with respect to each other. Based on the findings of the analysis

The derivation of a recommendation on how to assess the harmonic stability in the OWPP design phase based on the simulation cases is expected to made based on the findings in this research project.

PART II
POWER SYSTEM COMPONENT MODELLING AND EVALUATION

Part II of this dissertation presents an overview of the modular multi-level cascaded converters (MMCCs), the developed electromagnetic transient like modelling of the MMCCs, the measurement campaign at London Array Offshore wind power plant (OWPP) and the evaluation of the proposed MMCC modelling technique. Chapter 7 to 9 present the work realised during the author's stay at National Renewable Energy Laboratory (NREL). Chapter 10 focuses on the frequency domain modelling of the power electronic devices for the harmonic stability analysis carried out in Part III. The modelling of the passive components in the OWPP is presented in Chapter 11.

Chapter 3 Overview of the Modular Multi-level Cascaded Converters

This chapter presents and describes some of the various modular multi-level cascaded converter (MMCC) systems, which are commercially available and considered within the research project. An overview of the previous two- and three-level voltage-sourced converter high-voltage direct current (VSC-HVDC) is briefly presented. The review will focus on the technology evolvement, industrial installations, and the working principles of the MMCCs. The review is done on the evolvement of the VSC-HVDC and the static compensator (STATCOM)

3.1 Two- and Three-Level VSC-HVDC topologies

As indicated in Table 1-1, ABB was the only vendor of the two- and three level VSC-HVDC schemes. These schemes were developed over three generations of HVDC Light [41], which will be briefly described in the following.

The two- and three-level technologies enable switching between two or three different voltage levels to the AC terminals, respectively. The main drawbacks of these technologies include high switching losses, high dU/dt at relatively high switching frequency [25]. This necessitates high insulation requirements of the interfacing transformer, as well as extensive filter installations (although lower requirements than the line commutated converter (LCC-)HVDC scheme).

Although the switching frequency has decreased from approximately 2 kHz to 1 kHz within the last decade, the efficiency of each VSC-HVDC converter station is in the range of 98 %, which is inferior to 0.7 % losses per LCC-HVDC station [24, 25, 30].

1st Generation HVDC Light

Figure 3-1 shows the three phase two-level converter, where the phase-ground voltage (e.g. u_{a0}) can take the discrete values $\pm u_{DC}/2$, depending on the whether the upper or lower insulated gate bipolar transistor (IGBT) is on (S_1 or S_4 in phase A, respectively).

Due to the reverse blocking capability of the IGBT and the diode in the range of a few kilovolts [69, 70] multiple series-connected antiparallel IGBTs and diodes are used in each valve in order to provide a higher voltage blocking capability of the converter and thereby increase the DC voltage [30, 39, 40]. This is shown in Figure 3-1 for the lower phase valve in phase C. The series connected IGBTs have to switch simultaneously (within a few micro-seconds) in order to ensure uniform voltage distribution between the IGBTs statically as well as dynamically, which is not a straightforward task [42, 50].

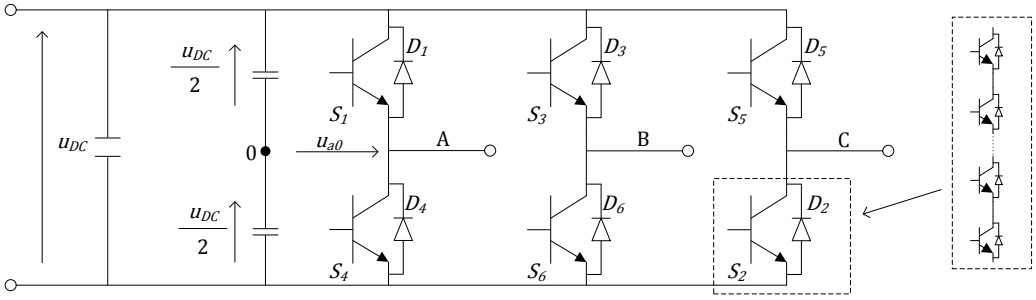

Figure 3-1 Three phase two-level VSC-HVDC, used in ABBs HVDC Light generation 1 and 3.

2nd Generation HVDC Light

The 2nd generation HVDC Light was applied in the Cross Sound Cable and Murray projects, shown in Table 1-1. The scheme introduced three-level converter valves with active neutral-point clamping (ANPC), which is an improvement of the neutral-point clamped (NPC) converter introduced in [71]. The losses were reduced from 3 % in the 1st HVDC Light generation to approximately 1.7 % in the 2nd generation [72]. Furthermore, the new concept also introduced the application of third harmonic injection for optimized utilization of the DC link voltage for HVDC transmission applications. A technique well known from drive technologies [72]. Figure 3-2 shows the single phase representation of the ANPC based VSC-HVDC. By turning on S_1 and S_2 or S_3 and S_4, the phase output voltage becomes $U_{DC}/2$ or $-U_{DC}/2$, respectively. The output voltage is equal 0 V in case S_2 and S_3 are turned on. In the diode NPC converter, where the IGBTs S_{c1} and S_{c2} are not included, the utilization of upper and lower NPC paths depends on the direction of the current flow. By actively clamping the neutral in the ANPC, it now becomes possible to optimize the loss distribution between the upper and lower NPC paths [73, 74].

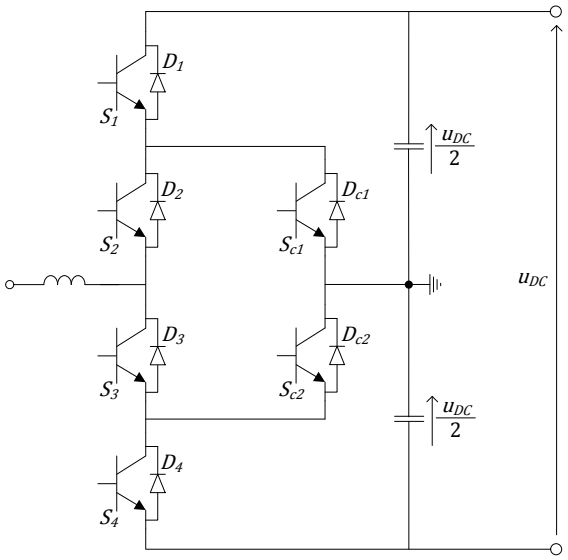

Figure 3-2 Single phase representation of ABBs 2nd generation HVDC Light. Each IGBT/diode represent more than 150 series connected IGBT/diode modules.

3rd Generation HVDC Light

The 3rd generation HVDC Light has been applied for the schemes installed by ABB in the years 2005-2012, outlined in Table 1-1. The three-level ANPC in Figure 3-2 uses a high number of IGBTs/diodes and has a more complex structure than the two-level converter shown in Figure 3-1. The two-level converter has to switch the full DC link voltage at higher frequency than the ANPC, which only switches between 0 V and $\pm u_{DC}$. Due to advancement in the IGBT and modulation techniques, ABB returned to the two-level topology in the 3th generation HVDC Light using optimized PWM (OPWM) [41]. The advantage of the OPWM is that it aims to eliminate lower order harmonics. Furthermore, the OPWM ensures lower switching density when the current is high and high switching frequency when the current is low, assuming high power factor [75]. OPWM (or selective harmonic elimination) consists of off-line calculation of the switching angles based on Fourier series in order to eliminate specific harmonics. The switching angles are calculated on basis of an odd function using half and quarter wave symmetries [67], hence only odd harmonics exist according to equation 3-1 [76].

$$a_n = \frac{4}{n\pi}\left[1 + 2\sum_{n=1}^{M_h}(-1)^n \cos(n\alpha_n)\right] \quad 3\text{-}1$$

Where a_n is the Fourier coefficient, n is the odd harmonic order and α_n is the switching angles. M_h is the number of harmonics considered. Because of the quarter wave symmetry, α_k is confined within 0 - $\pi/2$ radians.

From equation 3-1 it is evident that there exist M_h freedoms. One is used to control the magnitude of the fundamental frequency voltage component; hence it is possible to eliminate $M_h - 1$ harmonics. The offline calculated α_k are stored in a look-up table for different modulation indexes of the fundamental frequency voltage. The OPWM has a poor control performance under transient conditions due to the off-line calculated switching angles as shown in [76]. The OPWM is therefore only used during steady-state operating mode in the 3th generation HVDC Light. In order to handle e.g. AC side faults or other disturbances, an online carrier based PWM with a higher switching frequency is used during the transients [75].

3.2 Multi-Level Converters

The needs to improve the voltage waveform and reduce switching losses led to the development of multi-level converters [54]. These converters provide a number of levels in the voltage waveform, which are each only a fraction of the total AC voltage [29]. Different multi-level converters exist, including the flying capacitor and diode clamped converters. Both of these technologies have been found unsuitable for more than usually three or five voltage levels due to complex voltage balancing of the DC link capacitors [39,77-79]. Furthermore, the flying capacitor technology requires the use of large capacitors with different voltage ratings, which limits the modularity of the converter as well as increases the footprint [80]. In order to balance the capacitor voltages an auxiliary balancing network has been introduced, which significantly increases the complexity of the converter [77].

3.3 Overview of the Modular Multi-Level Cascaded Converters

The needs to ensure modularity, lowering the switching losses and lower the high filter requirements due to harmonics led to the introduction of the MMCC in [54]. The advancement of the MMCCs is considered a major step toward VSC applications for high power HVDC transmission [23].

The MMCC synthesizes a high quality sinusoidal voltage waveform by incrementally switching a high number of voltage levels. Furthermore, the switching frequency of the individual IGBT is lowered from 1-2 kHz for the two- and three-level converters to typically 100-150 Hz in the MMCC. This has reduced the losses to about 1 % at each converter station [25, 30]. Although the losses are still higher than for the LCC-HVDC technology, the many advantages outlined in the above make the multi-level VSC-HVDC a promising technology for future offshore wind power plants located far from shore [78].

3.3.1 The MMCC Family

Reference [17] together with [81] provide an extensive overview of the MMCC family, which can be categorized as in Figure 3-3a, where the three port MMCCs are shunts components, such as the STATCOM and the VSC-HVDC belongs to the five port category. The main characteristics of the application of MMCC at the medium voltage level have been pointed out in [81].

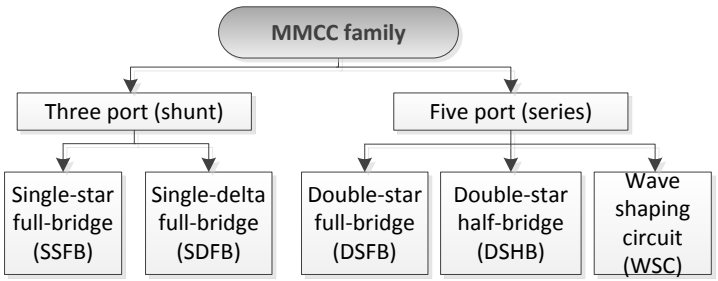

Figure 3-3 Classification and terminology of the MMCC family.

The five MMCC types in Figure 3-3 have in common that they are constructed using a "chain-link" or cascaded series connection of the half- or full-bridge sub-modules (SMs) shown in Figure 3-4.

The two MMCC building blocks will be described more carefully in the following.

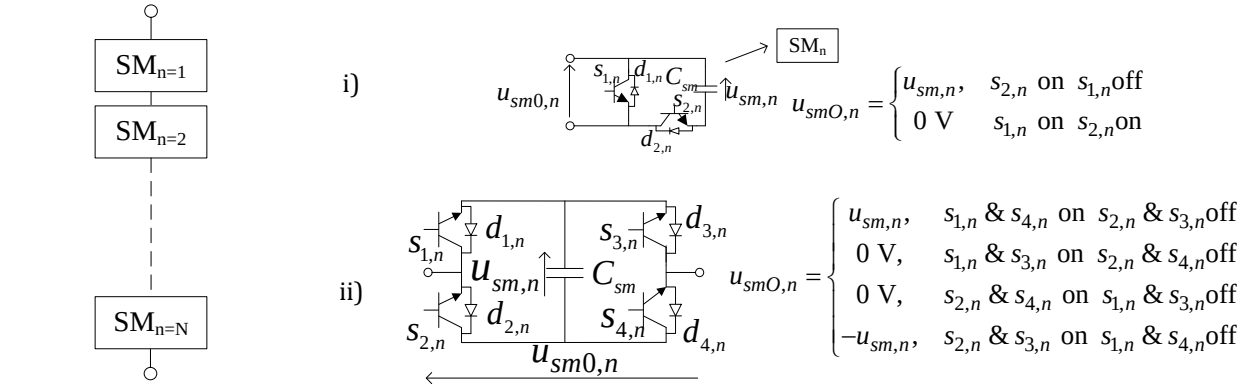

a) Cascaded connection of the half- or full-bridge SM in figure b.

b) MMCC building blocks.

Figure 3-4 Cascaded connection of MMCC building blocks. In figure b): i) Half-bridge ii) Full-bridge.

MMCC Building Blocks: The Half-Bridge

As seen in Figure 3-4b-i, the half-bridge SM consists of two pairs of an IGBT and an antiparallel diode (i.e. $s_{1,n}, d_{1,n}$ and $s_{2,n}, d_{2,n}$). The n^{th} SM can be switched in three different ways (neglecting the subscript n for simplicity):

- When s_1 is turned on the SM is bypassed (Figure 3-5a and b).
- When s_2 is turned on the SM is inserted. Depending on the current flow (i_{in}) the SM capacitor either charges (Figure 3-5c) or discharges (Figure 3-5d).
- When both s_1 and s_2 are turned off, the SM is by-passed (Figure 3-5b) or inserted (Figure 3-5c), depending on direction of current flow.

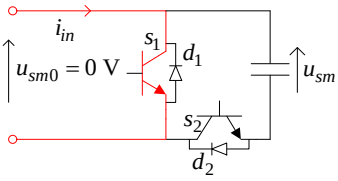

a) s_1 on, bypassed inverter.

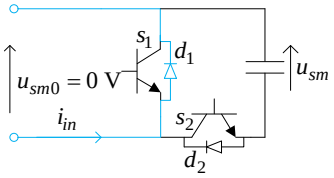

b) s_1 on or both off, bypassed rectifier.

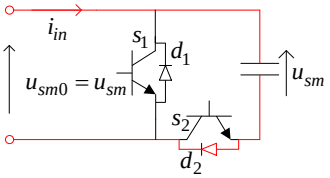

c) s_2 on or both off, inserted inverter. Capacitor charging.

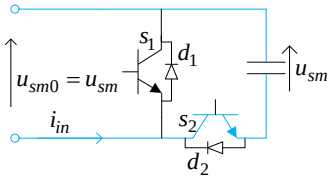

d) s_2 on, inserted rectifier. Capacitor discharging.

Figure 3-5 The six possible combinations for the two-level half-bridge converter.

Figure 3-6 shows the cascaded connection of two half-bridge SMs and the resulting three-level output voltage waveform (u_{out}), which is uni-polar, as the individual half-bridge SM can only produce the above two described output voltage levels ($u_{sm0,n} = u_{sm,n}$ and 0 V). As can be observed the same current flows through the two SMs ($i_{n=1} = i_2$) due to the chain-link structure.

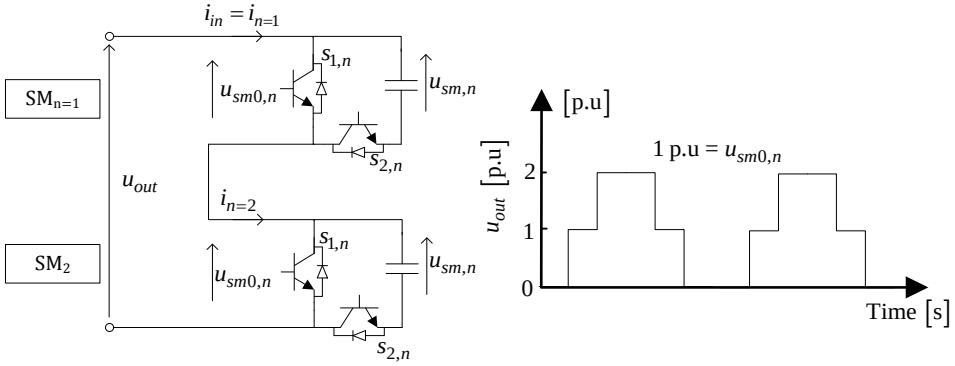

Figure 3-6 Cascaded connection of two half-bridge SMs and resulting (ideal) output voltage waveform.

MMCC Building Blocks: The Full-Bridge

As seen in Figure 3-4b-ii, the full-bridge SM consists of four IGBT/diode pairs, which enables the full-bridge SM to be switched to three output voltage levels ($u_{sm0,n} = \pm u_{sm,n}$ and 0 V) as shown in Figure 3-7. Please note the subscript n has been omitted from the figure for simplicity.

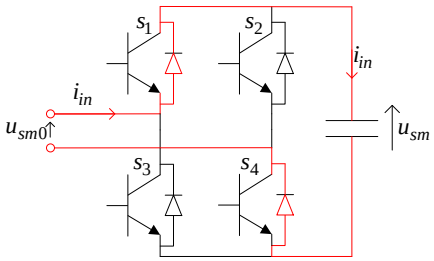

a) s_1/s_4 on, $u_{sm0} = u_{sm}$, charging.

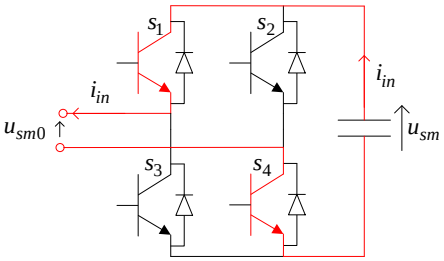

b) s_1/s_4 on, $u_{sm0} = u_{sm}$, discharging.

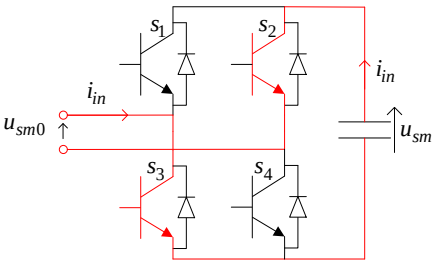

c) s_2/s_3 on, $u_{sm0} = -u_{sm}$, discharging.

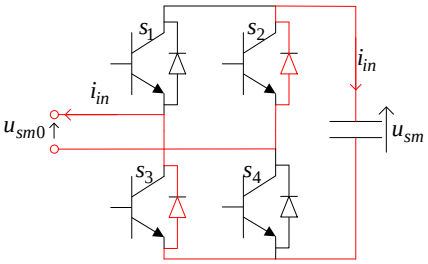

d) s_2/s_3 on, $u_{sm0} = u_{sm}$, charging.

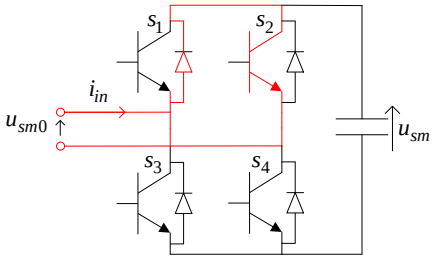

e) s_1/s_2 (or s_3/s_4) on, $u_{sm0} = 0$ V, bypassed.

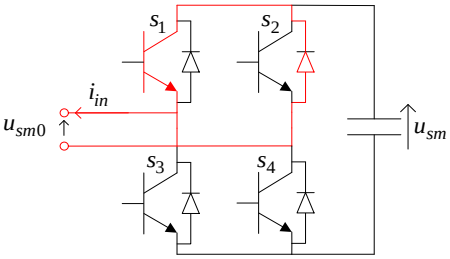

f) s_1/s_2 (or s_3/s_4) on, $u_{sm0} = 0$ V, bypassed.

Figure 3-7 Full-bridge topology and the eight possible combinations for a three-level full-bridge converter.

Figure 3-8 shows the cascaded connection of two full-bridge SMs and the resulting bi-polar five-level output voltage waveform (u_{out}). Similar to the cascaded connected half-bridge SMs in Figure 3-6, the same current flows through the two SMs ($i_{n=1} = i_2$) in Figure 3-8.

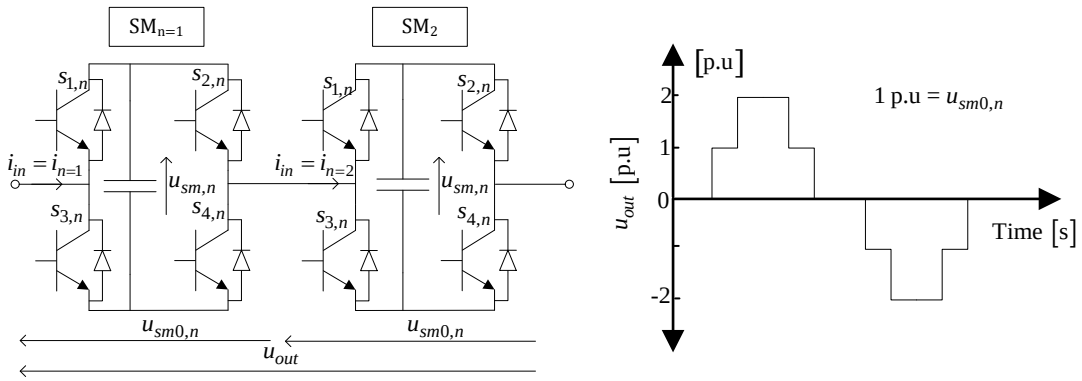

Figure 3-8 Cascaded connection of two full-bridge SMs and resulting output voltage waveform.

3.4 MMCC HVDC

Figure 3-9 shows the double star converter, which can either be equipped with the half- or full-bridge (DSHB and DSFB, respectively, see Figure 3-3). The original double star converter presented in [54] is based on the half-bridge, but there might be some advantages employing the full-bridge configuration in terms of short circuit handling. This is done at the expense of twice the number of semi-conductors per SM. Furthermore, the DSFB has a better DC link voltage controllability as the full-bridge essentially is a buck-boost converter [81].

Figure 3-9 shows the principle design of the MMCC, where each of the phase legs consists of two phase arms or valves. Each arm consists of *N* SMs connected in series with one converter reactor (L_r). The phase reactors are effectively placed in series in case of a DC fault and will lower the current rise so that the IGBTs can be turned off at uncritical current levels [82]. Furthermore, the reactors shown in Figure 3-9 are used to limit the balancing current [83], inherent to the DSHB and DSFB topologies, as will be described later.

Two of the three VSC-HVDC vendors identified in Table 1-1 employ the DSHB topology, with some minor differences, as will be described shortly. The third vendor, Alstom, has a 25 MW VSC-HVDC prototype in service based on the same topology as in [54], the future schemes will be based on the hybrid VSC-HVDC converter concept (i.e. the wave-shaping circuit (WSC)) [28, 84]. The Siemens HVDC Plus and ABB HVDC 4th Generation Light will be described in the following.

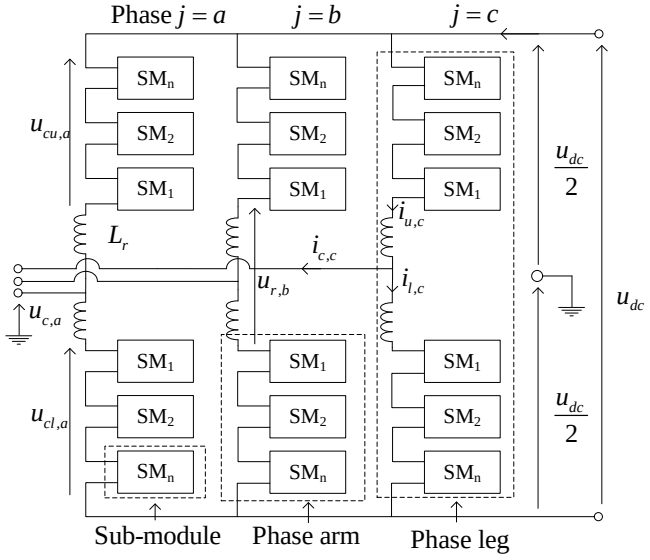

Figure 3-9 Double-star converter, utilizing either half- or full-bridge building blocks in Figure 3-4b (DSFB or DSHB, respectively).

3.4.1 SM Configuration in ABB's HVDC Light 4th Generation and Siemens' HVDC Plus

Figure 3-10 shows ABB's and Siemens' arrangement of the half-bridge SM. The arrangements are different as they are designed to handle faults differently as outlined in the following.

Two faults scenarios have been taking into consideration in the design of the SM: SM short circuit and DC pole-pole short circuit [25, 40]. SM short circuits can have various origins, but the most frequently observed is the insulation breakdown of the blocking switch, which in turn short-circuits the SM capacitor. Depending on the type of device used, an IGBT failure may lead to an open circuit, which is the case in the Siemens solution for the MMCC. Siemens utilizes industrial modular IGBTs with plastic casing, which results in an open circuit in case of a diode or IGBT chip failure. Open circuit in a converter for HVDC applications must be avoided, as the energy dissipation in the resulting arc causes

a trip of the converter each time an IGBT fails. Siemens employs standard IGBTs, adding a high speed mechanical closing switch (K_1 in Figure 3-10a), that bypasses the SM within a few milliseconds after the IGBT fault detection [23]. The SM is then permanently bypassed and needs replacement at the following scheduled maintenance. The remaining SMs in the converter arm (in the range of $N = 200$) must then accept the slight voltage increase until the damaged SM has been replaced. The SM is furthermore equipped with a thyristor (K_2), bypassing the SM in case of a DC pole-pole fault [40].

a) Siemens' SM arrangement. b) ABB's SM arrangement.

Figure 3-10 Arrangement of ABB HVDC Light's and Siemens HVDC Plus' SM.

ABB utilizes series connected press-pack IGBTs, which go into a short-circuit failure mode, leaving out the necessity of a mechanical bypassing switch to prevent arcing in the valve [25]. Eight IGBTs and associated anti-parallel diodes are series connected in each of the SMs, as indicated in Figure 3-10b. The IGBTs are designed to accept the voltage increase in case a failure occurs in one of the IGBTs. The SM diodes are designed to withstand the high overcurrent in case of a DC converter terminal fault until the AC breaker opens and disconnect the converter within 30-50 ms.

Fundamental Working Principle of the DSHB

The basic governing equations of the DSHB (and the DSFB) can be described based on the equivalent circuit shown in Figure 3-11, where the upper and lower arm valves are each represented by a controlled voltage source and the phase arm reactors are neglected for simplicity. The voltage of the upper ($u_{cu,j}$) and lower ($u_{cl,j}$) arm of the three phases ($j = a, b, c$) can be expressed as in equation 3-2, where $u_{c,j}$ is the phase to ground voltage (e.g. $u_{c,a}$ in Figure 3-11).

$$u_{cu,j} = \frac{u_{DC}}{2} - u_{c,j} \quad \text{3-2a}$$

$$u_{cl,j} = \frac{u_{DC}}{2} + u_{c,j} \quad \text{3-2b}$$

The equations for the DC link voltage can be expressed using Kirchhoff's voltage law on Figure 3-11, as in equation 3-3.

$$u_{DC} = u_{cu,j} + u_{cl,j} = u_{cu,a} + u_{cl,a} = u_{cu,b} + u_{cl,b} = u_{cu,c} + u_{cl,c} \quad \text{3-3}$$

Hence the three phases impress the same voltage u_{DC}. Because the converter is ideally symmetrical, the DC current (i_{dc}) will be divided equally between the three phases. Also, the phase current will be split equally between the upper and lower arms; hence the upper and lower arm currents can be expressed as:

$$i_{u,j} = \frac{i_{DC}}{3} + \frac{i_{c,j}}{2} \quad \text{3-4a}$$

$$i_{l,j} = \frac{i_{DC}}{3} - \frac{i_{c,j}}{2} \quad \text{3-4b}$$

The DC component in the arm current increases the conduction losses in the MMCC compared to the conduction losses in e.g. the two-level converter [85]. However, the overall losses of the MMCC are lower due to the decreased switching losses compared to the two-level converter.

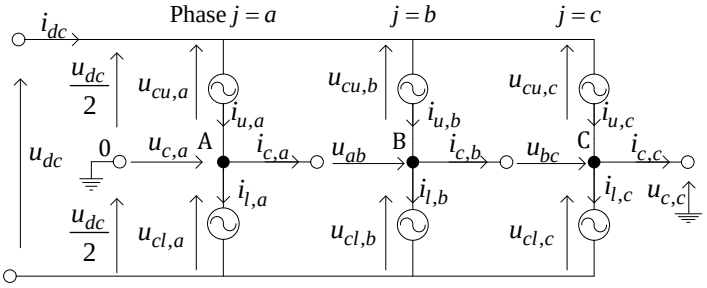

Figure 3-11 Equivalent circuit of the double star MMCC, where the phase arm reactors are omitted.

The arm currents $i_{u,a}$ and $i_{l,a}$ should according to equation 3-4 only contain the $1/3i_{DC}$ and $1/2i_{c,a}$ components. However, as demonstrated in [17], an additional component is also present, namely a circulation/balancing current, which is mainly the second harmonic component, which can be confirmed analytically based on a closer investigation on the MMCC equivalent in Figure 3-11 [82,86-90].

Siemens' Solution to the Balancing Current

Closed-loop control means are used in Siemens HVDC Plus scheme in order to limit the circulating currents [91]. Different closed-loop control schemes are presented in [87, 88, 89], which effectively eliminate the circulating currents.

ABB's Solution to the Balancing Current

The balancing currents are suppressed using a parallel resonant filter located at the centre of the phase reactors and tuned at the 2nd harmonic in ABBs HVDC Light [25, 92]. This is shown in Figure 3-12.

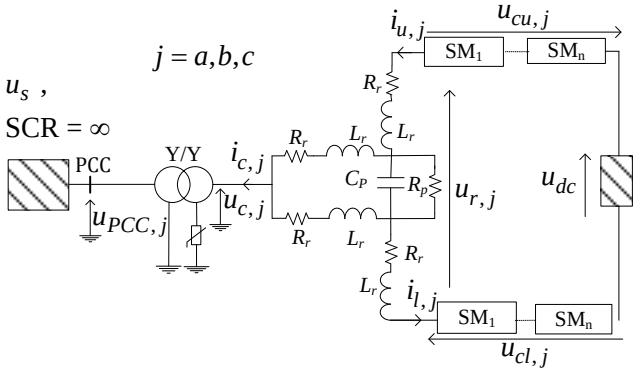

Figure 3-12 Second harmonic circulating current suppresion in ABB's HVDC Light using a passive filter mid-point of the arm reactor.

Third Harmonic Injection

Third harmonic injection technique [93] is used in both the HVDC Light and the HVDC Plus to optimise utilisation of the SM DC voltage [25, 26]. The third harmonic component is blocked from the grid by using the conventional Y/Δ transformer configuration in Siemens' HVDC Plus, whereas the second harmonic filter in Figure 3-12 eliminates the third harmonic, hence an Y/Y transformer is used in the HVDC Light [25, 92].

Number of SM in the HVDC Light and HVDC Plus

Different numbers of SMs are used in the two schemes, where 200 SMs are used in each phase arm in the HVDC Plus for a DC link voltage of $\pm$ 200 kV for the Trans Bay Cable Project [23]. 38 SM are used per phase arm in the HVDC Light for a DC link voltage of $\pm$ 320 kV [25]. There are no AC filter requirements in the HVDC Plus due to the high number of SMs, whereas a small filter is included in the HVDC Light.

3.4.2 The Double Star Full-Bridge Converter

There might be some advantages employing the full-bridge configuration in the SM, in terms of short circuit handling in case of a DC fault at the expense of twice the number of semi-conductors per SM. Furthermore, the DSFB has a better capability to control the DC link voltage as the full-bridge appropriately controlled is a buck-boost converter [81]. The DSHB converter type is the main commercially available MMCC VSC-HVDC described in the above, and the DSFB will therefore not be considered further.

3.4.3 Alstom's MaxSine HVDC (Wave-Shaping Circuit)

As outlined in section 3.1, the main limitations of the two-level converter is the high switching losses at relative high switching frequency, which necessitates high insulation requirements of the interfacing transformer, as well as extensive filter installations. The MMCC DSHB and DSFB previously described overcome many of the abovementioned shortcomings, but at the expense of a substantial higher number of semi-conductors (twice or more) and a very large amount of distributed capacitances, compared to the two-level converter. Recent research has indicated the advantages of combining the features of the two-level converter and that of the MMCC, and thus introducing a new hybrid family of VSC-HVDC topologies namely the WSC [27,84,94-98].

The main idea behind the hybrid VSC-HVDC converters is to use a two-level converter as the main switching component with a low switching frequency and then add a relatively small MMCC, which is used as an active filter or WSC in order to eliminate the harmonics generated by the two-level converter. The WSC family can broadly be divided into two categories, which can be further subdivided [17, 84]:

- Series Circuit
  - WSC on the AC side.
  - WSC in the phase arms.
- Parallel circuit
  - WSC on the DC side.

The WSC categories will be briefly described in the following subsections.

WSC on the AC Side (Series)

In the series WSC introduced in [95], the WSC is located on the AC side of the two-level converter as shown in Figure 3-13a. The WSC is composed of series connection of the full-bridge SMs. The main drawback of this topology is the high switching losses, as the two-level converter is hard-switched [84]. The produced voltage waveforms are also shown in Figure 3-13a. The output grid voltage (u_g) is calculated as:

$$u_g = u_c + u_{WSC} \qquad 3\text{-}5$$

Where u_c is the output voltage of the two-level converter and u_{WSC} is the voltage across the WSC, which is bi-polar due to the application of full-bridge SM in the MMCC WSC.

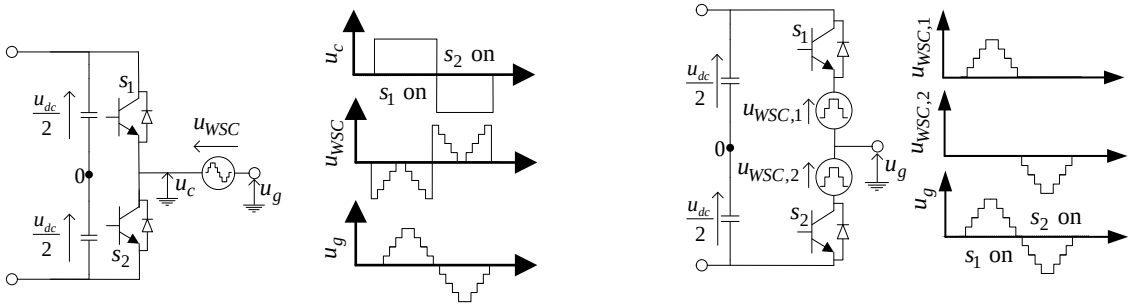

a) WSC on the AC side. Full-bridge SMs are used in the WSC.

b) WSC in the phase arms. Full-bridge SMs are used in the WSCs.

Figure 3-13 Single phase representation of two series WSCs.

WSC in the Phase Arms (Series)

Another series topology is proposed in [97], where the wave shaping circuit is located in the phase arms as shown in Figure 3-13b. The WSC is connected to the AC terminal, when the associated switch is on. The WSG,1 is for example connected when s_1 is in the conducting state.

The topology in Figure 3-13b fundamentally works similar to the DSHB, where the advantage compared to the DSHB used in ABB's and Siemens' VSC-HVDC schemes, is the blocking of the circulating current. Furthermore, the WSC topology in Figure 3-13b is capable to control the currents in case of a fault on the DC side, which is a major challenge in multi-terminal HVDC systems [99].

WSC on the DC Side (Parallel)

The hybrid converter with the VSC in parallel with the main phase switch was introduced in [94] and shown in Figure 3-14a. A full-bridge converter is used in each phase, connected in parallel with a VSC, composed of half-bridge SMs, as shown in Figure 3-14a. The three phases are connected in series seen from the DC side; hence there will not be any balancing current flow as in the DSHB. The main advantage of this topology is that the wave shaping circuit is located outside the main current path. The number of SMs is therefore greatly reduced compared to the DSHB topology, which furthermore reduces the ratings of the semiconductors and SM capacitors [84].

Figure 3-14b will be used to illustrate the working principle of the topology shown in Figure 3-14a. s_1 and s_4 will be switched on for the positive half-period of the 50 Hz period and the complementary switches s_2 and s_3 are on for the negative half-period. Any ripple present on the DC side will therefore be transferred directly to the AC side, which is exploited by inserting the series connected half-bridge SMs (i.e. the WSC) on the DC side, producing a rectified voltage sine wave as indicated in Figure 3-14b. The resulting AC output voltage will have little distortion, depending on the number of SMs used in the WSC. A large six harmonic component will be present at the DC side in the three phase converter shown in Figure 3-14a, which can be removed using either phase filters or by using active techniques such as adding zero-sequence third harmonics to the waveforms generated by the three WSCs, which will not affect the AC side waveforms [94].

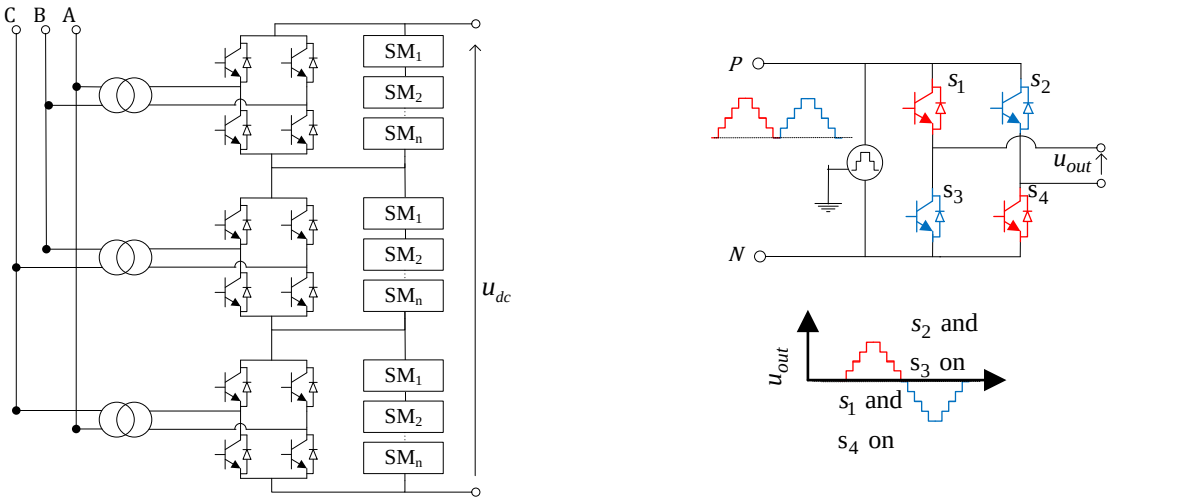

a) Three phase representation. b) Single phase full-bridge in parallel with a WSC.

Figure 3-14 Three and single phase representation of the parallel hybrid multi-level converter with the WSC on the DC side.

3.5 MMCC STATCOM

Figure 3-15 shows two possible circuit configuration of the STATCOM. The star (or single-star full-bridge (SSFB)) configuration in Figure 3-15a is capable of controlling positive-sequence leading and lagging reactive power. The delta (single-delta full-bridge (SDFB)) configuration in Figure 3-15b is on the other hand also capable of controlling negative-sequence reactive power by using the circulating current that flows in the Δ branches [100]. Balancing of the individual distributed DC-link voltage can be achieved by injecting a zero-sequence voltage in the star configured STATCOM. For the Δ configuration this can be achieved injecting zero-sequence current in the Δ branches. The Δ converter configuration has to have a $\sqrt{3}$ times higher voltage rating. The current rating of the Δ converter configuration is 15 % larger than for the star configuration, due to the injected zero-sequence current. Similarly, the voltage rating of the star configuration with zero-sequence voltage injection needs to be twice the normal phase voltage rating, or 15 % higher than that of the Δ converter [81, 101].

Reference [101] discusses the economic implications of the duality of the two configurations of the STATCOM. The higher voltage rating in the star configuration could result in a higher required number of SMs, or alternative to use higher voltage rating of the SMs. The higher current of the Δ configuration requires higher current ratings of the power electronics, but more importantly requires larger capacitances in the SM, due to the higher ripple in the DC link voltages.

Based on a review of practical state-of-the-art MMCC STATCOM (i.e. Siemens SVC Plus), it found that the preferred choice is the Δ configuration, mainly due to the capability of compensating unbalanced grids using negative-sequence current injection/absorption. The practical circuit will be presented in Chapter 5.

Based on the above consideration only the Δ configured STATCOM will be considered within the current research project.

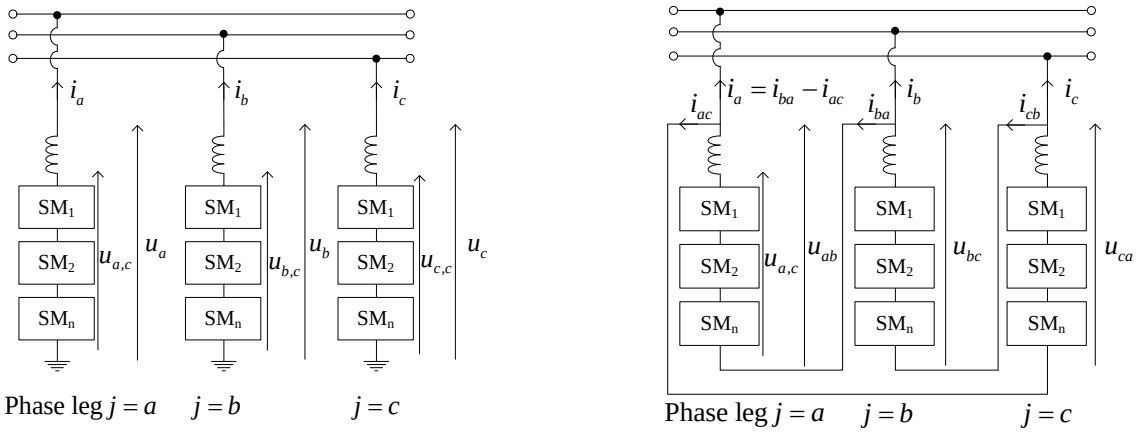

a) SSFB. b) SDFB.

Figure 3-15 Possible circuit configuration of MMCC STATCOM.

3.6 Chapter Summary

This chapter has presented a review of the state-of-the-art VSC-HVDC and the STATCOM technologies and presented the commercial available solutions.

Based on the review it has been found that there are some similarities between the available technologies MMCC VSC-HVDC technologies as they rely on a modular approach, which makes them relatively easy to scale to a desired DC link voltage.

Chapter 4 Detailed Equivalent Modelling of the Multi-Level Converters

An overview of the modular multi-level cascaded converter (MMCC) family was presented in Chapter 3. This chapter focusses on modelling of the MMCC voltage source converter high-voltage direct current (VSC-HVDC) and the static compensator (STATCOM) in electromagnetic transient programs (EMTPs).

4.1 Introduction

The relatively high number of non-linear semi-conductors in the MMCCs possesses some challenges in the EMTPs, as the semi-conductors are triggered by relatively high-frequency signals and as the electrical system's admittance matrix is altered at each switching instant. A significant computational effort is required for re-triangularisation of the electrical network subsystem's admittance matrix [78, 102]. The computational burden is considerably increased for the large number of semi-conductors, making the simulation of the MMCC in some occasions impractical when using a conventional modelling approach [29].

An efficient and accurate representation of each of the six phase arms of the MMCC VSC-HVDC was proposed in [29], which was based on the "Nested Fast and Simultaneous Solution" (NFSS) [103], referred to as "detailed equivalent model" (DEM) [104]. The DEM significantly increased simulation speed compared to the conventional modelling of the MMCC VSC-HVDC in the EMTPs where the semi-conductors and distributed capacitances are explicitly included in the main EMTP solver. However, the model in [29] is specifically intended for the MMCC VSC-HVDC employing the half-bridge converter, which is the case for Siemens' HVDC Plus and ABB's HVDC Light, see Chapter 3 [17] (i.e. the double star half-bridge (DSHB)). The third main vendor, Alstom, has indicated to use the full-bridge converter as the sub-module (SM) building block in their MaxSINE HVDC product [17], (i.e. wave-shaping circuit (WSC)). State-of-the-art STATCOMs such as Siemens SVC Plus are also using the full-bridge converter in the SMs [12] (i.e. three port single delta full-bridge (SDFB)).

The somewhat more complex structure of the full-bridge compared to the half-bridge SM building block makes it complex to apply the modelling approach proposed in [29] for the latter, in terms of derivation of the governing equations as well as in the model implementation.

In order to overcome the above mentioned challenges associated with modelling of the full-bridge equipped MMCCs, an effective (in terms of simulation speed) model technique was proposed in [105], which embraces both the half- and full-bridge converter based MMCCs. In the model in [105], the N_{sm} number of SMs in each of the converter arm are segregated into N sub-systems in the main EMTP and all semi-conductors (diodes and the insulated-gate bipolar transistors (IGBTs)) and capacitances are included explicitly. As N can be in the excess of 200 [17], the total number of IGBT/diode pairs per converter station is 200 SM/arm × 6 arms × 4 semi-conductors/SM = 2400 semi-conductors. Hence; the number of semi-conductors for a point-to-point HVDC using the DSHB is in the range of 5000, which requires substantial implementation effort using the approach proposed in [105]. This number would double if the HVDC converters are equipped with full-bridge converters in the SMs (i.e. the DSFB). Furthermore, tedious reconfiguration is needed in case N is altered in the model. Although the technique presented in [105] is promising, the simulation speed is inferior to the DEM in [29].

The purpose of this chapter is to develop a universal modelling technique, which is capable to represent both the half- and full-bridge based SM. The modelling technique is considered to alleviate the above mentioned drawbacks of the MMCC models in [29] and [105]. The governing equations of the proposed MMCC models are derived based on simple inspection of the equivalent SM using fundamental circuit laws [106].

The presented modelling approach can, due to its generality, easily be extended to even more complex converter structures than the full- and half-bridge based converters considered here. This is considered by the author to be an improvement compared to DEM of the MMCCs. The model proposed here is (similar to the model in [29]) interfaced with the main EMTP using a programming language (here Fortran 90), where the number of SMs/phase arm is an input parameter, alleviating one of the mentioned drawbacks of the model in [105].

The proposed model is benchmarked against the conventional modelling approach and an implemented DEM similar to the one presented in[29]. As described in the above, the simulation speed of the model in [29] is superior to the simulation speed in the model in [105] and hence the model proposed here is also superior to the model in [105] in terms of simulation speed.

The accuracy evaluation of the proposed models in [29] and [105] were based on comparing the time domain results with the conventional model in two separate graphs for the two models, which does not provide a good ground for comparison. Therefore, this chapter proposes the application of the least mean square error as a figure of merit of the accuracy. It will be shown that the simulation speed of the proposed model is practically identical to the model proposed in [29] without the loss of accuracy compared to the conventional model representation of the MMCC VSC-HVDC system.

An overview of the possible MMCC modelling techniques in EMTPs is given in the following section.

4.2 Overview of the MMCC Modelling Methods

A brief description of the different types available for MMCC model representation is given in the following. A more detailed description is given in [104].

Type 1: Full Physics-Based Models

Each semiconductor device is represented by differential equations or by an equivalent circuit. A detailed representation of the IGBT was proposed in [107] and compared with a finite element model. Type 1 models can accurately simulate switching losses at the expense of a very small integration time step (in the range of nanoseconds) in the EMTP and is therefore not usually applied for power system studies. On the other hand, type 1 models are useful for detailed analysis of the behaviour of the semiconductor device in the design phase of the converter.

Type 2: Detailed Nonlinear IGBT-Based Model

The anti-parallel IGBT/diode pair is in type 2 models represented by an ideal controlled switch, one series and one anti-parallel diodes and a snubber circuit, as shown in Figure 4-1 [104]. The non-ideal voltage-current characteristic of the diode is represented using a non-linear resistance, using manufacturer data. The advantage of type 2 models lie in the increased accuracy in the modelling of the IGBT/diode pair as the non-linear behaviour during the commutation is included. Because of the high number of semiconductor devices in the MMCC, type 2 models are mostly suitable for specific studies such as the converter start-up sequence and internal converter faults. Furthermore, type 2 models are useful as benchmarking in the evaluation process of less detailed MMCC models described in the following (i.e. type 3-5) [108].

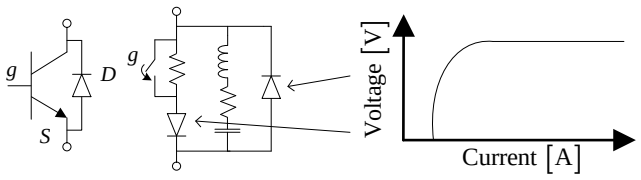

Figure 4-1 Type 2 representation of the IGBT/diode pair, with non-linear voltage-ampare characteristics of the diode.

Type 3: Simplified IGBT/diode-Based Model

This model is based on the assumption that the anti-parallel IGBT/diode pair act as a bidirectional switch, which is represented by a two-state resistance ($R_{DS} = R_{on}$ [mΩ] and $R_{DS} = R_{off}$ (MΩ), in conduction and blocking state, respectively), see also Figure 4-4 on page 43. Although less accurate compared to the type 2 models, the type 3 model is less computational heavy, which is of importance for power system studies [109].
The type 3 model will in this work be referred to as conventional EMTP representation of the MMCC for power system studies.

Type 4: Detailed Equivalent-Circuit-Based Model

Based on the NFSS derived in [103], an efficient and accurate (as accurate as type 3) representation of each of the phase legs of the MMCC VSC-HVDC was proposed in [29]. The large number IGBT/diode pairs and distributed SM capacitances in each converter leg are collapsed into a single Norton equivalent before interfaced with the main EMTP solver. The number of frequently switched branches in the resulting network admittance matrix is thereby significantly reduced, while all internal branch currents and node voltages information is retained within the Norton equivalent and accessible to the main EMTP solver. The NFSS and the previous type 4 MMCC VSC-HVDC model will be described in the following.

Type 5: Average Value Based Models

The IGBT/diode pairs are not explicitly represented in the type 5 average value models (AVMs) and the MMCC behaviour is modelled using controlled voltage and current, where it is assumed that all internal dynamics are well controlled and the circulating current is suppressed in the VSC-HVDC model [104].

4.2.1 Nested Fast and Simultaneous Solution

Most EMTPs applies Dommel's formulation, where each dynamic electrical element is converted into a Norton equivalent current source in parallel with a conductance, through the use of the trapezoidal integration rule [110, 111, 112].

The recent introduction of the FNSS [103] improved Dommel's network algorithm, where the two network partitions shown in Figure 4-2 are solves for the unknown voltage vectors u_1 and u_2 partitions 1 and 2. The sizes of the vectors are equal the number of nodes in the two partitions (i.e. $N1$ and $N2$ for partition 1 and 2, respectively). In the FNSS, the admittance matrices for partitions 1 and 2 (Y_{11} and Y_{22}, respectively) are inverted separately, before interfaced in the main EMTP solver. Although this introduces additional steps in the EMTP solution, the matrices to be inverted for the two partitions are only of the sizes $N1 \cdot N1$ and $N2 \cdot N2$, rather than one matrix of the size $N_{12} = (N1 + N2)^2$. For the MMCCs, the system partitioning is of high importance due to the high number of frequently switched branches in the full system of the size N_{12}.

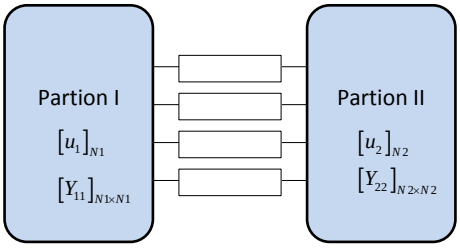

Figure 4-2 Partion of the electrical system into two subsystems.

The network equation for the system in Figure 4-2 is given in equation 4-1.

$$\begin{bmatrix} Y_{11} & Y_{12} \\ Y_{21} & Y_{22} \end{bmatrix} \cdot \begin{bmatrix} u_1 \\ u_2 \end{bmatrix} = \begin{bmatrix} j_1 \\ j_2 \end{bmatrix} \qquad 4\text{-}1$$

Where Y_{12} and Y_{21} are the interconnecting admittance matrices and j_1 and j_2 are the vectors of known current sources in the two partitions, obtained from numerical substitution and other sources [168]. Rearranging row 2 in equation 4-1 yields:

$$u_2 = (j_2 - Y_{21}u_1) \cdot Y_{22}^{-1} \quad 4\text{-}2$$

Substituting equation 4-2 into row 1 in equation 4-1 yields:

$$j_1 = Y_{11}u_1 + Y_{12}Y_{22}^{-1}(j_2 - Y_{21}u_1) \quad 4\text{-}3$$

Where the term $Y_{12}Y_{22}^{-1}j_2$ represents a Norton current source and $Y_{12}Y_{22}^{-1}Y_{21}$ represents the Norton admittance for partition 2, as seen from partitioning 1. Solving for u_1:

$$u_1 = (Y_{11} - Y_{12}Y_{22}^{-1}Y_{21})^{-1}(j_1 - Y_{12}Y_{22}^{-1}j_2) \quad 4\text{-}4$$

u_2 can be calculated by solving for u_1 and substituting into equation 4-2. The branch current can be calculated once the voltage vectors are known. The Norton equivalent current source is updated at each time-step and is a function of the history of the network in earlier time-steps.

4.2.2 Classification of the Considered Type 4 MMCC Models

Four DEMs are considered in the following. Table 4-1 present an overview of the DEMs in order to ease the reading. The DEM1 is similar to the original DEM of the HVDC presented in [29], valid for the DSHB. As previously stated, the DEM1 is used to benchmarking the DEM technique developed here. The DEM2 is applicable for the MMCCs with the half-bridge converter as the SM building block (i.e. the DSHB). The DEM3 is applicable for the DSFB, the SDFB as well as the WSCs, described in Chapter 3. DEM3 is essentially identical to the DEM2, except minor changes are made, which makes the DEM3 applicable to the DSFB, DSHB, SSFB (single star full-bridge), SDFB & WSCs (i.e. for the whole MMCC family described in Chapter 3). The modelling approach proposed here is therefore referred to as "universal" with the advantages outlined in section 4.1.

Table 4-1 Overview of the type 4 MMCC models considered in this chapter.

Abbreviation	Meaning	Applicable for:
DEM1	Original MMCC model developed in [29].	DSHB
DEM2	"Exact" HVDC model proposed here.	DSHB
DEM3	MMCC model of the STATCOM.	DSFB, SSFB, SDFB & WSCs
DEM4	Simplified HVDC model derived from the STATCOM model (from DEM3).	DSHB, DSFB, SSFB, SDFB & WSCs
CM	Conventional model (type 3 modelling type)	DSHB, DSFB, SSFB, SDFB & WSCs

The DEM1 and DEM2 are in this chapter used to represent the DSHB HVDC, the DEM3 is applied for the SDFB STATCOM and the DEM4 is implemented for the DSHB HVDC.

4.3 Original DEM1 SM Thévenin Equivalent

A description of the existing DEM1 is given in the following, as it is used benchmark the modelling technique developed here. Figure 4-3 shows MMCC HVDC converter station, which can be equipped with the half- or full-bridge converter as the SM building block.

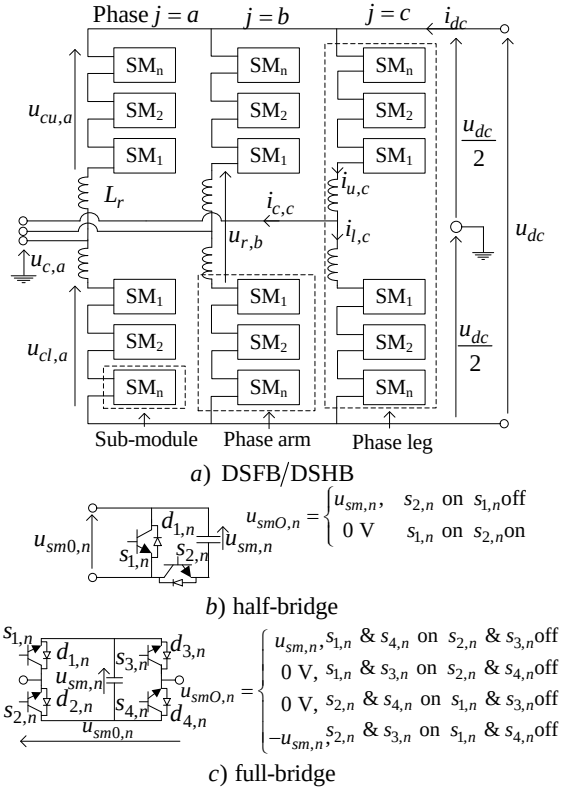

Figure 4-3 The double star MMCC VSC-HVDC, which can either be equipped with the b) half- or c) full-bridge converter in the SMs.

4.3.1 Equivalent Circuit of the Half-Bridge Converter Sub-Module

IGBT and Diode Representation

The IGBT/diode shown in Figure 4-4a are each represented as a two-state resistive switch in EMTPs [104,109,111] as shown in Figure 4-4b. As either the diode or the IGBT is conducting at a given instance, the IGBT/diode pair can still be treated as a single two state resistance [29], as in Figure 4-4c.

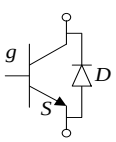

a) Anti-parallel IGBT/diode.

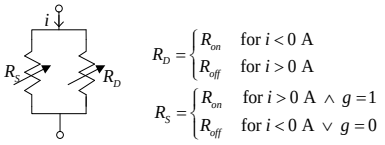

b) Type 3 and 4 representation of diode (D) and IGBT (S).

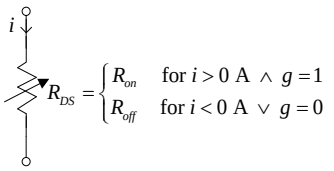

c) Type 3 and 4 representation of anti-parallel IGBT/diode.

Figure 4-4 Anti-parallel IGBT/diode and their type 3 and 4 representations. The IGBT switch S is controlled by the gating signal g ($g = 1$, conducting and $g = 0$, blocking).

SM Capacitor

The capacitor (C_{cap}) can be represented by its Thévenin or Norton equivalents by applying the trapezoidal rule of integration according to Dommel's formulation [111]. This numerical substitution will be used in the two detailed equivalent models described in the following. The trapezoidal rule is A-stable [113] and reasonably accurate for practical purposes [68]. The general Thévenin and Norton equivalents for the capacitor are derived as (equation 4-5 and 4-6, respectively):

$$\begin{aligned} u_{cap}(t) &= \frac{1}{C_{cap}} \int_{t_1-\Delta t}^{t_1} i_{cap}(t_1)\, dt + u_{cap}(t-\Delta t) \\ &\approx \underbrace{\frac{\Delta t}{2C_{cap}} \cdot i_{cap}(t)}_{cur.\ time\ step} + \underbrace{\left[u_{cap}(t-\Delta t) + \frac{\Delta t}{2C_{cap}} \cdot i_{cap}(t-\Delta t)\right]}_{prev.\ time\ step} \\ &= R_{cap} \cdot i_{cap}(t) + u_{Hist}(t-\Delta t) \end{aligned} \qquad 4\text{-}5$$

Where $R_{cap} = \Delta t/(2C_{cap})$. $u_{cap}(t)$ and $i_{cap}(t)$ are the voltage across and current through C_{cap}, respectively, see Figure 4-5a and b, where the Thévenin equivalent is shown. Δt is the simulation step size and hence $u_{cap}(t-\Delta t)$ and $i_{cap}(t-\Delta t)$ represents the voltage and current at the previous time step. The Norton equivalent is derived from equation 4-5 as in equation 4-6 shown in Figure 4-5c.

$$\begin{aligned} i_{cap}(t) &= \frac{2C_{cap}}{\Delta t}\left[u_{cap}(t) - u_{cap}(t-\Delta t)\right] - i_{cap}(t-\Delta t) \\ &= \underbrace{\frac{2C_{cap}}{\Delta t} u_{cap}(t)}_{cur.\ time\ step} + \underbrace{\left[-\frac{2C_{cap}}{\Delta t} u_{cap}(t-\Delta t) + i_{cap}(t-\Delta t)\right]}_{prev.\ time\ step} \\ &= \frac{u_{cap}(t)}{R_{cap}} + i_{Hist}(t-\Delta t) \end{aligned} \qquad 4\text{-}6$$

From equation 4-6 it is evident that the capacitor can be represented by an equivalent resistance $R_{cap} = \Delta t/(2C_{cap})$ in parallel with a current source $i_{Hist}(t-\Delta t)$ given as:

$$i_{Hist}(t-\Delta t) = -\frac{u_{cap}(t-\Delta t)}{R_{cap}} - i_{cap}(t-\Delta t) \qquad 4\text{-}7$$

The Thévenin and the Norton equivalents in Figure 4-5b and c, are the dual of each-other and just algebraic manipulations of the actual circuit. The Thévenin equivalent is used in the DEM1, whereas the Norton equivalent is used for the models proposed in this work.

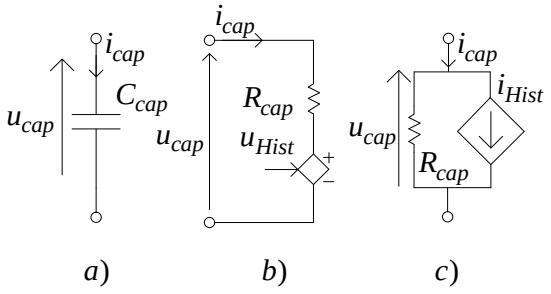

Figure 4-5 The capacitor and its b) Thévenin and c) Norton EMTP equivalents.

Using the Thévenin equivalent in 4-5 for the SM capacitor, the n^{th} SM half-bridge can be electrically represented as in Figure 4-6 [29].

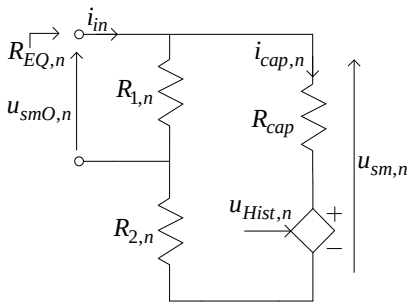

Figure 4-6 EMTP equivalent of the n^{th} half-bridge SM in DEM1.

The n^{th} SM output voltage can be expressed as:

$$u_{sm0,n}(t) = \frac{i_{in}(t)}{1/R_{2,n}(t) + 1/\left[R_{1,n}(t) + R_{cap}\right]} + \frac{R_{2,n}(t) \cdot u_{Hist}(t - \Delta t)}{1/R_{2,n}(t) + 1/\left[R_{1,n}(t) + R_{cap}\right]} = R_{EQ,n}(t) \cdot i_{in}(t) + u_{EQ,n}(t) \quad 4\text{-}8$$

Where $u_{Hist,n}(t - \Delta t) = u_{SM,n}(t - \Delta t) + R_c \cdot i_{cap,n}(t - \Delta t)$ from equation 4-5. The capacitor current in Figure 4-6 can be expressed as:

$$i_{cap,n}(t) = \frac{i_{in}(t)}{1/R_{2,n}(t) + 1/\left[R_{1,n}(t) + R_{cap}\right]} + \frac{u_{sm,n}(t - \Delta t) + R_c \cdot i_{cap,n}(t - \Delta t)}{R_{2,n}(t) + R_{1,n}(t) + R_{cap}} \quad 4\text{-}9$$

Similarly, the capacitor voltage is calculated as:

$$u_{sm,n}(t) = R_{cap} \cdot \left[i_{cap,n}(t) + i_{cap,n}(t - \Delta t)\right] + u_{sm,n}(t - \Delta t) \quad 4\text{-}10$$

The Thévenin parameters for the n^{th} SM ($R_{EQ,n}(t)$ and $u_{EQ,n}(t)$) are readily available in equation 4-8. As shown in this section, the derivation of the n^{th} SM Thévenin equivalent is straightforward using this approach and is suitable for the DEM1 when the MMCC employs half-bridges as proposed in [29]. However, when the MMCC is equipped with the full-bridges (such as e.g. the SDFB STATCOM), the derivation of the governing equations becomes more challenging.

4.4 DEM2 SM Thévenin Equivalent

The governing equations for the DEM2 are simply derived based on inspection and inversion of an 2×2 admittance matrix for the half-bridge SM and therefore suitable for more complex circuits such as the full-bridge SM, as demonstrated in the next section.

Using the Norton equivalent in equation 4-6 for the SM capacitor, the half-bridge SM can be electrically represented as in Figure 4-7 for the n^{th} SM for the proposed model. Three electrical nodes can be identified ($N_{m,n}$, $m = 1,2,3$) in the figure, where the SM output node $N_{3,n}$ is taken as the reference node in the nodal analysis. The fixed current source i_{in} represents the phase arm current, which is identical to the N SMs in the phase arm.

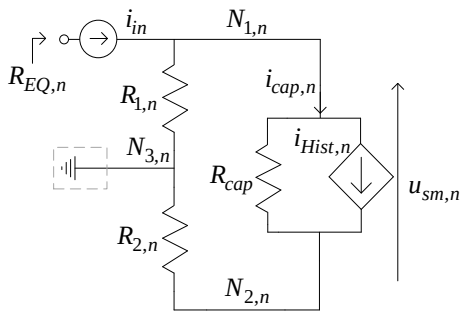

Figure 4-7 EMTP equivalent of the n^{th} half-bridge SM, where the independent current source (i_{in}) represents the current flowing into the SM and will be used in the development of the proposed MMCC VSC-HVDC.

The simultaneous equations for the circuit in Figure 4-7 can be described in matrix form:

$$i_n(t) = G_n(t)u_n(t) \tag{4-11}$$

Where the current vector i_n contains the known current source, u_n contains the unknown node voltages. G_n is the admittance matrix of the n^{th} SM, which can simply be obtained using circuit inspection and applying fundamental circuit laws [106]. A time dependency of G_n has been included in equation 4-11 and 4-12 in order to highlight that the half-bridge SM is a time-dependent piece-wise smooth dynamic system due to the switching devices $R_{1,n}(t)$ and $R_{2,n}(t)$.

$$\begin{aligned} G_n(t) &= \begin{bmatrix} G_{11,n}(t) & G_{12,n}(t) \\ G_{21,n}(t) & G_{22,n}(t) \end{bmatrix} \\ &= \begin{bmatrix} \frac{1}{R_{1,n}(t)} + \frac{1}{R_{cap}} & -\frac{1}{R_{cap}} \\ -\frac{1}{R_{cap}} & \frac{1}{R_{2,n}(t)} + \frac{1}{R_{cap}} \end{bmatrix} \end{aligned} \tag{4-12}$$

Where $G_{11,n}$ and $G_{22,n}$ are the sum of the admittances connected directly to node $N_{1,n}$ and $N_{2,n}$, respectively. $G_{12,n} = G_{21,n}$ is the negative sum the admittances connecting $N_{1,n}$ and $N_{2,n}$. Equation 4-11 in expanded form then becomes:

$$\begin{bmatrix} i_{in}(t) - i_{Hist,n}(t - \Delta t) \\ \\ i_{Hist,n}(t - \Delta t) \end{bmatrix} = \begin{bmatrix} \frac{1}{R_{1,n}(t)} + \frac{1}{R_{cap}} & -\frac{1}{R_{cap}} \\ -\frac{1}{R_{cap}} & \frac{1}{R_{2,n}(t)} + \frac{1}{R_{cap}} \end{bmatrix} \begin{bmatrix} u_{1,n}(t) \\ \\ u_{2,n}(t) \end{bmatrix} \tag{4-13}$$

By inversion of G_n, the unknown node voltages ($u_{1,n}$ and $u_{2,n}$ at node $N_{1,n}$ and $N_{2,n}$, respectively) can be obtained. The inversion is straightforward as shown in the following and is based on equation 4-14:

$$G_n^{-1}(t) = \frac{1}{det(G_n(t))} \cdot adj(G_n(t)) \tag{4-14}$$

Where $det(G_n)$ and $adj(G_n)$ are the determinant and adjoint matrix of G_n, respectively.

The determinant of G_n becomes:

$$det(G_n(t)) = \frac{1}{R_{1,n}(t) \cdot R_{2,n}(t)} + \frac{1}{R_{1,n}(t) \cdot R_{cap}} + \frac{1}{R_{2,n}(t) \cdot R_{cap}} \tag{4-15}$$

An interesting point worth noting from equation 4-15 is the possibility to emulate SM failures, where either R_1 or R_2 is set equal to 0 Ω, as G_n is still non-singular in that specific case.

The adjoint matrix of G_n is:

$$adj(G_n(t)) = \begin{bmatrix} \frac{1}{R_{2,n}(t)} + \frac{1}{R_{cap}} & \frac{1}{R_{cap}} \\ \frac{1}{R_{cap}} & \frac{1}{R_{1,n}(t)} + \frac{1}{R_{cap}} \end{bmatrix} \quad 4\text{-}16$$

G_n^{-1} can then be obtained:

$$G_n^{-1}(t) = \frac{\begin{bmatrix} \frac{1}{R_{2,n}(t)} + \frac{1}{R_{cap}} & \frac{1}{R_{cap}} \\ \frac{1}{R_{cap}} & \frac{1}{R_{1,n}(t)} + \frac{1}{R_{cap}} \end{bmatrix}}{\left[\frac{1}{R_{1,n}(t) \cdot R_{2,n}(t)} + \frac{1}{R_{1,n}(t) \cdot R_{cap}} + \frac{1}{R_{2,n}(t) \cdot R_{cap}} \right]} \quad 4\text{-}17$$

$i_{Hist,n}(t - \Delta t)$ in equation 4-13 is calculated from equation 4-7 using the capacitor current $i_{cap,n}(t - \Delta t)$ calculated in equation 4-6 (at the previous simulation time step) and the nodal voltages $u_{1,n}(t - \Delta t)$ and $u_{2,n}(t - \Delta t)$ found from equation 4-13 as:

$$i_{Hist,n}(t - \Delta t) = -\frac{u_{1,n}(t-\Delta t) - u_{2,n}(t-\Delta t)}{R_{cap,n}} - i_{cap,n}(t - \Delta t) \quad 4\text{-}18$$

The current flowing through the capacitor at the current time step is similarly calculated from equations 4-6 and 4-13:

$$i_{cap,n}(t) = \frac{u_{1,n}(t) - u_{2,n}(t)}{R_{cap,n}} + \left[-\frac{u_{1,n}(t-\Delta t) - u_{2,n}(t-\Delta t)}{R_{cap,n}} - i_{cap,n}(t - \Delta t) \right] \quad 4\text{-}19$$

The output voltage of the n^{th} SM is simply $u_{sm0,n} = u_{1,n}$ obtained from equation 4-13, as $N_{3,n}$ is taken as reference node in Figure 4-7. The Thévenin equivalent resistance is readily available from the admittance matrix($R_n = G_n^{-1}$) in equation 4-17 as $R_{EQ,n} = R_{11,n}$:

$$R_{EQ,n}(t) = \frac{\frac{1}{R_{2,n}(t)} + \frac{1}{R_{cap}}}{\left[\frac{1}{R_{1,n}(t) \cdot R_{2,n}(t)} + \frac{1}{R_{1,n}(t) \cdot R_{cap}} + \frac{1}{R_{2,n}(t) \cdot R_{cap}} \right]} \quad 4\text{-}20$$

Figure 4-8shows the Thévenin equivalent of the n^{th} SM, where the Thévenin resistance is calculated in equation 4-20 and the SM output voltage of $u_{sm0,n} = u_{1,n}$ obtained from equation 4-13. The Thévenin voltage source is then:

$$u_{EQ,n}(t) = u_{1,n}(t) - R_{EQ,n}(t) \cdot i_{in}(t) \quad 4\text{-}21$$

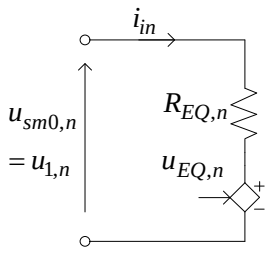

Figure 4-8 Thévenin equivalent of the n^{th} SM in the phase arm.

4.5 Phase Arm Equivalent in the DEM1 and DEM2

Similarly to the model presented in [29], by series connecting the N SMs in the phase arm as in Figure 4-9a, the arm equivalent shown in Figure 4-9b results, where the Thévenin parameters are:

$$u_{EQ,arm}(t) = \sum_{n=1}^{N} u_{EQ,n}(t) \tag{4-22a}$$

$$R_{EQ,arm}(t) = \sum_{n=1}^{N} R_{EQ,n}(t) \tag{4-22b}$$

Where $R_{eq,n}$ and $u_{eq,n}$ are given in equation 4-8 for the DEM1 and in equations 4-20 and 4-21 for the DEM2.

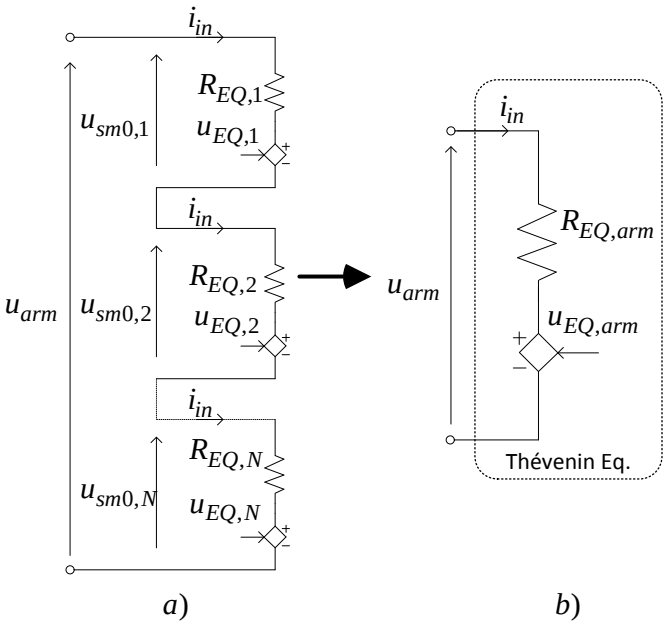

Figure 4-9 Thévenin equivalent of the MMCC VSV-HVDC phase arm.

The DEM1 to 4 in Table 4-1 are in this work implemented in the FORTRAN language and interfaced with PSCAD/EMTDC. It should be noted that the Thévenin and Norton equivalents are the dual of each other and are just algebraic manipulations of the circuit equations and the final equivalent can be easily converted to one form or the other, according to preference. All model interfaces to the PSCAD/EMTDC electric network solver will, regardless of the complexity of the model, be represented by a Norton equivalent [114]. PSCAD/EMTDC provides a subroutine as part of the interface, which automatically converts the Thévenin equivalent in Figure 4-9b to a Norton equivalent. However, as the conversion to a Norton equivalent is straightforward it will be conducted prior to the interfacing subroutine is executed for completeness. Figure 4-10 shows the interface of the proposed MMCC VSC-HVDC model with the main electrical network.

Although the derivation of $R_{EQ,n}$ in equation 4-20 for the DEM2 requires more steps than the DEM1 presented in [29], the modelling approach for the DEM2 is considered universal, as the approach can be readily applied to MMCCs using the full-bridge SM or even more complex structures, as the network equations are merely based on inspection, whereas in [29] more advanced network analysis is required in order to calculate e.g. the history terms of the capacitors and the input resistance of the full-bridge SM. Furthermore, from an implementation point of view, the model approach presented

here will only require very little modification in order to also model the full-bridge converter SM as will be shown in section 4.7.

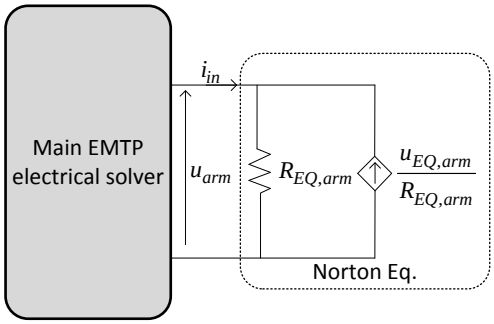

Figure 4-10 Norton equivalent of the MMCC VSC-HVDC phase arm with N SMs.

4.5.1 Recap on the DEM1 and DEM2 Modelling Steps

The modelling steps for the DEM1 and DEM2 are essentially the same. First, the SM equivalent in Figure 4-11a is derived as in Figure 4-11b. Then the Thévenin equivalent of the individual SM is derived. Finally the sum of the SM equivalents are merged into one Thévenin (or Norton) equivalent and interfaced with the main EMTP solver as shown in Figure 4-11c.

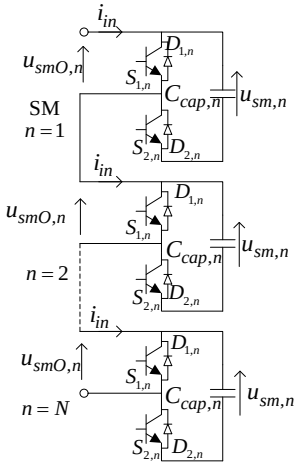

a) Series connection of N half-bridge SMs in the MMCC VSC-HVDC phase arm.

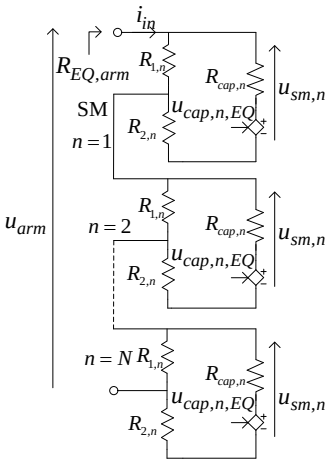

b) Electrical equivalent of figure a.

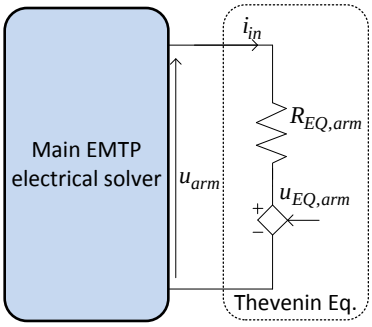

c) Aggregated Thévenin equivalent of the phase arm in figure a and its interface with the main EMTP solver.

Figure 4-11 Derivation of Thevenin equivalent representation of the MMCC VSC-HVDC phase arm.

4.6 DEM3 Modelling

The SDFB STATCOM in Figure 4-12 is used as reference in the DEM3 model description, although the modelling approach is valid also for the DSHB, DSFB, SSFB and the WSCs as indicated in Table 4-1.

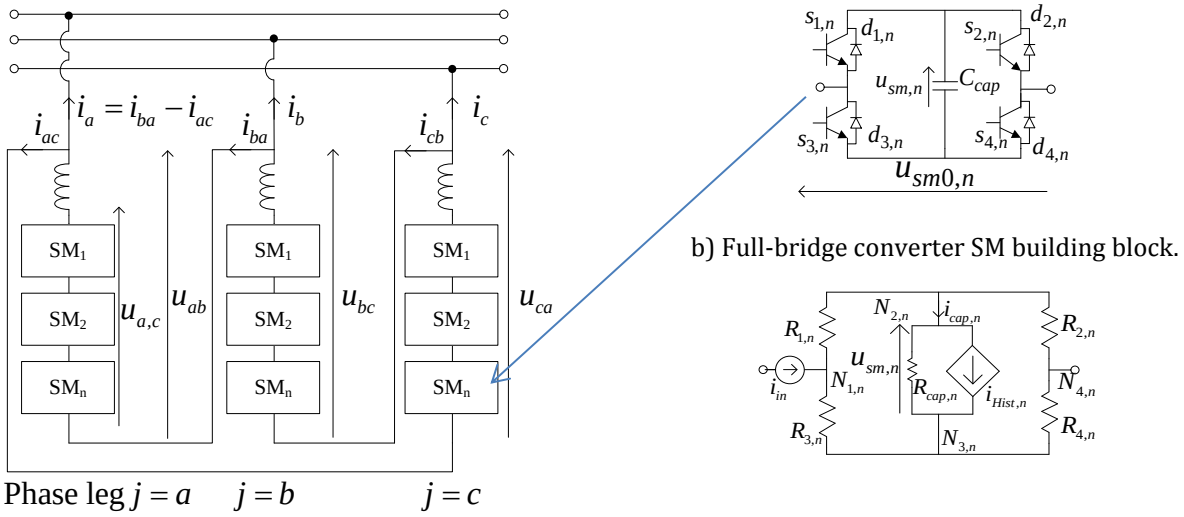

a) SDFB.

b) Full-bridge converter SM building block.

c) Equivalent circuit of the SM.

Figure 4-12 The SDFB STATCOM.

The equivalent circuit of the full-bridge converter in Figure 4-12b can be represented by the equivalent circuit in figure c, following the same reasoning as for the half-bridge SM in section 4.3.1.

Four electrical nodes can be identified ($N_{m,n}$, $m = 1,2,3,4$) in Figure 4-12c, where output node $N_{4,n}$ in the n^{th} SM is taken as reference node in the nodal analysis. The current flowing through the SM can be considered as an independent current source in the analysis, which is identical to the N_{sm} series connected SMs in the phase leg as shown in Figure 4-12a (e.g. i_{ba} flowing in the Δ-branch of phase A).

The simultaneous equations for the circuit in Figure 4-12c can described in matrix form as:

$$i_n(t) = G_{n,FB}(t)u_n(t) \tag{4-23}$$

Where $i_n(t) = \left[i_{in}(t), -i_{Hist,n}(t-\Delta t), i_{Hist,n}(t-\Delta t)\right]'$ and $u_n(t) = \left[u_{1,n}(t), u_{2,n}(t), u_{3,n}(t)\right]'$ is the known current source and unknown nodal voltage vector, respectively. The time variant admittance matrix of the n^{th} full-bridge SM is:

$$G_{n,FB}(t) = \begin{bmatrix} G_{11,n}(t) & G_{12,n}(t) & G_{13,n}(t) \\ G_{21,n}(t) & G_{22,n}(t) & G_{23,n}(t) \\ G_{31,n}(t) & G_{32,n}(t) & G_{33,n}(t) \end{bmatrix} \tag{4-24}$$

Where G_{kk} is the sum of the admittances connected to node k and and $G_{kj} = G_{jk}$ is the sum of the admittances directly connecting node k and j (k ≠ j). Inserting the parameters from Figure 4-12c into equation 4-23 yields:

$$\begin{bmatrix} i_{in}(t) \\ -i_{Hist,n}(t) \\ i_{Hist,n}(t) \end{bmatrix} = \begin{bmatrix} \frac{1}{R_{1,n}(t)} + \frac{1}{R_{3,n}(t)} & -\frac{1}{R_{1,n}(t)} & -\frac{1}{R_{3,n}(t)} \\ -\frac{1}{R_{1,n}(t)} & \frac{1}{R_{1,n}(t)} + \frac{1}{R_{2,n}(t)} + \frac{1}{R_{cap,n}} & -\frac{1}{R_{cap,n}} \\ -\frac{1}{R_{3,n}(t)} & -\frac{1}{R_{cap,n}} & \frac{1}{R_{3,n}(t)} + \frac{1}{R_{4,n}(t)} + \frac{1}{R_{cap,n}} \end{bmatrix} \times \begin{bmatrix} u_{1,n}(t) \\ u_{2,n}(t) \\ u_{3,n}(t) \end{bmatrix} \tag{4-25}$$

The unknown node voltages ($u_{1,n}(t), u_{2,n}(t)$ and $u_{3,n}(t)$ at node $N_{1,n}$, $N_{2,n}$ and $N_{3,n}$, respectively) can be obtained by inversion of $G_{n,FB}(t)$, as in equation 4-26, where the time dependency and the SM number index are omitted for simplicity:

$$R_{FB} = \frac{\begin{bmatrix} G_{22}G_{33} - G_{23}G_{32} & G_{13}G_{32} - G_{12}G_{33} & G_{12}G_{23} - G_{13}G_{22} \\ G_{23}G_{31} - G_{21}G_{33} & G_{11}G_{33} - G_{13}G_{31} & G_{13}G_{21} - G_{11}G_{23} \\ G_{21}G_{32} - G_{22}G_{31} & G_{12}G_{31} - G_{11}G_{32} & G_{11}G_{22} - G_{12}G_{21} \end{bmatrix}}{det(G_{n,FB})} \quad 4\text{-}26$$

Where the determinant is given as:

$$det(G_{n,FB}) = G_{11}(G_{22}G_{33} - G_{23}G_{32}) - G_{12}(G_{21}G_{33} - G_{23}G_{31}) + G_{13}(G_{21}G_{32} - G_{22}G_{31}) \quad 4\text{-}27$$

$i_{Hist,n}(t)$ in equation 4-25 is calculated from equation 4-7 using the capacitor current $i_{cap,n}(t - \Delta t)$ from equation 4-6 (at the previous integration time step). The nodal voltages $u_{2,n}(t - \Delta t)$ and $u_{3,n}(t - \Delta t)$ are solved from inversion of equation 4-25. The controlled current source in Figure 4-12c is therefore:

$$I_{Hist_n}(t) = -\frac{u_{2,n}(t-\Delta t) - u_{3,n}(t-\Delta t)}{R_{cap,n}} - i_{cap,n}(t - \Delta t) \quad 4\text{-}28$$

The current flowing through the capacitor at the current integration time step is similarly calculated from equation 4-6 and 4-25.

4.6.1 Thévenin Equivalent of the Full-Bridge SM

As demonstrated in [29] and in section 4.3, the input or Thévenin equivalent resistance ($R_{eq,n}$) is effortlessly derived for the half-bridge converter (i.e. the DEM1). Some further steps are required in determination of $R_{eq,n}$ for the full-bridge converter based SM, due to the slightly more complex structure of this converter as e.g. $R_{1,n}, R_{3,n}$ and $R_{cap,n}$ are neither connected in series nor in parallel. One could transform the loop comprising the said three resistances in Figure 4-12c from Δ- to a star configuration, which would simplify the circuit. However, $R_{EQ,n}$ is readily available from 4-26 as $R_{11,n}$ as:

$$R_{EQ,n} = R_{11,n} = \frac{G_{22}G_{33} - G_{23}G_{32}}{det(G_n)} \quad 4\text{-}29$$

The time varying Thévenin voltage source is then:

$$u_{EQ,n}(t) = u_{1,n}(t) - R_{EQ,n}(t) \cdot i_{in}(t) \quad 4\text{-}30$$

Now, the Thévenin equivalent parameters for the full-bridge converter SM is derived and the same phase arm/leg aggregation as for the DEM1 and DEM2 can be made in order to have the complete two node Norton equivalent interfacing with the main EMTP solver as in Figure 4-10.

The above derivation of the full-bridge converter's Thévenin/Norton equivalent is essentially as simple as solving a 3×3 matrix. Therefore, the above proposed method is directly applicable in determination of the Thévenin equivalent of a given SM with an arbitrary number ($N_{SM,nodes}$) electrical nodes. This includes both the half-bridge converter with $N_{SM,nodes} = 2$ as described in section 4.4 as well as more complex SMs with higher $N_{SM,nodes}$. This is considered by the author to be an improvement compared to existing detailed equivalent models of the MMCCs).

4.7 DEM4 Modelling

By assuming a short circuit of $R_{2,n}$ and an open circuit connection $R_{4,n}$ in Figure 4-13, it is possible to transform the circuit equivalent of the full-bridge converter to the half-bridge converter, as also shown in the figure. This approximation makes it possible to use the full-bridge converter equations derived in section 4.4 for the MMCCs with half-bridge in the SMs. Hence all the MMCCs can be modelled using the same source code, making it possible to only have to maintain one script. Although this approximation is not mathematical correct, it is practically as accurate and as fast as the DEM1 and DEM2. This is demonstrated in the model evaluation in section 4.8.1.

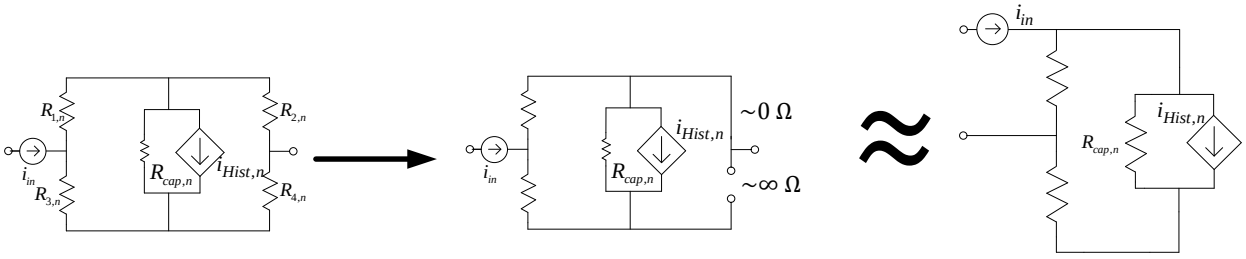

Figure 4-13 Transformation of the circuit equivalent of the full-bridge converter to the half-bridge converter.

4.8 Model Evaluation

The proposed DEM2 and DEM4 are benchmarked against the conventional non-reduced DSHB HVDC model (i.e. type 3 model in section 4.2) and the DEM1 from [29]. A single terminal HVDC system feeding a passive grid with open loop control is considered here for simplicity. The number of SMs in the HVDC converter phase arm is varied from $N = 5$ to 200. A fixed simulation time-step of Δt = 20 µs adapted from [29, 105] is used in evaluation of the proposed HVDC models.

The DEM3 model of a SSFB STATCOM is similarly evaluated with a type 3 model of the SSFB with a simulation time-step of Δt = 10 µs, where N is varied from 10 to 100.

All simulations are performed on a standard Windows 7 Enterprise platform with a 2.5 GHz Intel Core i5, 3.9 GB of RAM running PSCAD/EMTDC Professional version v4.5.

Similarly as in [29] and [105], the accuracy evaluation of the proposed modelling technique for the MMCC family will be made during steady-state operating mode. The evaluation of the accuracy of the proposed models in both [29] and [105] were based on comparing the time domain results with the conventional type 3 model in two separate graphs for the two models. In order to better correlate the simulation results here also the least mean square error is evaluated. Equation 4-31a calculates the normalised the least mean square error between the reference vector y^a and the vector y^b, respectively.

However, equation 4-31a does not account for errors due to short and possibly large discrepancies such as spikes in one of the vectors not replicated in the other. For this reason the maximum error is also calculated, as in equation 4-31b.

$$Er_{norm} = \frac{\sqrt{\sum_{i=1}^{K}(y_i^a - y_i^b)^2}}{\sum_{i=1}^{K}(y_i^a)^2} \quad \text{4-31a}$$

$$Er_{max} = max\left(|y_i^a| - |y_i^b|\right) \quad \text{4-31b}$$

4.8.1 DEM2 and 4 Evaluation

Accuracy

Table 4-2 shows the calculated normalised and maximum error between the reference converter phase output voltages from the CM ($y^{a=CM}$) and DEM1 ($y^{a=DEM1}$) to the proposed DEM2 ($y^{b=DEM2}$). Practically identical results are obtained using the three models, making the two DEMs very attractive for the model representation of the MMCC VSC-HVDC system, which will become obvious from the simulation time evaluation in the following.

Table 4-2 also shows the comparison of the approximated DEM4 ($y^{b=DEM4}$) to the mathematical correct DEM2. The results are practically identical making the approximated DEM model applicable to both MMCCs with full- and half-bridge converters in the SM.

Table 4-2 Evaluation of the accuracy of the proposed DEM2 against the CM and the DEM1 for the converter phase output voltage. The accuracy of the DEM4 against the DEM2 is shown in the last two columns.

N SM	$y^{a=CM}, y^{b=DEM2}$		$y^{a=DEM1}, y^{b=DEM2}$		$y^{a=DEM2}, y^{b=DEM4}$	
	Er_{norm} [10^{-6} p.u]	Er_{max} [kV]	Er_{norm} [10^{-6} p.u]	Er_{max} [kV]	Er_{norm} [10^{-6} p.u]	Er_{max} [kV]
5	0.927	0.590	0.142	0.001	0.319	0.018
10	1.070	0.916	0.023	0.000	0.209	-0.002
15	3.251	-8.488	0.189	-0.034	0.188	0.005
20	6.305	-5.998	0.551	-0.029	0.808	-0.028
25	5.829	-2.703	0.492	-0.010	0.448	0.000
40	1.959	-1.647	0.245	-0.019	0.233	-0.019
50	1.969	-0.405	0.260	-0.009	0.203	0.017
100	1.911	0.663	0.318	-0.015	0.240	-0.005
200	3.269	-1.203	0.444	-0.015	0.343	-0.014

Figure 4-14 shows simulation results for the DEM2 and the conventional model with N=10 SMs in order to ascertain the good model agreement in the time domain.

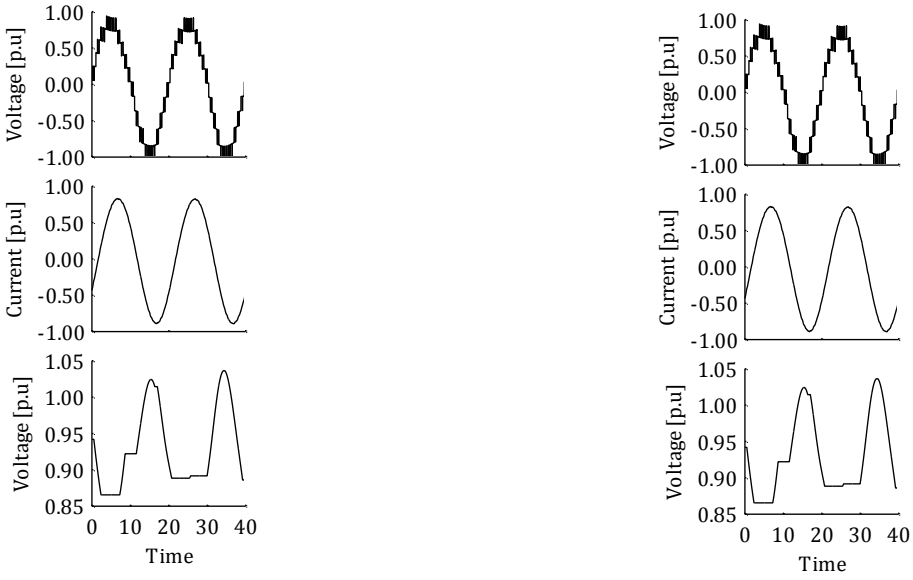

a) DEM2. b) Conventional type 3 HVDC model.

Figure 4-14 Simulated phase A voltage (top) and current (middle) using the DEM2 and the conventional model for $N = 10$. Lowest plot shows the output voltage of one of the SMs in phase A.

Simulation Speed

Table 4-3 shows the simulation run time for the three model for a 200 ms period with a Δt = 20 µs time step. Figure 4-15 presents a more visual comparison of the simulation times.

The simulation run times for of the three DEMs are practically identical and relatively insensitive to the number of SMs in the converter. The run time for the CM is for $N = 5$ SM is in the same time range as the DEMs. However, the run time for $N = 200$ SM is 13.5 hours or more than 1250 times than the DEMs, highlighting the need for DEM representation of the MMCCs with high N in the phase arm.

Table 4-3 Comparison of the simulation run time for a 200 ms period.

N SM	Running time (s)				Acceleration ratio (%)		
	CM	DEM1	DEM2	DEM4	CM/ DEM1	CM/ DEM2	CM/ DEM4
5	8.9	6.3	3.9	6.8	141	228	131
10	20.8	7.3	6.3	6.9	285	330	301
15	54.2	8.6	5.4	5.9	630	1004	919
20	54.6	9.4	5.9	7.1	581	925	769
25	153.1	14.3	7.6	6.9	1071	2014	2219
40	629.4	14.4	8.7	9.6	4371	7234	6556
50	951.1	16.7	12.1	9.6	5695	7860	9907
100	4493.1	27.3	24.0	18.2	16458	18721	24687
200	48963.4	38.1	39.0	32.4	128513	125547	151122

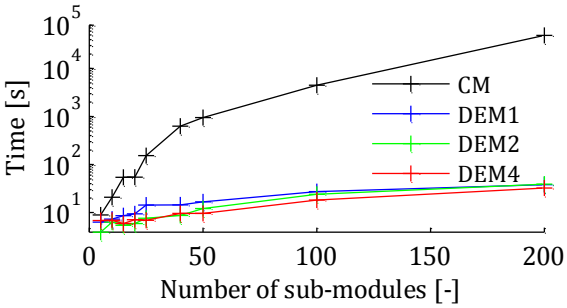

a) Simulation speeds of the four HVDC models.

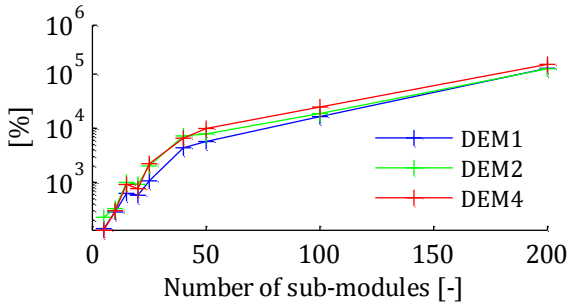

b) Acceleration ratios of the three DEMs with respect to the CM.

Figure 4-15 Simulation speeds for the CM, DEM1, DEM2 and DEM4 as a function of the number of SMs in the HVDC phase arm.

DEM2 and 4 Evaluation dynamic Evaluation

In [29] it was demonstrated that the DEM1 provided good agreement with the conventional MMCC model for power step changes. Taking into account the significantly simulation improvement of the DEMS compared to the CM from Table 4-2 and Table 4-3 it is considered sensible to evaluate the DEM2 and DEM4 against the DEM1 rather than the CM. This is done in Chapter 6 after the considered control system is described.

4.8.2 DEM3 Evaluation

Table 4-4 shows the simulation run time of the DEM3 and the CM of a SSFB STATCOM with varying number of SMs in the phase leg. Figure 4-16 shows a visual comparison of the simulation speed. Table 4-4 also shows the accuracy of the DEM3 with respect to the CM.

As for the HVDC models in the above, the simulation run time is heavily affected by the number of SMs considered for the CM, whereas it has only little influence on simulation speed of the DEM3. Inconsequential discrepancies are present for all considered cases, making the proposed modelling technique attractive for the MMCC family and its variants.

Table 4-4 Comparison of the simulation run times for a 100 ms time period and evaluation of the accuracy of the DEM3 against the CM of a SSFB STATCOM.

N SM	Running time (ms)		Acceleration ratio (%)	Accuracy	
	CM	DEM3	CM/ DEM3	$Er_{norm} \times 10^{-6}$	Er_{max} [10^{-3}p.u]
10	5897	1264	466	62	1.85
20	17160	2449	700	132	3.48
30	42619	2450	1740	201	4.92
40	81776	3229	2000	179	4.91
50	88530	4088	2749	172	3.21
100	1308770	7114	18000	117	3.37

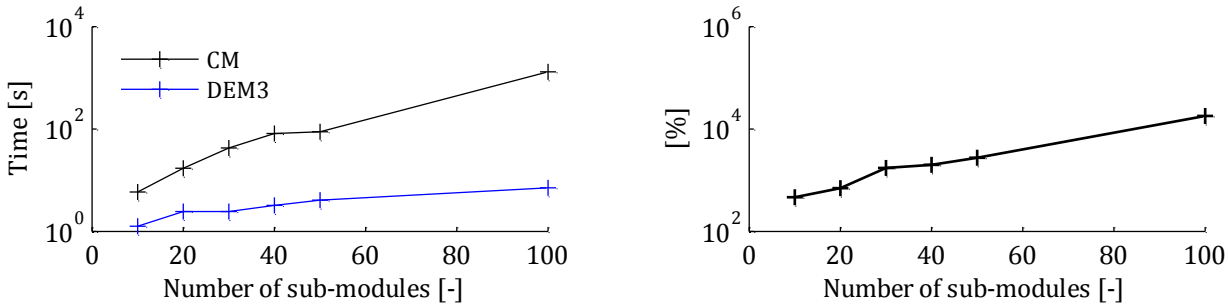

a) Simulation speeds of the two STATCOM models.

b) Acceleration ratios of the DEM3 with respect to the CM.

Figure 4-16 Simulation speeds of the SSFB CM and DEM3,as function of the number of SMs in the STATCOM converter leg.

4.9 Chapter Summary

An overview of the EMTP modelling techniques has been presented in this chapter. An EMTP based modelling technique has been derived, which is applicable for the MMCC family described in Chapter 3. The modelling technique is considered simple as the derivation of the SM Norton/Thévenin equivalent is merely based on circuit inspection. The accuracy of the technique is demonstrated by evaluating the least mean square error relative to the conventional MMCC modelling, yielding practical identical results.

Figure 4-17 shows an overview of the MMCC family and the five EMTP based models of the MMCC phase arm/leg representation considered in this chapter. Based on the overview, the modelling technique is applicable to the complete MMCC family.

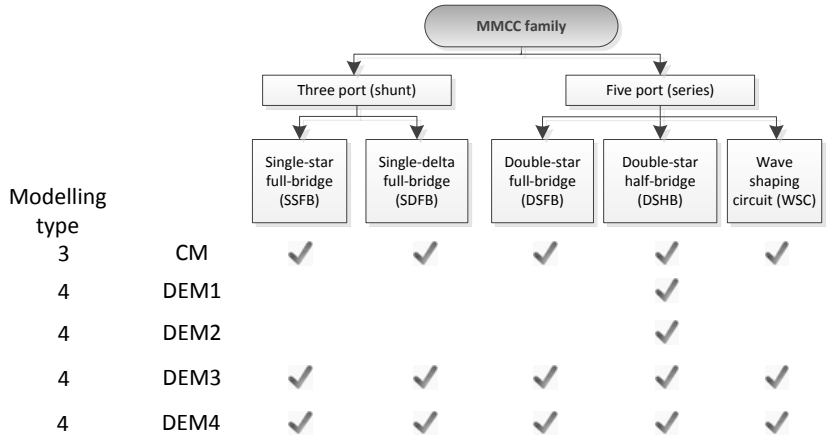

Figure 4-17 Overview of the five considered model representations of the converter phase arm/leg and their application for the MMCC family.

Chapter 5 Measurement Campaign at London Array Offshore Wind Power Plant

Real life measurement data constitute an important part in industry-oriented research. The purpose of this chapter is to describe the measurement campaign realised on a state-of-the-art static compensator (STATCOM) located at the onshore grid connection point of London Array offshore wind power plant (LAOWPP).

5.1 Relevance and Purpose of Measurement Campaign

Measurement data is an important part in the evaluation process of wind power plants (WPPs), including passive and active WPP components such as the STATCOM [115]. Long term quality measurement allows the researcher to obtain real life knowledge on the operating characteristics of the component for various operating scenarios.

Therefore, a long term harmonic measurement campaign has been prepared and conducted within the PhD project at Clevehill substation, UK, where four STATCOMs are installed. Clevehill substation serves as grid connection for LAOWPP.

The purpose of the measurement campaign is foremost to obtain real life knowledge on the working mechanism of the converter as well as for model development and validation. A review of modular multi-level cascaded converters (MMCCs) was made at the start of the PhD project and described in Chapter 3. Based on the review it was found that, in some perspective, there is a high degree of similarities between the working principles of the MMCC voltage sourced high-voltage direct current (VSC-HVDC) and the MMCC STATCOM technologies, especially seen from a model development point of view. It was therefore initially assumed that the obtained knowledge and validated modelling procedure for the STATCOM could be extended to also cover the MMCC VSC-HVDC system. This thereby introduces a high degree of synergy between the development of models of MMCC VSC-HVDC and the MMCC STATCOM, as well as it provides a platform for also validating the developed model of the MMCC VSC-HVDC without having actual measurement data. This consideration will be evaluated in Chapter 6.

Extensive offshore WPP (OWPP) harmonic field measurement campaigns have previously been conducted and post-processed in the previous Industrial PhD project "Harmonics in Large Offshore Wind Farms" [58] at DONG Energy Wind Power (DEWP). The previous harmonic measurement campaigns focused on the full-scale two-level converter used in the wind turbine generators (WTGs). Therefore, the measurement campaign conducted within this research project focuses on the STATCOM and high frequency measurements have therefore not been made in the WTGs.

5.2 Purpose of Measurements

The purpose of the measurement campaign was initially to obtain real life knowledge on harmonic emission of the STATCOM, the applied pulse width modulation (PWM) type and the dynamic response of the STATCOM for different power system events. The measurement campaign was intended for time and frequency domain analysis in order to gain detailed knowledge of the characteristics of the STATCOM. Furthermore, the measurement data constitutes an important part in the modelling and model evaluation of the MMCC STATCOM as well as a platform for MMCC VSC-HVDC model development and validation, as described in the above.

According to the authors' knowledge, the presented results are the first high quality measurement to be made on a STATCOM in situ for research purposes.

5.2.1 Limitations LAOWPP

The measurement campaign was continuously conducted throughout February 2013, where the OWPP was not fully commissioned and thus not operating at full capacity. The time period was selected due to the authors time limited access to the STATCOM, because of the offshore transmission system ownership (OFTO) regime in the UK [116]. The author considers the obtained measurement data sufficient for the validation of the proposed model of the STATCOM, described in this work.

5.3 System Description LAOWPP

The LAOWPP is located 20 km off the east coast of the UK at the mouth of the Thames, see Figure 5-1a. The OWPP is built in two phases, where Phase 1 was partly commissioned at the end of 2012. LAOWPP Phase I comprises 175 × 3.6 MW type 4 full-scale converter (FSC) WTGs, yielding a total capacity of 630 MW, making it the largest OWPP in the world. Phase 2 is constructed it would extend the total capacity to 870 MV. Two offshore platforms are installed in phase one, whereas one substation, Clevehill, was constructed onshore, as shown in Figure 5-1b. LAOWPP I is made up of four sections, where a STATCOM is located in each of these section as shown in the picture. Two pods are prepared for the possible extension.

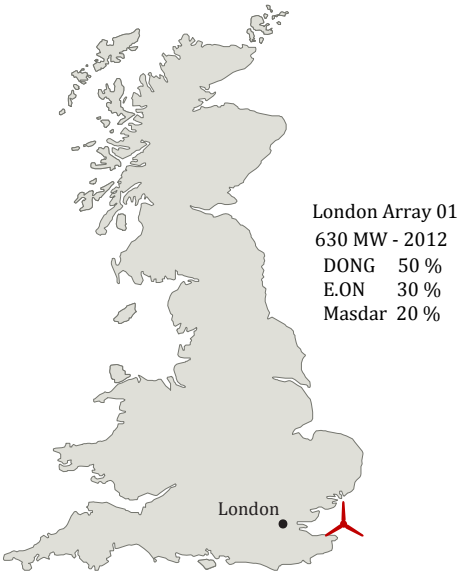

a) LAOWPP location.

b) Photo of Clevehill substation, where the voltage on the four circuits of LAOWPP01 is being transformed from 150 to 400 kV. Photo is adapted and modified from [116].

Figure 5-1 LAOWPP location and photo of Clevehill substation.

A simplified single-line diagram of the LAOWPP is shown in Figure 5-2 and Figure 5-3 shows a close-up of one of these sections.

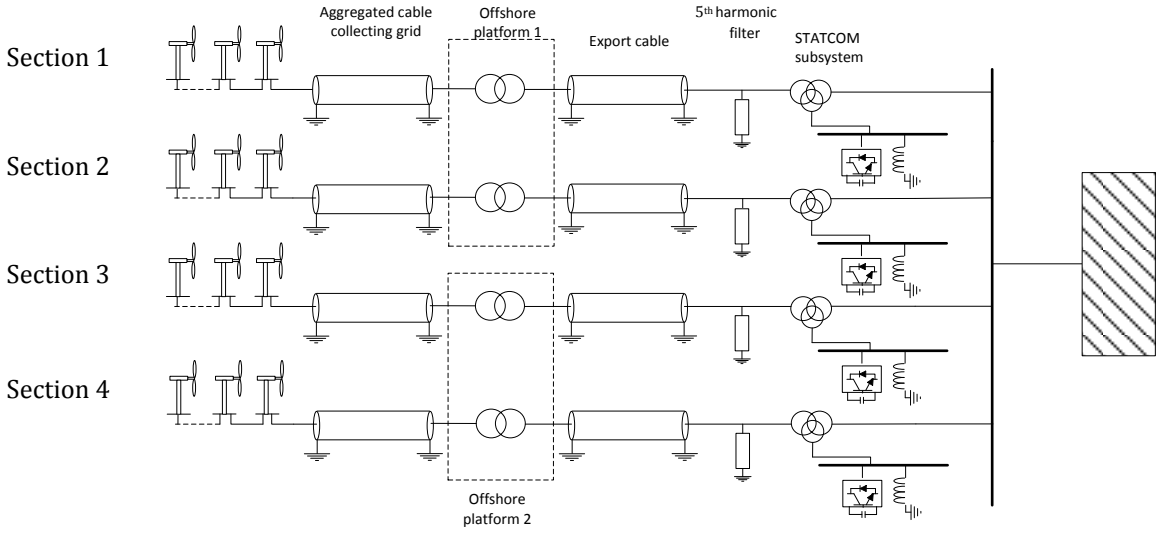

Figure 5-2 Simplified single-line diagram of LAOWPP.

As indicated in Figure 5-2 and Figure 5-3, a combination of a STATCOM and a mechanically switched reactor (MSR) is connected to the tertiary winding of a 400/150/13.9 kV – 180/90/90 MVA onshore transformer in each of the four OWPP sections. The purpose of the STATCOMs is to comply with the transmission system operator's (NGET's) steady-state and dynamic reactive power requirements [56].

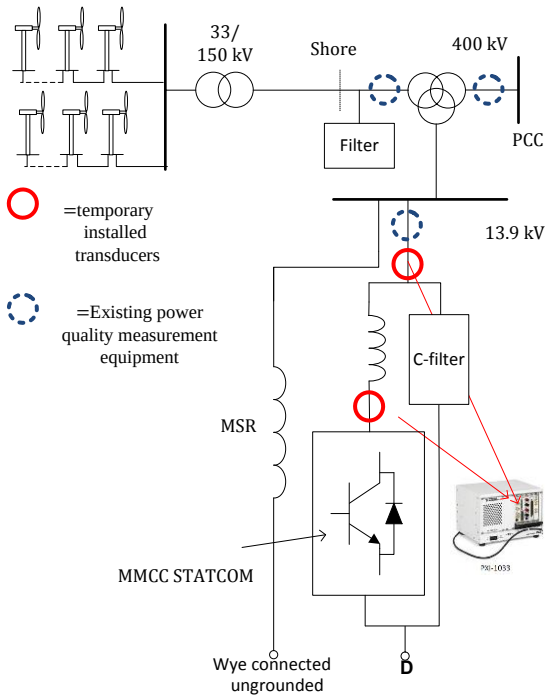

Figure 5-3 Simplified single line diagram of one of the four sections of the LAOWPP. Transducer locations are indicated.

5.3.1 STATCOM Subsystem

Figure 5-4 shows a simplified three-phase diagram of the STATCOM and associated filter.

The STATCOM is equipped with 22 full-bridge sub-modules (SMs) per phase, where two are redundant, but still in service during normal operating mode [118]. The efficient operating number of SMs is therefore $N = 20$, resulting in a 41-level line voltage waveform as the STATCOM is connected in delta (i.e. the STATCOM is connected as a three port single delta full-bridge (SDFB) converter, see the definition in Chapter 3). The measurements point are also indicated in Figure 5-3 and Figure 5-4, as will be described in the following section.

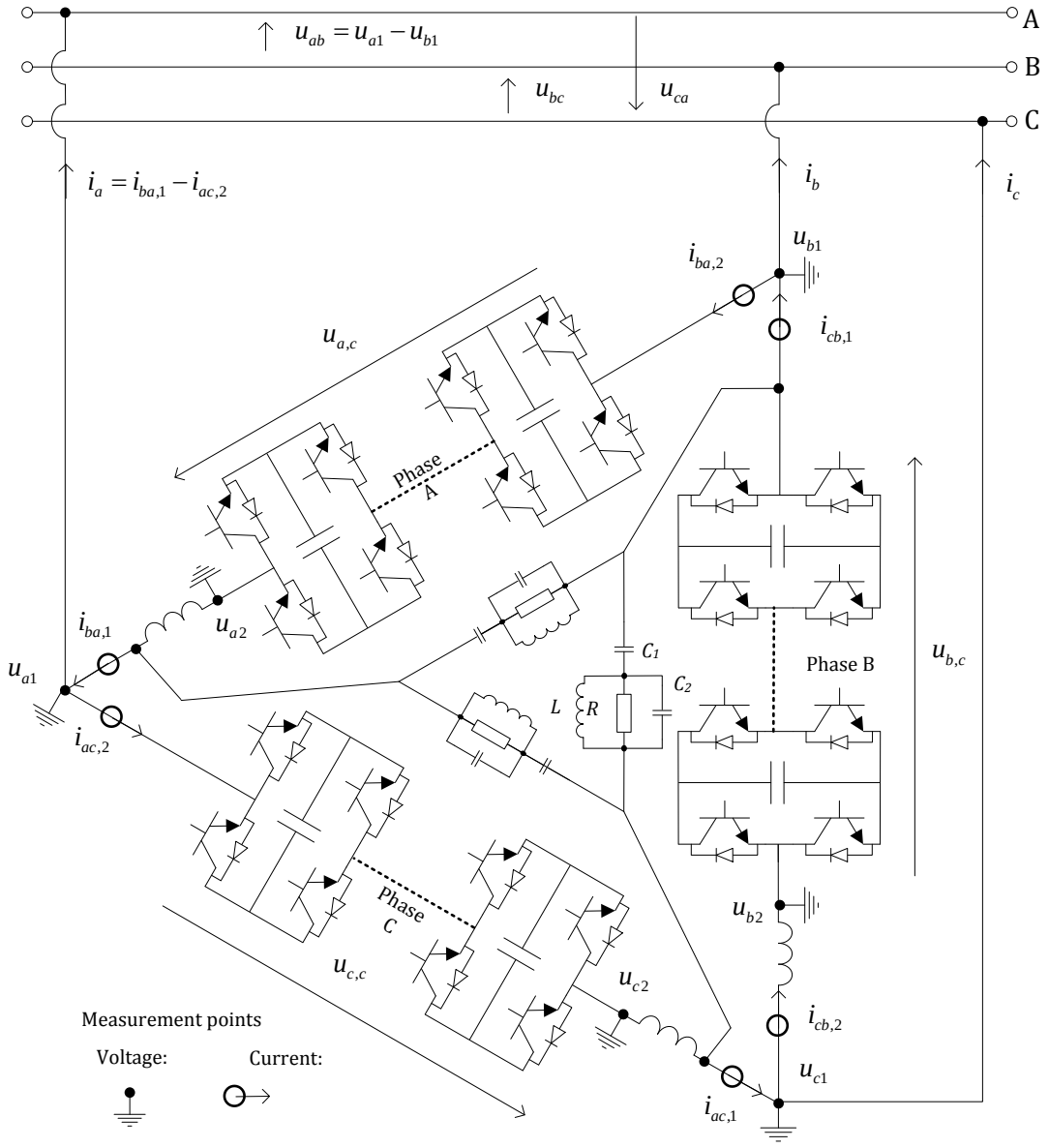

Figure 5-4 Simplified three-phase diagram of the STATCOM and associated filter.

5.4 Measurement system

A robust and flexible high frequency measurement system was developed in [1,58], where also appropriate post-processing methods were proposed. Therefore, the measurement campaign at Clevehill substation was prepared and executed taking into account the experience and methods gained during the previous measurement campaigns. Also, it was considered that existing or similar voltage and current transducers (VTs and CTs, respectively) as well as the data logging equipment used in the previous campaigns were appropriate for the STATCOM measurements. The STATCOM measurement campaign was executed outdoor; hence the sensitive equipment had to be adapted to this environment.

As indicated Figure 5-3 and Figure 5-4, measurements will only be made on the 13.9 kV side of the tertiary winding of the grid connection transformer; therefore no measurements were recorded from the OWPP directly. Both the substation and the OWPP were under construction during the installation of the measurement equipment, hence there were a number of uncertainties during the planning of the campaign and only a short window for installing the measurement equipment. Furthermore, offshore measurement campaign is associated with a high cost as well as uncertainties regarding access to the WTGs due to weather conditions. As mentioned, extensive OWPP measurement campaigns have previously been conducted by DEWP, focusing on the WTG as a harmonic source. Therefore, the offshore measurement data acquisition was omitted in the campaign. Elspec power quality meters are installed on the 150 kV side at Clevehill substation, which were used in order to obtain knowledge on the operating conditions and power production level from the OWPP.

It was demonstrated in [58] that Elspec power quality meters are not suitable for harmonic assessment where the generated harmonics are not only linked to the fundamental frequency, but also affected by the applied modulation technique in the power electronic devices (e.g. the type 4 WTG and the STATCOM). The Elspec equipment performs online data processing, where synchronisation (i.e. sample rate adjustment according to the fundamental frequency) is made. This therefore only allows appropriate harmonic assessment of baseband harmonics, which are only affected by the fundamental frequency. Furthermore, the Elspec applies lossy compression, where only estimated harmonics above a certain threshold are saved. Therefore, the Elspec power quality meters can only be applied for harmonic assessment if one is very critical about the obtained results.

5.4.1 Voltage Transducer Installation

Figure 5-5 shows the location of the VTs on the three-phase diagram (indicated with red). Also the voltages indicated with green can be obtained based on the actual voltage measurements. The phase voltages are measured at both sides of the reactor in each phase.

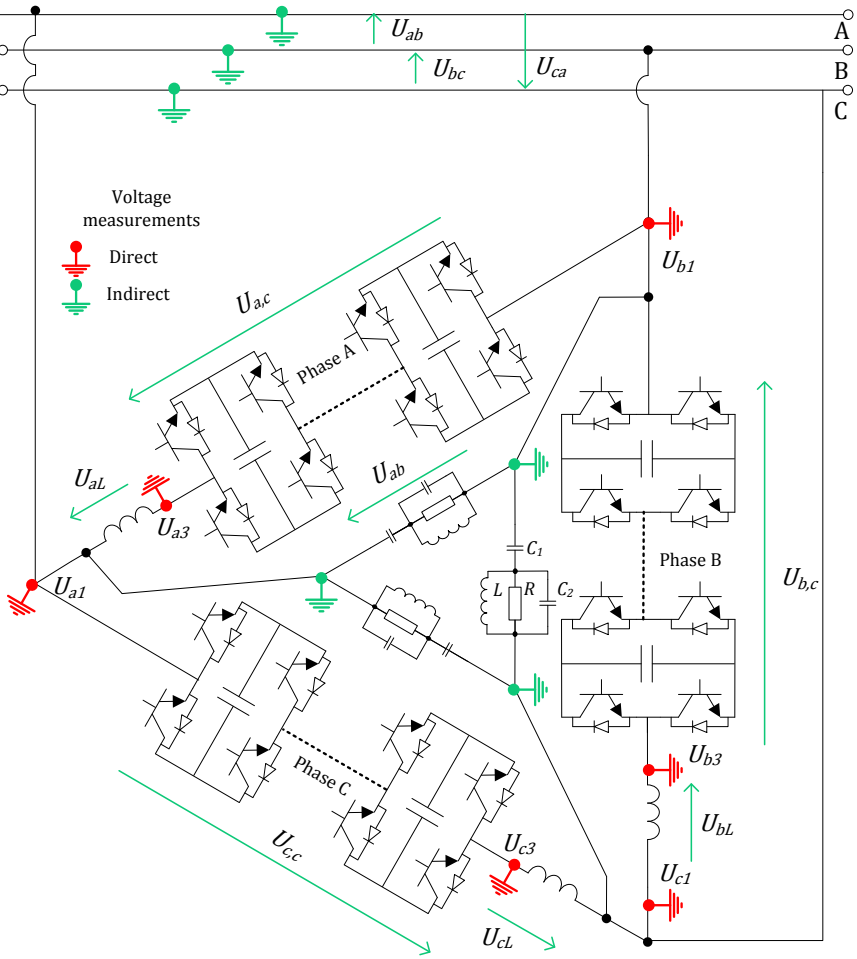

Figure 5-5 Simplified three phase diagram of the STATCOM and associated filter. Locations of the VTs are indicated with red.

The phase to ground voltage is measured using a capacitive divider which is composed of a standard "dead-end" 36 kV T-connector and an amplifier developed in [119], with bandwidth 1 Hz – 1 MHz [115].

Examples of the VT installation are shown in Figure 5-6.

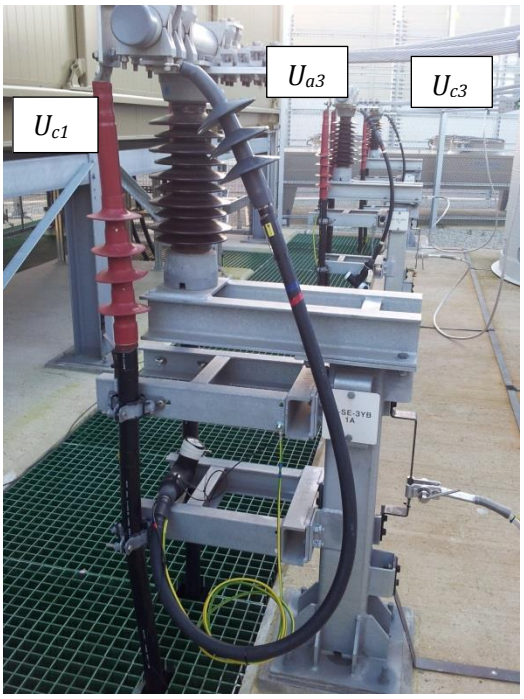

a) Voltage sensors installed on three bus bars, physically located between converter container on the left and phase reactors on the right hand side.

b) Voltage sensor measuring U_{b1}. The filter is connected to the open bus bar (see Figure 5-5a. The phase reactors and converter container can be seen in the background.

Figure 5-6 Installation of four of the six voltage sensors.

5.4.2 Current Transducer Installation

Figure 5-7 shows the location of the CTs (indicated with red) as well as the currents that can be obtained from the measurement (indicated by green). The convention of power flow is positive when leaving the STATCOM as indicated in the figure. Hence; the reactive power is negative when the STATCOM operates as an inductor during normal operating condition, compensating the export cable capacitive charging current. The author considers it more convenient to consider the STATCOM as a variable capacitor, hence the applied power convention.

The currents are measured using Powertek CWT30 Flexible Rogowski Coil with 55 mHz – 3 MHz minimum bandwidth [120]. The CTs were installed outdoor hence appropriate shielding against water etc. was needed for the integrators, as shown in Figure 5-8.

As can be seen in Figure 5-7, the currents are physically measured on both side of the converter leg and the filter branch in order to obtain both the current through the converter (e.g. I_{ab3}) and the current that flows through both filter and converter (e.g. I_{ab1}). Therefore it is possible to obtain the filter current (e.g. $I_{ab2} = I_{ab1} - I_{ab3}$). The filter current is not measured directly due to two main concerns. Firstly, the filter is connected by the busbar shown in Figure 5-6b (where I_{bc2} flows through). Therefore the Rogowski coil would have to be insulated at 13.9 kV, which is not considered appropriate. Also a custom made arrangement would have to be built to fix the coil for safety reasons as the equipment was installed outdoor for approximately 4 months. Secondly, by measuring only at the six indicated locations in Figure 5-5b it is possible to install the CTs at the same physical location, and therefore limits the number of specially designed cases to two, as shown in Figure 5-8.

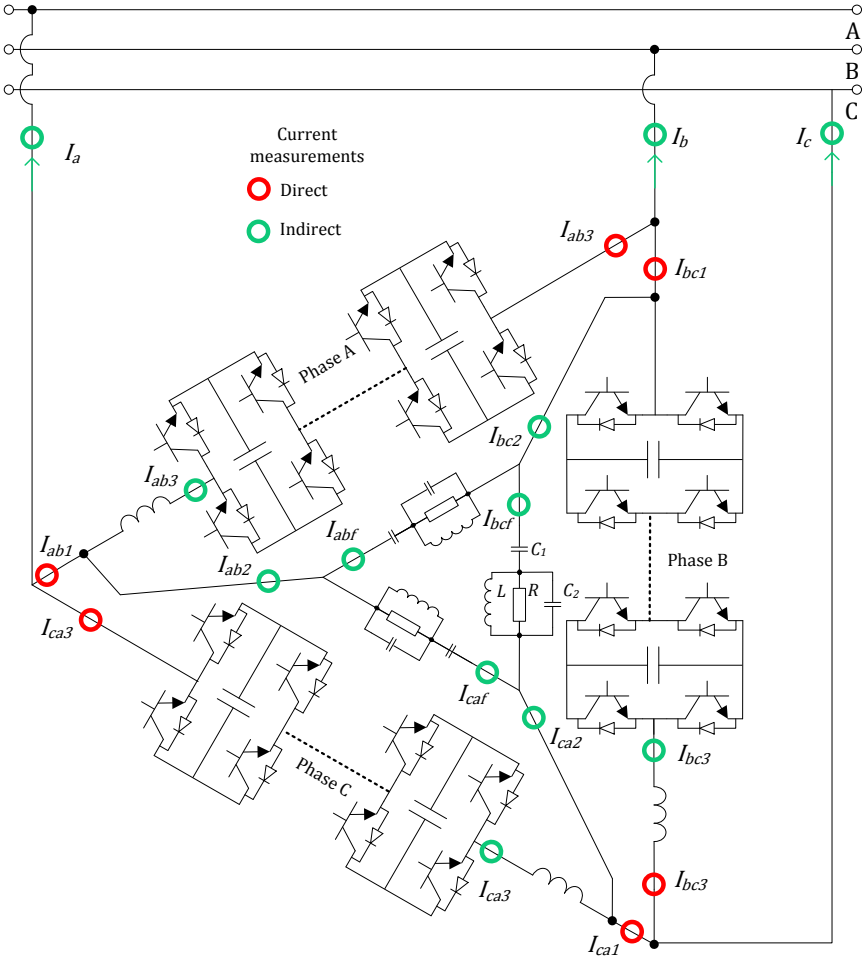

Figure 5-7 Simplified three phase diagram of the STATCOM and associated filter. Locations of the CTs are indicated with red.

Figure 5-8 Installation of CTs.

5.4.4 Sampling Rate

The sampling rate was set at 51.2 kS/s/ch for approximately half the duration of the measurement campaign and at 102.4 kS/s/ch for the remainder of the one-month measurement campaign, resulting in approximately 11 TB of data (12 channels).

5.5 Measurement Results

Figure 5-9 and Figure 5-10 show measurement results for two STATCOM operating points. From the figures it can be observed that the converter waveforms (2nd graph from the top) have a stair case waveform due to the MMCC technology. These high frequency waveforms are attenuated in the line-line voltage in the top graphs of Figure 5-9 and Figure 5-10. The current waveforms have a small harmonic content in both operating modes.

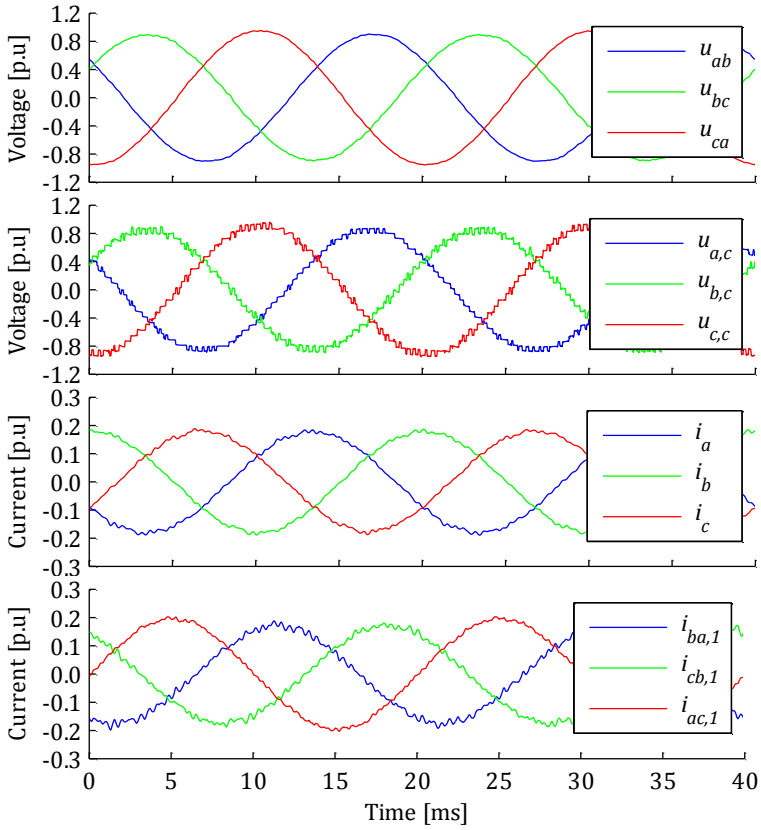

Figure 5-9 Measured STATCOM waveforms.

From the two figures it can be observed that the measurement system is capable of logging the measurement data with high resolution.

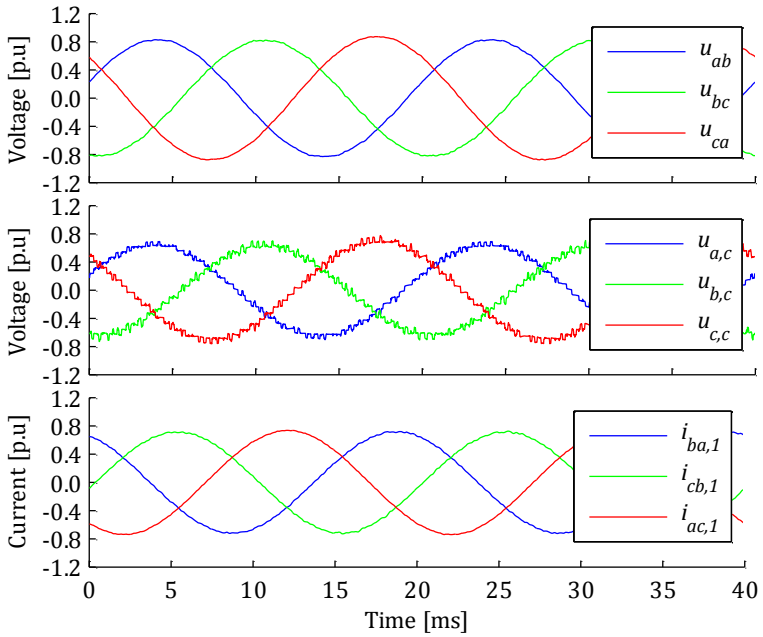

Figure 5-10 Measured STATCOM waveforms.

5.6 Chapter Summary

A description of the measurement campaign realised at the STATCOM, located at the onshore grid connection point of LAOWPP has been presented. The measurement data has provided useful insight of the commercial MMCC STATCOM's operating characteristics. The measurement data will in Chapter 6 be used to evaluate the developed time domain model of the STATCOM.

Chapter 6 Multi-Level Converter Modelling and Evaluation

This chapter present the time domain models of the modular multi-level cascaded converter (MMCC) implemented in PSCAD/EMTDC. The chapter focusses on generic modelling of the commercial available voltage-sourced high-voltage direct current (VSC-HVDC) and the static compensator (STATCOM) described in Chapter 3 and Chapter 4. The detailed equivalent modelling technique proposed in Chapter 4 is considered in the representation of the MMCCs. The low level control, ensuring the stabilisation of the distributed sub-module (SM) voltages in the MMCCs are described and implemented. The generic modelling approach taken is evaluated based on comparison with the field measurements at London Array offshore wind power plant (OWPP).

6.1 STATCOM

Previous research on the modelling of the MMCC STATCOM has mainly been focused on the control system design and performance of the converter using a switching model (e.g. [121]), an analytical model (e.g. [122]) or a detailed model of the PED (e.g. [123]). None of these publications consider the accuracy of the model representation based on comparison with measurement data. This section aims at filling this gap, by providing a comparison between a generic, yet detailed STATCOM model and field measurements from London Array OWPP.

6.1.1 Studied MMCC System and its Control

The ±50 MVar Siemens SVC Plus described in Chapter 4 is taken into consideration. The STATCOM is shown in Figure 6-1.

One of the main challenges related to MMCCs is the control of the distributed SM capacitor voltages dynamically as well as in steady-state [17]. A brief description of the implemented controller will be given in the following, with reference to Figure 6-2. Figure 6-2a shows the upper-level controller, which is a conventional cascaded PI controller with the inner-loop current controller operating in the rotating reference frame (RRF) [124, 125].

The two outer loops are responsible for controlling the at the point of common coupling (PCC) reactive power (Q_{PCC}) (q-axis) and the average SM capacitor voltage of the three phases ($u_{dc,AV}$) in the d-axis, respectively. $u_{dc,AV}$ is calculated as in equation 6-1 and is compared with rated SM voltage ($u^*_{dc,sM}$) in the outer control loop.

$$u_{dc,AV} = \frac{1}{3N}\sum_{j=1}^{J=3}\sum_{n=1}^{N} u_{dc,j,n} \qquad 6\text{-}1$$

The converter phase leg voltage controller in Figure 6-2b controls the average converter leg voltage ($u_{dc,AV,j} = 1/N \sum_{n=1}^{N} u_{dc,j,n}$) in the j^{th} phase leg ($j = a, b, c$) to follow $u_{dc,AV}$ from equation 6-1. The output of the P4 controller in the j^{th} phase is then multiplied by a cosine wave which is in phase with $u^*_{c,j}$ obtained from Figure 6-2a. Summing the output of the three P4 phase controllers is then a zero-sequence reference current i^*_0. In the existence of an imbalance between the phase leg voltages, e.g. $u_{dc,AV} > u_{dc,AV,a}$, the product of $u_{a,c} \cdot i_0$ forms a positive active power charging the capacitors in phase leg A in Figure 6-2c. The current loop forces i_0 to follow its command signal i^*_0.

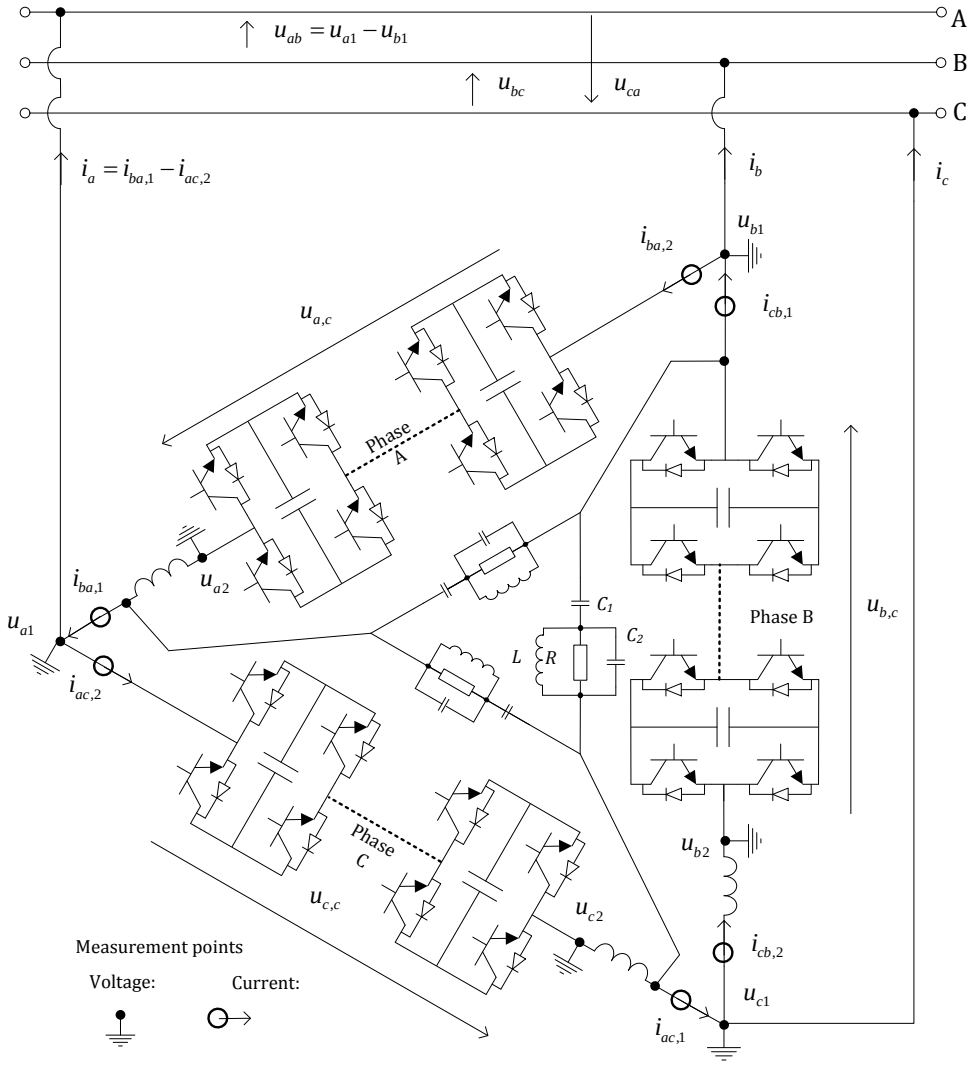

Figure 6-1 Simplified three-phase diagram of the STATCOM and associated filter. The figure is identical to Figure 5-4 in Chapter 5.

A distributed SM voltage controller has been included as shown in Figure 6-2 c-i. The controller is responsible for maintaining the capacitor voltage of the n^{th} SM in the j^{th} phase ($u_{dc,j,n}$) at the reference value $u_{dc,AV}$. The controller forms an active power between $u_{dc,j,n}$ and the leg current ($i_{k,2}$ ($k = ba, cb, ac$), see Figure 6-2c) [126]. In [100] it was shown that no coupling exists between the zero-sequence current controller in Figure 6-2b and the individual SM controller in Figure 6-2c-i. Figure 6-2c-i shows the addition of the reference signals from the three main controllers in Figure 6-2a, b and c. The resulting reference signal $u^*_{j,n}$ for the n^{th} SM ($n = 1,2, \dots N$) in the j^{th} phase ($j = a, b, c$) is then fed to a modulator, where it is compared to a triangular-wave carrier (TWC_n, $n = 1,2, \dots N$) that is individual for the n^{th} SM (Figure 6-2d). Phase opposition disposition (POD) phase-shifted carrier-based pulse-width modulation (PSCPWM) [57] with a phase shift of $\theta_{ps} = 2\pi(n-1)/N$ between two adjacent carriers (e.g. TWC_n and TWC_{n+1}) has been used. The frequency of the carriers has been selected as $f_{TWC_n} = 3.37 \cdot 50$ Hz. This value of f_{TWC_n} has been chosen as a non-integer pulse number has a balancing effect on the SM capacitors [127].

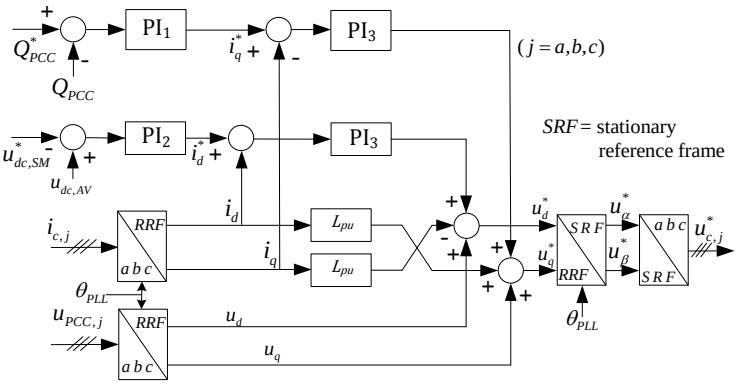

a) Upper-level controller with current controller operating in the RRF.

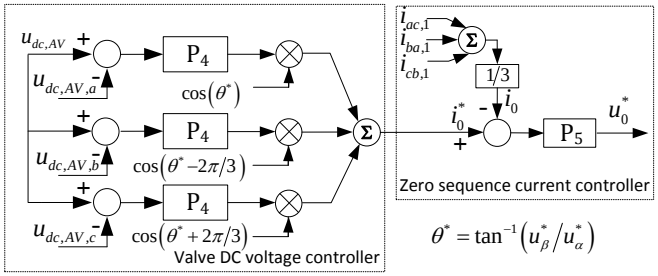

b) Phase-valve voltage and zero-sequence current controller.

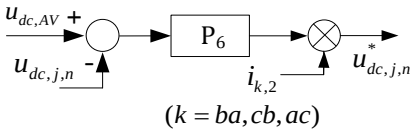

c-*i*) Individual SM controller.

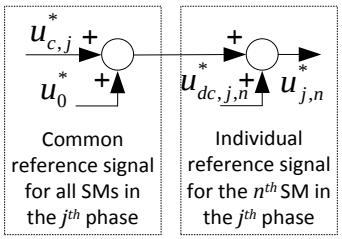

c-*ii*) Reference signal for the n^{th} SM.

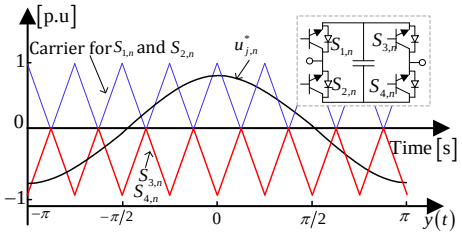

d) POD PSCPWM for the n^{th} SM.

Figure 6-2 Implemented STATCOM controller. Figure c) – *i*) shows the individual capacitor voltage controller for the n^{th} SM in j^{th} phase ($j = a, b, c$). Figure c) – *ii*) shows the reference signal for the n^{th} SM.

6.1.2 STATCOM Model Evaluation

The detailed equivalent model of the STATCOM (DEM3) developed in Chapter 4 is evaluated based on comparison with data obtained in the measurement campaign at London Array OWPP described in Chapter 5. The above described control system is included in the model.

The STATCOM model will be validated based on comparison with obtained measurement results during steady-state operating mode and during a transition from $Q \approx -0.73$ p.u to $Q \approx -0.79$ p.u. The evaluation will be based on a qualitative approach comparing measurement and simulation results and will be done in the time domain. The model could additionally have been evaluated in the frequency domain (e.g. calculating the frequency components of the time domain waveforms), as has been done for the CGI in Chapter 9. However, this has been omitted as knowledge of the background harmonics (from the grid and from the OWPP) is considered to be needed in order to make a useful frequency domain evaluation.

Figure 6-3 shows the measured and simulated voltages and the line currents during steady-state (see Figure 6-1 for symbol description). Subscripts "*m*" and "*s*" denote measurement and simulation, respectively. As evident from the figure, the measurement system is capable of capturing the measured waveforms with high resolution. The figure also clearly shows that the converter terminal voltages with a good approximation appear to be sinusoidal waveforms due to the MMCC technology. Very little harmonic residue is present in the output line current as also replicated in the simulation.

A good agreement can in general be observed between measurements and simulations. Some differences can be observed in especially phase C currents. This could be caused by a possible slight imbalance in the grid voltage. An imbalance in the line voltages was sustained throughout the measurement period as shown in Figure 6-4. The voltage imbalance has been compensated for in the simulation by adjusting the amplitude of the individual Thevenin phase voltage sources. This is

considered appropriate since no detailed information of the external grid was available. This adjustment is not very precise and might explain the above mentioned discrepancies.

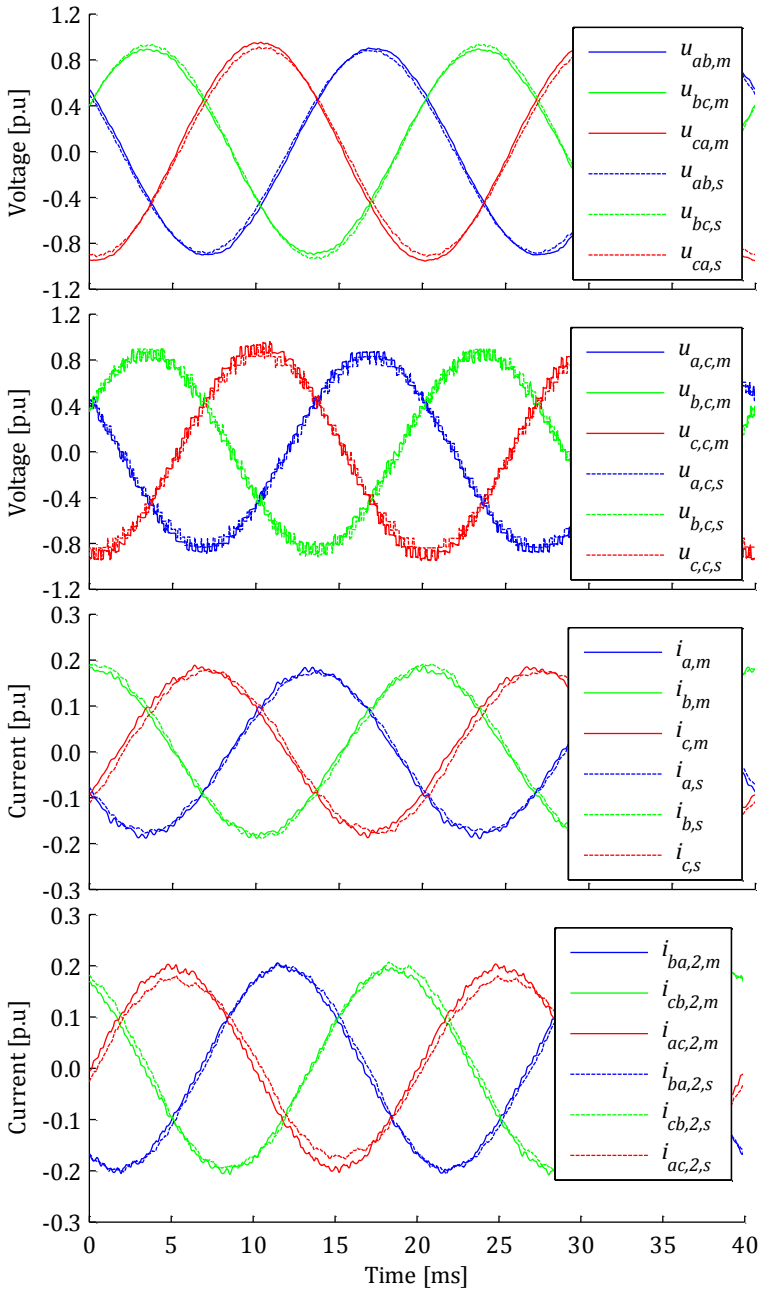

Figure 6-3 Comparison between measurement and simulation during steady-state operating mode. Subscripts "*m*" and "*s*" denote measurement and simulation, respectively.

Figure 6-5 shows the measured and simulated phase A quantities. The simulated converter voltage $u_{a,c,s}$ has a very similar time domain characteristics as the measured $u_{a,c,m}$ although no information was available on the control and modulation technique applied in the commercial STATCOM. In addition, a relatively good agreement exists for the line and delta currents.

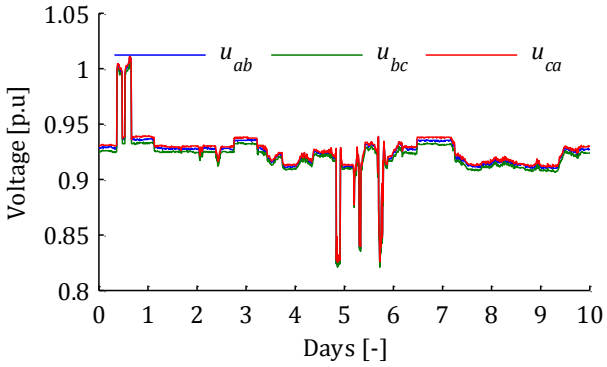

Figure 6-4 10-minute average RMS line voltage at the STATCOM 13.9 kV busbar for a 10 day sample during the one-month measurement campaign.

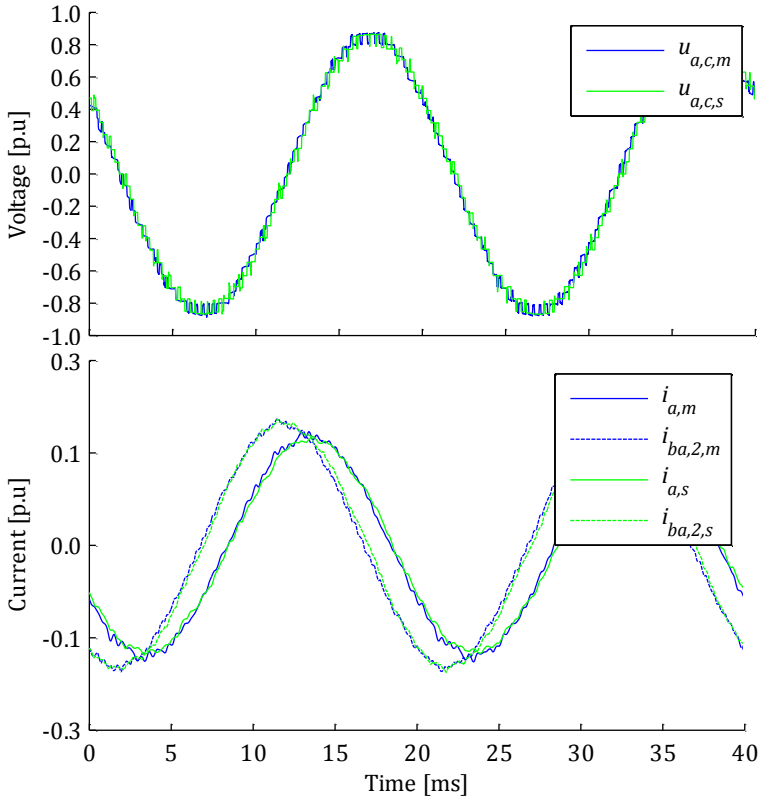

Figure 6-5 Comparison between measurement and simulation during steady-state operating mode. Subscripts "*m*" and "*s*" denote measurement and simulation, respectively.

Figure 6-6 shows the model evaluation for a different STATCOM operating point. Comparing with the STATCOM currents in Figure 6-5, it is evident that the harmonics are less pronounced at the higher operating point. This is well replicated in the simulation.

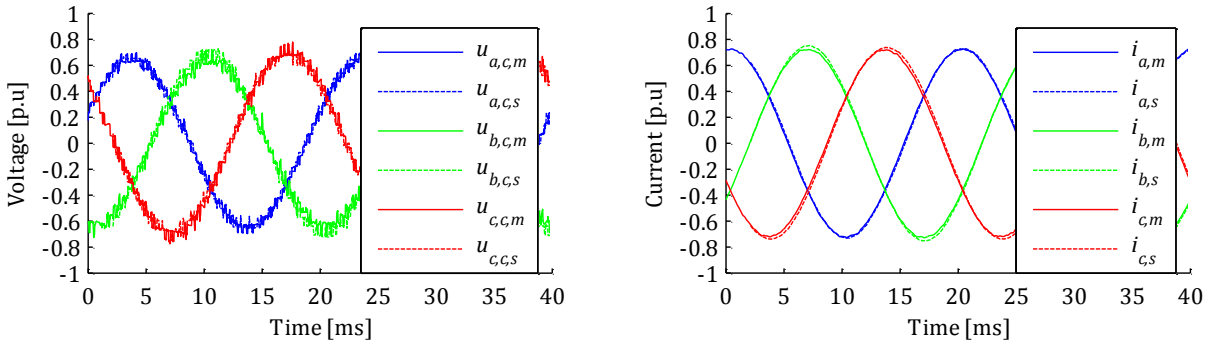

a) Measured and simulated leg voltages. b) Measured and simulated line currents.

Figure 6-6 Comparison between measurement and simulation during steady-state operating mode. Subscripts "*m*" and "*s*" denote measurement and simulation, respectively.

Figure 6-7 shows the phase A converter leg and phase A to B line voltages ($u_{a,c}$ and u_{ab}, respectively, see Figure 6-1) during a shorter time span than in Figure 6-6, in order to more clearly show the high quality of the measurements and the validity of the proposed model. The incremental step increase in the converter voltage is clearly observable in the measurement and well replicated by the simulation results ($u_{a,c,m}$ and $u_{a,c,s}$, respectively). The model is to a high extent capable of replicating the measured variation in $u_{a,c,m}$ caused by the switching action of the STATCOM.

Figure 6-8 shows a comparison between measured and simulated phase A line current during the transition in the STATCOM operating point from $Q \approx -0.73$ to approximately -0.79 p.u. A good agreement can be observed between measurements and simulations in this case.

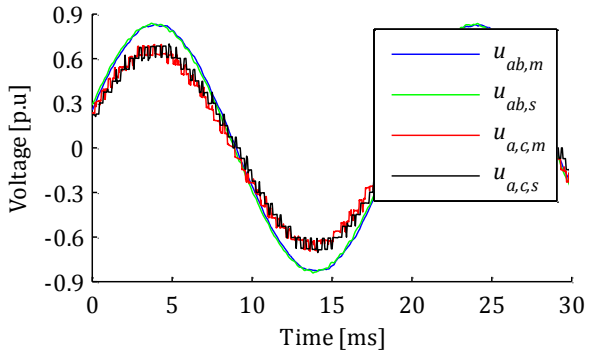

Figure 6-7 Comparison of measurement and simulation results for phase A voltages.

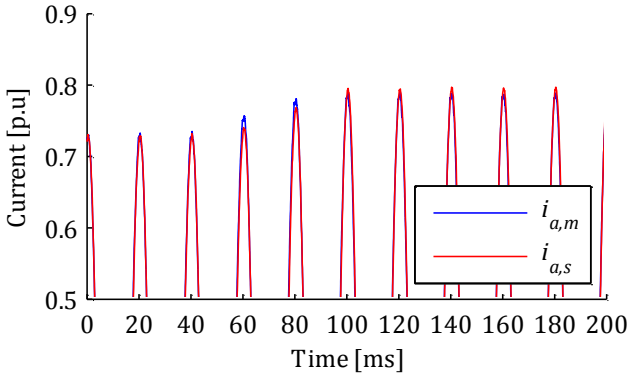

Figure 6-8 Comparison between simulated and measured phase A line current during reactive power transition.

From the evaluation it is considered that the proposed generic model is highly capable to replicate the measured waveforms, even with no information available of the control and modulation technique applied in the commercial STATCOM.

6.2 HVDC

6.2.1 Studied MMCC System and its Control

The MMCC VSC-HVDC system considered in this work is inspired by ABB's 4th generation HVDC Light [25], described in Chapter 3. Figure 6-9 shows the double star MMCC VSC-HVDC equipped with either half- or full-bridge converter in the SMs (DSHB and DSHB, respectively). The HVDC Light employs the DSHB.

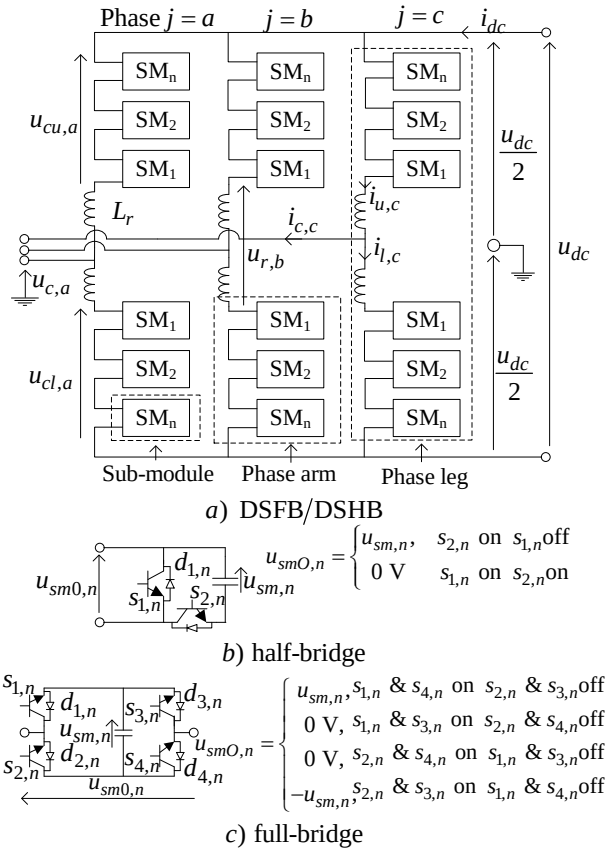

Figure 6-9 The double star MMCC VSC-HVDC, which can either be equipped with the b) half- or c) full-bridge converter in the SMs.

Only one converter terminal will be considered and the AC and DC sides are each represented by an ideal Thevenin equivalent network, as shown in Figure 6-10.

A capacitor (C_p) is inserted in the mid-point of the arm reactor in Figure 6-10, which together with the reactor forms a filter with the purpose of reducing the alternating part of the circulating current [25], which mainly consist of a 2nd harmonic component.

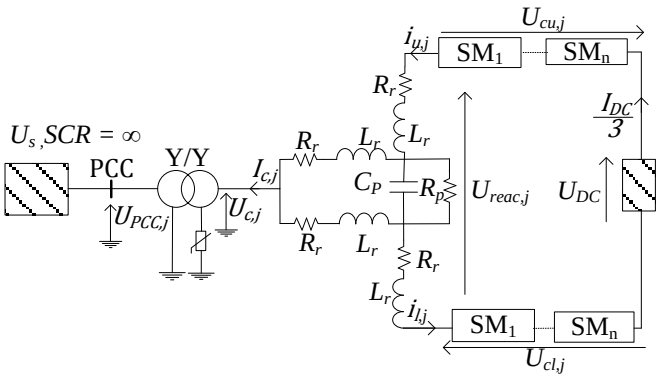

Figure 6-10 Single line diagram of the studied MMCC VSC-HVDC one terminal system.

Table 6-1 shows the electrical parameters of the studied system. The parameters will be described in the following. The reactor resistance (R_r) and filter capacitance (C_p) have been adapted and calculated according to [92], respectively. C_p is calculated as follows, where ω_0 is the fundamental frequency in rad/s:

$$C_p = \frac{1}{8\omega_0^2 L_r} \text{ [F]} \qquad 6\text{-}2$$

The energy stored in the SM capacitances (E_{tot}) is selected based on trade-off between arm voltage ripple requirement and capacitor size. The value of E_{tot} = 40 kJ/MVA is selected according to [25], giving a ripple in u_{sm} in the range of 10 %. The SM capacitance is calculated as:

$$\begin{aligned} E_{tot} \cdot S_{vsc} &= 6 \cdot N \cdot ½ \cdot C_{sm} \cdot u_{sm}^2 \rightarrow \\ C_{sm} &= \frac{E_{tot} \cdot S_{vsc}}{3 \cdot N \cdot u_{sm}^2} \\ &= \frac{N \cdot E_{tot} \cdot S_{vsc}}{3 \cdot U_{dc}^2} \text{ [F]} \end{aligned} \qquad 6\text{-}3$$

Where $U_{dc} = N \cdot u_{sm}$. Inserting the values from Table 6-1 into equation 6-3 yields C_{sm} = 1.5 mF for $N = 38$.

Table 6-1 System electrical parameters.

Parameter		Symbol	Value	Unit
AC Grid	Nominal voltage L-L	U_{PCC}	400	kV
	Short circuit ratio	SCR	∞	-
	Fundamental frequency	f_0	50	Hz
DC grid	Nominal voltage	$U_{dc}/2$	±320	kV
VSC Converter	Rated power	S_{VSC}	1216	MVA
	SM cascade number	N	38	-
	SM rated voltage	$U_{sm,r}$	16.84	kV
	Energy stored in SM capacitors per MVA	E_{tot}	40	kJ/MVA
	SM switching frequency	f_{sw}	3.37*f_0	Hz
	Total reactor inductance	L_r	75 (0.16 PU)	mH
	Reactor resistance	R_r	50	mΩ
	Reactor filter capacitance	C_p	17	μF
	Reactor filter resistance	R_p	50	MΩ
VSC Trans-former	Rated power	S_{trf}	1290	MVA
	Short circuit voltage	U_k	12	%

6.2.2 Considered Control System

The control system in this work is divided into two levels:

- *Upper level,* which regulates the power transfer between the AC and DC sides (conventional VSC control).
- *Lower level*, responsible for controlling the internal dynamics of the converter, such as ensuring voltage balancing between the SMs (MMCC control).

Upper level

Conventional cascaded control is employed in ABB's HVDC Light 4th Generation [25], with slower outer loop control responsible for determining the references for the fast inner current control (ICC) loop. The ICC operates in the RRF, where a phase-locked loop (PLL) is used for synchronization between the natural reference frame and the RRF.

Lower level

Balancing of the SM voltages is useful in the MMCC model, so as to ensure e.g. that the voltage of the n^{th} SM converges to $U_{sm,r}$. Phase shifted pulse width modulation (PWM) with a pulse number of 3.37 for each SM has been adapted from [25]. This is used as it has been shown that a non-integer value has a balancing effect on the SM capacitors [127]. Furthermore, active control is used for the balancing, which, with reference to [126], can be divided into two parts: Leg averaging and individual SM balancing.

Leg averaging, ensuring that the phase leg voltage converges to U_{dc}.

The average SM voltage of the j^{th} phase leg (j=a,b,c) is calculated as:

$$U_{AV,j} = \frac{1}{2 \cdot N} \sum_{n=1}^{2 \cdot N} U_{sm,j,n} \tag{6-4}$$

Where $U_{sm,j,n}$ is the voltage across the capacitor in the n^{th} SM in the j^{th} phase leg. The following DC loop equation exists in Figure 6-9 for the j^{th} phase leg (neglecting R_r, R_c and C_P for simplicity):

$$\begin{aligned} U_{dc} &= U_{cu,j} + U_{cl,j} + U_{reac,j} \\ &= \sum_{n=1}^{2 \cdot N} U_{sm0,j,n} + U_{reac,j} \\ &= \sum_{n=1}^{2 \cdot N} U_{sm0,j,n} + 2L_r \frac{d}{dt}\left(i_{u,j} + i_{l,j}\right) \\ &= \sum_{n=1}^{2 \cdot N} U_{sm0,j,n} + 4L_r \frac{d}{dt}\left(\frac{i_{u,j} + i_{l,j}}{2}\right) \end{aligned} \tag{6-5}$$

Where $U_{sm0,j,n}$ is the output voltage of the n^{th} SM in the j^{th} phase leg (see Figure 6-9). $i_z = (i_{u,j} + i_{l,j})/2$ is the circulating current flowing along the DC loop for the j^{th} phase. As evident from equation 6-5, i_z can be used to control $U_{AV,j}$. Figure 6-11 shows the implemented average controller, which is divided into an outer voltage and inner current loop. The voltage loop controls the $U_{AV,j}$ by determing the reference, i_z^* for the current loop compensator. For example, I_z^* increases if $U_{sm}^* > U_{AV,j}$. I_z^* is then substracted from the measured i_z in the current loop, reducing the voltage command $U_{AV,j}^*$. $U_{AV,j}^*$ is then added to $U_{cu,j}^*$ and $U_{cl,j}^*$, causing an increase in i_z, responsible for increasing $U_{AV,j}$.

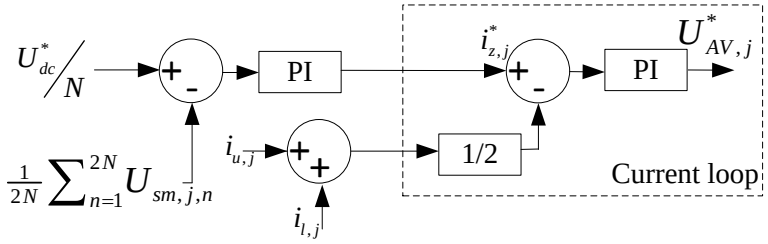

Figure 6-11 Average SM voltage controller for the j^{th} (j=a,b,c) *phase.*

Individual SM balancing, ensures that the voltage in the n^{th} SM converges to $U_{sm,r}$

The individual balancing control forms an active power component ($P_{ind,u/l,j,n}$) between the fundamental component (i.e. 50 Hz) of the output voltage ($U_{smO,u/l,j,n}$) of the nth SM in the upper or lower arm (u/l, respectively) and the corresponding frequency component in the arm current (i_u and i_l for the upper and lower phase arm, respectively). Therefore the reference for the n^{th} SM is as in equation 6-6a and b for the upper (u) and lower arm (l), respectively.

$$U_{ind,cu,j,n}^* = \begin{cases} K_{ind}\left(U_{AV,j} - U_{sm,u,j,n}\right) & (i_u > 0) \\ -K_{ind}\left(U_{AV,j} - U_{sm,u,j,n}\right) & (i_u > 0) \end{cases} \tag{6-6a}$$

$$U_{ind,cl,j,n}^* = \begin{cases} K_{ind}\left(U_{AV,j} - U_{sm,l,j,n}\right) & (i_l > 0) \\ -K_{ind}\left(U_{AV,j} - U_{sm,l,j,n}\right) & (i_l > 0) \end{cases} \tag{6-6b}$$

The polarity for the individual balancing reference ($U_{ind,cu/l,,j,n}^*$) has been aligned with the polarity of the arm current in equation 6-6a and b. As an example $P_{ind,u/l,j,n} > 0$ for $U_{AV,j} > U_{SM,j,n}$ charging the

n^{th} SM in the upper/lower arm capacitor (u/l, respectively) from the DC side of the converter regardless of the polarity of the arm current.

Figure 6-12 shows the derivation of upper a) and lower b) arm voltage commands for the n^{th} SM in the j^{th} phase. U_j^* is the output reference signal from the inner current controller. $U_{AV,j}^*$ is obtained from the average leg voltage controller and $U_{ind,cu/l,,j,n}^*$ is calculated from equation 6-6a and b for SMs in the upper and lower arms, respectively.

a) b)

Figure 6-12 Reference signals for the n^{th}SM in the j^{th} phase in the a) upper arm and b) lower arm.

Modulation Strategy

The modulation methods typically used in MMCCs include the carrier phase shifted sinusoidal pulse width modulation (CPS-SPWM) and staircase modulation methods, such as the nearest level modulation method [12,105,128,129].

The CPS-SPWM is mainly suitable for fewer SMs due to a higher computational time, making the realisation of the real-time control challenging [105]. The nearest level modulation on the other hand is found suitable for large number of SMs as the technique approximates the voltage reference to the closest possible voltage level of the phase arm [130]. The CPS-SPWM technique is adapted here as the commercial MMCC VSC-HVDC presented in [25] applies this technique, as mentioned previously. A pulse number of 3.37 for each SM has been adapted from [127], as a non-integer pulse number has a balancing effect on the SM capacitors [12, 25].

6.2.3 Dynamic Characterisation of the MMCC HVDC Model

As mentioned in Chapter 4, the evaluation of the developed DEMs of the MMCC HVDC (i.e. DEM2 and DEM4) will be evaluated against the DEM1 from [29].

Table 6-2 reports the step changes imposed on the system during the simulations for the MMCC system in Figure 6-10 for $N = 38$.

The comparison is in the following done for the DEM1 and DEM2. The DEM4 yields practically identical results as the DEM2. Figure 6-13 shows the simulated i_d and i_q together with the average SM voltages in the three phases together with the overall average SM voltage of the MMCC station calculated as:

$$U_{AV,tot} = \frac{1}{3}\sum_{j=1}^{3} U_{AV,j} \qquad 6\text{-}7$$

The DEM1 and DEM2 (and 4) are practically providing identical simulations results. Small spikes are present in the average SM voltages (up to ≈ 5 %) each time a step change is ordered but the MMCC controller is capable to quickly restore 1 p.u. A cross coupling between the i_d and i_q components is noticeable, which is not normally present for VSCs due to the decoupling strategy implemented in the RRF. This coupling can be explained by considering the SM voltage dynamics at the instant the power order change is commanded and thus not a direct consequence of improper decoupling of the i_d and i_q components.

Table 6-2 Simulated step changes at specified times.

t [ms]	i_d^* [p.u]	i_q^* [p.u]
0	0.0	0.0
200	0.5	0.0
700	0.5	0.5
1200	-0.5	0.0
1700	-0.5	-0.5

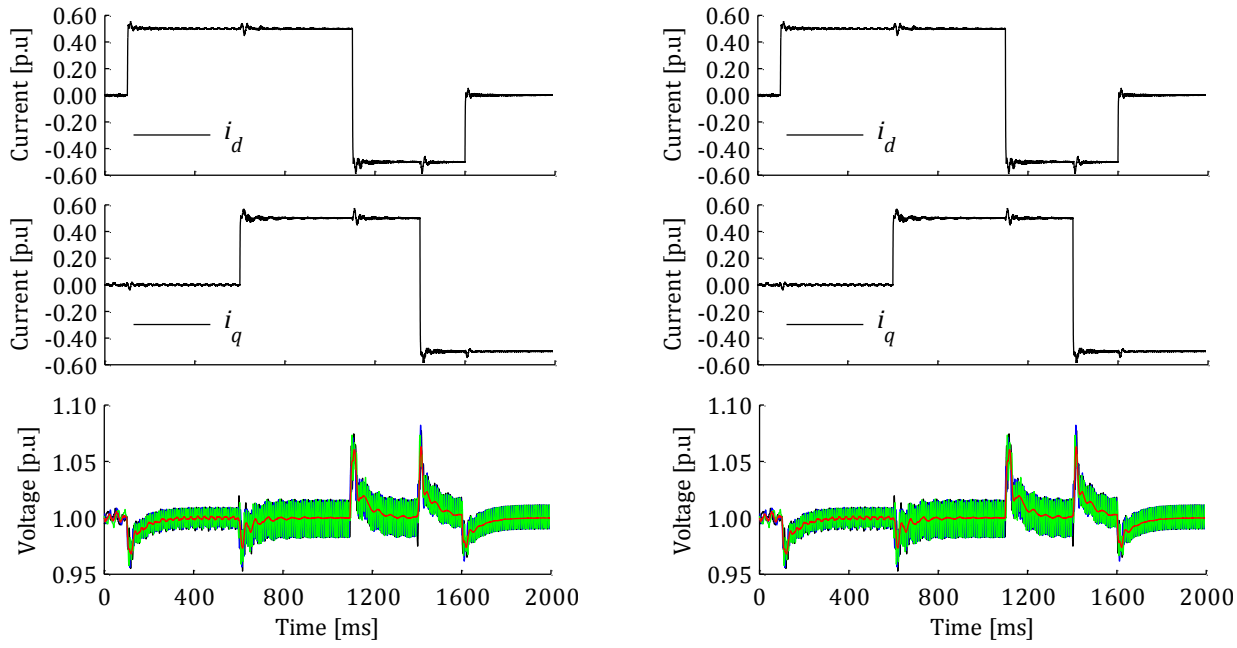

a) DEM1. b) DEM2.

Figure 6-13 Simulated i_d and i_q (top and midle graphs, respectively). Bottom graphs shows simulated average SM voltage in phase a, b and c ($U_{av,a}$ (black), $U_{av,b}$ (blue) and $U_{av,c}$ (green), respectively) and total average SM voltage ($U_{AV,tot}$ (red)).

6.2.4 Evaluation of the HVDC's Low Level Controller

Average SM Voltage Controller

In order to evaluate the efficiency of the low level controller system, the simulation from the previous section has been repeated with the average controller disabled from 1100 ≤ t ≤ 1400 ms. Figure 6-14a shows the simulated phase a top arm SM voltages with the average controller enabled and disabled in the top and bottom graph, respectively. Figure 6-14b shows the corresponding average SM voltages of the three phases and the total average SM voltage from equation 6-7. Only simulation results using the DEM2 are shown as the results are practically identical to the results using the DEM1 or the DEM4.

The efficiency of the average SM voltage controller is evident by comparison of the two cases in Figure 6-14. The transient oscillations in the case with the controller deactivated are not present in the case with the controller enabled. The individual and average SM voltages are stably controlled back to the

reference value of 1 p.u. after the transients caused by the simultaneous change in i_d and i_q at $t = 1200$ ms (refer to Table 6-2). When the controller is reactivated at $t = 1400$ ms the SM voltages are also been stably controlled back to 1 p.u in the lower graphs, indicating the efficiency and importance of the implemented MMCC controls.

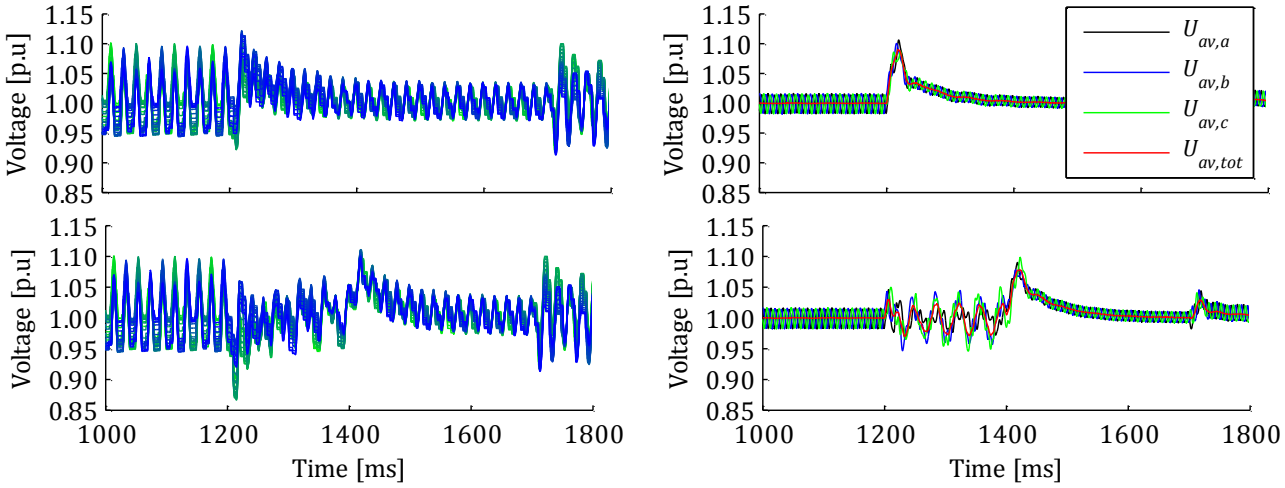

a) b)

Figure 6-14 Simulated (figure a) voltages of the 38 SMs in the top arm in phase a and (figure b) average SM voltage in the three phases. The top plots in both (a) and (b) are for normal operation, whereas bottom plots are with the average SM voltage controller disabled from $1100 \leq t \leq 1400$ ms.

Circulating Current Suppression Filter

In order to evaluate the application of the circulating current filter in Figure 6-10, two simulation cases have been executed at 1 p.u active power reference as shown in Figure 6-15. In Figure 6-15(a) the phase a line and converter arm currents for normal operating conditions are presented. The capacitive filter branch in the converter arm is switched off from $200 \leq t \leq 400$ ms in Figure (b). As can be appreciated the harmonic content in the circulating current is signficantly increased during the blocking of the capacitance branch. The 2nd harmonic distortion is practically removed when the branch is being reconnected at $t = 400$ ms. The arm currents are slightly affected by the disconnection of the filter, whereas the line current is unaffected.

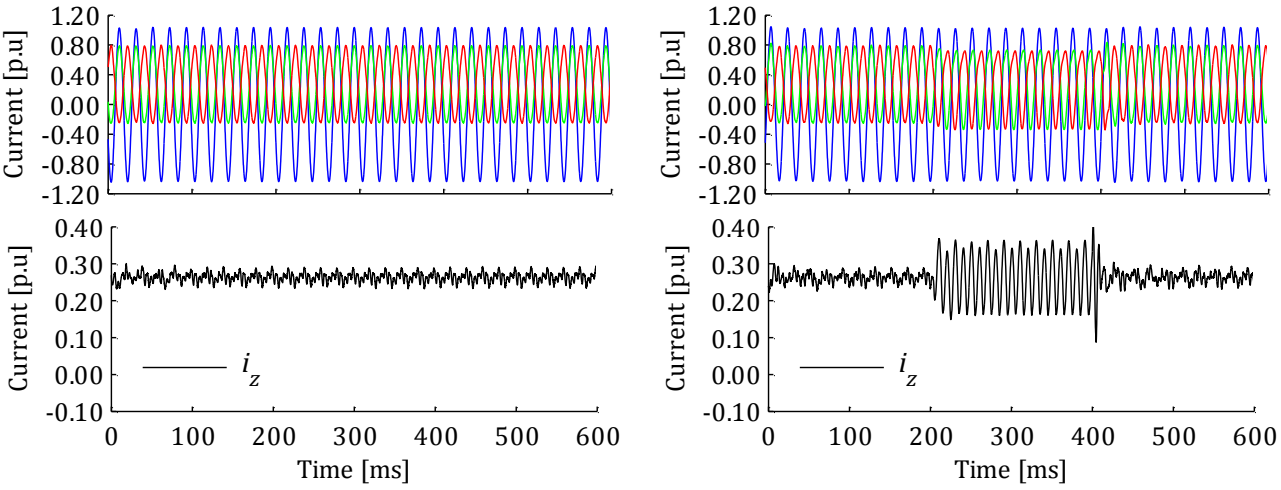

Figure 6-15 Simulated phase A line and upper and lower arm currents (blue, green and red, respectively) in top graphs and circulating current in phase A in bottom graphs: Figure (a) simulation results with normal operating conditions with 1 p.u active power reference and (b) identical operating conditions but with the 2nd harmonic passive filter capacitance branch switched off from $200 \leq t \leq 400$ ms.

6.3 Chapter Summary

The derivation of the time domain models of the MMCC STATCOM and VSC-HVDC has been described in this chapter. The low level control, ensuring the stabilisation of the distributed SM voltages in the MMCCs has been described and successfully implemented for both the STATCOM and the HVDC.

Measurement data obtained from the London Array OWPP measurement campaign has successfully been applied in the evaluation of the generic model of the STATCOM implemented in PSCAD/EMTDC. In general it can be said that the proposed generic model is highly capable to replicate the measured waveforms even with no information available of the control and modulation technique applied in the commercial STATCOM.

The evaluated STATCOM model has enabled the development of a trustworthy, full model of the MMCC HVDC, which has been implemented in PSCAD/EMTDC. Simulation studies on the HVDC has demonstrated the converter's ability to successfully control distributed SM voltages, dynamically and for steady-state operating conditions.

Chapter 7 Power Electronic Grid Simulator for Wind Turbine Generator Compliance Testing

The author has had the pleasure of being a guest researcher at the National Renewable Energy Laboratory (NREL) in Colorado, US. NREL commissioned an advanced multi-megawatt sized power electronic grid simulator test system during the author's stay-abroad. An overview of the test system is presented in this chapter. The obtained test results are used to develop and evaluate time domain models of the grid simulator (referred to as controllable grid interface, CGI) and a commercial multi-megawatt sized type 4 wind generator turbine (WTG) in Chapter 8 and Chapter 9.

7.1 Background

The trend in power generation is to partly replace conventional power plants (CPPs) with renewable energy sources. Offshore wind power has been selected to take up a significant proportion of the renewable energy supply [1, 2]. The system operation will be heavily reliant on wind power generation and the relevant grid codes have been updated to accommodate the rising wind power share to ensure system stability during and post network faults [6, 10, 131, 132]

Manufacturers, wind power plant (WPP) developers and operators need to perform a series of tests and accurate transient simulation studies to better understand the behaviour of the WTGs during grid disturbances. The latest edition of the IEC 61400-21 standard describes methods for such tests that include low voltage ride-through (LVRT), active power set-point control, ramp rate limitations and reactive power capability tests [133]. The IEC methods are being widely adopted on both national and international levels by the WTG manufactures, certification authorities, and WPP developers. WPP developers together with the transmission system operators need to map how much active and reactive power the WPP is capable to provide for frequency and voltage support, respectively, when there is an immediate need for additional energy supply. WTG manufacturers may be required to retest their WTGs after possible design or control software modifications. WTG testing in the field can be a lengthy and expensive process, especially for offshore installed WTGs, which is the predominant installation type in e.g. northern Europe [17]. Field testing often requires the manufacturer or the WPP owner to send equipment and personnel to remote locations for long periods of time.

NREL has in order to accommodate the stringent WTG testing requirements and to expedite the compliance testing, commissioned an advanced multi-megawatt sized power electronic grid simulator test system, located at the National Wind Technology Center (NWTC) in Colorado, US. The grid simulator (referred to as controllable grid interface, CGI) can support multiple types of grid compliance tests, including LVRT and high-voltage fault ride-through (HVRT), frequency response, and voltage support for WTGs and other types of renewable energy sources and storage units. NREL's new CGI test system can significantly reduce certification-testing time and costs while providing a platform for the system designers to gain in-depth understanding of the WTGs for different operating conditions, and allows the WTG designer to efficiently optimize e.g. the fault-ride-through (FRT) capability.

7.2 System Description

Figure 7-1 shows a simplified single line diagram of the grid simulator test system and Figure 7-2 shows an overview of the NWTC's test site. The system is based on the new 7 MW back-to-back CGI converter system, an existing and a new back-to-back converter based dynamometers (2.5 and 5 MW, respectively) fed from the external network and the two devices under test (DUTs), connected during the commissioning stage. The two DUTs (DUT1 and DUT2, respectively) are mechanically fed by the two dynamometers as indicated in Figure 7-1. The 13.2 kV sides of the two WTG transformers are configured as Δ-connection, so there is no neutral wire connected coming out of the DUTs. For this reason, the neutral terminal of CGI transformer is grounded.

The type 4 WTG (DUT1) is a commercial multi-megawatt sized WTG equipped with a permanent magnet generator (PMG) and the type 1 WTG (DUT2) is equipped with an induction generator (IG) and a soft starter.

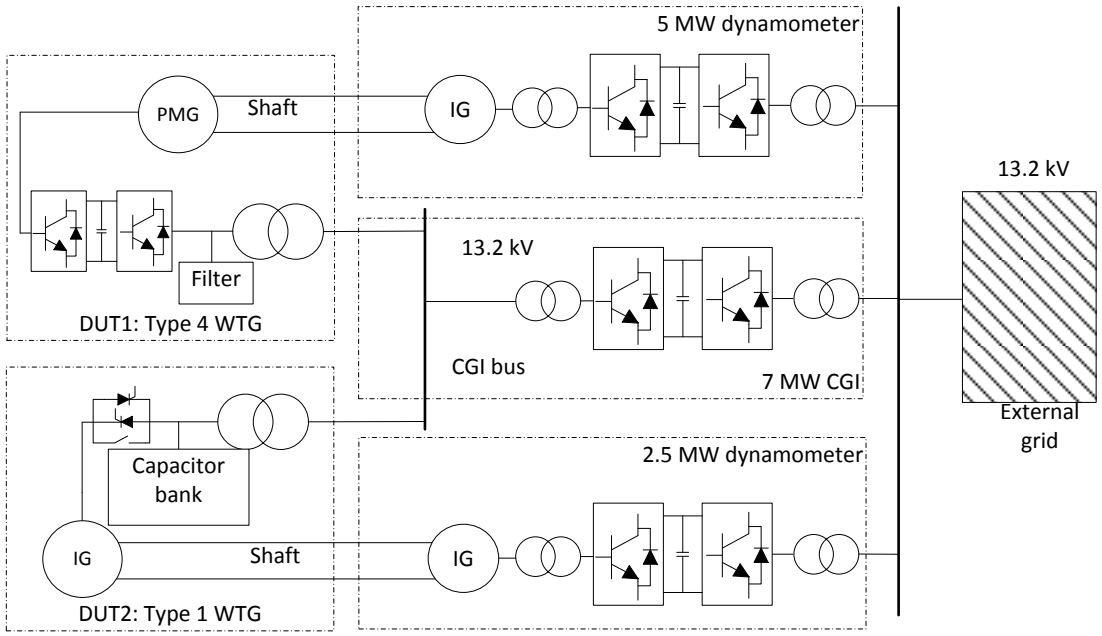

Figure 7-1 Simplified single line diagram of the grid simulator based test system with a commercial type 4 WTG and a type 1 WTG as DUTs.

The test setup in Figure 7-1 has, after the author's stay at NREL, been expanded to also include a few of the commercial field WTGs located at the NWTC test site shown in Figure 7-2.

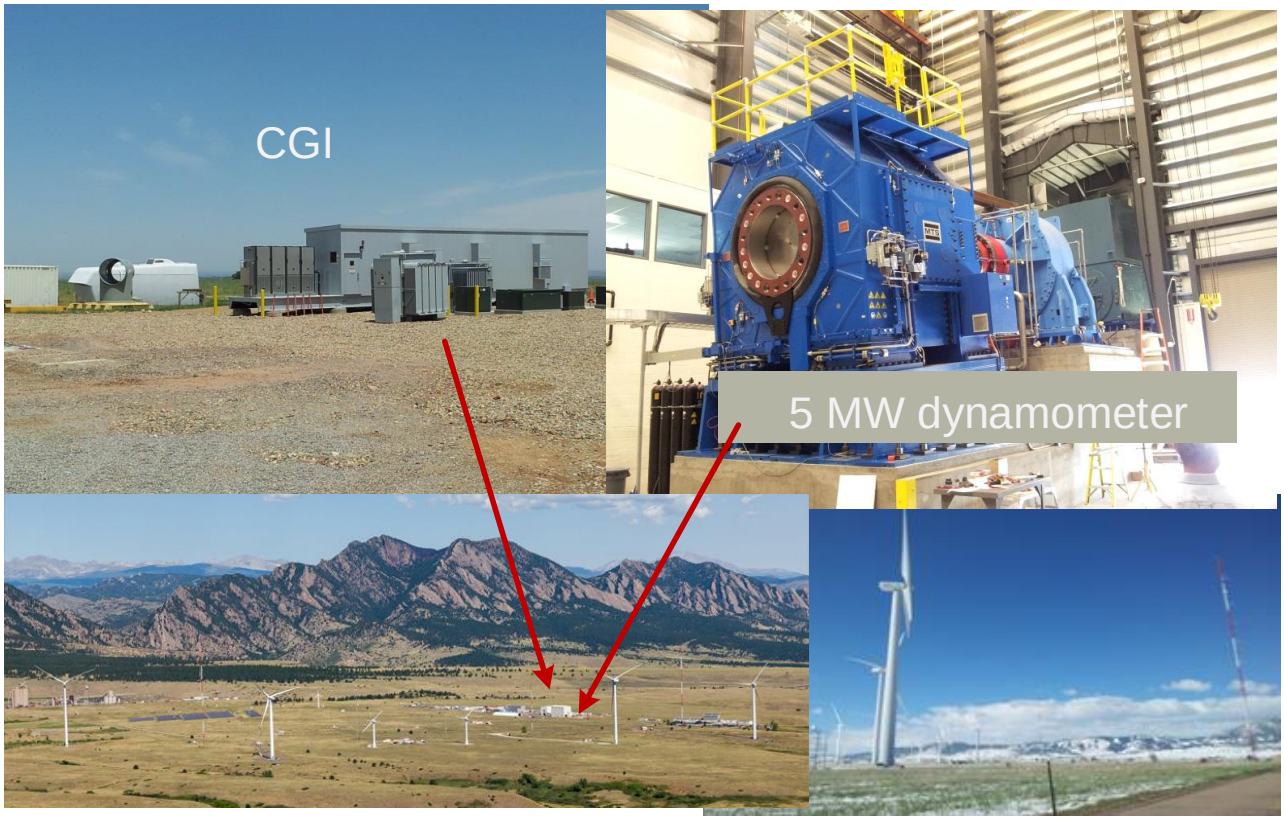

Figure 7-2 Overview of the NWTC test site. Top photos show the CGI and the 5 MW dynanometer. Commercial and test WTGs situated at the NWTC test site are shown in the two photos at the bottom of the figure.

7.3 Controllable Grid Interface

Figure 7-3 shows the simplified single line diagram of the j^{th} $(j = \mathrm{a, b, c})$ phase of the CGI. The test side of the CGI is composed of four neutral point clamped inverter (NPC) units (see Figure 7-4), connected in parallel on the DC side and one NPC unit on the grid side of the converter. A six-phase transformer is used at the test side to raise the voltage from 3.3 to 13.2 kV. With reference to Figure 7-3, the relationship between the m^{th} $(m = 1,2,3,4)$ NPC unit and the test grid side voltage is:

$$u_{CGIg} = (u_{c1} + u_{c2})n_1/n_2 = ([u_1 - u_2] + [u_3 - u_4]) \cdot n_1/n_2 \qquad 7\text{-}1$$

Where the subscript j has been omitted for simplicity.

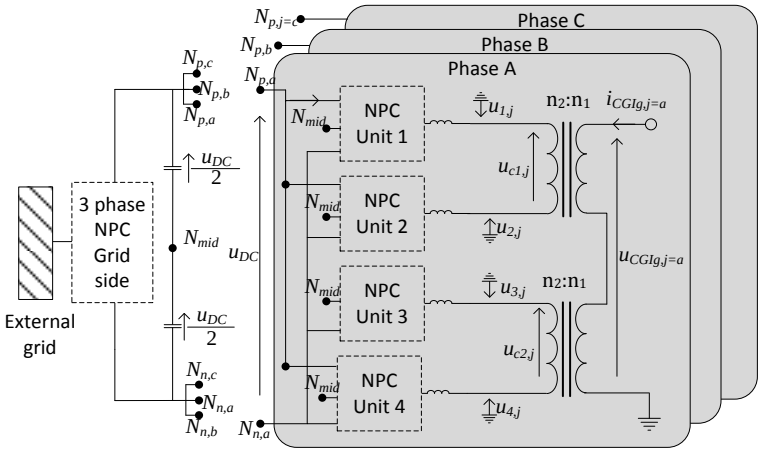

Figure 7-3 Simplified single line diagram of the CGI.

Figure 7-4 shows the single phase test side NPC unit, which structure is identical to the grid side unit, except the DC current is four times higher. The NPC is a three level converter ($\pm u_{dc}/2$ and 0 V) and by appropriate control it follows from equation 7-1 that u_{CGIg} is a nine level waveform.

Exact knowledge of the shunt filter is unknown to the author. The filter is as shown in Figure 7-4 assumed to be a second order band pass filter ($R_f L_f C_f$).

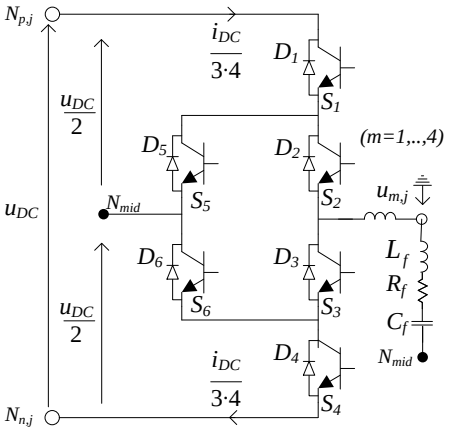

Figure 7-4 m^{th} ($m = 1,2,3,4$) NPC unit.

According to the author's knowledge the CGI shown in Figure 7-3 and in Figure 7-4 is a modified version of ABB's SVC Light (PCS 6000) [66].

Differential voltage transducers were installed at the initial no-load commissioning stage, measuring the differential NPC unit voltages u_{c1} and u_{c2} in Figure 7-3. Figure 7-5 shows the fundamental frequency phasor diagram, where a 60° phase shift between U_{c1} and U_{c2} (where the capital letters indicate RMS values) can be observed. $U'_{CGIg} = U_{c1} + U_{c2}$ (calculated from equation 7-1) is also shown in the phasor diagram, which is leading and lagging U_{c1} and U_{c2} by 30°, respectively. U'_{CGIg} has a magnitude of $|U'_{CGIg}| = \sqrt{3}|U_{c1}| = \sqrt{3}|U_{c2}|$, as can be verified by geometry.

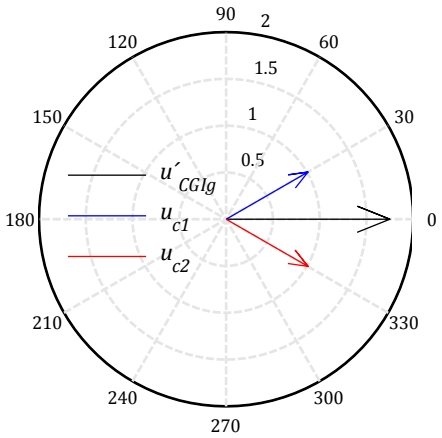

Figure 7-5 Measured phasor diagram of the fundamental frequency components of CGI phase A.

Figure 7-6 shows the corresponding time domain results, where 1 p.u is the peak value of u_{c1} and u_{c2}. It can be seen that the differential NPC unit voltages are each a five level waveform and the sum $u'_{CGIg} = u_{c1} + u_{c2}$ is a nine level waveform.

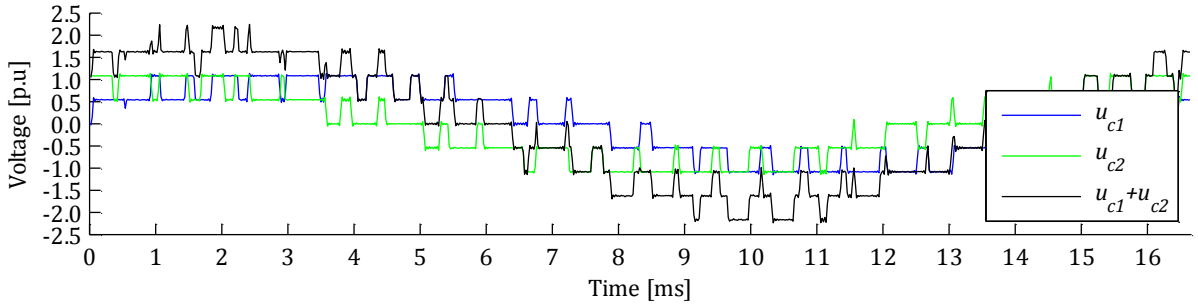

Figure 7-6 Measured no-load voltage waveforms of CGI phase A.

7.4 Measurement System

NREL has built a custom high bandwidth / high accuracy instrumentation system to monitor and analyse the CGI voltage and current waveforms, which are measured at the 13.2 kV CGI bus bar in Figure 7-1.

The CGI voltage measurements are based on CIC precision high-voltage differential probes (model DP20-10K [134]) rated for 20 kV peak-to-peak voltages with up to 100 MHz frequency bandwidth. The CGI current measurements are based on Powertek RCTi 1.3 kA flexible Rogowski probes [135]. The probes are connected to the 13.2 kV CGI bus shown in Figure 7-1.

National Instruments cDAQ-9172 chassis [136] with NI 9229 24-bit analogue input modules [137] are used to sample the three-phase voltage and current waveforms from the medium voltage (MV) instrumentation at a sample rate of 50 kS/ch/s. An NREL-developed LabVIEW interface is used to record, process, analyse and visualize the data collected from the CGI instrumentation. The active and reactive powers, power factor, electrical frequencies, RMS voltages and currents, harmonics and distortions factors are calculated by NREL's LabVIEW system from the measured voltage and current waveforms.

7.5 Test Results

Here only a brief overview of the obtained test results and the CGI's capabilities are presented. A joint paper between DONG Energy Wind Power and NREL provides additional description and analysis [138].

7.5.1 CGI No-load Voltage Waveform Characterization

Characteristics of no-load voltage waveforms are important since they determine the quality of the MV waveform produced by the CGI. Characteristics of no-load voltage waveforms are important for several reasons:

(i) High level of voltage distortion can cause test equipment malfunction, transformer overheating, and create conditions for harmonic resonances.

(ii) Excessive voltage distortions can become a problem for synchronizing a DUT with the CGI. For these reasons it was required during the design stage for CGI no-load voltage total harmonic distortion (THD) not to exceed 5 % (up until the 50th harmonic) and with no significant contribution from lower harmonics. Figure 7-7 shows the no-load harmonics of the CGI bus voltage with a THD of 2 %.

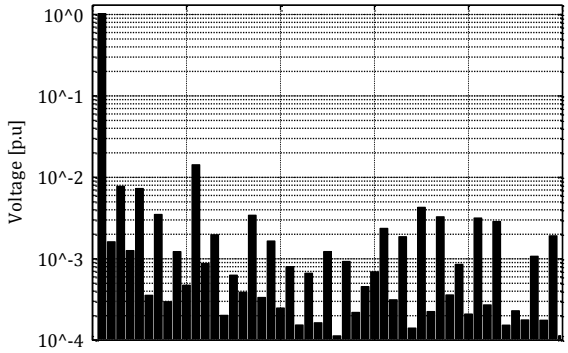

Figure 7-7 No-load harmonics in phase A voltage.

7.5.2 LVRT Testing Capability for Commercial Type 4 WTG

Series of low voltage tests have been conducted on the commercial multi-megawatt sized type 4 WTG (DUT1) as indicated in Table 7-1. The 1.0 p.u voltage drop (or zero voltage) cases are the most challenging ones for both the CGI and the WTG. The CGI terminal voltages were in the test commanded from their nominal 13.2 KV values to zero level. Two recovery cases were emulated for all fault conditions: (*i*) fast recovery case when the CGI voltages were commanded back to their nominal pre-fault value in a 100 millisecond interval; and (*ii*) slow recovery case when voltages where commanded to restore their nominal pre-fault level with slow 2 or 3 seconds ramping, as indicated in Table 7-1.

As an example, Figure 7-8 shows the test results of the two phase full voltage drop, when the WTG is operating at full load. From Figure 7-8 as well as for all symmetrical and non-symmetrical test conditions in Table 7-1, the CGI acts as a stable voltage source, despite of the dynamic WTG behaviour. The WTG introduces oscillatory dynamics in both active and reactive powers, especially for the two non-symmetrical cases (single and two-phase faults). The CGI is capable of accurate control of its terminal voltage in accordance to the specified set points, despite of large swings in the active and reactive powers [138].

Table 7-1 Type 4 WTG LVRT characterization matrix.

Test type*	Duration [ms]	WTG loading [p.u].					
		0.0	0.2	0.4	0.6	0.8	1.0
1 phase drop	100	✓	✓	✓	✓	✓	Figure 9-10 (1.0 p.u)
	3000	✓	✓	✓	✓	✓	✓
2 phase drop	100	✓	✓	✓	✓	✓	Figure 7-8 (1.0 p.u)
	3000	✓	✓	✓	✓	✓	✓
3 phase drop	100	✓	✓	✓	✓	✓	✓
	1000	✓	✓	✓	✓	✓	Figure 9-9 (1.0 p.u)

*) LVRT tests were done for voltage drops of 0.2, 0.4, 0.6, 0.8 and 1.0 p.u.

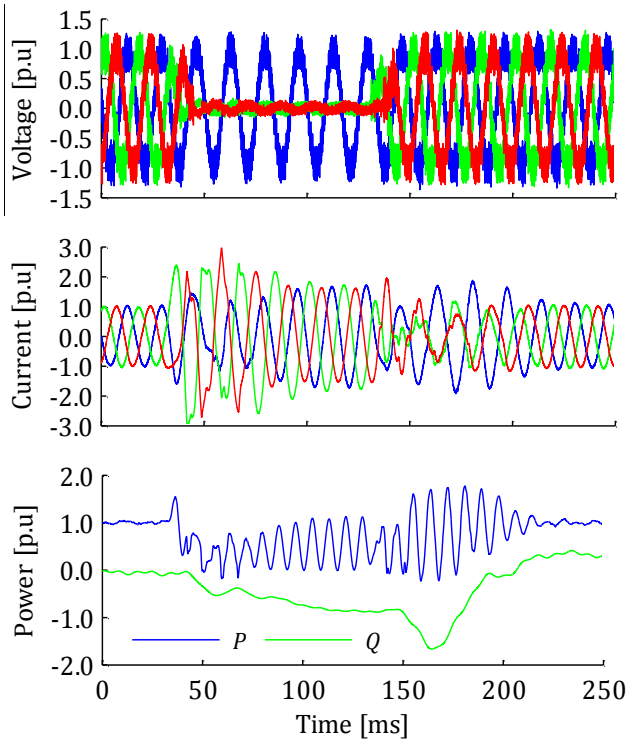

Figure 7-8 Test results of the two phase full voltage drop, when the WTG operates at full load.

7.6 Chapter Summary

This chapter has presented the system description of NREL's new CGI. The commissioning and grid compliance testing capabilities of the CGI has been outlined and is more thoroughly described in [138]. These tests have verified that the CGI can provide stable and reliable waveforms under both steady-state and transient conditions when operating with a commercial multi-megawatt type 4 WTG. Special features of the CGI, such as its capability to reproduce frequency excursions observed in actual power system and grid strength emulation are described in [138]. These are considered, useful in the compliance testing of renewable energy sources such as WTGs. The test results obtained at NREL will be used in Chapter 9 for time domain model evaluation of the CGI and the type 4 WTG.

Chapter 8 Wind Turbine Generator and Grid Simulator Modelling

The description of the National Renewable Energy Laboratory's (NREL's) grid simulator (referred to as controllable grid interface, CGI) and the commercial multi-megawatt sized type 4 wind turbine generator (WTG) was given in Chapter 7. This chapter focusses on the time domain modelling of the CGI and the WTG. The models of the power electronic devices (PEDs) are implemented in PSCAD/EMTDC. The obtained test results are used to evaluate the time domain models of NREL's test setup including the PEDs in Chapter 9.

8.1 WTG Modelling

The generic model of the type 4 WTG shown in Figure 8-1 [139] and its associated control system is divided into a grid and a generator side, described in the following subsections.

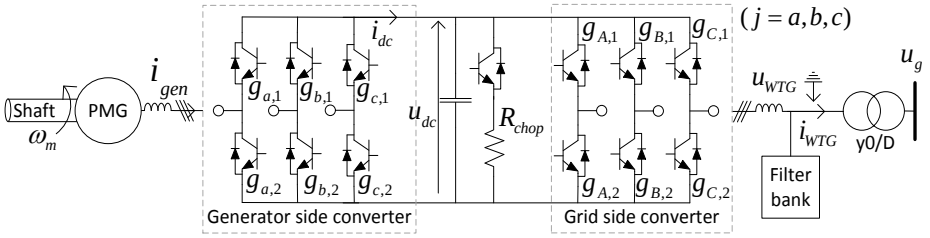

Figure 8-1 Simplified diagram of the type 4 WTG.

8.1.1 Generator Side Control

Due to the back-to-back converter structure of the type 4 WTG shown in Figure 8-1, the generator side is decoupled from the grid. The commercial WTG considered here is equipped with a chopper controlled resistor, which is used to dissipate the excess power. Type 4 WTGs with choppers on the DC link can, according to the IEC 61400-27 standard, be modelled neglecting the aerodynamic and mechanical parts [140]. A detailed model of the generator side is used in the evaluation of the generic model of the commercial WTG installed at NREL, whereas a simplified model representation of the generator is used in the harmonic stability analysis in Part III.

Detailed Generator Model and Control

A substantial effort on the modelling of the components that comprise the generator side of the WTG can be found in the literature e.g. [141, 142, 143].

A hysteresis current PWM controller with a fixed hysteresis band is used, since it is widely used and has a simple implementation, is independent of load parameter changes, and has a very good dynamic performance [144]. The disadvantage of the fixed-band hysteresis controller is the irregular switching frequency and the relatively large current ripple. More advanced hysteresis controllers have been devised, but at the expense of more complex implementations [145].

The PMG is modelled using the PSCAD/EMTDC built-in model of the permanent magnet machine [114] and is operated in constant speed mode. In the fixed-band hysteresis controller methodology, a comparator and a hysteresis band is included in each phase as shown in Figure 8-2. The switching signals ($S_{j,gen}, j = a,b,c$) are generated by the error between the measured generator output current and the reference current, which is calculated using two PI controllers, responsible for the control of the active and reactive power, respectively. The transfer function of the PI controller is given as:

$$G_{PI}(s) = k_p + k_i/s \qquad 8\text{-}1$$

Where k_p and k_i are the proportional and integral gains, respectively.

The output of the controllers are transformed from DC signals into the natural reference frame using the rotor position (θ_r) as shown in Figure 8-2.

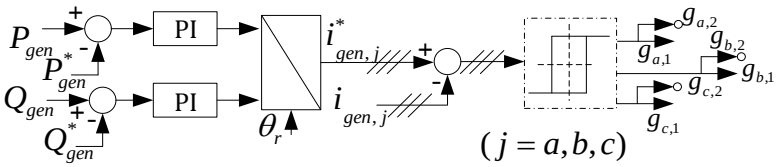

Figure 8-2 Hysteresis current controller for the PMG side converter.

Simplified Generator Model and Control

As previously mentioned, it is possible to neglect the dynamics of the generator and the generator side converter in the time domain modelling. The generator and the generator side converter are collectively represented by a first-order DC Norton equivalent, shown in Figure 8-3. The time constant is 100 ms, adapted from [12,18,19].

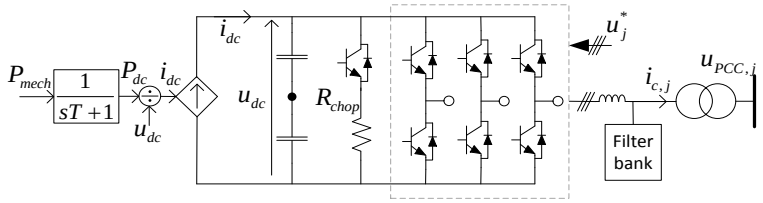

Figure 8-3 Simplified WTG model.

8.1.2 Grid Side Control

The grid side controller (GSC) is set to regulate the DC link voltage in order to maintain power balance and to regulate the reactive power at the high voltage side of the WTG transformer in Figure 8-3 using cascaded controllers. The control of the GSC can be realised in a variety of reference frames (e.g. natural, stationary and synchronous) [125]. The current control is in this work realised in the SRF.

Figure 8-4a shows grid side converter of the PED and the grid-interfacing reactor. The relation between the converter output voltage and current (u_c and i_c, respectively) and the measured voltage (u_g) is:

$$s \cdot L \cdot i_c = u_c - u_g \tag{8-2}$$

Where L is the inductance of the interfacing reactor.

Equation 8-2 can be transformed into the RRF using the transformation matrix derived in [146] and shown in equation 8-3.

$$H^{dq2\alpha\beta}(s) = \frac{1}{2}\begin{bmatrix} H^{\alpha\beta}(s+j\omega_0) + H^{\alpha\beta}(s-j\omega_0) & j \cdot H^{\alpha\beta}(s+j\omega_0) + j \cdot H^{\alpha\beta}(s-j\omega_0) \\ -j \cdot H^{\alpha\beta}(s+j\omega_0) - j \cdot H^{\alpha\beta}(s-j\omega_0) & H^{\alpha\beta}(s+j\omega_0) + H^{\alpha\beta}(s-j\omega_0) \end{bmatrix} \tag{8-3}$$

Equation 8-2 expressed in the RRF is then as in equation 8-4.

$$\begin{gathered} s \cdot L \cdot i_c = u_c - u_g \Rightarrow \\ \begin{bmatrix} Ls & -L\omega_0 \\ L\omega_0 & Ls \end{bmatrix}\begin{bmatrix} i_d \\ i_q \end{bmatrix} = \begin{bmatrix} u_{c_q} - u_{g_d} \\ u_{c_q} - u_{gc_q} \end{bmatrix} \Rightarrow \\ s \cdot L \cdot \begin{bmatrix} i_d \\ i_q \end{bmatrix} = \begin{bmatrix} u_{c_q} - u_{g_d} \\ u_{c_q} - u_{gc_q} \end{bmatrix} - \begin{bmatrix} 0 & -L\omega_0 \\ L\omega_0 & 0 \end{bmatrix} \cdot \begin{bmatrix} i_d \\ i_q \end{bmatrix} \end{gathered} \tag{8-4}$$

A cross coupling between the d and q axes is present in equation 8-4, which is cancelled by the cross-decoupling in the control system arrangement in Figure 8-4b. Furthermore, the grid voltage in the RRF

($u_{g_{dq}}$) is fed-forward in order to improve the controller performance during grid voltage fluctuations. Hence, any voltage deviation will be reflected in the control reference almost instantaneous [58,125].

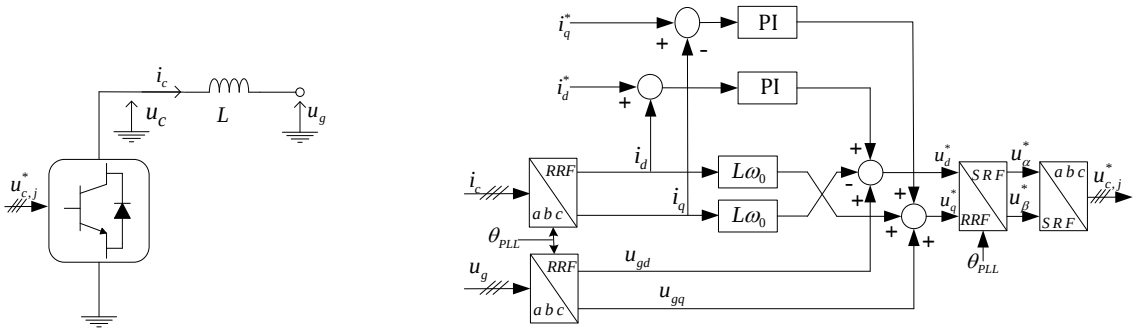

a) b)

Figure 8-4 a) The PED and its grid interfacing reactor and b) current controller in the RRF.

8.1.3 Active Harmonic Controllers in the PED

Additional harmonic controllers can be implemented in the RRF using resonant controllers or in nested rotating frames [58]. The resonant controllers are only affecting the response in a narrow frequency band around the frequency at which they compensate. The resonant controllers would ideally not be influencing the converter's dynamics and stability. However, complications may arise since the resonant controller affects both magnitude (increases) and phase (adds additional lag) of the current loop in a narrow frequency band around the tuned frequency harmonic controller [8]. The considered electrical system in [8] was composed of an inductive grid. In OWPPs, multiple resonances may exist in the low frequency range due to the extensive cabling. Hence, the use of resonant harmonic controllers may be even more challenging in large OWPPs. It is therefore decided not to include such controllers in the current work. This is recommended as future work

8.1.4 Dual Current Controller for Handling of Unbalanced Faults

Voltage imbalance during e.g. an unbalanced fault deteriorates the performance of the PED by causing a $2\omega_0$ ripple in the DC voltage and increase in the reactive power. In order to supress the unbalance, two current controllers in two RRFs are commonly used: A positive and negative sequence RRF, rotating in the counter-clockwise and clockwise directions, respectively [147, 148]. The positive sequence component of the current appears as DC in the positive RRF, whereas it appears as a $2\omega_0$ frequency component in the negative sequence. Similarly, the negative sequence component appears as DC in the negative sequence and as a $2\omega_0$ frequency component in the positive sequence. Different filter types described in [149] can be used to eliminate the $2\omega_0$ frequency component in the current controller. Based on a litterature review, the notch filter (or band rejection filter (BRF)) seems to be a widely used filter in the dual current controller [7, 147] and will therefore be considered in this work. A typical notch filter can be represented as [58]:

$$G_{BRF}(s) = \frac{s^2 + \frac{\omega_n}{Q_n}s + \omega_n^2}{s^2 + \frac{\omega_n}{Q_d}s + \omega_n^2} \qquad 8\text{-}5$$

Where ω_n is the tuned angular frequency of the notch filter.

The dual current controller with notch filters is shown in Figure 8-5, where the reference signals in the negative sequence RRF have been set to zero.

The notch filter affects the direct control chain, reducing the phase margin of the system stability, if the damping coefficient of the filter is too high, as shown in [58]. Lower values of the damping coefficient

would cause lower settling time, but at the expense of a more selective filter, which would impede the performance of the filter in case of grid frequency deviations.

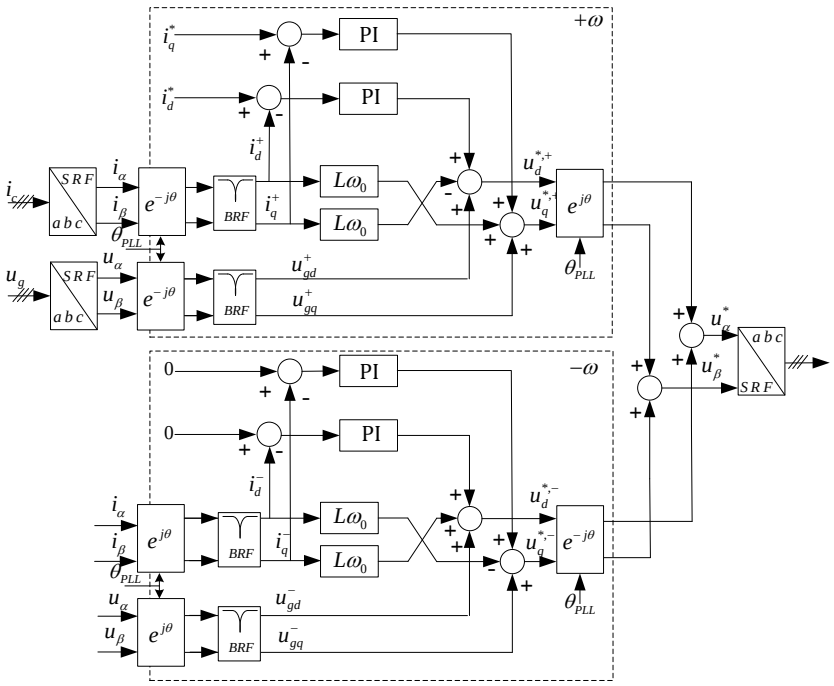

Figure 8-5 Dual current controller with notch filters installed in the main control.

8.1.5 Fault-Ride Through Strategy

The WTG model is evaluated against test data from NREL for both normal and abnormal operating conditions. Therefore, a fault-ride through (FRT) strategy is considered and implemented.

The WTGs are not required to provide voltage support in the U.S (where the measurement are realised) [150]. However, this feature is included in the model as the actual WTG injects reactive power when it enters the FRT mode, as obvious from the measurements shown in Chapter 9. Once the WTG detects an FRT event (i.e. when the RMS voltage at the high voltage side of the WTG transformer goes below 0.9 p.u). In this case, the voltage support is given priority over active power production in the FRT mode. This allows the WTG to provide voltage support during the fault by injecting reactive current as a function of retained voltage without exceeding the current rating of the GSC.

In Europe, the general requirement is to provide a minimum of 2 % positive sequence reactive current for every percent the voltage drops below 100 % once the FRT mode is initiated [150].

The following relationship between the RMS voltage and the injected reactive current is in Chapter 9 found to produce similar dynamic events in the measured and simulated results:

$$i_{q,FRT}^{*+}(U_{RMS}) = k_Q \cdot (1 - U_{RMS}) \qquad 8\text{-}6$$

Where the gain k_Q is set equal to 2. A limit of $|i_q^{*+}|$ = 1.3 p.u is imposed due to the physical contraints of the WTG and as this has been observed in the measurement to be the maximum injected reactive power.

An approximation of the relationship between the RMS voltage during the fault and the injected active power is additionally obtained from the measurement data as:

$$i_{d_{FRT}}^{*+}(U_{RMS}) = \begin{cases} k_P \cdot U_{RMS} + b, & 0.4 < U_{RMS} \leq 0.9 \\ 0 & 0.4 \leq U_{RMS} \end{cases} \qquad 8\text{-}7$$

Where K_P =1.5 and $b = -0.4$. This implies that zero active power is injected by the WTG for grid voltages below 0.4 p.u. It should be noted that the above control of the positive sequence FRF

reference values in equation 8-6 and 8-7 are developed based on observation of the measurement data in Chapter 9, as there is no information of the actual FRT.

The expression of the active power comprises an average power and oscillatory cosine and sine terms under unbalanced operating conditions when both the positive and negative sequence voltage and current components are present [147,151-153].
These power oscillations can be supressed if the coefficients of both of the oscillatory terms and are equated to 0, as demonstrated in [18]. The negative sequence current reference values are in this case calculated as:

$$\begin{bmatrix} i_d^{-*} \\ i_q^{-*} \end{bmatrix} = \begin{bmatrix} u_d^+ & u_q^+ \\ -u_q^+ & u_d^+ \end{bmatrix}^{-1} \cdot \begin{bmatrix} u_d^- & u_q^- \\ u_q^- & u_d^- \end{bmatrix} \quad 8\text{-}8$$

Thus, the active and reactive power references are not required in this formulation.

The formulation in equation 8-8 has been included in the preliminary FRT model. The inclusion did not provide additional correlation between measurement and simulation results. Hence; it was decided to set the reference values of the negative sequence controllers equal to zero as in Figure 8-5 (i.e. $i_d^{-*} = i_q^{-*} = 0$ p.u). This is furthermore considered realistic as the IEC 61400-27 only specify evaluation of the positive sequence components [140].

Based on the evaluation of the measurement data it is found in Chapter 9 that the negative sequence is controlled once the WTG enters the FRT mode. Therefore, the control structure in Figure 8-4b is used in steady-state (i.e. when $U_{RMS} > 0.9$). The dual controller in Figure 8-5 is then applied once the relationship $U_{RMS} > 0.9$ is fulfilled.

8.2 Controllable Grid Interface

A description of the CGI was given in Chapter 7. The CGI's test side converter (TSC) shown in Figure 8-6 sets up the test grid voltage at the 13.2 kV side of the six phase transformer. No information has been available to the author regarding the control and modulation principle of the CGI. Obtained measurement data will therefore be used to gain the information needed for appropriate modelling of the TSC. It should be noted that two models of the CGI has been developed within this project.

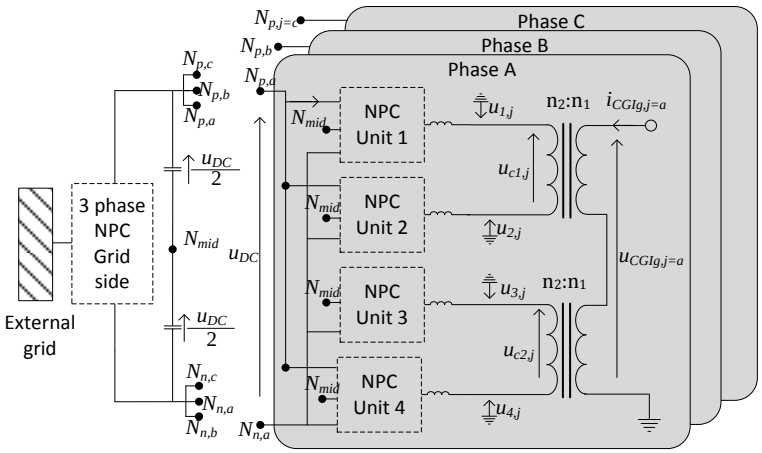

Figure 8-6 Simplified single line diagram of the CGI. The figure is identical to Figure 7-3 on page 84.

With reference to Figure 8-7a, it was observed in Chapter 7 (Figure 7-5 and Figure 7-6 on page 85) that U_{c1} is lacking U_{c2} by 60° and the phase of the output voltage of the transformer, U_{CGIg}, is located between U_{c1} and U_{c2}.

Similar as for the WTG, the control of the CGI is realised in the RRF using the dual control scheme described in section 8.1.4. Two augmented inverse Clark transformations are used to transform the reference signals into the natural reference frame given in equation 8-9. The transformation matrix is

phase shifted by +30° for NPC unit 1 and 2 and -30° for unit 3 and 4 in accordance with the phasor diagram of the measured converter terminal voltages in Figure 8-7a. Figure 8-8 provides a visual description of the transformation into the natural reference frame. An FRT block is also added, as will be described momentary.

$$T_{Clarke}^{-1}\left(\pm\frac{1}{6}\pi\right)=\begin{bmatrix} cos\left(\pm\frac{1}{6}\pi\right) & sin\left(\pm\frac{1}{6}\pi\right) \\ cos\left(\pm\frac{1}{6}\pi-\frac{2}{3}\pi\right) & sin\left(\pm\frac{1}{6}\pi-\frac{2}{3}\pi\right) \\ cos\left(\pm\frac{1}{6}\pi-\frac{2}{3}\pi\right) & sin\left(\pm\frac{1}{6}\pi-\frac{2}{3}\pi\right) \end{bmatrix} \quad 8\text{-}9$$

Finally, a 180° phase shift is added to the reference signals of NPC units 2 and 4 as the grid side voltage given in equation 7-1 (page 83) is the sum of the differential voltages across the two single-phase transformers in the j^{th} phase. Alternative phase opposition disposition (APOD) is used, where the carriers in the adjacent bands are phase shifted by 180°, a commonly applied PWM technique for NPC converters [57]. Figure 8-7b shows the applied PWM strategy, which has been developed within this project. The carrier frequency is selected as $f_{sw,cgi}$= 850 Hz based on evaluation of the measured harmonic spectra of the CGI, as described Chapter 9.

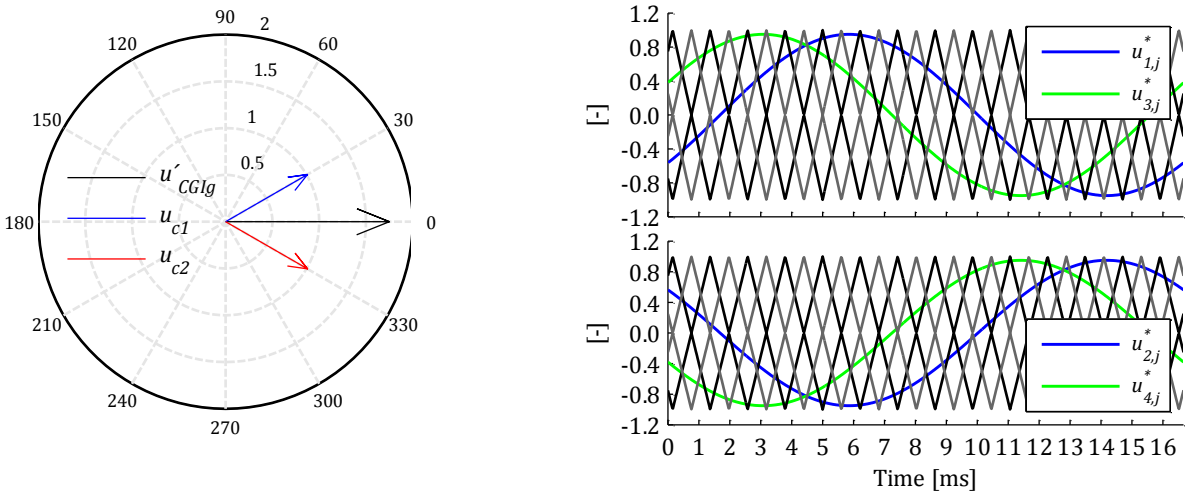

a) Phasor diagram of the CGI's no-load voltages. Figure is identical to Figure 7-5.

b) Applied modulation strategy.

Figure 8-7 Measured no-load voltage and model applied PWM strategy developed in this project.

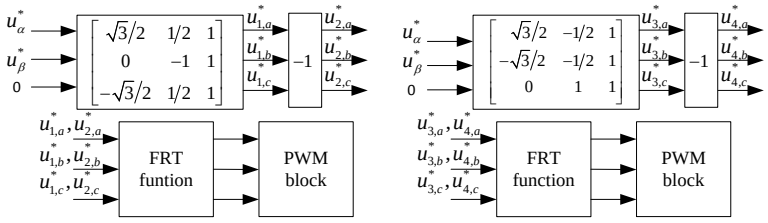

Figure 8-8 Transformation from the stationary to the natural reference frame.

8.2.1 Fault Emulation

CGI sets up the 13.2 kV test grid voltage. The CGI is capable of emulating balanced and unbalanced faults or high voltage conditions. As an example, Figure 8-9 shows the measured test grid voltage (un-filtered and filtered, top and bottom graph) in case of a single-phase full voltage drop. As can be seen from especially the bottom graph, the voltage in the "faulty" phase is not immediately set to zero. Therefore, an FRT block is included in the CGI model as shown in Figure 8-8. This is used in order for the CGI model to emulate both balanced and unbalanced faults and high voltage conditions. Figure 8-10 shows the details of the single-phase FRT block. The FRT block in Figure 8-10 is the multiplication of the reference signals for the j^{th} phase ($u^*_{1,j}, u^*_{2,j}$) with the fault emulator (FRT_2). The fault emulator consists of a 1st order delay with a time constant of 5 ms which is added to a unity constant. The value of D is less than 0 for low voltage faults and higher than 0 for high voltage conditions.

Figure 8-11 shows the simulated phase A voltage together with FRT_2 for both a single phase full voltage drop ($D = -1$, top graph) and in case of a 1.2 p.u overvoltage ($D = 0.2$, bottom graph). Comparing top graph in Figure 8-11 with the bottom graph in Figure 8-9, similar dynamic responses can be observed in the simulation and measurement.

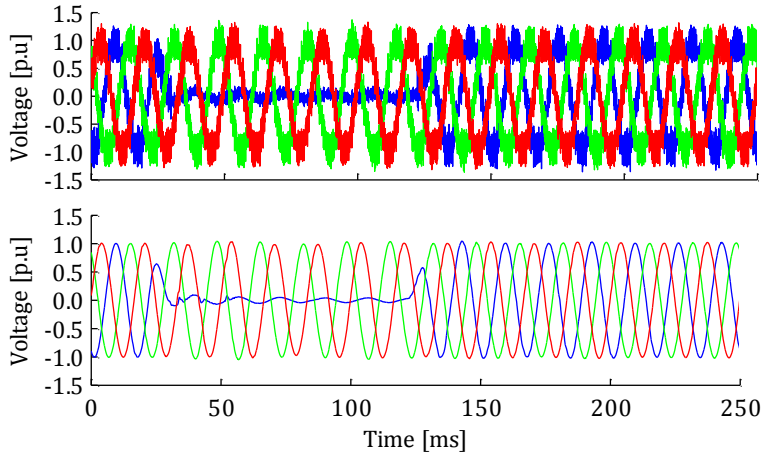

Figure 8-9 Measured 13.2 kV test grid voltage. A fifth order low-pass filter tuned at 1 kHz is used in the bottom graph.

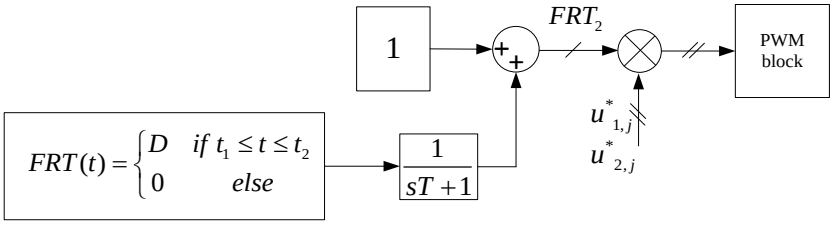

Figure 8-10 FRT block in the CGI model, used to emulate low and high voltage faults. $D < 0$ in case of a fault emulation and $D > 0$ in case of an overvoltage test condition.

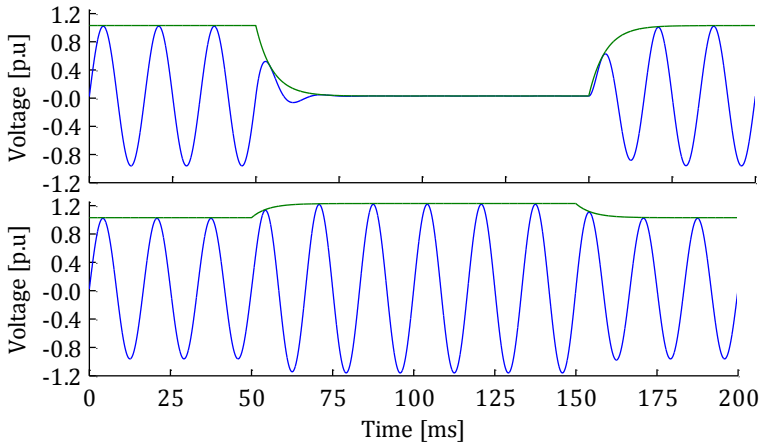

Figure 8-11 Simulated single phase faults, where D = -1 and D = 0.2 in the top and bottom graph, respectively. t_1 = 50 ms and t_2 = 150 ms. Green curve is the FRT_2 signal.

8.3 Chapter Summary

The CGI and the commercial type 4 WTG installed at NREL have been modelled in PSCAD/EMTDC in this chapter. The models will be evaluated in Chapter 9 based on comparison with measurement.

Chapter 9 Evaluation of the Time Domain Models of the Wind Turbine Generator and the Power Electronic Grid Simulator

The system description of the controllable grid interface (CGI) and the commercial multi-megawatt sized type 4 wind turbine generator (WTG) installed at the National Renewable Energy Laboratory (NREL) was presented in Chapter 7. Detailed, generic electromagnetic transient (EMT) models of the CGI and the WTG were developed in Chapter 8. The purpose of this chapter is the evaluation of said models. The models are implemented in PSCAD/EMTDC and evaluated for steady-state operating conditions and for various transients (including balanced and unbalanced low and high voltage ride-through (LVRT and HVRT, respectively)).

9.1 Background

As stated in Chapter 7, the WTG manufacturers, wind power plant (WPP) developers and operators need to perform a series of tests and accurate transient simulation studies to better understand the behaviour of the WTGs during grid disturbances. The IEC 61400-21 standard describes methods for such tests that include LVRT, active power set-point control, ramp rate limitations and reactive power capability tests [133].

Simulation results using detailed WTG models are therefore an important method to analysis the WTG grid integration behaviour. The model must be able to accurately replicate real life WTG behaviour and therefore validation of the applied model needs to be undertaken [154, 155, 156].

Once the accuracy of the model is known, the grid compliance evaluation of the whole WPP can be done based on simulation results. Models developed by the WTG suppliers generally reproduce the behaviour of their products quite accurately. However, the models are often using proprietary data, making it difficult to distribute. Additionally, erroneous results (e.g. numerical instability) have been observed in a manufacturer supplied WTG model [157]. The WTG supplier provided models are typically provided to the transmission system operator (TSO) or the WPP developer in an encrypted format, which limits the transparency. Moreover, the WTG manufacturers often implement the models in their own developed software, which the end-user may have little experience with.
The Irish TSO EirGrid has in a publication from 2007 described that none out of 20 received WTG models from manufacturers have been evaluated [157, 158].
The IEC 61400-27 standard [140] defines a standard for public available WTG and WPP models, which are intended for dynamic analysis such as switching and LVRT capabilities. An evaluation of the fundamental frequency, positive-sequence response of the model against measurements for both balanced and unbalanced voltage drops is required in order for the model to be compliant with the standard. The current version of IEC 61400-27 does not require the evaluation of the negative sequence response. The generic models must according to the standard be validated against tests specified in the IEC 61400-21 [140].
A significant effort of generic modelling of both type 3 and type 4 WTGs (double fed induction generator and full-scale converter (FSC) equipped, respectively), has recently been made e.g. [159] for type 3 and [12, 18, 160] for the type 4 WTG. Whereas [159] validated the generic model against field measurements from an offshore located commercial type 3 WTG, there exist (to the author's knowledge) no validated generic models of the type 4 WTG.

9.2 Overview

Table 9-1 shows the study cases considered in the evaluation of the developed time domain WTG and CGI models. The developed models are intended for the harmonic stability evaluation and hence the abnormal operating cases (LVRT and HVRT) could essentially have been omitted. However, these cases are included for a few reasons (see also the approach and methodology section in Chapter 2):

It was observed in the evaluation that only positive sequence components are controlled by the WTG during normal operating mode. The control of the negative sequence components was activated once the WTG went into the LVRT mode (see section 9.6). The dynamics prior to the FRT activation are therefore assumed to be caused by the WTG's normal operating control system. Therefore, it is considered that the unbalanced operating conditions are useful not only for FRT validation but also for the evaluation of the steady-state control system.

Table 9-1 Overview of model evaluation study cases.

Section	Test type	Description
9.4	No Load CGI Validation	Evaluation of the generic modulator model of the CGI.
9.5	Normal Operating Mode	WTG active power step changes
9.6	Low Voltage Ride-Through	1.0 p.u three phase fault of 100 ms and 1000 ms duration 1.0 p.u single phase fault of 100 ms duration
9.7	High Voltage Ride-Through Evaluation	1.3 p.u two phase voltage rise of 100 ms duration

Additionally, the modelling, simulation and measurement analysis of the unbalanced operating conditions has provided the author to better understand and develop appropriate models of the power electronic devices (PEDs) used in the offshore WPP (OWPP) for the harmonic stability assessment.

A Cooperative Research and Development Agreement (CRADA) was signed between NREL and DEWP in order for the author to be employed as a guest researcher at NREL. Deliverables from the CRADA include both modelling and evaluation of the PED models. Thus, the modelling and validation of the abnormal operating conditions was a prerequisite for the establishment of the CRADA.

As described in section 9.1, there is a lack of validated generic models of the PEDs; hence it is valuable for the project to deliver such validated models.

9.3 WTG Representation

The representation of the WTG is described in Chapter 8, where also the FRT strategy was described.

Based on the evaluation of the measurement data it is found in the following, that negative sequence is controlled once the WTG enters the FRT mode. Therefore, the control structure in Figure 9-1a is used in steady-state (i.e. when $U_{RMS} > 0.9$). The dual controller Figure 9-1b is then activated when the WTG enters the FRT mode.

As discussed based on comparison with simulation results in this chapter, the exclusion of the negative sequence control for unbalanced transients when $U_{RMS} > 0.9$ impede the performance of the WTG.

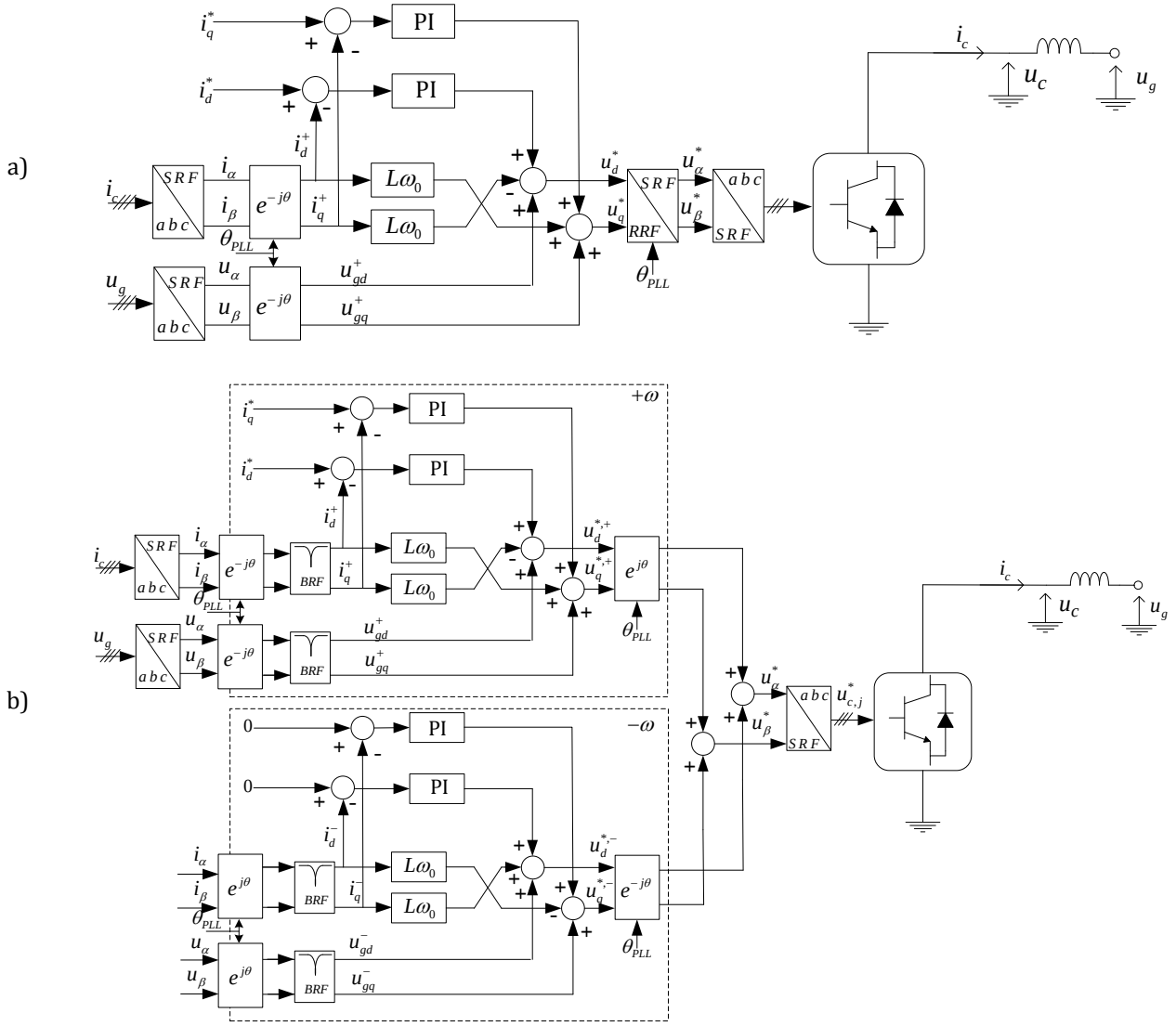

Figure 9-1 Considered WTG's inner current control system for: a) normal operating conditions and b) during FRT conditions when $U_{g,RMS} < 0.9$ p.u.

9.4 No Load CGI Validation

Alternative phase opposition disposition (APOD) is used in the model, where the carriers in the adjacent bands are phase shifted by 180°. The carrier frequency is selected as $f_{sw,cgi}$= 850 Hz based on evaluation of the measured harmonic spectra of the CGI (see Figure 9-3).

Figure 9-2 shows the comparison of no-load measurements at the CGI converter terminals with PSCAD/EMTDC simulation results for the CGI's phase A voltages. Subscripts "*m*" and "*s*" denote measurement (blue waveforms) and simulation (green), respectively.

The top plot shows the differential voltage between unit 1 and 2 (u_{c1}). Bottom plot shows the phase output voltage $u_{CGIg} = u_{c1} + u_{c2}$, where 1 p.u is for the peak voltage of the differential transformer unit output voltage. Minor differences are present in both u_{c1} and u_{c2} (not shown). These differences are summed up in u_{CGIg}. In order to further evaluate the generic model, Figure 9-3 shows the PWM generated harmonic spectra for measured and simulated u_{CGIg}. The equivalent switching frequency is $2 \cdot f_{sw,cgi}$ in both measurement and simulation. The energy content is more spread out in the

measured u_{CGIg}, whereas the energy is concentrated into only a few sideband harmonics (± 1 and ± 5) in the simulation model. This indicates that the model implemented control and PWM strategy is not identical to that of the actual converter (which is confidential and unknown to the author). However, the model is in general capable of replicating the commercial converter's terminal behaviour, when considering that the model is generic and no information is available for the applied modulation technique.

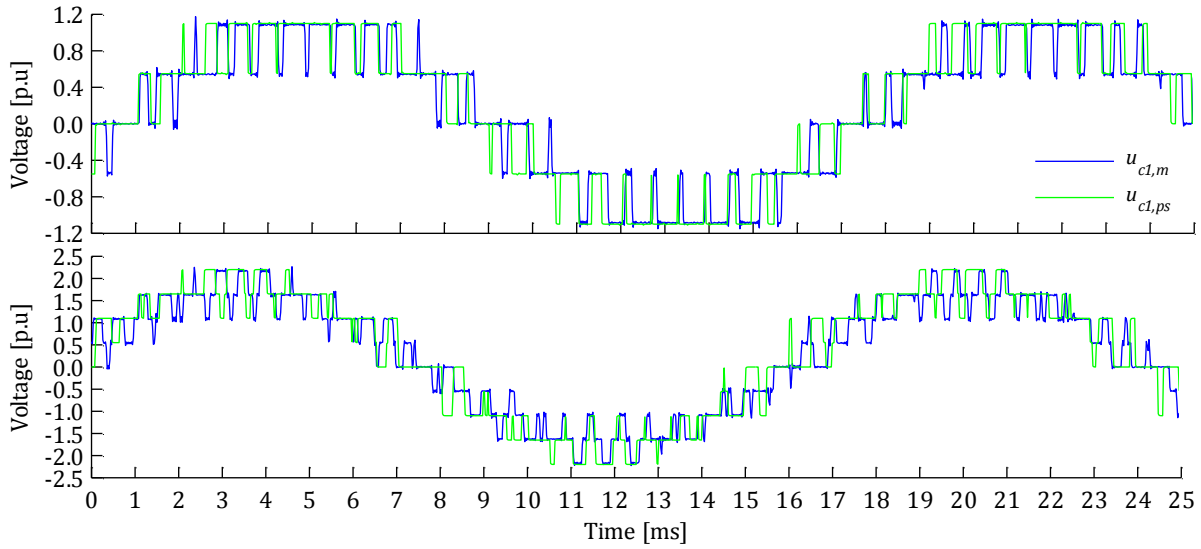

Figure 9-2 compare no-load measurement and pscad CGI differential probes and summed in phase A

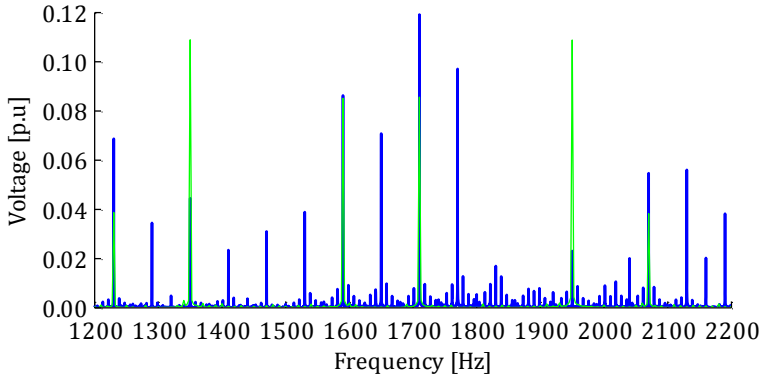

Figure 9-3 Calculated harmonic spectra from measurement (blue) and PSCAD/EMTDC simulations for the first carrier group with a center frequency of $2 \cdot f_{sw,cgi}$ = 1650 Hz.

9.5 Normal Operating Mode

Two active power set-point changes have been realised on the test setup at NREL; a set-point change from 0.2 to 0.4 p.u and from 1.0 to 0.4 p.u. The evaluation is done both in the natural and in the synchronous rotating reference frame (RRF). Figure 9-4a Figure 9-6a show the measured results at the CGI's 13.2 kV busbar for a set-point change from 0.2 to 0.4 p.u. Figure 9-7a and Figure 9-8a show the measured results of a set-point change from 1.0 to 0.4 p.u.

9.5.1 Set-Point Step Change From 0.2 to 0.4 p.u

A relatively good agreement can be observed between the measurement (figure a) and simulation (figure b) results in Figure 9-4 and Figure 9-6. The CGI is both in real-life and in simulation able to maintain the voltage at 1.0 p.u; hence it acts a stiff voltage source. A similar minor transient can be observed in the negative sequence current components (i_d^- and i_q^-) in the measurement and simulation in the bottom graph of Figure 9-6a and b.

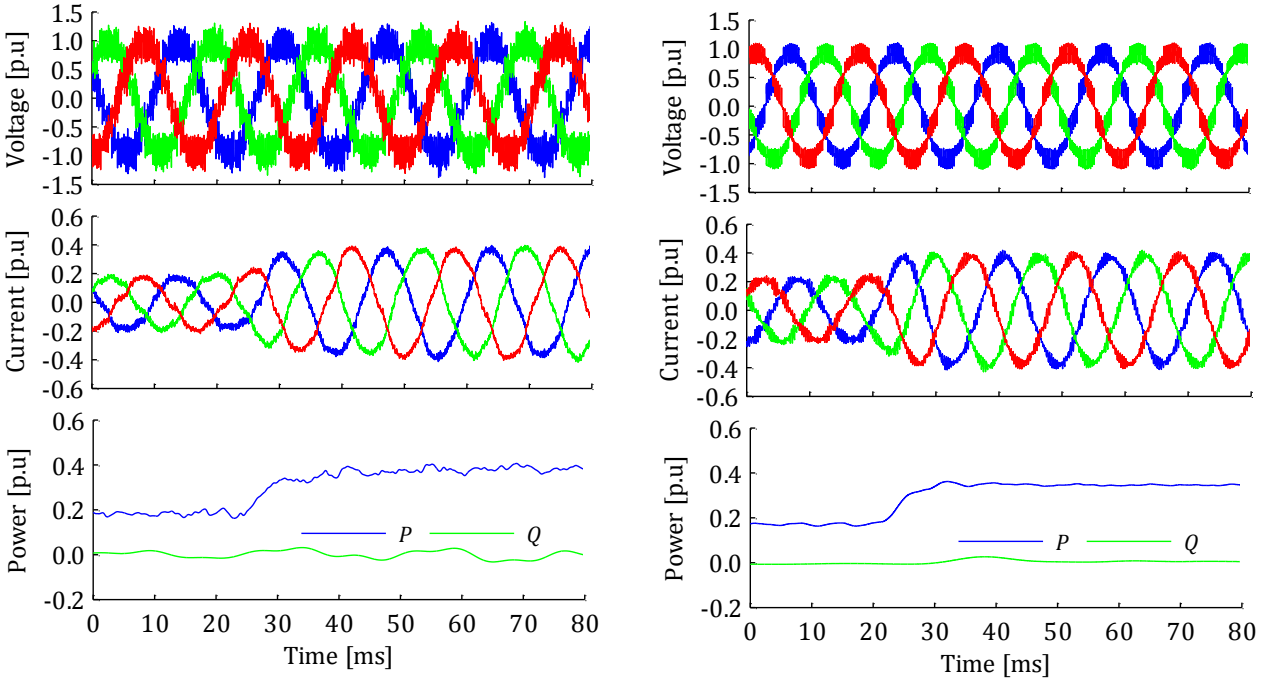

a) Measurements.

b) Simulations.

Figure 9-4 5 Active power order step from 0.20 to 0.40 p.u.

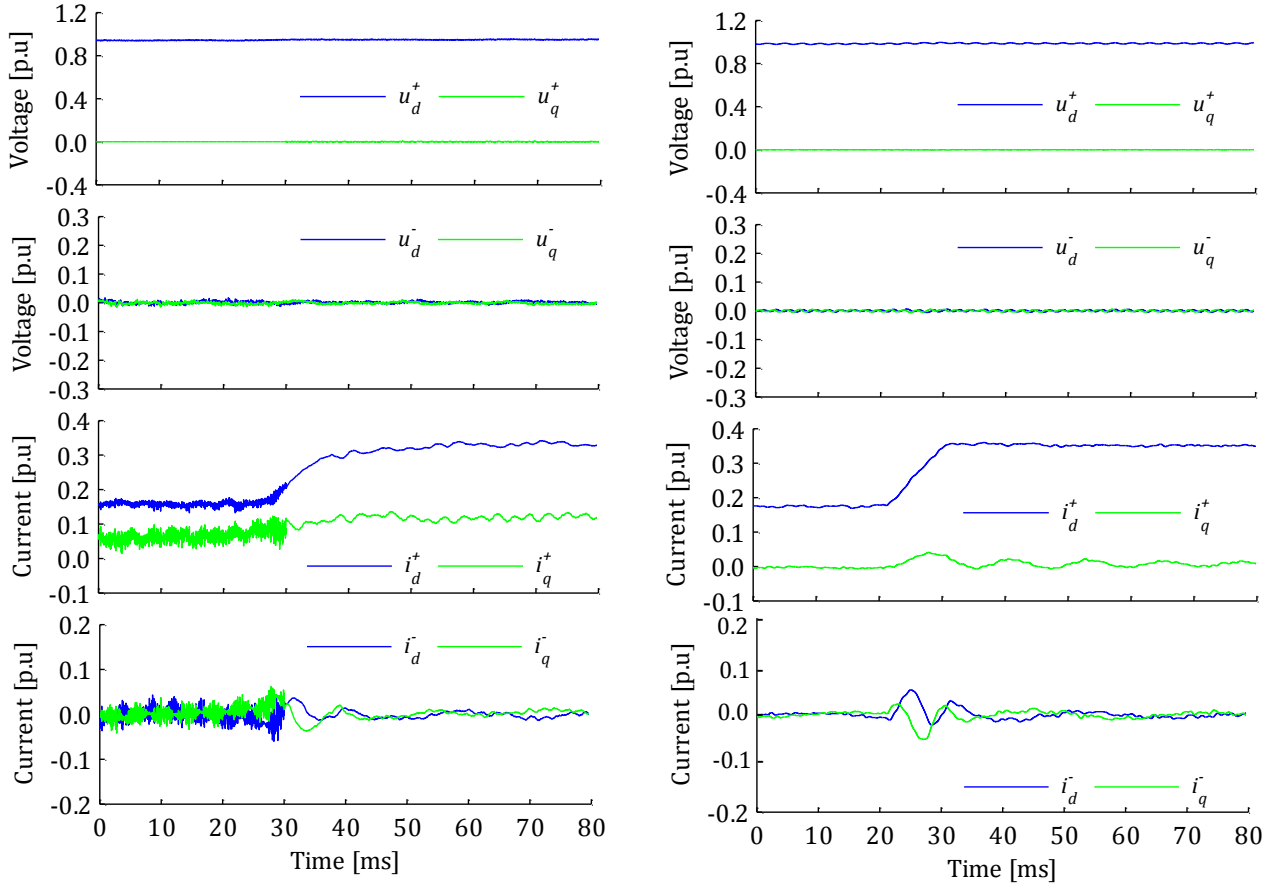

a) Measurements. b) Simulations.

Figure 9-6 Active power order step from 0.20 to 0.40 p.u in the RRF. Top graphs show the positive direct and quadrature voltage components (u_d^+ and u_q^+, respectively). The second graphs from the top show the negative sequence voltage components(u_d^- and u_q^-). The third and fourth graphs from the top show respectively the positive (i_d^+ and i_q^+) and negative (i_d^- and i_q^-) current components, respectively.

9.5.3 Set-Point Step Change from 1.0 p.u to 0.4 p.u

Figure 9-7a and Figure 9-8a show the measured results of a set point change from 1.0 to 0.4 p.u. A similar agreement exists between the measured and simulated waveforms as for the previous case. The CGI does still act as a relatively stiff source, a minor change appears in measured and simulated positive sequence direct voltage component (u_d^+). The simulated positive sequence quadrature current component (i_q^+) exibits a more apparent transient behaviour than the measured waveform. On the other hand, the transient spikes are higher in the measured i_d^- and i_q^- , than in the simulated currents.

In general, it is considered that the measured dynamics during the normal operating range are well replicated in the developed models of the PEDs.

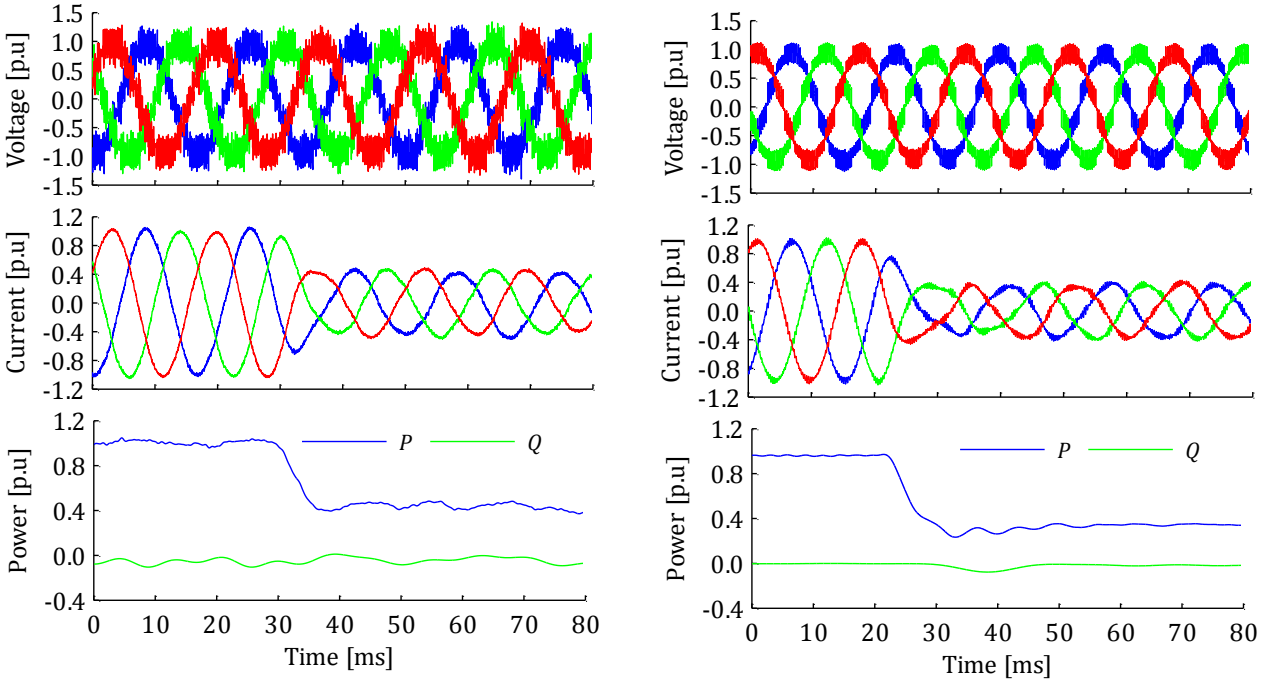

a) Measurements. b) Simulations.

Figure 9-7 Active power order step from 1.00 to 0.40 p.u.

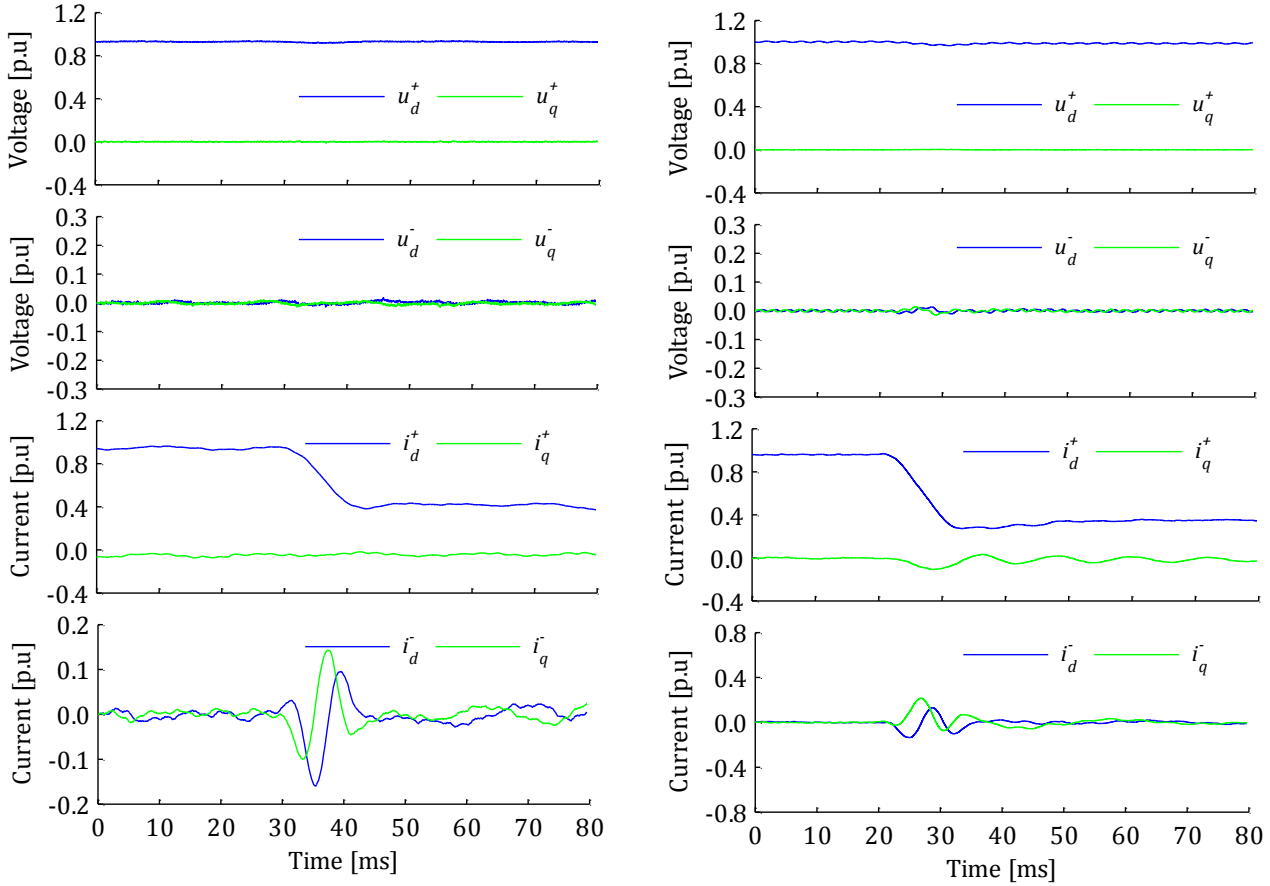

a) Measurements. b) Simulations.

Figure 9-8 Active power order step from 1.00 to 0.40 p.u in the RRF.

9.6 Low Voltage Ride-Through

The single and three phase faults are the most common and worst type of faults appearing in the power system [3, 161]. Therefore, the PED models are evaluated for these types of faults.

9.6.1 Three Phase Full Voltage Drop of 1000 ms Duration

Figure 9-9 shows the measured and simulated results for the balanced full voltage drop with a rise time of 1000 ms. Generally, the simulated results are well correlated with the test measurements. However, large transitory currents are present in the measured currents (peak value approximately 2.8 p.u). This transient behaviour is not replicated in the simulations, where the WTG is well controlled according to the design requirements described in Chapter 8.

Similar behaviour is present in the measured and simulated results during the slow recovery Figure 9-9.

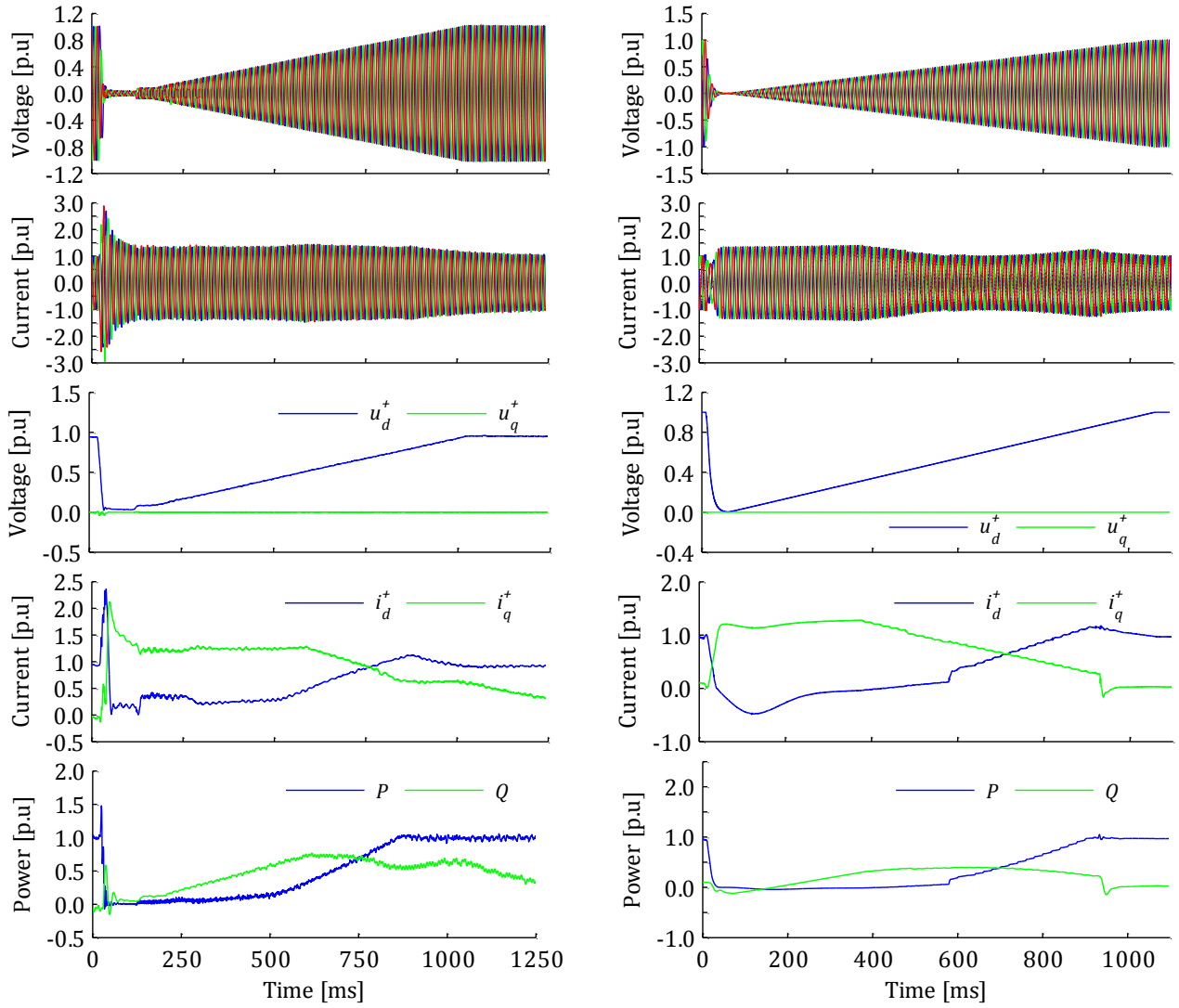

a) Measurements. b) Simulations.

Figure 9-9 Comparison of measured and simulated waveforms for a full three phase voltage drop with a rise time of 1000 ms.

9.6.3 Single Phase Full Voltage Drop of 100 ms Duration

Figure 9-10 shows the comparison of measurement and simulation results for the single phase full voltage drop. As for the symmetrical operating conditions described in the above, a good correlation exists between the simulation and measurement results.

The measured currents are highly unsymmetrical before and after the FRT mode is enabled. The currents are relatively balanced during the "steady-state" part of the single phase fault (i.e. when the voltage magnitude is maintained at 0 p.u in the faulted phase). This indicates that the negative sequence controller is only enabled when the WTG is in the FRT mode. This asymmetry is to a high degree replicated in the simulation results.

The active power oscillation is more pronounced in the measurements and even reaches negative values. The magnitude of the simulated injected reactive power is lower than in the measurements. This indicates that the gain k_Q in equation 8-6 in Chapter 8 could be set higher than 2. The measured and simulated i_q^+ for the three phase fault in Figure 9-9 are relatively identical and hence it was decided to keep k_Q fixed at 2, regardless of the characteristics of the fault.

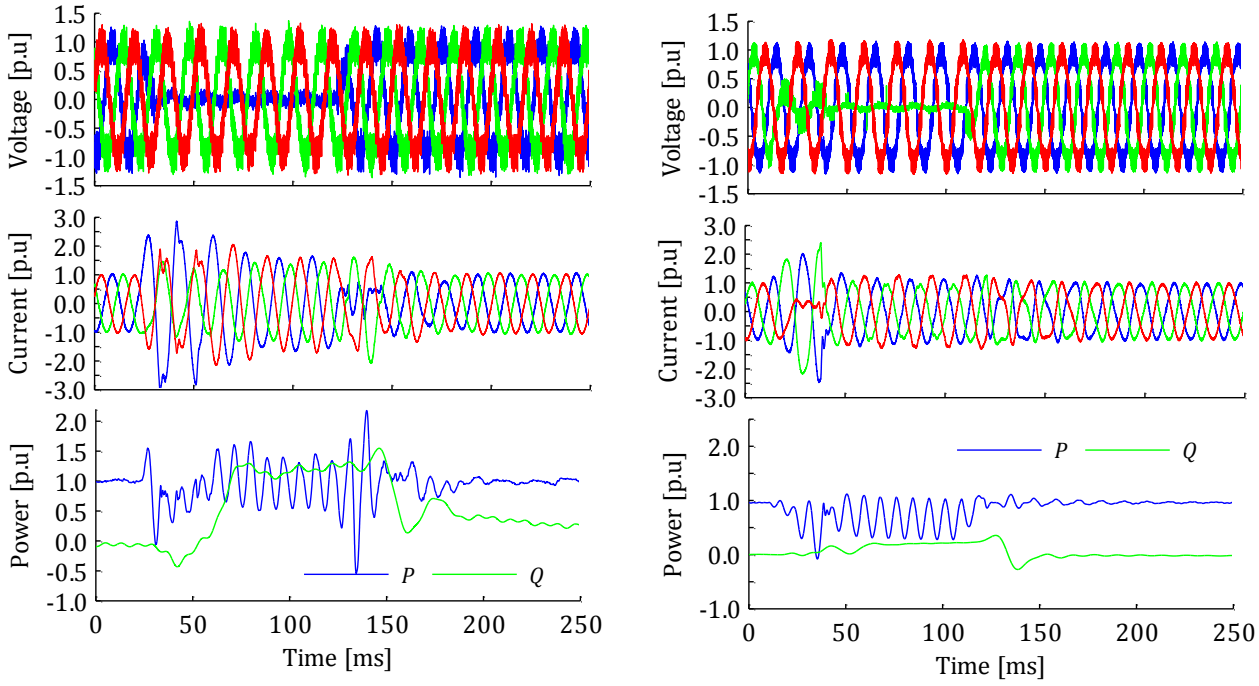

Figure 9-10 Comparison of measured and simulated waveforms for a full single phase voltage drop for a duration of 100 ms.

Negative Sequence Controller Enabled by Default in the Model

In order to illustrate the effect of having the negative sequence controller enabled at all times, Figure 9-11 shows the simulation results with the negative sequence control enabled only in the FRT mode and by default (figure a and b, respectively).

The currents are relatively symmetrical during the whole transient when the negative controller is enabled by default in Figure 9-11b, whereas asymmetry is present in figure a as described in the above. This therefore strongly indicates that the negative sequence is only controlled in the FRT mode in the commercial WTG.

The initial active power oscillations are lessened when the controller is enabled by default. The oscillations are essentially identical during the steady-state part of the fault, where the negative sequence controller is enabled in both cases.

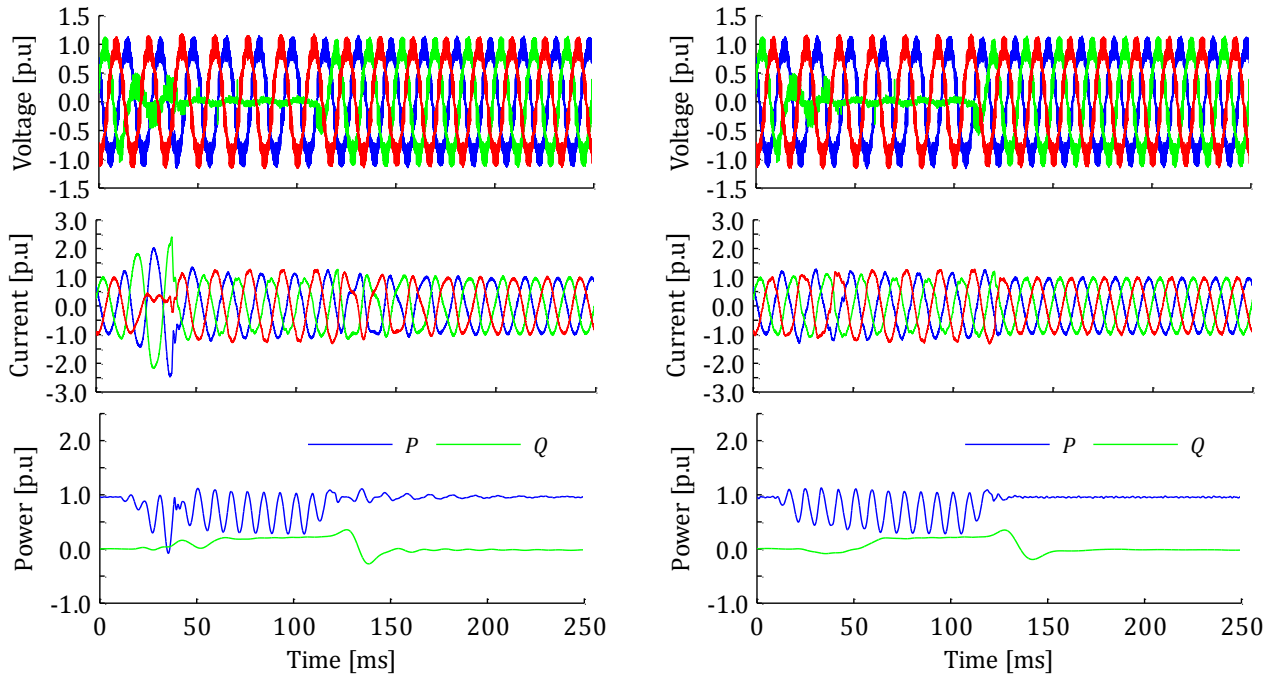

a) Negative sequence controller enabled in the FRT mode. (same as Figure 9-10b).

b) Negative sequence controller enabled by default.

Figure 9-11 Comparison of the simulation results, showin the effect of having the negative sequence controller enabled a) only in the FRT mode and b) by default.

9.7 High Voltage Ride-Through Evaluation

9.7.1 Two Phase 1.3 p.u Voltage Rise of 100 ms Duration

Figure 9-12 shows the comparison of the measurement and simulation results for a two-phase voltage of 1.3 p.u. The measured currents are highly unsymmetrical. This asymmetry is also present in the simulations, as the FRT controller is only activated when the condition $U_{g,RMS} \leq 0.9$ is satisfied.

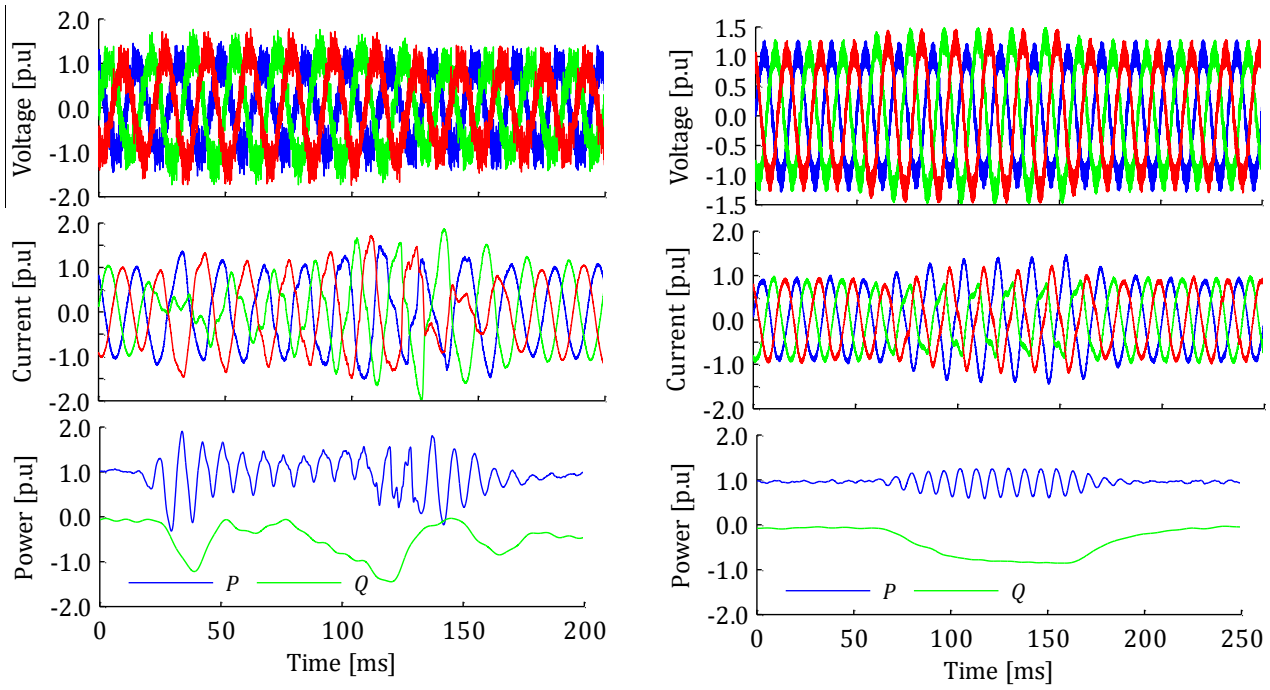

a) Measurements. b) Simulations.

Figure 9-12 Comparison of measured and simulated waveforms for a two phase voltage increase of 1.3 p.u for a duration of 100 ms.

Negative Sequence Controller Enabled by Default in the Model

As for the previous unbalanced LVRT case, the effect having the negative sequence controller enabled by default is investigated. Figure 9-13 shows the two cases where the negative sequence controller is only enabled during a LVRT situation and by default (figure a and b, respectively). The currents are significantly more balanced in the case when the negative sequence controller is enabled.

The comparison of Figure 9-13b with the measured HVRT in Figure 9-12a, strongly indicates that the negative sequence is only controlled in the LVRT mode in the commercial WTG, as also observed in the previous section.

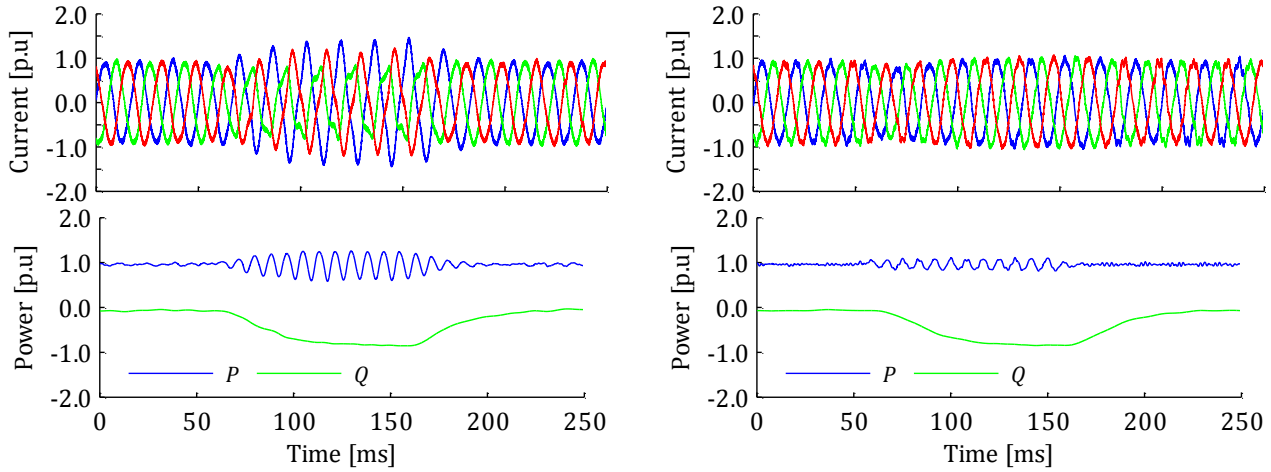

a) Negative sequence controller enabled in the FRT mode (same as Figure 9-12b).

b) Negative sequence controller enabled by default.

Figure 9-13 Comparison of the simulation results, showing the effect of having the negative sequence controller enabled a) only in the FRT mode and b) by default.

9.8 Chapter Summary

This chapter has presented the measurement results obtained at NREL. The measurement data has been used to develop and validate generic, yet detailed time domain models of the PEDs at NREL, realised in PSCAD/EMTDC. The evaluation has been done considering the CGI's no-load waveforms, the WTG's active power set-point step changes and symmetrical and unsymmetrical low and high voltage operating conditions. It has been shown that it is possible to accurately simulate measured waveforms with little or even no information available of the parameters influencing the characteristics of both the CGI and the WTG. The successful validation gives credibility to the time domain modelling for the harmonic stability assessment in OWPPs.

Chapter 10 Power Electronic Device Modelling in the Frequency Domain

The power electronic devices (PEDs) considered in this work have been described in the previous chapters. The PEDs have been modelled in the time domain and the models have successfully been evaluated based on comparison with measurement data. This chapter presents the frequency domain modelling of the PEDs. The comparison of the simulated results in time and frequency domain related to the harmonic stability evaluation in offshore wind power plants (OWPPs) is given in Part III.

10.1 Stability Evaluation

The stability issues in power systems employing PEDs is mainly attributed to [162, 163]: a) The violation of the admittance ratio or Nyquist stability criterion, studied in e.g. [164-170]. A more thorough review is given in [171]. For PEDs with equivalent load and source impedances ($Z_{load}(s)$ and $Z_{source}(s)$, respectively), the system is guaranteed to be stable if the ratio $Z_{load}(s)/Z_{source}(s)$ does not encircle the point (-1;0) on the Nyquist contour plot [9]. This well-established technique to investigate the system stability is referred to as the impedance-based stability criterion developed in [172]. b) The real part of input/output impedance of a voltage source converter (VSC) might appear as negative resistance in the low frequency range due to the controllers parameters, reducing the system's damping [162, 163, 173].

The Nyquist stability criterion is used in the analysis in this work.

10.1.1 Stability Indices

The Nyquist contour shows the number of encirclements and thus the stability of the closed-loop system [7, 21, 58]. The commonly applied gain and phase margins (GM and PM, respectively) provide a two-point measure on how close the Nyquist contour is to encircle the (-1;0) point. The GM is the factor that the amplitude of the open-loop transfer function ($G_{ol}(s)$) can be increased before the system becomes unstable. The GM is the inverse of $G_{ol}(s)$, when the phase of $G_{ol}(s)$ is 180°. The PM is a measure of how much additional phase lag or time delay the system can tolerate [174].

The GM and PM are useful in the evaluation of the relative stability of the system but can be misleading as in the design of realistic control systems [58]. Alternatively, the vector gain margin (VGM) can be used [175]. The VGM is based on a sensitivity function and is defined as the shortest distance of the Nyquist contour of $G_{ol}(s)$ and the point (-1;0). For the stability evaluation in OWPPs, the VGM has previously found to provide a more realistic insight on the system's relative stability [21, 58].

10.2 Frequency Domain Representation of the PED

The frequency domain representation of various types of PEDs has previously been presented in e.g. [59,176-185]. The control of the PEDs considered in this work is realised in the rotating reference frame (RRF or dq) [125, 147, 148] as described in chapter Chapter 2.

The continuous frequency domain representation of each converter can be defined as in Figure 10-1. The figure shows the admittance $Y(s)$ seen from the converter terminals and the impedance $Z_d(s)$ seen from the voltage feedforward measurement point. Low-pass filters ($G_{LPF}(s)$) are used in the measured converter output current and filter bus voltage ($i_g(s)$ and $u_g(s)$, respectively), which are used as feedback and feedforward signals in the control system, respectively. A notch or band rejection filter (BRF, $G_{BRF}(s)$) is furthermore used to attenuate the $2\omega_0$ negative sequence component in the positive sequence frame and vice versa when using a dual controller [125, 147, 148].

The transfer functions $G_i(s)$ and $G_{VSC}(s)$ constitutes the control system and the non-ideal properties of the converter bridge, respectively. $G_i(s)$ and $G_{VSC}(s)$ will be described shortly.

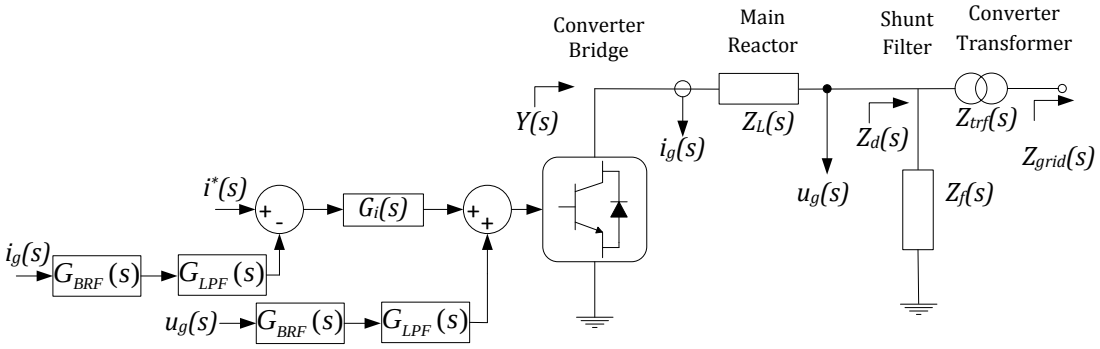

Figure 10-1 Converter control single line diagram.

A voltage feed forward and direct/quadrature component de-coupling are introduced in order to suppress possible grid voltage variations and to improve the control performance. The block diagram in Figure 10-2 can be developed from Figure 10-1.

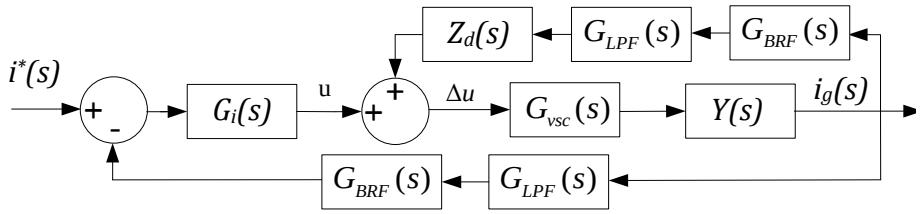

Figure 10-2 Current control for the converters.

The control system represented by $G_i(s) = G_{pi}^{dq}(s) \cdot G_{SH}(s)$ in Figure 10-1 and Figure 10-2 includes the analogue to digital conversion ($G_{SH}(s)$) and a PI controller of the standard form $G_{pi}^{dq}(s) = K_p \cdot (1 + T_i s)$, where K_p and T_i are the proportional gain and integral time constant, respectively.

The transformation from the stationary reference frame (SRF or $\alpha\beta$) to the RRF performs a frequency shift, which can be misleading when analysing control interaction with the electrical system [21]. Therefore, it is beneficial to express the controller in the SRF. This can be accomplished by using the transformation matrix derived in [146] and shown in equation 10-1 (identical to equation 8-3 on page 90):

$$H^{dq2\alpha\beta}(s) = \frac{1}{2}\begin{bmatrix} H^{\alpha\beta}(s+j\omega_0) + H^{\alpha\beta}(s-j\omega_0) & j \cdot H^{\alpha\beta}(s+j\omega_0) + j \cdot H^{\alpha\beta}(s-j\omega_0) \\ -j \cdot H^{\alpha\beta}(s+j\omega_0) - j \cdot H^{\alpha\beta}(s-j\omega_0) & H^{\alpha\beta}(s+j\omega_0) + H^{\alpha\beta}(s-j\omega_0) \end{bmatrix} \quad 10\text{-}1$$

Where ω_0 is the fundamental angular frequency.

Equation 10-2 shows the positive sequence PI controller expressed in the RRF.

$$G_{PI}^{dq} = G_{PI}^{dq(+)} = \begin{bmatrix} k_p + \frac{k_i}{s} & 0 \\ 0 & k_p + \frac{k_i}{s} \end{bmatrix} \quad 10\text{-}2$$

Using equation 10-1, the controller can be expressed in the SRF, as in equation 10-3.

$$G_{PI}^{\alpha\beta(+)}(s) = \begin{bmatrix} k_p + \dfrac{k_i}{s^2+\omega_0^2} & \dfrac{k_i\omega_0}{s^2+\omega_0^2} \\ -\dfrac{k_i\omega_0}{s^2+\omega_0^2} & k_p + \dfrac{k_i}{s^2+\omega_0^2} \end{bmatrix} \quad 10\text{-}3$$

Similarly, the negative sequence controller can be expressed in the SRF:

$$G_{PI}^{\alpha\beta(-)} = \begin{bmatrix} k_p + k_i\dfrac{s}{s^2+\omega_0^2} & -\dfrac{k_i\omega_0}{s^2+\omega_0^2} \\ \dfrac{k_i\omega_0}{s^2+\omega_0^2} & k_p + k_i\dfrac{s}{s^2+\omega_0^2} \end{bmatrix} \quad 10\text{-}4$$

Joint operation of positive and negative sequence control in the RRF is equivalent to the application of resonance controllers in the SRF as can be realised from equation 10-5 [124].

$$\begin{aligned} G_{PI}^{\alpha\beta}(s) &= G_{PI}^{\alpha\beta(+)}(s) + G_{PI}^{\alpha\beta(-)}(s) \\ &= 2 \cdot \begin{bmatrix} K_p \cdot \left(1 + \dfrac{1}{T_i \cdot (s^2+\omega_0^2)}\right) & 0 \\ 0 & K_p \cdot \left(1 + \dfrac{1}{T_i \cdot (s^2+\omega_0^2)}\right) \end{bmatrix} \end{aligned} \quad 10\text{-}5$$

The analogue to digital conversion is typically represented by the first order Padé approximation (i.e. first order transfer function) [186]:

$$G_{SH}(s) = \frac{1}{sT_s + 1} \quad 10\text{-}6$$

Where T_s is the sampling period. Additionally, the non-ideal switches and the statistical delay of the pulse-width modulation (PWM) process ($T_{PWM} \approx 0.5 \cdot T_s$) have been taking into account according to [58]:

$$G_{VSC}(s) = \frac{K_c \cdot e^{-s\tau_0}}{sT_{PWM} + 1} \quad 10\text{-}7$$

Where $K_c (\approx 1)$ is the converter gain, $\tau_0 (= 0$ s for an ideal converter) is the dead time of the converter.

Figure 10-3 shows the open-loop frequency characteristics of the PI controller and the analogue to digital conversion and PWM. The delay associated with the converter and the analogue to digital is noticeable and has a degrading effect of the system stability.

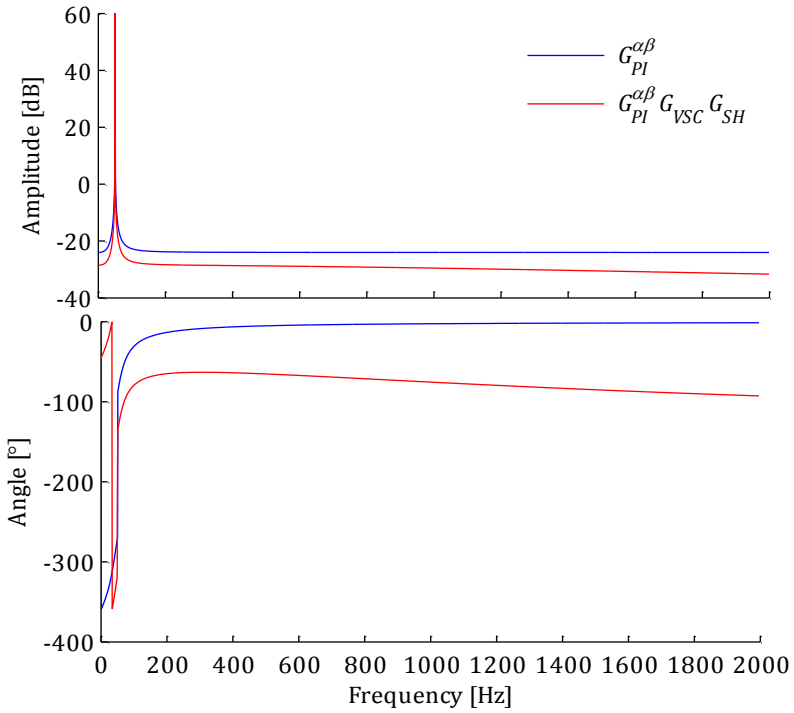

Figure 10-3 Frequency characteristics of the current control system implemented in the RRF and represented in the SRF.

10.2.1 BRF Representation

The cross-coupling terms in equation 10-2 and 10-4 (i.e. the off-diagonal terms) result in the $2\omega_0$ ripple discussed in chapter 8 [125, 147, 148]. This cross coupling needs to be supressed in order to improve the performance of the controller. As, discussed in chapter 8, the BRF is commonly used [7, 147] and therefore considered here. The considered notch filter is defined as:

$$G_{BRF}(s) = \frac{s^2 + \frac{\omega_n}{Q_n}s + \omega_n^2}{s^2 + \frac{\omega_n}{Q_d}s + \omega_n^2} \qquad 10\text{-}8$$

As the BRF is situated in the feedback path in Figure 10-2 it affects directly the open loop stability of the PED. Appropriate adjustment of the Q_n and Q_d parameters can alter the selectivity of the BRF as shown in Figure 10-4. In case of a highly selective filter, the angular frequency ω_n should be adaptive depending on the angular grid frequency ω_0 [124].

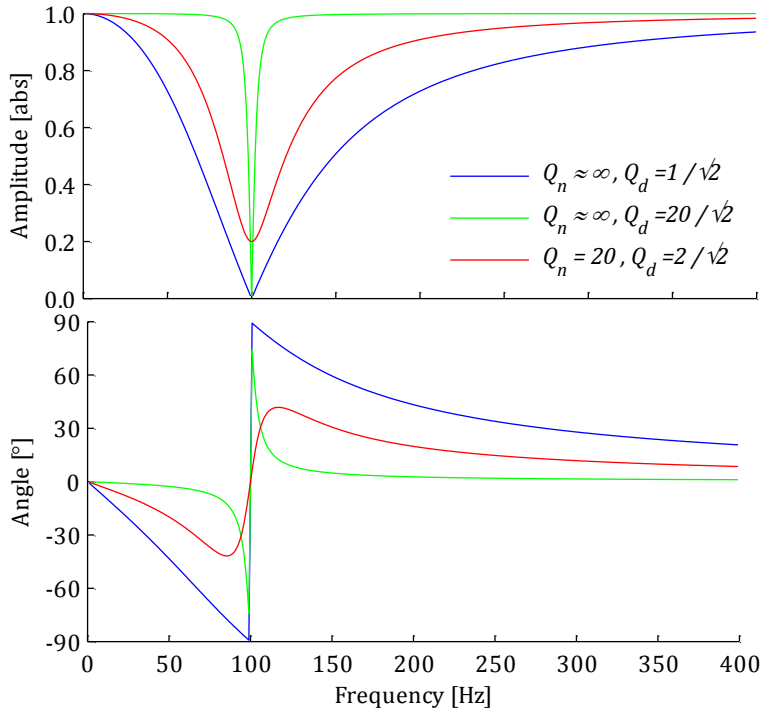

Figure 10-4 Frequency dependent characteristics of the BRF depending on the parameters Q_d and Q_n ($\omega_n = 2\omega_0$). Expressed in the RRF.

The BRF tuned at $2\omega_0$ in equation 8-5 is similar to the PI controller implemented in the RRF and must thus be transformed into the SRF for the system analysis purposes. Similarly as for the PI controller, this is done using the transformation matrix given in equation 10-1. Equation 10-9 shows expression for the diagonal components of the notch filter, where it assumed that perfect decoupling is present between the direct and quadrature components. This is a common assumption [21].

$$G^{\alpha\beta}(s) = \tfrac{1}{2}\cdot[G^{dq}(s+j\omega_0) + G^{dq}(s-j\omega_0)] \rightarrow$$

$$G_{BRF}^{\alpha\beta}(s) = \frac{Q_d}{Qn}\cdot\left(\frac{\begin{bmatrix} s^4 Q_n Q_d + 3(Q_n+Q_d)\omega_n \\ +s^2(2Q_nQ_d[\omega_0^2+\omega_n^2]+\omega_n^2) \\ +s[Q_n+Q_d]\cdot[\omega_0^2\omega_n+\omega_n^3] \\ +Q_nQ_d[\omega_0^4+\omega_n^4-2\omega_0^2\omega_n^2]+\omega_0^2\omega_n^2 \end{bmatrix}}{\begin{bmatrix} s^4Q_d^2 + s^3 2Q_d\omega_n \\ +s^2(2Q_d^2[\omega_n^2+\omega_0^2]+\omega_n^2) \\ +s(2Q_d[\omega_0^2\omega_n+\omega_n^3]) \\ +Q_d^2[\omega_0^4+\omega_n^4]+\omega_0^2\omega_n^2[1-2Q_nQ_d] \end{bmatrix}}\right) \qquad 10\text{-}9$$

Figure 10-5 shows the characteristics of the BRF for $Q_n = 10/\sqrt{2}$ and $Q_d = 2/\sqrt{2}$ (i.e. same parameters as for the red curve in Figure 10-4) expressed in the RRF and SRF from equation 8-5 and 10-9, respectively. In the figure a ±50 Hz a frequency shift to 50 and 150 Hz is obvious, caused by the transformation from the RRF to the SRF.

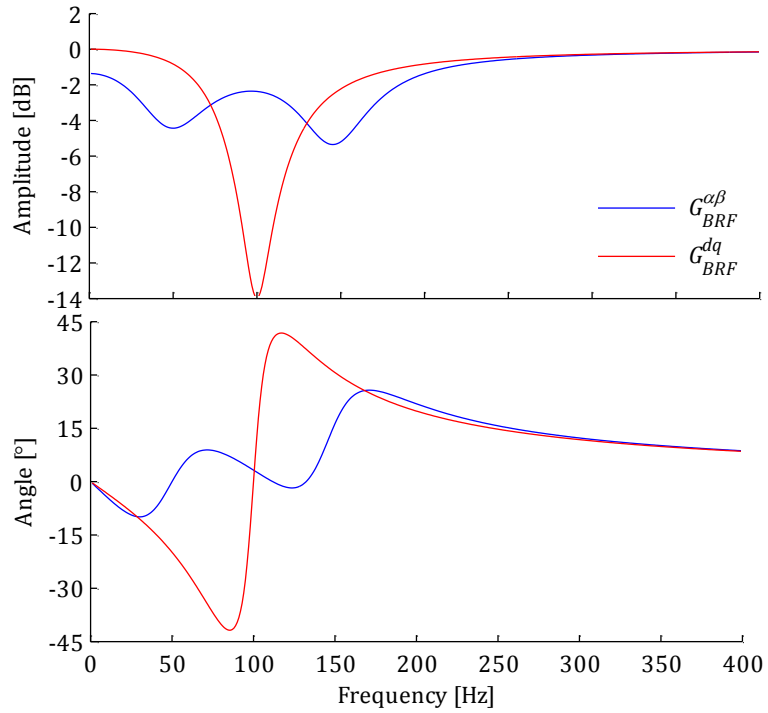

Figure 10-5 Frequency dependent characteristics of the BRF in the RRF and in the SRF (red and blue curve, respectively).

Figure 10-6 shows the impact of the BRF on the open-loop characteristic of the current control system. The effect of the BRF is mainly noticeable in the lower frequency range (i.e. up to around 400 Hz) as it improves slightly the phase characteristic.

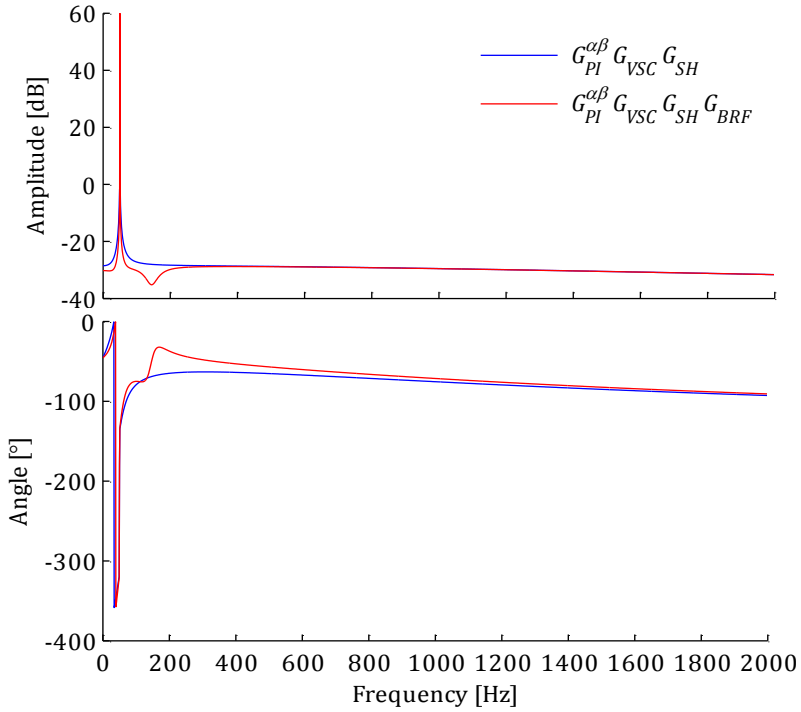

Figure 10-6 Frequency characteristics of the current control system implemented in the RRF and represented in the SRF.

10.2.2 Low-Pass Filtering

Low-pass filtering with a cut-off frequency of 1 kHz is used for conditioning of the signals prior to the analogue to digital conversion. These are implemented in the SRF and given as [187]:

$$G_{LPF}^{\alpha\beta}(s) = \frac{A_0}{b_i \cdot s^2 + a_i \cdot s + 1} \qquad 10\text{-}10$$

Where $b_i = 0$ for the first order filter. A_0 is the gain of the filter.

Figure 10-7 shows the well-known frequency dependent characteristics of the 1st and 2nd order filters (G^{1st}(s) and G^{2nd}(s), respectively) with unity gain. The combined effect of the higher amplitude of G^{2nd}(s) from one decade below and up to the cut-off frequency and the greater phase lag possesses challenges to the harmonic stability in OWPPs as will be demonstrated in Chapter 12.

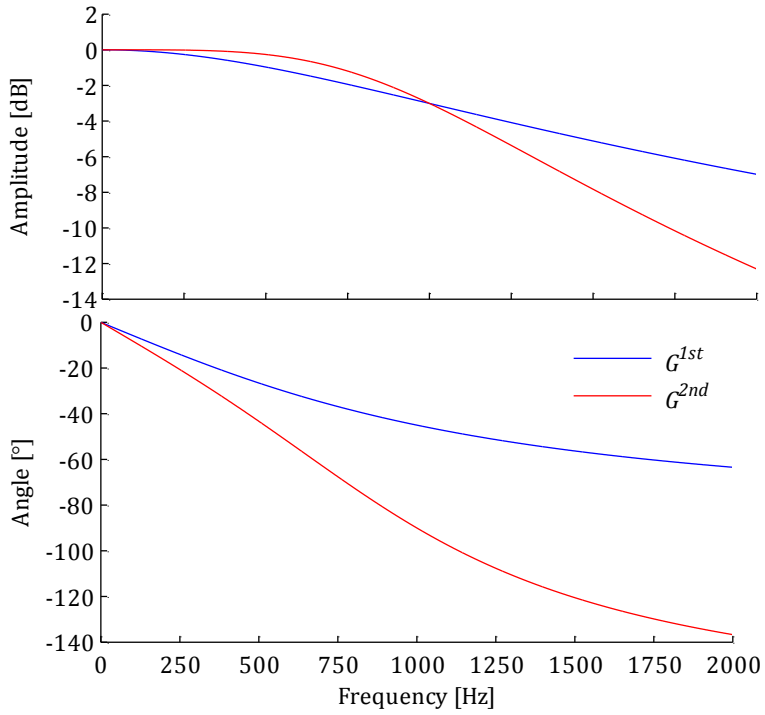

Figure 10-7 Frequency dependent characteristics of the 1st and 2nd order filters with a cut-off frequency of 1 kHz.

Figure 10-8 shows the effect of the applied feedback filter on the overall frequency dependent characteristic of the PED. The additional delay caused by the 2nd order filter (red curve) becomes significant at higher frequencies compared to the case using the 1st order filter (blue curve).

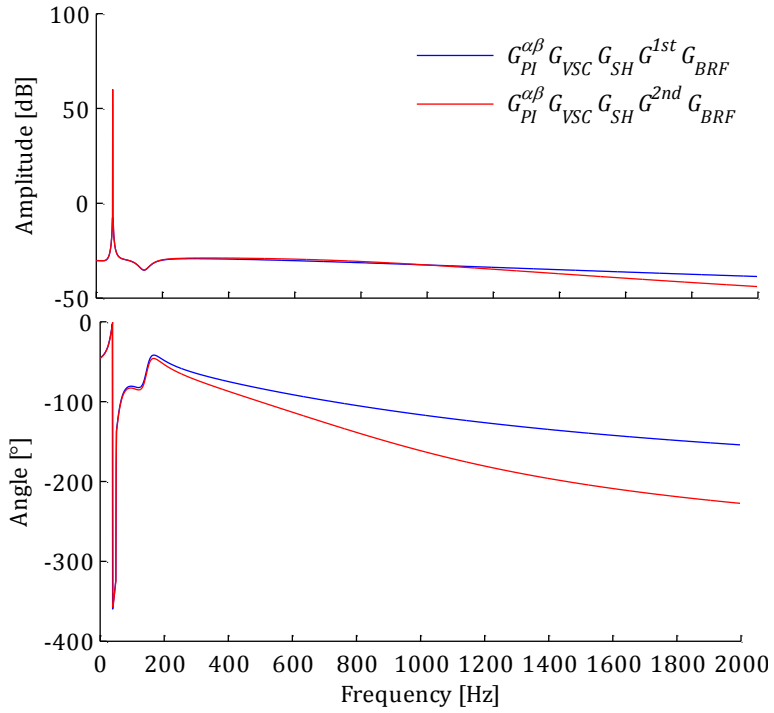

Figure 10-8 Frequency characteristics of the current control system implemented in the RRF and represented in the SRF.

10.2.3 Active Harmonic Stability Filter

A BRF of the form in equation 8-5 is often used to supress the undesirable harmonic interaction between the PED and the plant [7, 58]. Figure 10-9 shows the effect of the additional stability filter (BRF,stab) tuned at 500 Hz, where $Q_n = 12$ and $Q_d = 1/\sqrt{2}$. The BRF,stab in this case is effective at a broad range of frequencies. This implies that the BRF,stab is less sensitive to the number of wind turbine generators (WTGs) in service as well as the layout and tolerances of the system parameters such as the available short circuit power and the cables properties. The BRF,stab is intended to operate autonomously from other WTGs in the OWPP without knowledge of the system impedance. The bandwidth of the PED's current control system is according to [7] sufficient to provide fault ride through capability. Other advantageous of the BRF,stab is that it is considered universal and does not affect the PI controller performance. Hence; the parameters of the PI controller do not need to be determined on a site specific basis [7].

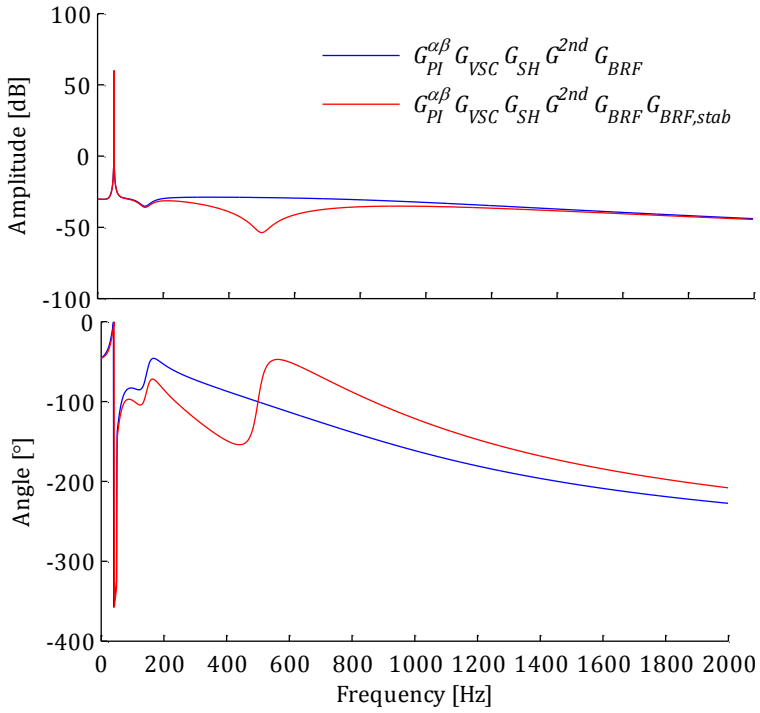

Figure 10-9 Frequency characteristics of the current control system implemented in the RRF and represented in the SRF.

10.3 Chapter Summary

A presentation of the frequency domain representation of the PED considered in this work has been given in this chapter. The comparison of the simulated results in time and frequency domain related to the harmonic stability evaluation in OWPPs is given in Part III.

Chapter 11 Modelling of the Passive Power System Components

The main scope of this research project is the evaluation of the frequency and time domain harmonic stability evaluation methods in converter rich offshore wind power plants (OWPPs). In order to do this it is considered sensible to make identical representations of the passive components such as the export cable and the external power system in the two domains. This ensures that the possible discrepancies in the obtained results are related to the way the power electronic devices (PED), including their respective control systems, are represented in the two domains. The purpose of this chapter is to develop suitable methods for modelling the passive components in the two domains as a number of challenges were encountered in the preparation of this work.

11.1 External Network Representation

The impedance of the external high voltage alternating current (HVAC) network ($Z_{grid}(f)$) is inductive at fundamental frequency but can change from inductive to capacitive and back again many times with increasing frequency. This creates a number of resonances, which can be series or parallel. Furthermore, a number of minor resonances where the sign of the reactance does not change can be present. The network exhibits different frequency dependent impedance characteristic for all possible network configurations [188].

A family of impedance loci plots are typically calculated by the transmission system operator (TSO) and provided to the OWPP developer. This significantly simplifies e.g. filter design at the onshore substation [56]. Based on DEWP's experience, this is not sufficient for the harmonic stability evaluation, where discrete values at discrete frequencies (e.g. a 1 Hz resolution) is preferred for a certain number of operating scenarios of the external system. $Z_{grid}(f)$ is by the TSO found by performing a frequency sweep in the TSO's power system simulation tool (e.g. DigSILENT PowerFactory) and provided to the OWPP developer in a look-up table format.

The implementation of such a frequency dependent network equivalent (FDNE) possesses some challenges when implemented in some simulation tools such as EMT programs (EMTPs) as the FDNE needs to be described by a rational function. This can be achieved by using some of the available system identification methods, such as e.g. the vector fitting [189]. The implementation of the FDNE in EMTPs such as PSCAD/EMTDC requires further manipulation of the rational function, which should be discretized. The discretized FDNE can then be implemented in PSCAD/EMTDC auto regressive moving average (ARMA) model representation (i.e. represented as a Norton equivalent) [68]. The FDNE is not available in the current version of PSCAD/EMTDC (v4.5). The ARMA representation will be available in the upcoming v4.6, according to the author's knowledge.

The implementation of the ARMA model in PSCAD/EMTDC is essentially identical to the implementation of the Norton equivalents of the modular multilevel-cascaded converters developed in chapter 4. Hence; the author has demonstrated the skill needed to implement such a model. Furthermore, as well known, the focus of this research project is the evaluation of the time and frequency domain methods using realistic models of the involved power system components models.

It was therefore decided to use a simpler model representation of the FDNE, as described in the following. The FDNE can be emulated by a number of parallel RLC branches which has been done since the 1960'ties [190, 191, 192]. The FDNE with N RLC branches is shown in Figure 11-1, where L_o and R_0 represent the fundamental frequency impedance. This representation will provide a good approximation only at specified frequencies and a high N is therefore more suitable but at the expense of increased complexity.

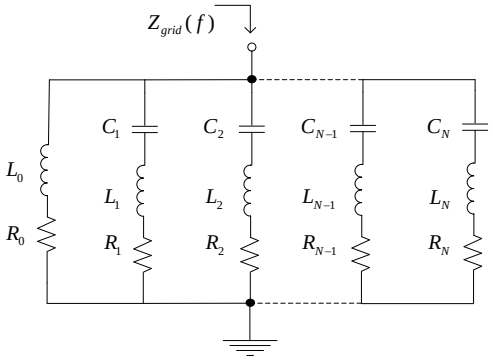

Figure 11-1 FDNE using of N number of RLC branches.

The FDNE in Figure 11-1 can be analytically express in the Laplace domain as:

$$Z_{grid}(s) = R_0 + sL_0 + \sum_{n=1}^{N}\left(R_n + sL_n + \frac{1}{sC_n}\right) \quad 11\text{-}1$$

Where the RLC parameters in the n^{th} branch are calculated as:

$$R_n = \omega_n \cdot \frac{L_n}{Q_n} \quad 11\text{-}2a$$

$$C_n = \frac{1}{\omega_n^2 \cdot L_n} \quad 11\text{-}2b$$

Where L_n, ω_n and Q_n are the tunable parameters of the n^{th} branch (inductance, resonance frequency and quality factor, respectively).

In order to illustrate the usefulness of the FDNE in Figure 11-1, Figure 11-2 shows the comparison between the frequency response of the admittance of an actual power system, as seen from the grid connection point of an OWPP, and a calculated FDNE with $N = 3$. The FDNE are tuned at the three main resonances in the range 800 – 1000 Hz. A higher number of branches should be considered in order to improve the FDNE and to emulate the minor resonances at lower frequencies. The small resonance at 1013 Hz is difficult to emulate using this low number of branches because it is very close to the major resonance at 983 Hz. The parameters of equation 11-1 and the required number of branches could be found by using an optimisation technique, which would be useful in an actual OWPP design, as an alternative to the ARMA model if not available. Also, the FDNE in Figure 11-1 is useful in the early design of an OWPP, where the frequency response of the external grid data might not yet have been provided by the TSO. Also the simple representation is flexible as the parameters are easily tuned in case a sensitivity of the external system's impact of the PED's susceptibility is investigated. As discussed in chapter 13, this is useful as there are uncertainties in the TSO provided data as it is a forecast of the system's harmonic characteristics as well as the data only covers some of the power system's many possible operating conditions.

The use of a high number of branches will not significantly impede the EMTP simulation speed or expand the system's admittance matrix. Inductors and capacitors are modelled using the trapezoidal integration rule as in chapter 4. By mathematical manipulation it is possible to merge the RLC into one two-node component with only one history term (i.e. one storage element).

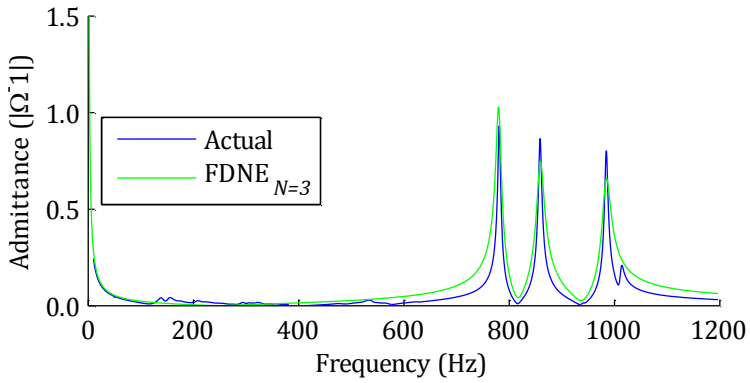

Figure 11-2 Frequency response of the admittance of an actual power system and a FDNE with $N = 3$.

11.2 Export Cable

One of the observed challenges when comparing the frequency and time domain approaches for harmonic stability assessment is the representation of the export cable in the two domains. MatLab and PSCAD/EMTDC are used as the two simulation tools, as previously mentioned. The cable modelling is an important aspect for harmonic stability studies in OWPPs as resonances in the export cable are in the lower frequency range as the cable is long (e.g. 50 km).

The cable representation must be implemented manually by the user in MatLab, whereas there are a few cable models available in PSCAD/EMTDC [114]. The Frequency Dependent Phase Model (FDPM) is the most accurate cable model available in all EMTP tools (and in general) [193, 194]. The model takes into consideration the frequency dependency and distribution of the inductance, capacitance and resistance.

A frequency sweep in PSCAD/EMTDC on the FDPM could be used in the frequency domain analysis. However, the frequency response of the cable is affected by the cable loading. Hence; each time a parameter change is made in the external system seen from the OWPP in Figure 11-3 (e.g. the FDNE or the HVDC system) a new frequency sweep is needed. This is demonstrated in Figure 11-4, where the frequency response of the cable input impedance $Z_{cab}(s)$ terminated by 1 and 10 kΩ resistive impedances. The application of the frequency sweep in PSCAD/EMTDC is thus not considered appropriate to use in the frequency analysis.

Alternatively, the cable (and in general, other multi-port components) can be represented by rational function-based models that characterize the component's port behavior as a function of frequency using the impedance or admittance matrixes [189,195-197].
Another method is to characterize the port behavior by incident and reflected waves, which are related via the scattering parameter matrix [195,198,199].
The implementation of these rational function-based models in EMTPs such as PSCAD/EMTDC is not straightforward and they can even be prone to accuracy problems with the admittance/impedance based models [200]. Most EMTPs do not provide a platform for interfacing the scattering parameter matrix [195]. Reference [195] has devised a unified procedure using a convolution-based Norton equivalent, which can represent the above-mentioned matrixes (admittance/impedance and scattering parameter matrix) using a convolution-based Norton equivalent. Due to the relatively complex task of implementing such a two-port model representation of the cable, it was decided to apply a much more simplified and easily realisable model representation of the cable as discussed in the following.

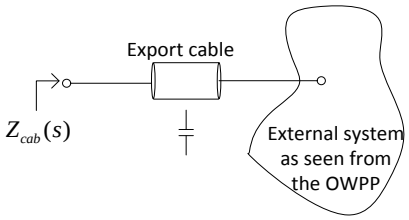

Figure 11-3 Cable input impedance, which is affected by the cable loading.

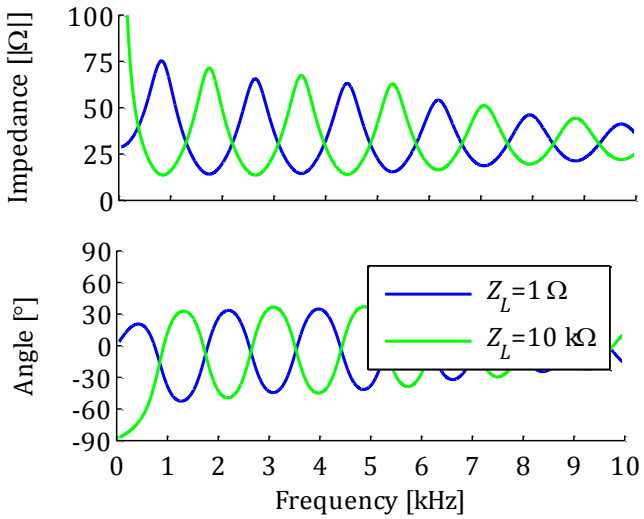

Figure 11-4 Cable loading's influence on the cable input impedance.

11.2.1 PI Cable Model

Instead of the relatively complex modelling of the export cable described in the above, the use of PI cable models are used, which can be represented in a quite straightforward way in the two simulation tools considered. These are described in the following and benchmarked against the FDPM.

Figure 11-5a shows the π representation of the cables, which are termininated by the frequency dependent load Z_{load}(s), which will be used in order to determine an analytical description of the cable input impedance $Z_{cab}(s)$.

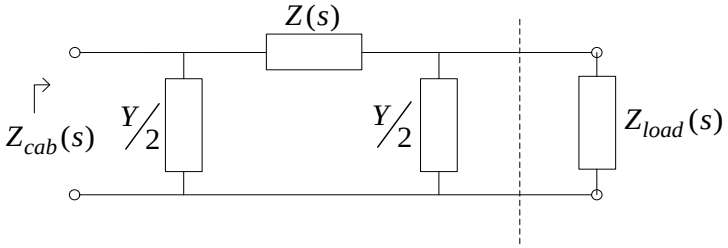

Figure 11-5 π representation of the cables, including the frequency dependency of the skin effect of the conductor.

Nominal PI Cable Model Representation

The lumped parameters of the nominal π circuit in Figure 11-5a are calculated from equation 11-3.

$$Z = (r(\omega) + j\omega l) \quad [\Omega] \quad \text{11-3a}$$

$$Y = (g + j\omega c) \cdot l_{cab} = 1/X_c \quad [S] \quad \text{11-3b}$$

Where r, g, l, c are the resistance, conductance, inductance and capacitance per unit length, respectively. In this work $g = 0$ S·km^{-1}. The frequency dependency of $r(\omega)$ is due to the skin effect described shortly.

Equivalent PI Cable Model Representation

The distributed nature of the cable parameters are included by using the correction factors in equation 11-4 [67]:

$$Z' = Z \cdot \frac{sinh(\gamma \cdot l)}{\gamma \cdot l} \quad [\Omega] \quad \text{11-4a}$$

$$\frac{Y'}{2} = \frac{Y}{2} \cdot \frac{tanh\left(\frac{\gamma \cdot l}{2}\right)}{\frac{\gamma \cdot l}{2}} \quad [S] \quad \text{11-4b}$$

Where γ is the propagation cofficient given in equation 11-5.

$$\gamma = \alpha + j\beta = \sqrt{(r + j\omega l) \cdot (g + j\omega c)} \quad \text{11-5}$$

Where α is the attenuation coefficient in Nepers·m^{-1}, β is the phase coefficient in rad·m^{-1}.

Frequency Dependency of the Cable Conductor

The alternating current in a cable tends to flow near the surface of the conductor due to induced currents, which decreases the effective conductor core cross section. The effect of the current displacement caused by the skin effect becomes significant at higher frequencies. The frequency dependency can according to IEC 60287-1-1 be included using equation 11-6 [201, 202]:

$$r_{ac}(\omega) = r_{dc} \cdot \left[1 + y \cdot \left(k_s + k_p\right)\right] \quad [\Omega \cdot km^{-1}] \quad \text{11-6}$$

Where $y = 1$ for 1-, 2-, and 3-core cables, k_s and k_p are the skin and proximity variables, respectively. r_{dc} is the DC resistance per unit length. Only the skin effect will be considered here. An expression for k_s is given in equation 11-7:

$$k_s = \begin{cases} \dfrac{z^4}{0.8z^4 + 198} & for\ 0 < z \leq 2.8 \\ 0.0563z^2 - 0.0177z - 0.136 & for\ 2.8 < z \leq 3.8 \\ 0.354z^2 - 0.733 & for\ z > 3.8 \end{cases} \quad \text{11-7}$$

Where $z = \sqrt{4\omega/(10^4 \cdot r_{dc})}$. The skin effect calculated from equation 11-6 and 11-7 introduces an error less than 0.5 % at fundamental frequency [201] and is therefore considered suitable for the frequency range considered in this research (i.e. up to the bandwidth of the controllers in the active OWPP components).

Cable Input Impedance

The input impedance of the load terminated cable in Figure 11-5a is given as:

$$Z_{cab}(s) = 2X_C(s)||[Z(s) + 2X_C(s)||Z_{load}(s)] = \frac{1}{\frac{1}{2X_C} + \frac{1}{Z(s) + \frac{1}{\frac{1}{2X_C} + \frac{1}{Z_{load}(s)}}}} \quad 11\text{-}8$$

Where $X_C(s)$ is the reactance of the capacitor in Figure 11-5a.

Figure 11-6 shows the frequency response of $Z_{cab}(s)$ using the FDPM in PSCAD/EMTDC (time domain model, TDM) and calculated from equation 11-8 (frequency domain model, FDM) with $Z_{load} = 10$ kΩ (resistive) for a three-core 50 km long cable. The FDM and TDM exhibit similar frequency characteristics, hence the equivalent π cable model can be considered useful in the frequency domain analysis. It should be noted that the author is unaware of how the skin (and the proximity) effect is modelled in the FDPM. The main focus of this study is the evaluation of the two domains for harmonic stability studies, where the model representation of the PED is the main scope. Therefore, it was decided to have a 1:1 representation of the passive components in the two domains. Therefore, additional considerations were found needed.

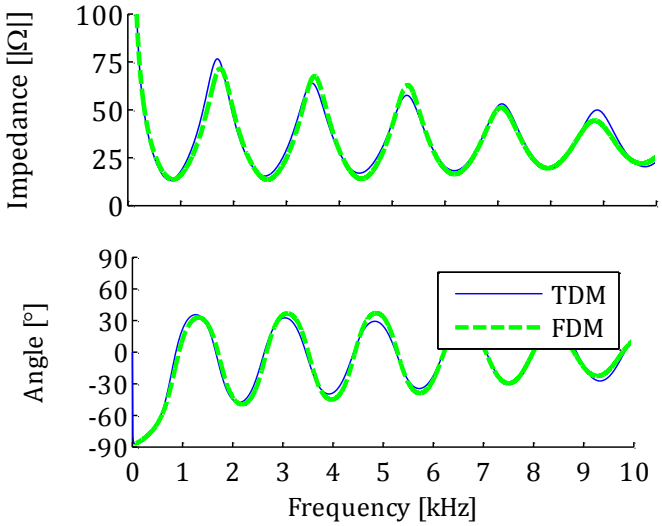

Figure 11-6 Cable input impedance using the FDPM in PSCAD/EMTDC and the equivalent π cable model in MatLab. Z_{load} =10 kΩ.

11.2.2 Cascaded PI Cable Modelling

It is not straightforward to include the distributed nature of the cable parameters in equation 11-4 and 11-5 and the skin effect in according to equation 11-6 in EMTPs (the above mentioned rational function methods should be considered [189]).

A simplistic method for taken into consideration the distributed nature of the parameters is to use a cascaded nominal π-model as shown in Figure 11-7.

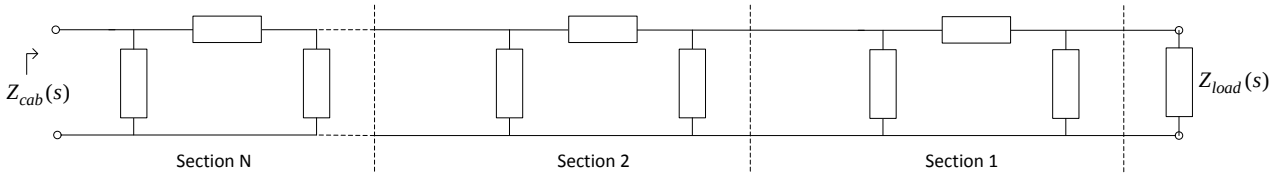

Figure 11-7 Cascaded nominal π cable model.

Figure 11-8a shows the frequency response using the equivalent and the cascaded nominal π cable models (π_{eq} and π_{nom}, respectively) for a 50 km long cable terminated by a resistive load of 10 kΩ. 50 π sections are used in the nominal model. The damping caused by the skin effect is which is not taken into consideration for the cascaded nominal model is the main reason for the discrepancy. As mentioned previously, this frequency dependency is not straightforward to implement in EMTPs. Therefore, a blunt approximation of increasing the value of the series resistance by a factor 10 is used in the nominal model. This approximation yields a quite good correlation between the observed results as shown in Figure 11-8b, especially in the lower frequency range up to a few kilohertz. The approximation is not considered to be affecting the outcome of this work.

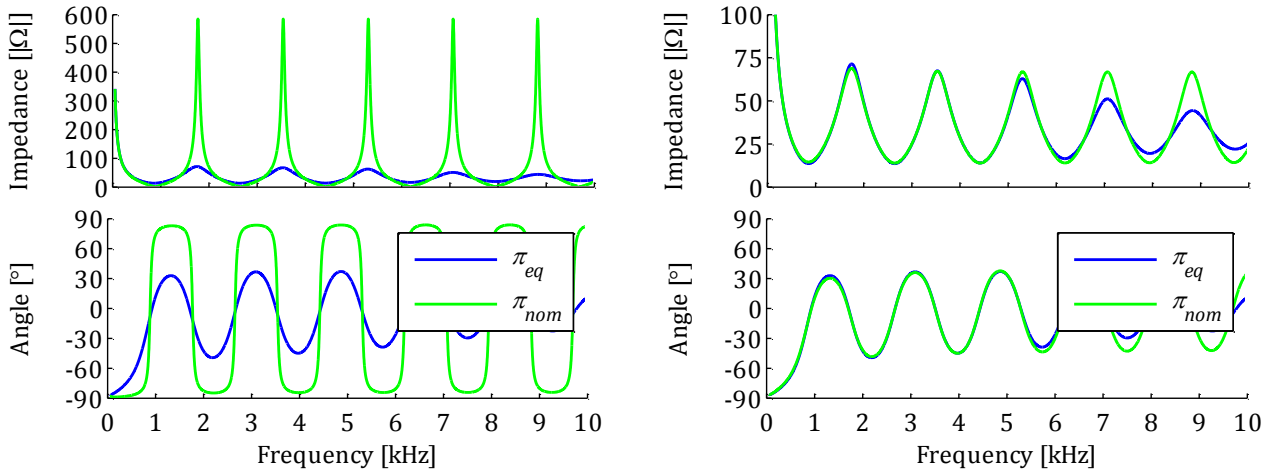

Figure 11-8 Frequency response using the equivalent and the cascaded nominal π cable models (π_{eq} and π_{nom}, respectively) for a 50 km long cable. The cable is terminated by a resistive load of 10 kΩ. 50 π sections are used in the nominal model. Series resistance for nominal cascaded π cable model: a) $r = 1$ p.u. and b) $r = 10$ p.u.

Figure 11-9 shows the frequency response in FDM and in the TDM using 50 cascaded nominal π sections. As can be seen, using the above approximations and simplifications it is possible to model the export cable 1:1 in the two domains, which was required.

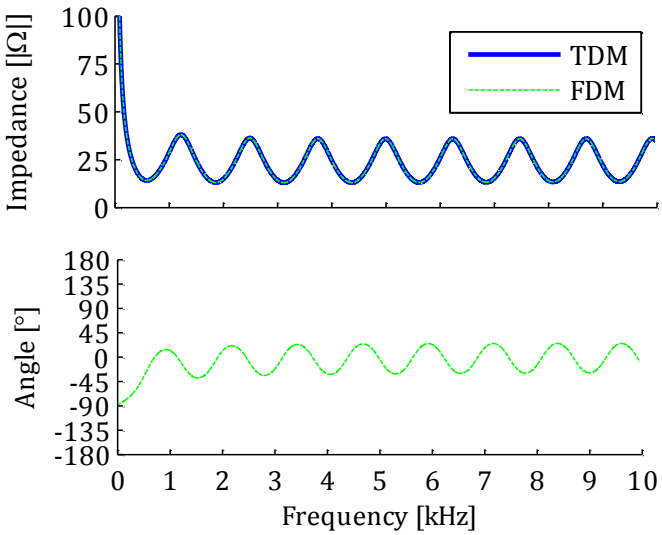

Figure 11-9 The export cable's frequency response in MatLab and PSCAD/EMTDC using 50 cascaded π sections. The simplications done to have the same models in the two domains are considered realistic when using the FDPM as benchmark.

Comparing with the results of the FDPM in Figure 11-6, it is considered that these simplifications provide a realistic cable model, which is possible to model in both the time and frequency domain.

11.3 OWPP Aggregation

The OWPP is normally aggregated in the stability studies. A brief description on how to aggregate the OWPP is given in the following. A more through description is given in [58].

The s^{th} OWPP section cable collection grid consists of a certain number of radials (M_s), where a certain number of WTGs (N_{m_s}) are connected to the m_s^{th} radial as shown in Figure 11-10a. In order to simplify the OWPP for different types of studies, an aggregation of the cable collection grid is suitable, where the complete cable grid impedance is lumped into one equivalent impedance (Z_{MV} in Figure 11-10c). Also the WTGs, transformers etc. contained within the OWPP section should be aggregated [58]. Various aggregation methods exists [21,203,204], which are suitable depending on application (e.g. load flow calculations and stability assessment). An overview of some of the aggregation methods is given in [58], where it is also stated that the aggregation method based on voltage drop is the most suitable for stability studies. This method is therefore applied in this work.

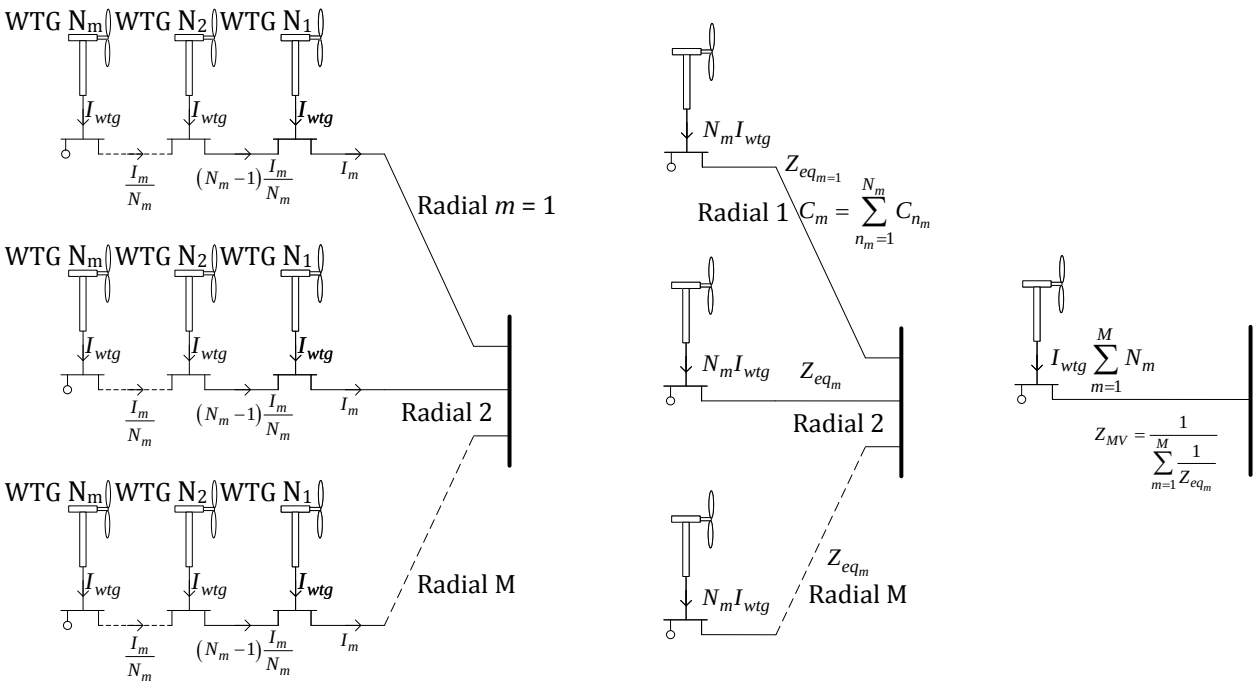

a) Simplified original network.

b) Individual aggregation of the M radials.

c) Aggregation of the M radials.

Figure 11-10 Steps in the aggregation of the cable collection grid of the s^{th} OWPP section.

11.4 Chapter Summary

This chapter has presented the methods for modelling the passive OWPP components in the time and frequency domains.

PART III
System Studies and Conclusion

Chapter 12 of Part III of the dissertation presents the power system studies, which are realised based on the developed models in Part II. Chapter 13 presents a discussion of the findings and how to relate these to industrial applications. Chapter 14 presents the concluding remarks and the list of publications realised within the confines of this Industrial PhD project.

Chapter 12 Harmonic Stability Analysis

This chapter presents the harmonic stability evaluation in offshore wind power plants (OWPPs) employing power electronic devices (PEDs) in the transmission system. The primarily focus of the analysis is the evaluation of conventional and linearized frequency domain analysis methods such as the Nyquist stability criterion against the full time domain model realised in PSCAD/EMTDC. The comparison of the two domains is done for a voltage sourced converter high-voltage direct current (VSC-HVDC) grid connected OWPP, where the validated model of the controllable grid interface (CGI) is used to emulate the HVDC system. Additionally, an analysis of the harmonic stability in a high-voltage alternating direct current (HVAC) grid connected OWPP with a static compensator (STATCOM) located at the grid connection point is carried out in the time domain.

12.1 Overview

As mentioned in Chapter 1, the application of the frequency domain in the stability analysis rises the conceptual challenge of recognising the source and the load (i.e. the plant), as either the grid (in HVAC grid connected OWPPs) or the WTG converters can be treated as the source in the analysis, yielding different results [9]. The challenges become even more relevant in case of HVDC grid connected OWPPs. In this case both the load and the source are actively controlled power system devices. The time domain approach on the other hand provides a holistic approach, without the need to assign the source in the analysis.

Here the aggregated WTGs are taken as the source in the evaluation. The procedure is essentially identical when considering the HVDC as the source in the evaluation and proposed for future work.

The harmonic stability is evaluated for an HVDC grid connected OWPP in section 12.3 and for a STATCOM grid connected OWPP in section 12.4.

Before attending the full system analysis a simple study case is presented in section 12.2, where the time and frequency domain methods are evaluated for a WTG connected to an inductive grid.

12.2 Correlation with Time Domain Model

The frequency domain model (FDM) described in chapter 10 is evaluated against a time domain model (TDM) realised in PSCAD/EMTDC, where the effect of the switching devices has been omitted (the switching devices are included in the full system analyses in section 12.3 and 12.4). An inductive grid with a short circuit power (S_{grid}) twice that of the nominal power of the WTG (S_{WTG}=5 MW = $S_{grid}/2$) is considered as shown in Figure 12-1 is considered.

The comparison is done in the RRF in the time domain. The MatLab Control Toolbox is used in the FDM.

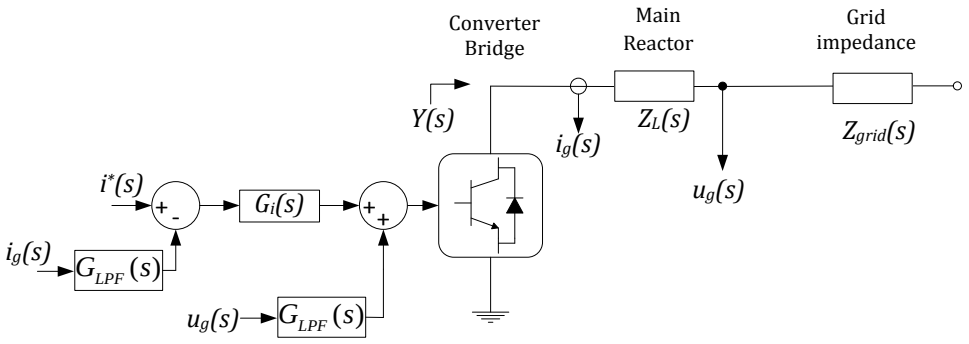

Figure 12-1 Simple system setup.

Based on frequency domain analysis a $G_m \approx 13$ is found for the system in Figure 12-1. Figure 12-2 shows the comparison between the two domains for unit step responses for varying gain factors. K_p is the gain of the proportional-integral (PI) controller and G_{inc}=1,4,8,12 is a multiplied gain factor. A good correlation between the TDM and the FDM can be observed in these stable study cases. The damping is slightly higher in the FDM as can be seen in the case when G_{inc}=12 in the bottom graph in figure b. This could be caused by differences in the calculation methods in the two programs and/or by inaccuracies in the applied parameters.

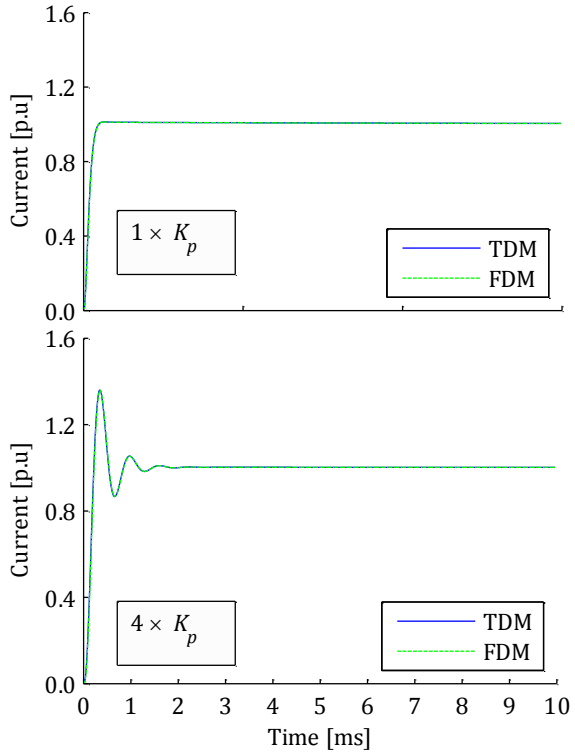

a) Top graph: G_{inc}=1. Bottom grahp: G_{inc}=4.

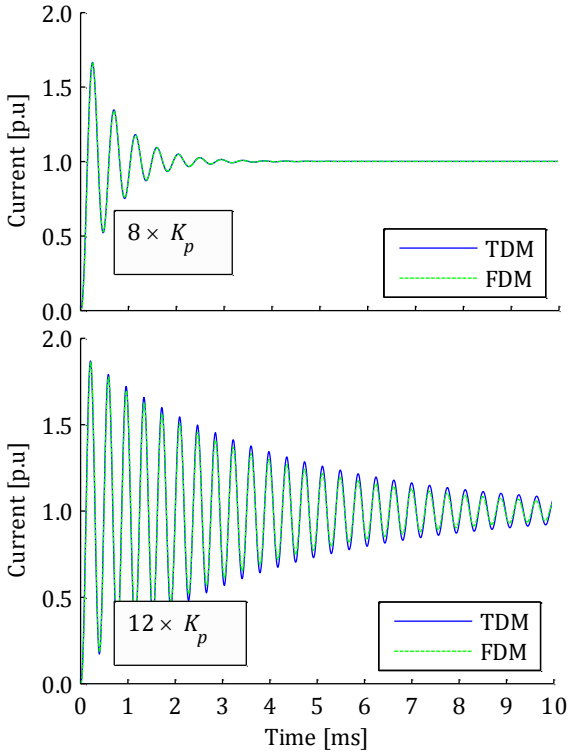

b) Top graph: G_{inc}=8. Bottom grahp: G_{inc}=12.

Figure 12-2 Step responses for TDM and FDM models in the RRF for varying G_{inc}=1,4,8,12.

Figure 12-3 shows the step response for three cases: Stable, marginally stable and unstable (top to bottom) as calculated from the FDM, where $G_m \approx 13$ as described in the above (the actual value of G_m is used in both tools). Although the system is operating at the brink of stability, it can be seen that the results of the two domains are very similar (i.e. the system is stable when $0.98G_m \cdot k_p$ and unstable when $1.01G_m \cdot k_p$). The current calculated in the TDM slowly increases in the middle graph, where the FDM has predicted a marginally stable case.

In real-life, operating at the boundary of stability is of course unacceptable, and the purpose of the study cases presented in Figure 12-2 and Figure 12-3 is to evaluate the agreement between the two simulation tools before considering more complex system studies, with PEDs in the transmission system in section 12.3 and 12.4.

As mentioned, an average model of the converter bridge is assumed in the TDM. Additionally, the control variable limiters used in the final PED models are disabled. Therefore, the current is able to escalate towards infinity (i.e. until the model becomes numerical unstable). This is not the case in real-life and in the models considered in the following. Hence, it is more difficult to observe whether or not the system is unstable or if it is at the verge of instability.

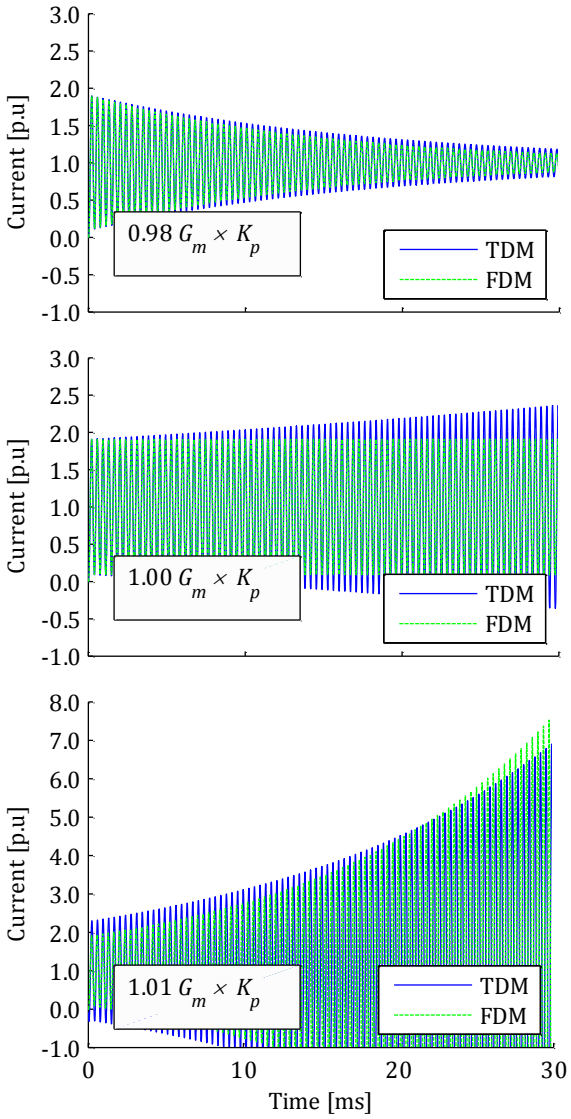

Figure 12-3 Step responses for TDM and FDM models in the RRF.

12.3 Harmonic Stability Analysis in an HVDC Grid Connected OWPP

12.3.1 System Description

The HVDC grid connected OWPP in Figure 12-4 is equipped with 100×5 MW type 4 WTGs. The individual WTG is connected to the 34 kV cable collecting grid (CC) through a WTG transformer (WTG_{TRF}). The CC connects the WTGs to a 500 MW 34/220 kV park transformer ($PARK_{TRF}$) situated at an offshore platform. A 15 km export cable (EC) interconnects the $PARK_{TRF}$ to the HVDC transformer. A 500 MW DC link cable transmit the generated power to an offshore HVDC converter station.

As mentioned, the CGI is used to emulate the HVDC system. This is done as the CGI has been validated in chapter 9. The CGI is scaled up to the ratings of the 500 MW HVDC systems with a DC link voltage of $u_{dc}/2 = \pm 320$ kV.

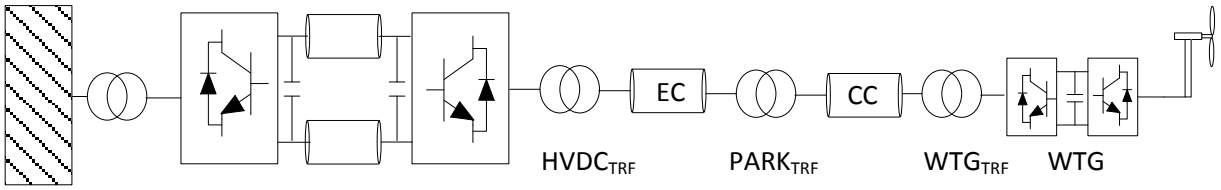

Figure 12-4 Simplified single line diagram of the considered HVDC grid connected OWPP.

12.3.2 Harmonic Stability Evaluation

As previously mentioned, the number of WTGs in service (n_{WTG}) is known to be the main contributor to possible harmonic unstable operating conditions in OWPPs [12,21] and is thus taken into consideration in the stability assessment in this chapter for both the HVDC and the STATCOM grid connected OWPPs. As mentioned in the introduction, the frequency domain approach requires the selection of the source in the evaluation (i.e. either the WTGs or the HVDC). The time domain, on the other hand, provides the complete solution of the overall system stability. Here the aggregated WTGs are taken as the source in the evaluation. The procedure is essentially identical when considering the HVDC as the source in the evaluation and is suggested as future work.

12.3.3 Frequency Domain Analysis

Figure 12-5 shows the frequency response of the admittance seen from the aggregated WTG's terminals, where n_{WTG} is varied in increment of one per iteration from 1 to 100 WTGs in service. The figure provides useful information of the system characteristics. Three resonance spikes are present, located in the lower frequency range (a few hundred Hertz), mid and higher range of the frequencies considered (i.e. from 51 Hz to 2 kHz). Each of these spikes varies both in amplitude and the frequency at which they appear, depending on the number of WTGs in service.

It should be noted that the obtained frequency characteristics in Figure 12-5 are calculated under the assumption that the system is symmetrical (e.g. the involved transformers, cables etc. each present equal phase impedance). In real life, inaccurate cable parameters for example, are unavoidable due to e.g. fabrication errors [205], which will also cause the phase impedances to become asymmetric. Additionally, the admittance seen from the individual WTG is different from that seen from the aggregated WTG due to the asymmetric CC grid system's layout in an actual OWPP. The simplifications caused by the aggregation procedure described in chapter 11 should be evaluated based on comparison with a full representation of the OWPP during the design phase of an OWPP. In [58] it was observed that the influence of the aggregated CC on the frequency response of the OWPP is less pronounced for large OWPPs. The aggregation of the OWPP might therefore have increased credibility in the harmonic stability analysis for very large OWPPs (e.g. for 0.8 GW and above). As stated, this should be evaluated during the OWPP design phase.

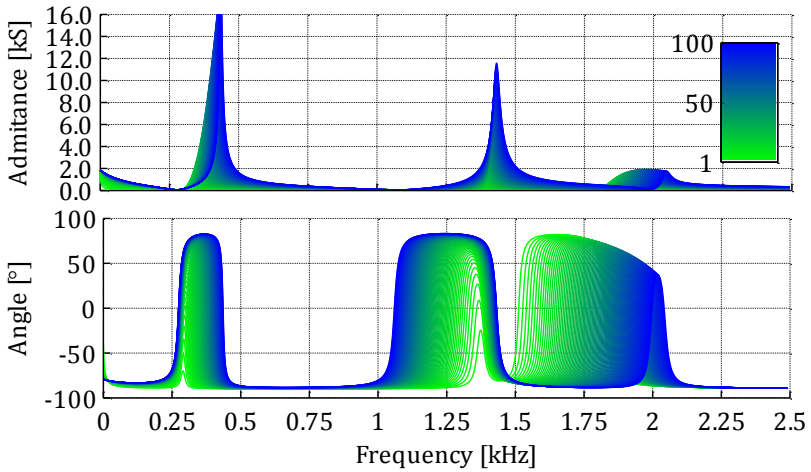

Figure 12-5 Admitance seen from WTG terminal for varying n_{WTG} from 1 (light green) to 100 WTGs (dark blue).

Figure 12-6 and Figure 12-7 show the calculated open loop Nyquist contour when 1st and 2nd order filters are used in the WTG current control system in Figure 12-1, respectively.

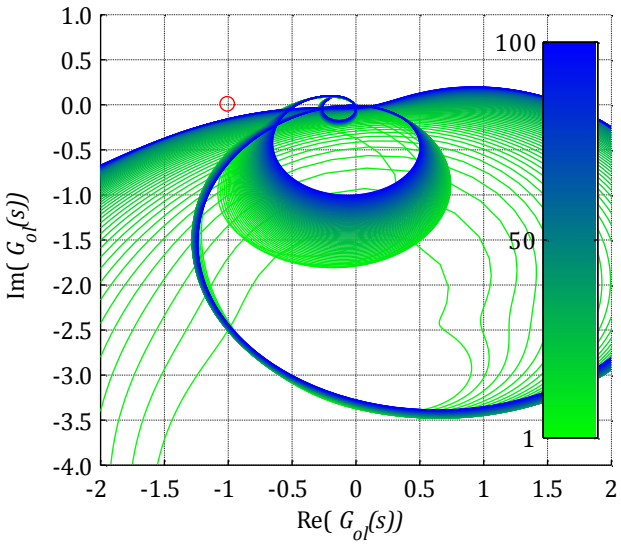

Figure 12-6 Open loop Nyquist contour, employing 1st order low-pass filtering in the WTG control feedback system.

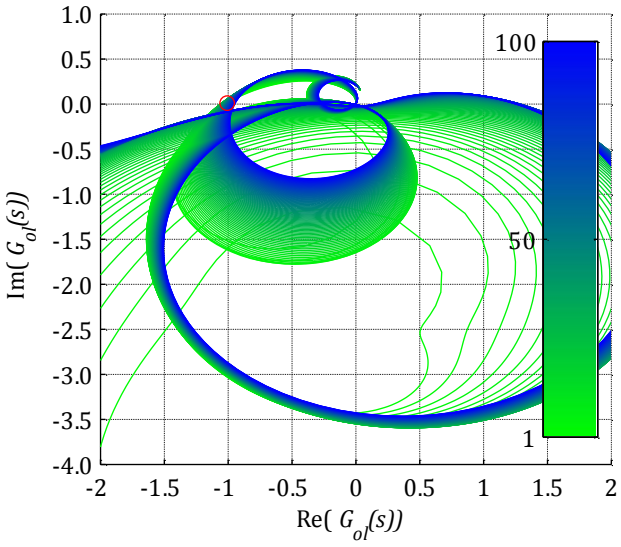

Figure 12-7 Open loop Nyquist contour, employing 2nd order low-pass filtering in the WTG control feedback system.

Figure 12-8 and Figure 12-9 show the corresponding Bode plots. The 1st order filter is used in the HVDC current controller in both cases. From the calculated Nyquist contours in Figure 12-6 and Figure 12-7 it is evident the applied low-pass filtering characteristics are significantly affecting the stability of the system. Comparing the Bode plots in Figure 12-6 and Figure 12-7, it can be noted that the additional phase lag is added in the higher frequency range to the open-loop system in the case with the 2nd order filter is employed.

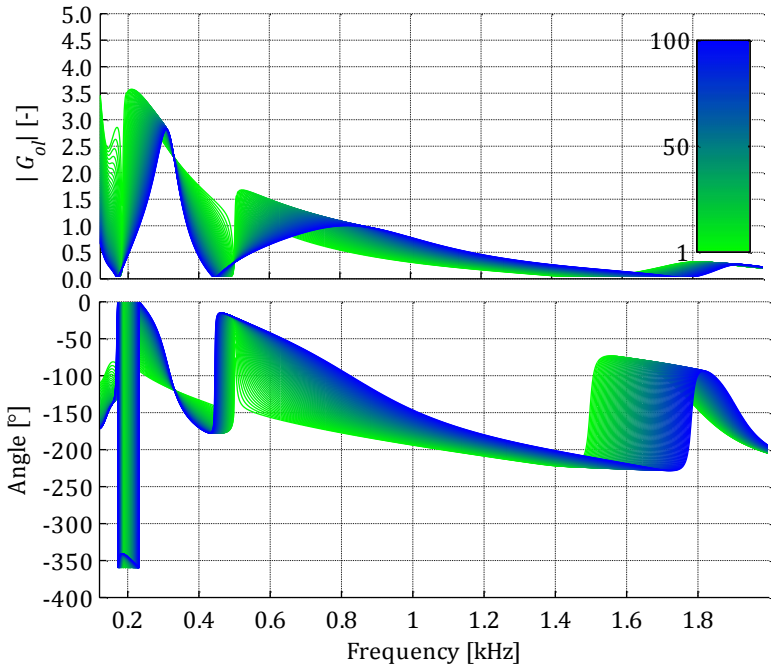

Figure 12-8 Open loop Bode plot, employing 1st order low-pass filtering in the WTG control feedback system.

The GMs for the case with the 2nd order filters in Figure 12-7 and Figure 12-9 would in a real-life OWPP be unacceptable and typically a minimum GM in the range of 1.4 accompanied by a minimum phase margin (PM) in the range 30-45° would be required [58]. Addtionaly, the vector GM (VGM) can be evaluated. The VGM is based on a sensitivity function and can actually detect the frequency the closest to losing the stability [21].

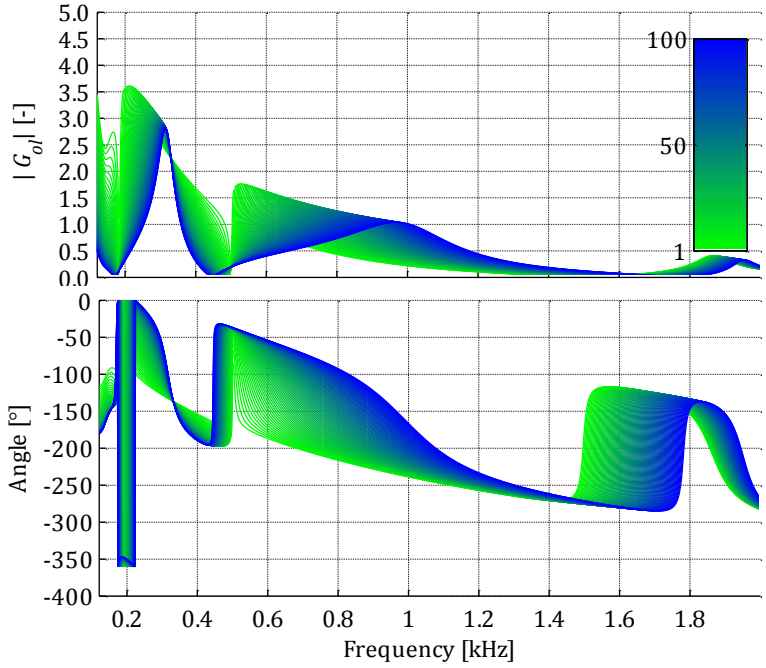

Figure 12-9 Open loop Bode plot, employing 2nd order low-pass filtering in the WTG control feedback system

The additional phase delay caused by the 2nd order filter deteriorate and even causes the system to become unstable for certain operating conditions. The system is unstable when the gain margins (GM) is less than unity, which is the case for n_{WTG} ≤50 WTGs, as seen from the calculated GMs in Figure 12-10.

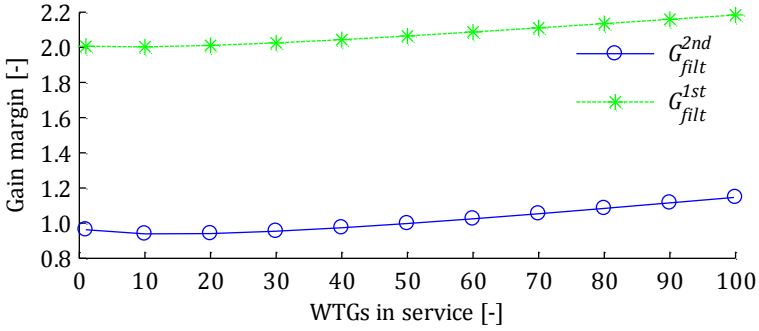

Figure 12-10 Gain margin when n_{WTG} is varied in increment of 10 WTGs/calculation.

The case with n_{WTG}= 50 WTGs in service is considered as the system becomes unstable at this operating scenario. The calculated critical frequency in this case is 833 Hz, when the GM becomes less than unity. A band-rejection filter (BRF) included in the inner current controller is used to improve the WTG's robustness toward this unstable operating condition as shown in Figure 12-11. Figure 12-12 shows the calculated Nyquist contours with and without the stability BRF included (blue and green curves, respectively). Introducing the BRF significantly improves the stability. A GM of 1.4 is observed for n_{WTG}= 50 WTGs, which is considered appropriate.

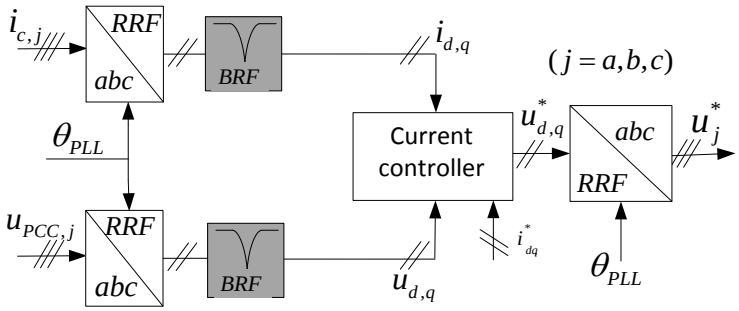

Figure 12-11 Positive sequence inner current controller equipped with the BRF for attenuating possible interaction with the electric system external to the PED. The negative sequence controller is not shown in the figure, but has a similar structure.

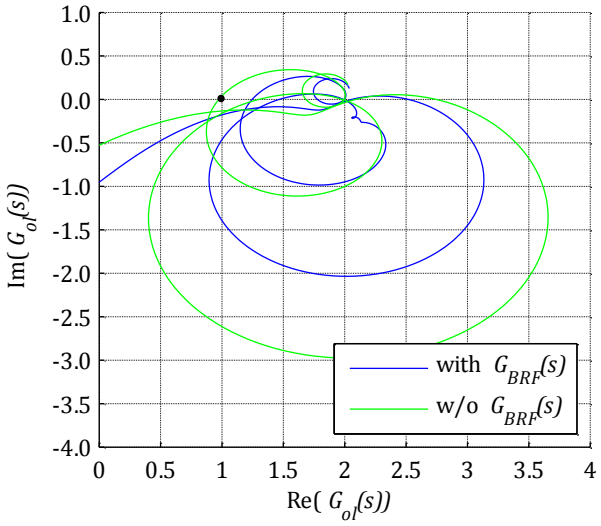

Figure 12-12 Open loop Nyquist plot with and without the BRF in the direct chain of the current controller.

Figure 12-13 shows the obtained Nyquist contour plot when the BRF is employed in the current controller for all possible number of WTGs in service, where the system is found stable for all cases.

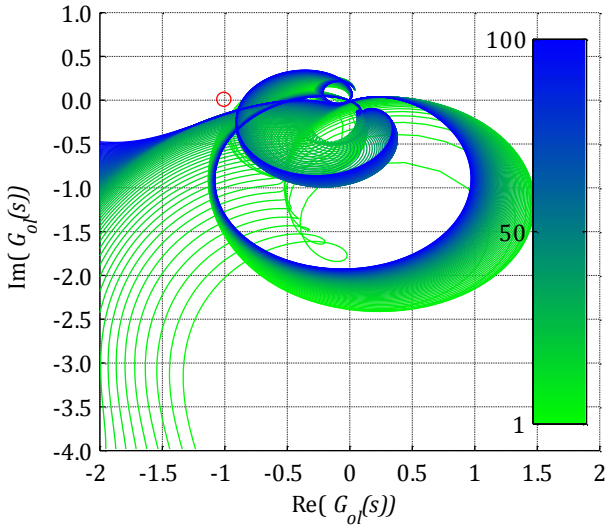

Figure 12-13 Open loop Bode plot with and without the BRF in the direct chain of the current controller.

The calculated GM for the two study cases when the 2nd order filter is considered is shown in Figure 12-14, where the stability BRF is included for the blue trace and the green trace is the case without the stability filter. The introduction of the BRF significantly improves the GM for $n_{WTG} \leq 50$ WTGs, whereas the GM is comparable for the two cases for higher number of n_{WTG}.

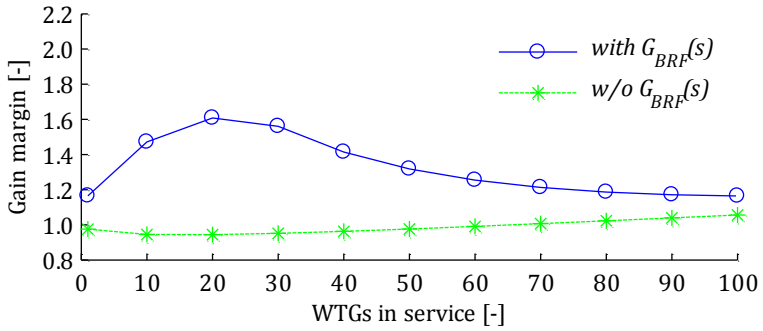

Figure 12-14 Gain margin when n_{WTG} is varied in increment of 10 WTGs/calculation.

12.3.1 Time Domain Analysis

The frequency components of interest in the harmonic stability analysis are rarely interconnected with the main frequency component and with the sampling period, hence errors are encountered due to spectral leakage [58]. In the evaluation of a time domain signals, it is practical to limit the time over which the signal is observed, which especially is useful for non-stationary signals, which may be divided into short segments of a quasi-stationary nature with an implicit infinite periodicity. This is referred to as windowing [67, 206]. The effect of the spectral leakage can be reduced by changing the form of the window, especially if the amplitude of the window is reduced toward zero at the boundaries of the window. The Hanning (or cosine-squared) window defined as in equation 12-1 is used, where T is the sampling window, $T = 200$ ms = 10 cycles of the fundamental frequency is used, yelding a resolution of 5 Hz/bin.

$$W(t) = \frac{1}{2}\left(1 - cos\frac{2\pi t}{T}\right) \quad -\frac{T}{2} < t < \frac{T}{2} \qquad 12\text{-}1$$

Window functions do not accurately determine the inter-harmonic components, especially if multiple are closely spaced in the frequency domain. The use of the zero padding technique can result in a much more accurate determination of the actual inter-harmonic frequency component magnitudes and frequencies [67, 206]. As an example, Figure 12-15 shows the fast Fourier transformation (FFT) results with a square window (green) and with the Hanning window using a 4 fold zero padding (blue) for one of the time domain study cases described in the following.

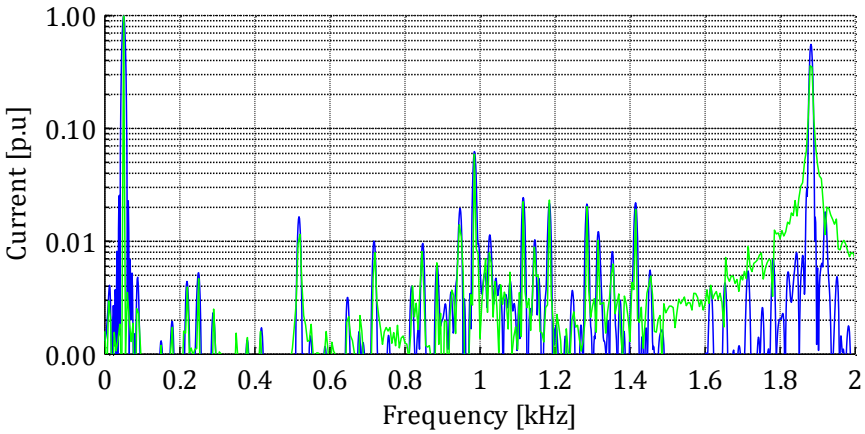

Figure 12-15 FFT results with a square window (green) and with the Hanning window using a 4 fold zero padding (blue). The resolution is 5 and 1.25 Hz/bin for the green and blue curve, respectively.

The use of the zero padding technique can result in a much more accurate determination of the actual inter-harmonic frequency component magnitudes and frequencies, which especially is the case in the higher frequency range in the figure.

Stability Evaluation without Inclusion of Active Stability Filtering

In order to correlate the above frequency domain results to the time domain model, Figure 12-16 shows the simulated voltage and currents at the 34 kV side of the WTG transformer for n_{WTG}=50 WTGs when using the 2nd order low-pass filter. As predicted by the Nyquist and Bode plots in Figure 12-7 and Figure 12-9, respectively, the time domain model is unstable for this operating scenario. The unstable system's variables would increase toward infinity if there were no limiting factors present such as e.g. the DC-link voltage of the converters. It is therefore challenging to access whether the system is stable or not, such as the considered operating scenario of 50 WTGs in service in Figure 12-16. It is assumed in the following that the system is unstable when the noise level is comparable with Figure 12-16. In section 12.4 the total harmonic and inter-harmonic distortion indexes (THD and TIHD, respectively) will be introduced in the time domain evaluation of the stability of an HVAC grid connected OWPP, which provide some useful identification of a possible unstable operating condition.

Figure 12-17 shows the FFT results of Figure 12-16 (at steady-state) shows that the dominating frequency component (approximately 860 Hz) is comparable with the 833 Hz frequency component observed from the frequency domain. Hence, a good correlation exists between the two domains.

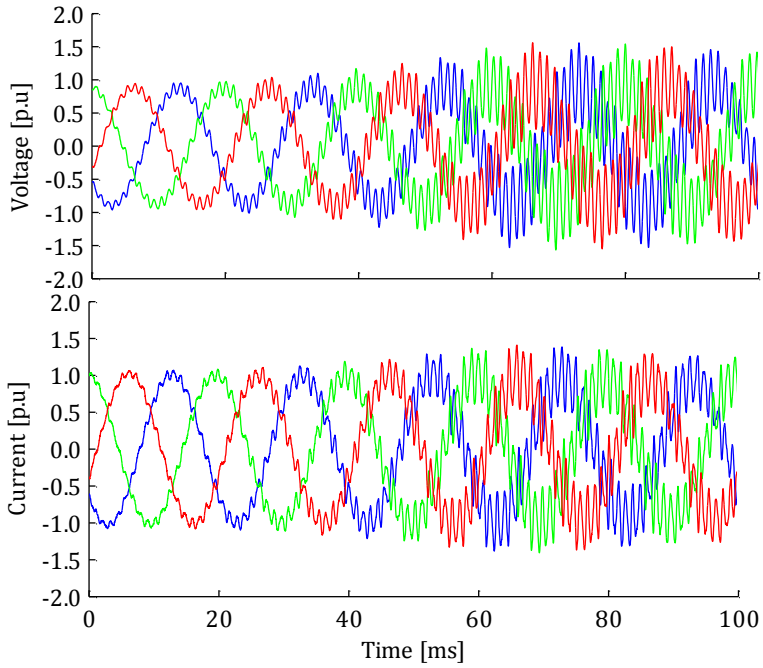

Figure 12-16 Time domain waveforms at the 34 kV side of the WTG transformer for n_{WTG}=50 WTGs.

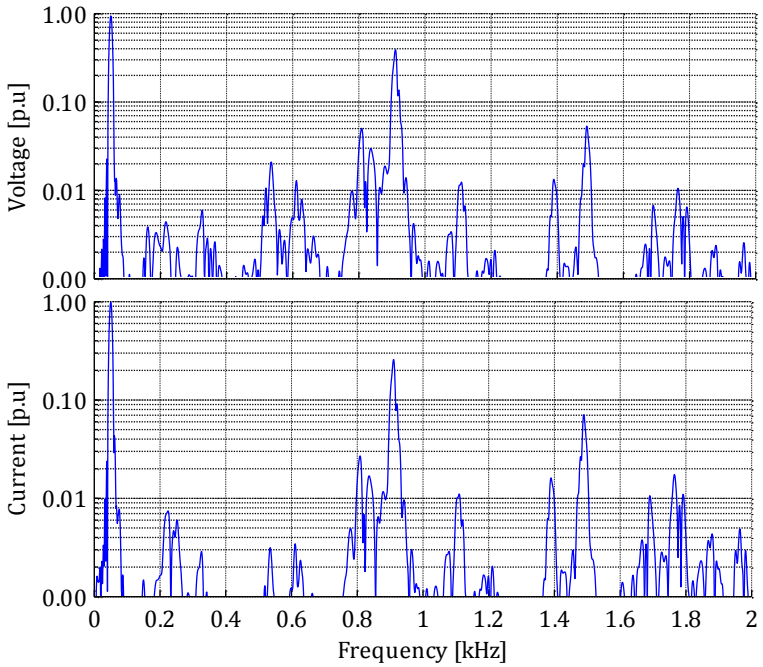

Figure 12-17 FFT plot of the phase A voltage and currents in Figure 12-16.

Stability Evaluation with the Inclusion of Active Stability Filtering

In the preceding frequency domain evaluation, it was possible to stabilise the system by the introduction of the stability BRF in Figure 12-11, see e.g. Figure 12-13 and Figure 12-14.

However, the inclusion of the BRF in the time domain model do not yield a stable system as can be seen in Figure 12-18 and Figure 12-19, where a 0.2 and 0.5 p.u frequency component located at 1882 Hz is superimposed on the voltage and current waveforms, respectively as can been seen in Figure 12-19. This frequency correlates well with the highest resonance in the admittance plot in Figure 12-5. However, the value of the open loop transfer function G_{ol} at 1882 Hz is $0.13\angle -230°$ obtained from the frequency domain model, which is far from the unstable region (i.e. neither the minimum GM, PM or VGM are violated).

There are therefore some limitations to the frequency domain, as it only considered valid in the frequency range well below the switching frequency [8]. Care should therefore be exercised when using the frequency domain in the stability evaluation.

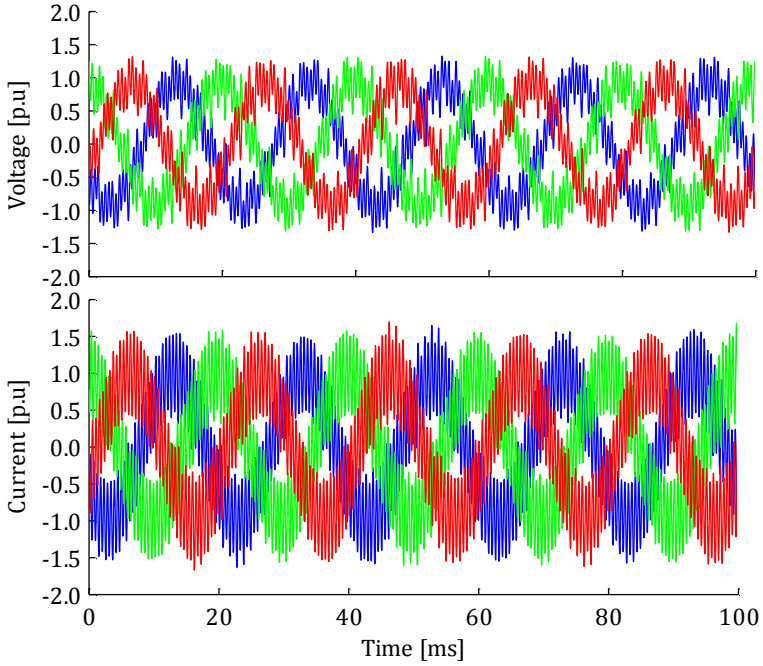

Figure 12-18 Time domain waveforms at the 34 kV side of the WTG transformer for n_{WTG}=50 WTGs employing active filtering.

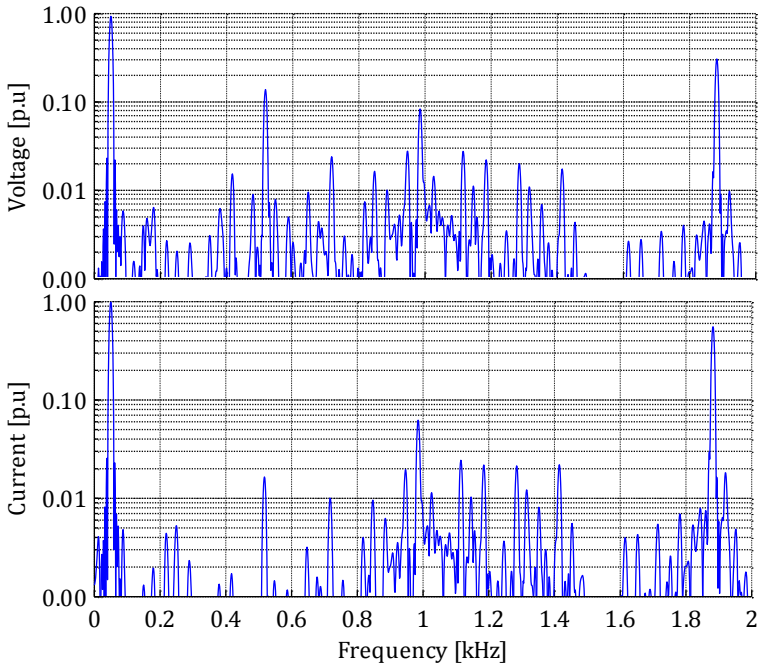

Figure 12-19 FFT plot of the phase A voltage and currents in Figure 12-18.

Stability Evaluation with the Inclusion of Additional Active Stability Filtering

The further inclusion of a BRF tuned 1882 Hz is considered as shown in Figure 12-20. The application of the two BRFs in the current control system successfully suppresses the new instability observed in the time domain in Figure 12-18 and Figure 12-19. The results with the additional BRF are reported in Figure 12-21 and Figure 12-22.

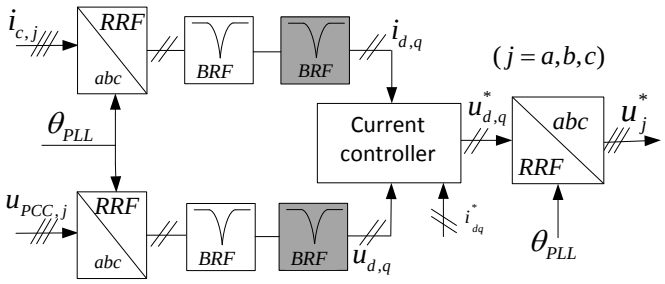

Figure 12-20 Positive sequence inner current controller equipped with the BRF for attenuating possible interaction with the electric system external to the PED.

The frequency components present in Figure 12-19 are practically eliminated in Figure 12-22, demonstrating the successful application of active filtering.

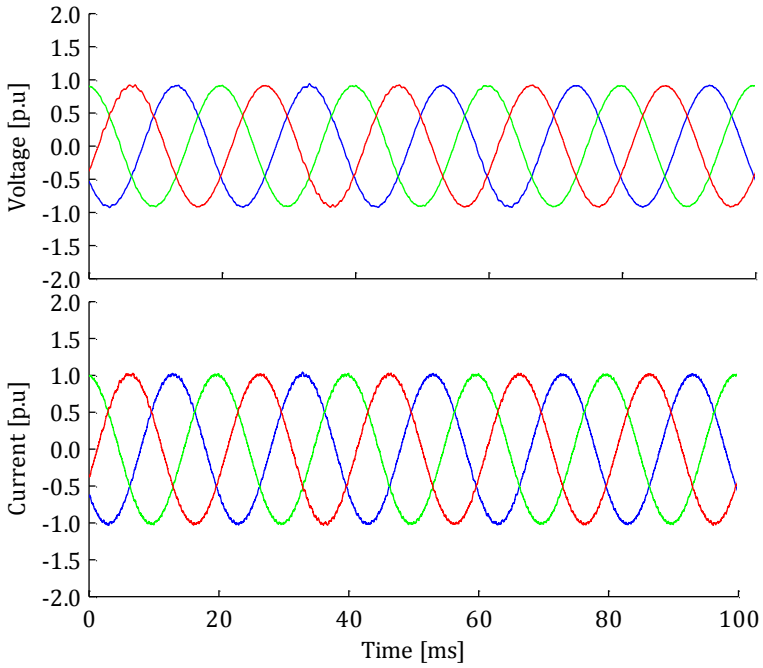

Figure 12-21 Time domain waveforms at the 34 kV side of the WTG transformer for n_{WTG}=50 WTGs employing additional active filtering.

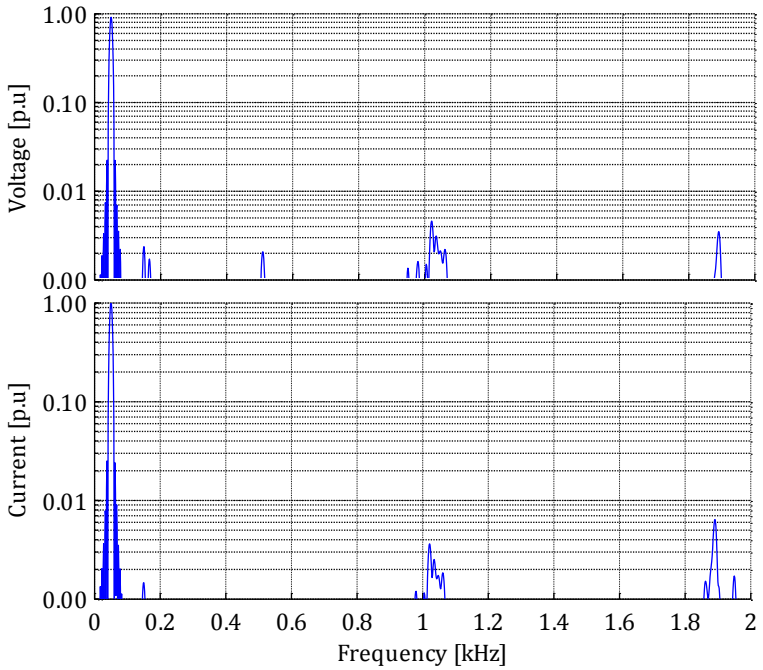

Figure 12-22 FFT plot of the phase A voltage and currents in Figure 12-21.

12.4 Harmonic Stability Analysis in an HVAC Grid Connected OWPP with a STATCOM Situated in the Grid Connection Point.

The harmonic stability evaluation of the HVDC grid connected OWPPs in the previous section demonstrated generally good correlation between the time and frequency domain methods. The stability evaluation in the STATCOM grid connected OWPP is only carried out in the time domain using the validated generic models of the STATCOM and the WTG in chapters developed in chapter 6 and 8, respectively. The THD and TIHD are taken into consideration in the time domain evaluation, described in section 12.4.1.

12.4.1 Total Inter-Harmonic Distortion Index

The THD and TIHD are calculated according to IEC 61000-4-7 [207], where the sampling interval is fixed at 10 cycles for fundamental frequency ($f_1 = 50$ Hz). Thus frequency bins in the discrete spectrum estimated using discrete Fourier transform are with $\Delta f = 5$ Hz resolution. The standard proposes to group the spectra into harmonic and inter-harmonic subgroups (HSGs and IHGs, respectively). The HSG for the n^{th} harmonic ($n = 2,3, \dots N = 50$) consists of the $n \cdot f_1$ harmonic component and the two adjacent frequency bins (e.g. {95, 100, 105 Hz} from the HSG of second harmonic ($n = 2$)). Similarly, the seven frequency bins {60, 65,..., 90 Hz} from the first IHG ($n = 1$). The THD is defined as the ratio of the RMS value of the harmonic subgroups (HSGs) to the RMS value of the f_1 component (U_1) as in equation 12-2a, where $U(n \cdot f_1 + i \cdot \Delta f)$ is the RMS value of the $n \cdot f_1 + i \cdot \Delta f$ frequency bin. The TIHD is calculated similarly, as in 12-2b.

$$THD = \frac{\sqrt{\sum_{n=2}^{N}\left(\sqrt{\sum_{i=-1}^{I=1}[U(n \cdot f_1 + i \cdot \Delta f)]^2}\right)^2}}{U_1} = \frac{\sqrt{\sum_{n=2}^{N}\left(\sum_{i=-1}^{I=1}[U(n \cdot f_1 + i \cdot \Delta f)]^2\right)}}{U_1} \quad \text{12-2a}$$

$$TIHD = \frac{\sqrt{\sum_{n=1}^{N}\left(\sum_{i=2}^{I=8}[U(n \cdot f_1 + i \cdot \Delta f)]^2\right)}}{U_1} \quad \text{12-2b}$$

12.4.2 System Description

A simplified representation of London Array OWPP has been implemented in PSCAD/EMTDC, as will be briefly described. Only one of the four sections is modelled, as shown in Figure 12-23. The WTGs located in the section are aggregated into one equivalent type 4 WTG, employing positive sequence current control in the RRF. The model is described in chapter 8.

The 34 kV cable collection grid is aggregated into one nominal PI section with a length of 1 km, which is considered sufficient for the frequency range considered in the current work. The approximately 50-km-long 150 kV export cable is modelled using the Frequency Dependent Phase Model (FDPM), which is the most accurate model available in all EMTP tools [193,194] as stated in chapter 11. The 400 kV grid is represented by a 22 GVA Thevenin equivalent with $X/R = 22$, given in the as-built documentation of London Array OWPP.

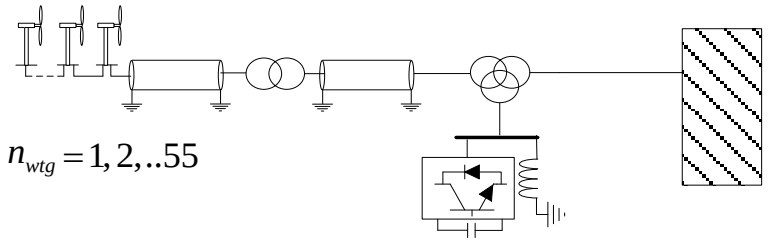

Figure 12-23 Simplified single line diagram of one of the four sections of London Array OWPP, implemented in PSCAD/EMTDC. The number of WTGs in service is varied from $n_{WTG} = 1$ to 55 in the analysis.

12.4.3 Harmonic Stability Evaluation

An analysis of the harmonic stability in an HVAC grid connected OWPP with a STATCOM located at the point of common coupling (PCC) is presented in this section. As previously mentioned, the analysis is only carried out in the time domain. The stability analysis is done by performing simulation with the BRF in Figure 12-24 activated ($G_{BRF}(s)$ from equation 10-8 on page 114 and deactivated ($G_{BRF}(s) = 1$).

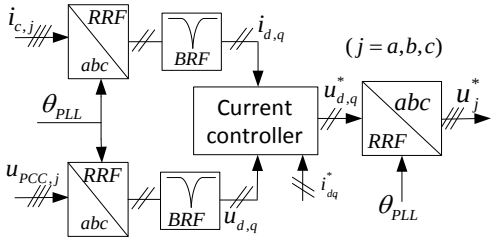

Figure 12-24 Positive sequence inner current controller equipped with the BRF for attenuating possible interaction with the electric system external to the PED.

The focus of the analysis for the HVDC grid connected OWPP was the waveforms at the high-voltage side of the aggregated WTG transformer in section 12.3. This section focusses on the STATCOM's generated waveforms in order to highlight the application of the developed modular multi-level cascaded converter (MMCC) STATCOM.

A number of study cases have been realised on the model in Figure 12-23, where the number of WTGs in service is varied from $n_{WTG} = 1$ to 55 with and without the BRF in the WTG's current controller. As described more carefully in the following, the STATCOM's waveforms become highly distorted for $n_{WTG} > 35$ WTGs. As an example, Figure 12-25 shows the STATCOM's phase A leg voltage and current with the BRF activated and deactivated (subscripts BRF and Non-BRF-respectively) for n_{WTG}= 40 WTGs in service. The waveforms are significantly distorted when the BRF is disabled, whereas the BRF efficiently truncates the distortion.

Calculating the THD indexes over 10 cycles on the converter leg voltages in Figure 12-25 results in THD_{BRF} = 0.083 p.u and $THD_{Non\text{-}BRF}$ = 0.077 p.u for the two cases. This is very misleading, as observed from the figure. Calculating the total inter-harmonic distortion (TIHD) indexes yields $TIHD_{BRF}$ = 0.065 p.u and $TIHD_{Non\text{-}BRF}$ = 0.124 p.u, which is in better correlation with Figure 12-25. The THD index alone does therefore not indicate possible harmonic controller interaction. The TIHD index will therefore be introduced in the stability assessment.

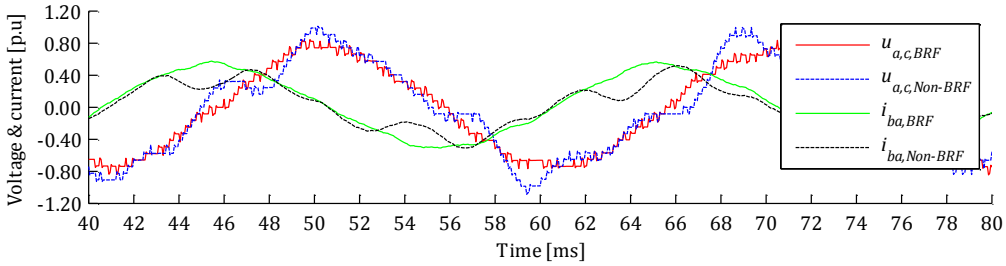

Figure 12-25 Phase A leg voltage and current with the BRF activated and deactivated for n_{WTG} = 40 WTGs.

Figure 12-26 shows the simulated SM capacitor voltages with the BRF activated and deactivated (top and bottom, respectively) for 500 ms. In both cases the SM voltages are in general well centred around the reference value, whereas there is some divergence in the case where the BRF is disabled. The controller interaction between the WTGs and the STATCOM therefore deteriorates the controllability of the internal dynamics of the STATCOM, implying that simplified STATCOM models such as those outlined in chapter 6 cannot directly be used to accurately assess the controller interaction between multiple PEDs, where the MMCC technology is applied. According to the authors' experience it is not straightforward to derive the transfer function between the n^{th} SM voltage and the SM's control signal ($u_{dc,j,n}$ and $u^*_{j,n}$, respectively) in Figure 6-2 on page 69. This relies on a number of simplifications and omissions and is considered outside the scope of the current. This therefore highlights the need to not only perform the harmonic stability assessment in the frequency domain, but also to perform a specified number of study cases in the time domain, as described in section 12.3.

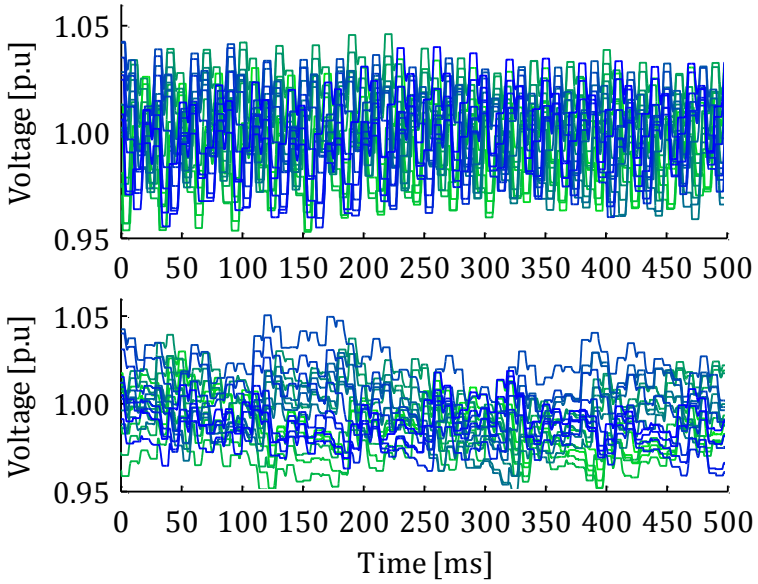

Figure 12-26 SM voltages for phase A leg with BRF enabled and disabled (top and bottom, respectively).

In order to correlate the harmonic stability of the OWPP with n_{WTG}, Figure 12-27 shows the calculated THD_{BRF} and $THD_{Non\text{-}BRF}$ (top figure) and $TIHD_{BRF}$ and $TIHD_{Non\text{-}BRF}$ (bottom figure). A resolution of Δn_{WTG} = 5 WTG/bin is used. Furthermore, the case with n_{WTG} = 36 WTGs is also included, as this is where the controller interaction becomes critical, as can also be noted from the spike at $TIHD_{Non\text{-}BRF}(36)$ in the bottom graph in Figure 12-27.

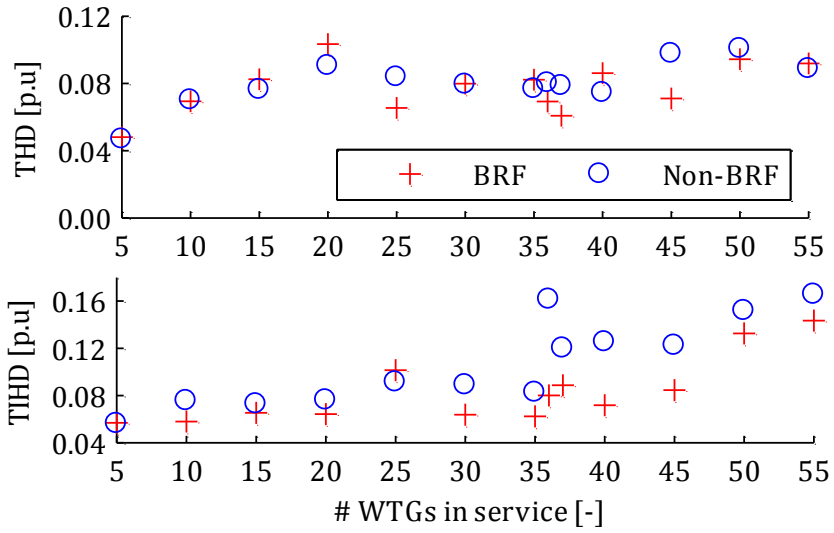

Figure 12-27 Calculated THD (top) and TIHD with BRF enabled and disabled (red and blue, respectively).

There is a relatively good correlation between the THD_{BRF} and $THD_{Non\text{-}BRF}$ for all considered cases up to n_{WTG}= 55 WTGs, which again implies that the THD index alone is insufficient in the harmonic stability evaluation. A similar correlation between $TIHD_{BRF}$ and $TIHD_{Non\text{-}BRF}$ is observed for n_{WTG}≤ 35 WTGs. The $TIHD_{BRF}$ is relatively constant for n_{WTG} ≤ 45. The $TIHD_{BRF}$ approaches $TIHD_{Non\text{-}BRF}$ for n_{WTG}> 45, indicating that the BRF is not capable to supress the controller interaction for this range of n_{WTG}. The harmonic impedance of the OWPP ($Z_{OWPP}(\omega, n_{WTG})$) and the corresponding resonance frequency ($\omega_r(n_{WTG})$) are functions of n_{WTG}. The high number of n_{WTG} most likely causes $\omega_r(n_{WTG} \geq 50\text{WTG})$ to be shifted away from $\omega_{n,BRF}$, meaning that the BRF is not capable of affectively attenuating the resonance. Frequency domain techniques would be useful to assess the frequency-dependent characteristics and the change in resonances. The $TIHD_{BRF}$ could be improved by e.g. increasing the bandwidth of the BRF, which might deteriorate the stability at other frequencies and is therefore not desired [58]. Another viable option would be to apply adaptive BRFs in the WTG controller [58]. The inclusion of BRFs in the STATCOM control system could also be considered. The studied system has in this work been one section of the LAOWPP, where the average number of installed WTGs per section is $175/4 \simeq 45$. Based on Figure 12-27, it can therefore be concluded that the OWPP section is stable for all possible number of n_{WTG}, when using the BRF tuned at 118 Hz in the WTG and considering that generic models have been used to represent both the aggregated WTG and the STATCOM. Furthermore, the highest possible available short circuit power at the PCC has been used in this work. It is therefore also necessary to assess the harmonic distortion as a function of short circuit power in order to assess the overall stability of the system. The possible effect of the remaining three OWPP sections should also be investigated. The purpose of this section has been to investigate the application of time domain analysis in the harmonic stability assessment and not the actual stability of the system, which is suggested as future work.

12.5 Chapter Summary

This chapter has addressed the harmonic stability in OWPPs with PEDs in the transmission system. The focus has been on the evaluation of conventional and linearized frequency domain analysis methods such as the Nyquist stability criterion. The evaluation has been conducted using time domain simulations in PSCAD/EMTDC with validated model representations of the WTG, the MMCC STATCOM and the CGI (emulating an HVDC system), including the switching devices in the PEDs.

The chapter has demonstrated good correlation between the time and frequency domain methods for the stability analysis. However, limitations of the frequency domain were observed when resonances at higher frequencies exist (i.e. near the switching frequency and above the bandwidth of the current controller). Therefore, it is proposed to conduct the analysis primarily in the frequency domain. Once all the considered operating scenarios are covered (typically in the excess of 1000) a few cases should be selected and repeated in the time domain, which is both more challenging and more time consuming than the frequency domain method.

It was shown that the undesirable controller interaction between the WTGs and the STATCOM deteriorates the controllability of the internal dynamics of the MMCC STATCOM.

It was found that the TIHD index according to IEC Standard 61000-4-7 is useful to assess possible and undesired control interaction between the PEDs in OWPPs. The THD index, on the other hand, is found to contain very little information on possible PED controller interaction.

It was shown that an application of active filtering in the WTGs by means of BRF (i.e. notch filter) in the main control chain can potentially reduce the harmonic emission and improve the overall stability in OWPPs without interfering with the OWPP overall design. This can be achieved by providing additional damping or shifting the resonance frequencies. Improving the PED controllers' rejection capability called active damping is a certain type of active filtering. The converter may be controlled adaptively or tuned to suppress selected harmonic components. The application of active filtering was demonstrated for OWPPs with a STATCOM or an HVDC system located in the transmission system. The active filtering was found to improve the internal dynamics of the MMCC STATCOM.

Chapter 13 Recommended Practice for Harmonic Stability Evaluation in Wind Power Plants

The scope of this Industrial PhD project has primarily been to investigate the best possible way(s) to perform the harmonic stability studies in high-voltage alternating and direct current (HVAC and HVDC, respectively) grid connected offshore wind power plants (OWPPs). This chapter outlines the various OWPP system design studies and put forward a proposal for a "best practice" in the harmonic stability evaluation in OWPPs. The best practice is based on the knowledge sharing available when working with colleagues at DONG Energy Wind Power (DEWP), as well as the experience gained working on this project. These findings/recommendation can be incorporated in the design of future OWPPs employing power electronic devices (PEDs) in the transmission system.

13.1 System Design Studies in OWPPs

A number of studies such as load flow analysis, fault level, reactive power control and optimisation are done in the OWPP design phase. Furthermore, the level of the background harmonics is studied and possible harmonic amplifications are investigated and mitigated based on a filter design study. Additional studies are needed for the complete design of the OWPP, such as protection, insulation coordination, harmonic stability and switching transient studies. These specialised studies require valid final design data of the involved power system components. For example, the frequency characteristic of the WTG's current control system is needed in the harmonic stability evaluation in order for the study to valid. Such data is typically delivered after the procurement phase of the OWPP project.

13.2 Uncertainties in the Harmonic Stability Evaluation

A number of uncertainties are inherent in the OWPP's harmonic stability evaluation, including simplified models of the PEDs, the passive components such as transformers and cables. Additionally there are tolerances to all relevant components. The OWPP is typically aggregated in the design study. This might result in a potential risk as a possible unstable operating condition might not be observed as it is not modelled due to the simplifications needed in the aggregation. The chance of this is limited by also calculating the stability margins for a discrete number of study cases in a full model of the OWPP. A full model will be available from the load flow studies. The frequency dependent characteristics of the external power system provided by the TSO also add to the uncertainty of the obtained results in the harmonic stability evaluation. This is simply because the provided data is only applicable to a discrete number of operating scenarios and is based on planned expansions of the power system within the OWPP's lifetime.

The work presented in this dissertation has demonstrated good correlation between the time and frequency domain methods for the stability analysis. However, limitations of the frequency domain were observed when resonances at higher frequencies exist (i.e. near the switching frequency and above the bandwidth of the current controller). There are therefore some uncertainties in the harmonic stability evaluation. The question is whether the time or the frequency domain method provide the most accurate and trustworthy picture of the stability in the actual OWPP. As previously mentioned, it is sensible to apply the frequency domain in the primary stability evaluation and then repeat the analysis for a selected few operating conditions using detailed time domain simulation studies as a second opinion tool, see also Chapter 12.

13.3 PED Modelling for Harmonic Stability Studies

Most PED suppliers are generally concerned about minimal disclosure of the characteristics of their product. For this reason both the time and frequency domains models are delivered either as object code or in a table format, which then do not provide the complete description of the PED. This is reasonable if the model has been tested comprehensively and is in a mature state. However, the lack of information makes it less straightforward to diagnose problems encountered during the application of the model. All problems need to be solved by the model developer, regardless the complexity of the modelling issue. Reference [157] advocates the use of generic models in the large-scale power system stability studies. Reference [157] furthermore describes many advantages of applying generic models for these type of studies. On the other hand, there is a need to have specific models of the PEDs for local, small-scale harmonic stability studies in the final system evaluation in e.g. OWPPs. However, as previously mentioned, it is the author's opinion that generic models, such as those developed in this project, are useful in the preliminary design studies of OWPPs with and without employment of PEDs in the transmission system. It would be useful to include a paradigm for the modelling of the PEDs for harmonic stability studies in time and in frequency in relevant standards related to the modelling of the PEDs such as e.g. IEC 61400-27 standard [140] for WTG models and the Cigré WG B4-57 Technical Brochure 604 [208] for the HVDC system.

13.4 Recommendation for Harmonic Stability Evaluation in OWPPs

A proposal for best practice in the harmonic stability evaluation in OWPPs is presented in the following. The best practice is based on the knowledge sharing available when working with colleagues at DEWP, as well as the experience gained working on this project. These findings/recommendation can be incorporated in the design of future OWPPs employing PEDs in the transmission system.

13.4.1 Involvement of Relevant Parties

All relevant parties (the TSO, the OWPP developer and the PED manufacturers (of the WTGs and the PED in the transmission system)) should be involved at an early stage of the OWPP project. DEWP has found through experience that a close collaboration between the relevant parties can be very constructive.

The TSO should provide data on the frequency dependent characteristics of the power system's impedance ($Z_{grid}(f)$), seen from the grid connection point of the OWPP. As discussed in Chapter 11, a family of impedance loci plots are typically calculated by the TSO and provided to the OWPP developer. This simplifies e.g. the filter design at the onshore substation [56]. Based on DEWP's experience, this is not sufficient for the harmonic stability evaluation, where discrete values at discrete frequencies (e.g. at 1 Hz resolution) is preferred for a certain number of operating scenarios of the external system. Z_{grid} is by the TSO found by performing a frequency sweep in the TSO's power system simulation tool (e.g. DigSILENT PowerFactory) and provided to the OWPP developer in a look-up table format.

It is advisable for the possible PED suppliers to be actively involved in the technical requirements specification process, which is defined by the OWPP developer. This would enable the OWPP developer to define realistic specifications, which can be met by the PED supplier. It is furthermore recommended that the PED model development for harmonic stability (as well as for the other system studies defined in section 13.1) should be carried out in close collaboration between the OWPP developer and the PED supplier, in order to expedite the compliance evaluation of the OWPP.

The collaboration would limit the possibility of misunderstandings in the model specifications, as well as the OWPP developer could provide useful feedback based on the experience gained using the model which can be taken into account by the PED supplier in the following model update.

It is advantageous at an early stage of the OWPP design to agree on the format, in which the PED models are provided (e.g. simulation platform, look-up table and model transparency). For this purpose e.g. the IEC 61400-27 standard [140] can be applied for the WTG models and the Cigré WG B4-57 Technical Brochure 604 [208] can be considered for the HVDC system. An agreement between the OWPP developer and the PED supplier on how the supplier should evaluate the provided PED model should be made. For example, the PED supplier should demonstrate the model robustness related to numerical stability, which is caused by round-off and truncation errors produced during the numerical simulation and will develop in an unbounded manner over the course of a simulation [68, 157]. The PED supplier should also demonstrate the initialization capability of the provided model. If the model is not able to initialize in an orderly way, the values of the dynamic system will not be able to converge and stay at their intended steady-state values [209].

It is sensible that the PED supplier continually improves the PED models, based on their own experience as well as the feedback given by the customer (e.g. the OWPP developer). The development could be achieved using the test facilities at the National Renewable Energy Laboratory (NREL), presented in Chapter 7. Furthermore, the supplier should continually work on improving the PED's susceptibility to the harmonic stability as well as design/improve active filtering strategies, which can be used to supress the occurrence of harmonic unstable operating conditions at power system level. This can successfully be achieved in close collaboration with other entities, such as the OWPP developer and academia. The dynamic impact of the inclusion of the active harmonic filtering such as the BRF considered in this project, should be evaluated, using both simulations as well as test results realised e.g. at NREL, if practical.

It is sensible at an early stage to define the right and responsibilities related to ensuring that the OWPP is compliant with regard to the harmonic stability requirements. It should be agreed whether the WTGs or the PEDs in the transmission system (or a combination of both) should be equipped with mitigation means. It should be noted that in this work only active filtering in the WTGs is considered. Active filtering could equally have been applied in the PEDs in the transmission system. The possible advantage of this would be the centralised instalment of the active filtering, rather than equip all the WTGs with the active filter algorithm. This would first of all simplify the reconfiguration of the filter if needed after the OWPP has been commissioned.

13.4.2 Harmonic Stability Studies

Preliminary Design Studies

It is considered sensible for the OWPP developer to make a preliminary assessment of the harmonic stability at an early stage of a project in order to map possible risks (i.e. to identify the frequency range where the dominant resonances are expected to be located in the final system). This would most appropriately be done in the frequency domain. This preliminary evaluation would then enable the OWPP developer to make more specific design requirements to e.g. the WTG supplier, regarding mitigation means in order to damp these resonances. Vendor specific models of the PEDs provided in a previous OWPP project could be used in this preliminary assessment, if such models exist. However, such a model is typically highly project specific, meaning that e.g. the active controlled harmonic filter (e.g. a band rejection filter (BRF)) is tuned to the frequency range where possible risks were observed in that specific project. Such a converter model might not be applicable to the new project, as the BRF's frequency characteristics might cause additional delay at the plant's resonance frequency. This would aggravate the PED's current control system's susceptibility to harmonic instability. Therefore, it would be more appropriate to apply a generic model of the PED in this early design stage. A generic frequency domain representation, as described in Chapter 10 of this thesis, is considered appropriate for this, where an aggregated model of the OWPP is considered. In this case the OWPP designer has the full controllability of the model including the parameters of the BRF filter. By enabling the OWPP developer to have a more project realistic picture of the harmonic stability by making a premature

mitigation design would further enable the OWPP developer to define specific design requirements to the PED suppliers. The PED supplier could then, based on the specifications, design appropriate mitigation means in order to avoid harmonic instability in that specific OWPP project.

It is sensible for the OWPP developer to have frequency characteristics of the external power system to which the OWPP is connected (i.e. in HVAC grid connected OWPPs). These characteristics should be provided by the TSO, who has specified a number of possible operating conditions of the system. These data would preferably be available in the early design stage, as they would add to the accuracy of the preliminary harmonic stability evaluation studies described in the above.

Final Design Studies

Once all the electrical components in the OWPP (e.g. cables, WTGs and PEDs in the transmission system) are procured and as-built documentation is available to the OWPP developer, the final harmonic stability evaluation should be carried out.

The first step in the evaluation would be the definition of possible outages, which should be taken into consideration in the harmonic stability evaluation.

Based on the findings in this project it is considered that these studies should be carried out in the frequency domain for all possible operating conditions of both the internal OWPP and the external power system (for HVAC connected OWPPs).

Based on this research project and the author's working experience at DEWP it is sensible to perform these studies using an aggregated model of the OWPP, as has been done in this research project.

The stability studies should be done in multiple stages, where the aggregated WTG and e.g. the HVDC converter is the source and load in one stage, respectively. The HVDC converter would then be the source in the analysis of the next stage. Additional stages could be included where a non-reduced representation of the internal OWPP is considered (i.e. not aggregated) and the stability margins are evaluated for few selected WTGs spread out in the OWPP. The same procedure is considered appropriate for an HVAC grid connected OWPP with a STATCOM situated at the grid connection point.

The simplifications caused by the aggregation procedure described in chapter 11 should be evaluated based on comparison with a full representation of the OWPP during the design phase of an OWPP.

The harmonic stability evaluation in Chapter 12 demonstrated good correlation between results obtained from the time and frequency domain models. However, limitations of the frequency domain were observed in the higher frequency range. Therefore, it is proposed to conduct the analysis primarily in the frequency domain. Once all the considered operating scenarios are covered (typically in the excess of 1000) a few cases should be selected and repeated in the time domain, which is both more challenging and more time consuming than the frequency domain method. The identified worst cases (i.e. where the Nyquist stability margins are lowest or instability is observed) should be repeated using time domain analysis methods as a second opinion tool. For practical reasons, this should only be done when using an aggregated OWPP representation.

The advantage of the time domain analysis is foremost the holistic evaluation of the harmonic stability in an OWPP with PED in the transmission system. Additionally the time domain allows the application non-linearized models of all components including the control system, the cables etc.

The time domain method allows the usage of the Frequency Dependent Phase Model (FDPM), which is the most accurate cable model available in all EMTP tools (and in general) [193, 194]. As discussed in section 11.2, there are relatively complex means to include the frequency dependent characteristics in the frequency domain, regardless of the cable termination conditions. On the other hand, the application of an analytical model such as the equivalent π-model representation taken into consideration the frequency dependency of the skin effect according to IEC 60287-1-1 (see section 11.2) is useful in the frequency domain evaluation. The credibility of the equivalent π-model in the lower frequency range is evident from Figure 11-6 on page 126.

In the case the calculated stability margins are within the specified ranges (defined based on previous experience) for all possible operating conditions and no discrepancies are observed in the results obtained in the time and frequency domain analysis, the harmonic stability evaluation is successfully completed. Additional analysis is required in case the stability margins are violated in order for the e.g. the PED developer to redesign the harmonic stability means and/or for the OWPP developer to retune and/or add passive filters e.g. at the onshore substation. The harmonic stability evaluation should then be repeated for this new system and additional harmonic mitigation means should be added, if required.

A number of uncertainties related to the harmonic stability evaluation in OWPPs were described in section 13.2. Based on these uncertainties, it is advisable to do a number of study cases, investigating the PED current control system's sensitivity to changes in the electrical system as well as to changes in the control system itself such as alterations in the active filtering control block. This sensitivity analysis could be based on the generic frequency and/or time domain models developed in this work of e.g. the PEDs and the simplified frequency dependent network equivalent (FDNE) model described in Chapter 11.

In Chapter 12 it was found that the total inter-harmonic distortion (TIHD) index according to IEC Standard 61000-4-7 is useful to assess possible and undesired control interaction between the PEDs in OWPPs in the time domain evaluation. The total harmonic distortion (THD) index, on the other hand, is found to contain very little information on possible PED controller interaction. Both indexes are recommended to be taken into consideration in the time domain harmonic stability evaluation when a high number of study cases are evaluated.

13.5 Chapter Summary

This chapter has outlined the various OWPP system design studies and put forward a proposal for best practice in the harmonic stability evaluation in OWPPs. The best practice is based on the knowledge sharing available when working with colleagues at DEWP, as well as the experience gained working on this project. These findings/recommendation can be incorporated in the design of future OWPPs employing PEDs in the transmission system.

Chapter 14 Conclusion

The scope of this Industrial PhD project has primarily been to investigate the best possible way(s) to perform the harmonic stability studies in high-voltage alternating and direct current (HVAC and HVDC, respectively) grid connected offshore wind power plants (OWPPs). This chapter presents the concluding remarks and the list of publications realised within the confines of this Industrial PhD project. Suggested future work is also outlined in this chapter.

14.1 Background

OWPPs can be characterized as a power electronic device (PED) rich grid. The project was initiated in order to meet an industrial need to develop a deeper understanding on how the PEDs and associated control systems interact (from a harmonic perspective) with each-other and with the passive electrical components in the OWPPs, such as the extensive submarine cabling.

The purpose is to meet a need to develop and strengthen DONG Energy Wind Power's (DEWP's) in-house competencies with regard to electrical system modelling and analysis of large OWPPs employing PEDs in the transmission system, such as the Static Compensator (STATCOM) and the voltage-sourced converter (VSC)-HVDC.

The primary focus of this Industrial PhD project is on the development of best possible way(s) to perform harmonic stability studies in HVAC and HVDC grid connected OWPPs. The project aimed at gaining new insight, methods and models, which will contribute to achieve a better understanding of the harmonic stability phenomena in OWPPs. The knowledge and applicable models developed within the project will enable the involved parties (e.g. the OWPP developer and the PED supplier) to improve e.g. the filter design.

By achieving a better understanding of the complexity of how such systems (e.g. the wind turbine generators (WTGs) and the HVDC station) interact with each other, seen from a harmonic perspective, it becomes possible to make a better and more cost-efficient design of e.g. harmonic filters and reactive compensation. Having a better understanding of the harmonic stability phenomena will in general ensure a high degree of reliability of future OWPPs where PEDs are widely applied. Furthermore, the outcome of the project will enable the OWPP developer, such DEWP, to better provide relevant input for the grid code compliance of an OWPP as well as define technical requirements to potential suppliers.

14.2 Summary of the thesis

The purpose of this Industrial PhD project has been to investigate and address the interaction (from a harmonic perspective) between the OWPP and the associated control systems in the WTGs and other PEDs typically located in the transmission system of large OWPPs with focus on the VSC-HVDC and the STATCOM systems. The main scope has been on the assessment of the frequency domain evaluation approach, commonly applied in the OWPP design phase. This has been accomplished by comparing results obtained from conventional and linearized frequency domain analysis methods such as the Nyquist stability criterion against the detailed electromagnetic transient (EMT) based model realised in PSCAD/EMTDC.

The aim of the project was to fulfil the requirements of describing the state-of-the-art PEDs in OWPPs, to conduct field measurement campaigns and to apply the measurement data to validate the developed models. Finally, the main scope has been to conduct harmonic stability simulations studies in both the time and frequency domain and evaluate the results. A best practice recommendation on how to assess the harmonic stability in the OWPP design phase based on simulation studies has been put forward. The best practice has been implemented in DEWP's design procedure of future OWPPs.

With reference to section 2.2, the following goals have been achieved:

- To obtain knowledge of the modular multi-level cascaded converters (MMCCs) for wind power integration (HVDC and STATCOM, in Chapter 3 to Chapter 6).
- **Generic Models of the PEDs, including the MMCCs have been developed and validated based on measurement campaigns.**
    - In time and frequency domain, where found applicable. (Chapter 4, 6, 8 and Chapter 10).
    - Completion of field measurement campaigns for model validations. (Chapter 5 and Chapter 7).
- **Investigate OWPP harmonic stability issues** for frequencies above the fundamental frequency with widespread use of actively controlled PEDs.
    - Compare different stability assessment methods **in time and frequency domain.** (Chapter 12).
- **Development of a best practice for harmonic stability assessment in OWPPs (Chapter 13).**

14.2.1 Summary of Literature study and Theoretical Analysis

Theoretical analysis is a suitable method during the study of the PEDs used in the WTGs and in the transmission system. The review has included the working principle of the state-of-the-art type 4 WTGs, the MMCC HVDC and the MMCC STATCOM, on their topology and control methodology. The state-of-the-art review on the MMCC technology includes both previous work in academia and especially what relevant suppliers offer, as this is relevance to OWPP developers such as DEWP. The review focused on the topology of relevant PED systems and on the structure of the applied control system.

A fundamental understanding of the time and frequency domains has been obtained in order to assess their application for harmonic stability studies in OWPPs. This was achieved by reviewing the existing methods used in the industry as well as academic contributions.

A review on the typical modelling of the internal OWPP cable collecting grid and the external power system (in HVAC grid connected OWPPs) has enabled the development and implementation of a suitable aggregated model in the simulation tools (i.e. PSCAD/EMTDC and MatLab for the time and frequency domain analysis, respectively).

14.2.2 Summary of Measurement Data Acquisition and Processing

Measurements constitute a core part in industry-oriented research. Due to this fact, the research project owes its uniqueness and contributes new insight to the academia. Test and field measurements have therefore been conducted on commercial PEDs such as ±50 MVar Siemens SVC Plus, the 7 MW ABB SVC Light (modified back-to-back configuration) and a commercial multi-megawatt sized type 4 WTG. The main purpose of the measurement campaigns has been for the author to acquire in-depth knowledge of the main characteristics of the PEDs. This is deemed desirable for the development of detailed, generic models of the PED, suitable for the harmonic stability analysis in OWPPs employing PEDs in the transmission system. The outcome of the measurement campaigns has furthermore been used to validate the developed generic EMT like models in order to ensure their trustworthiness for the stability investigations.

14.2.3 Summary of Component Modelling and Validation

The relatively high number of non-linear semi-conductors in the MMCCs possesses some challenges in the EMT programs, such as PSCAD/EMTDC, as the semi-conductors are triggered by relatively high-frequency signals and as the electrical system's admittance matrix is altered at each switching instant. A significant computational effort is required for re-triangularisation of the electrical network's subsystem admittance matrix. The computational burden is considerably increased for the large

number of semi-conductors typically employed in state-of-the-art MMCC based PEDs, making the simulation of the MMCC in some occasions impractical when using a conventional modelling approach. Previously, a detailed equivalent model of the MMCC VSC-HVDC has been devised based on the "Nested Fast and Simultaneous Solution". However, there are some limitations to the previous model as it is specifically intended for the MMCC employing half-bridge converters in the sub-module (SM) building block. The somewhat more complex structure of the full-bridge converter employed in the MMCC STATCOM makes it complex to apply the existing modelling approach for the STATCOM. A universal modelling technique is derived in this work, which is able to represent both the half- and full-bridge based SMs. The modelling technique is simple as the derivation of the SM's Norton equivalent is merely based on circuit inspection. The measurement data from the London Array OWPP measurement campaign has successfully been applied in the evaluation of the generic model of the STATCOM implemented in PSCAD/EMTDC. In general, it can be said that the proposed generic model is highly capable to replicate the measured waveforms even with no information available of the control and modulation technique applied in the commercial STATCOM.

The evaluated STATCOM model has enabled the development of a trustworthy, full model of the MMCC HVDC, which has been implemented in PSCAD/EMTDC. Simulation studies on the HVDC system has demonstrated the converter's ability to successfully control the distributed SM voltages, dynamically and for steady-state operating conditions.

The model evaluation of the commercial WTG and the CGI has been done for both normal and abnormal operating conditions, such as fast and slow balanced and unbalanced faults realised at the test facility at NREL. The evaluation demonstrated that it is possible with a high degree of accuracy to simulate the measured waveforms with little or even no information available applied PED control methodology as well as the control system parameters, which are influencing the characteristics of both the CGI and the WTG. The successful validation gives credibility to the time domain modelling of the involved PEDs for the harmonic stability assessment in OWPPs.

14.2.4 Summary of Power System Simulations

Harmonic stability studies have been realised in OWPPs employing PEDs in the transmission system. The harmonic stability in an HVDC grid connected OWPP has been investigated in both the frequency and time domain using the validated models of the PEDs. The application of the frequency domain method in the stability analysis raises the conceptual challenge of recognising the source and the load (i.e. the plant), as either the WTG or the HVDC system can be treated as the source in the analysis, yielding different results. In this case both the load and the source are actively controlled power system devices. The time domain approach on the other hand provides a holistic approach, without the need to assign the source in the analysis.

Based on a number of study cases, it is demonstrated that a good correlation exists between the time and frequency domain methods for the stability analysis. However, limitations of the frequency domain were observed when resonances at higher frequencies exist (i.e. near the switching frequency and above the bandwidth of the current controller). Therefore, it is proposed to conduct the analysis primarily in the frequency domain. Once all the considered operating scenarios are covered (typically in the excess of 1000) a few cases should be selected and repeated in the time domain, which is both more challenging and more time consuming than the frequency domain method.

Time domains studies in an HVAC grid connected OWPP with a STATCOM located at the grid connection point have shown that the undesirable controller interaction between the WTGs and the STATCOM deteriorates the controllability of the internal dynamics of the MMCC STATCOM.

It was found that the total inter-harmonic distortion index according to IEC Standard 61000-4-7 is useful to assess possible and undesired control interaction between the PEDs in OWPPs. The total harmonic index, on the other hand, is found to provide very limited information on possible PED controller interaction.

It was shown that an application of active filtering in the WTGs by means of band-rejection filters (BRF or notch filter) in the main control chain could potentially reduce the harmonic emission and improve the overall stability in OWPPs without interfering with the OWPP overall design. This can be achieved by providing additional damping or shifting the resonance frequencies, or a combination of both. Improving the PED controllers' rejection capability called active damping is a certain type of active filtering. The converter may be controlled adaptively or tuned to suppress selected harmonic components. The application of active filtering was demonstrated for OWPPs with either a STATCOM or an HVDC located in the transmission system. The active filtering was found to improve the internal dynamics of the MMCC STATCOM.

Based on the findings of the research project, a recommendation for best practice for the evaluation of the harmonic stability in OWPPs employing PEDs in the transmission system has been formulated and is enclosed in the dissertation.

14.3 Conclusion

The main scope of the research project has been achieved as the harmonic stability assessment method used by DEWP among others has been evaluated against time domain simulation results using validated, generic models of the considered PEDs, including the switching devices. Furthermore, a recommendation for a best practice procedure for the harmonic stability evaluation in OWPPs is proposed, based on the findings of this research project, described in Chapter 13.

With reference to the specific research questions formulated in section 2.2.1, the following conclusions are drawn based on the findings in this research project:

A literature review of the state-of-the-art MMCC technology employed in Siemens SVC Plus (STATCOM), Siemens HVDC Plus, ABB HVDC Light and Alstom MaxSine HVDC has been made and presented in Chapter 3.

It is found possible, based on the literature study of the PEDs, to develop and implement generic, yet detailed EMT like models of the four types of PEDs considered in this project, namely the type 4 WTG, the CGI and the MMCC family (with focus on the single-delta full-bridge STATCOM and the double-star half-bridge based HVDC, defined in Chapter 3).

Based on evaluation of the simulation results with respect to field and test measurements at London Array OWPP and at NREL, respectively, it is found that the developed generic model are, with a high degree of accuracy, capable of replicating the measured waveforms. This is found true for both steady state operating conditions and for dynamic events such as low-voltage ride-through etc. It has therefore been shown that it is possible to develop truthful models of the PEDs, without having information on the control principle and parameters influencing the characteristics of the commercial WTG, the CGI and the STATCOM. The successful validation gives credibility to the time domain modelling for the harmonic stability assessment in OWPPs.

Based on the harmonic stability evaluations in Chapter 12 it is found that the commonly applied frequency method provides trustworthy results. More detailed time domain simulations are useful as a second-option evaluation method. Furthermore, the time domain approach removes the need to specify the source in the evaluation, when multiple PEDs are present in the OWPP or in the transmission system.

The commonly used active filtering methods for attenuating possible interaction between the PED's current control system and the electrical system are found applicable to OWPPs with PEDs in the transmission system.

A recommendation for best practice procedure for the evaluation of the harmonic stability in OWPPs employing PEDs in the transmission system has been formulated. The procedure utilises the advantages of both the frequency and time domain methods.

14.4 Contributions

The author considers the following to be new contributions, resulting from the work on the current project:

- Development and evaluation of generic EMT model of a commercial mega-watt sized type 4 WTG.
    - Evaluated during both normal and abnormal operating conditions using test measurements.
- Evaluation of the performance of a commercial mega-watt sized type 4 WTG during normal and abnormal operating conditions.
- Generic EMT like modelling of ABB's PCS 6000 (SVC Light) [66]
    - STATCOM
    - CGI
    - No-load, normal and abnormal operating conditions
- Preparation, conduction and evaluation of measurement campaign on a commercial MMCC STATCOM.
    - Development of a robust out-doors measurement system for long term measurement campaigns.
- Development of a universal EMT like modelling technique for MMCCs.
    - Inclusion of the least mean square error as a figure of merit in the evaluation of the proposed models.
    - Applicable for harmonic stability studies.
- Generic detailed equivalent EMT like modelling of ABB's MMCC VSC-HVDC Generation 4.
    - Including low-level control (of the sub-module voltages).
- Generic detailed equivalent EMT like modelling of Siemens MMCC SVC Plus.
    - Including low-level control.
- Validation of the MMCC modelling approach using field measurements.
    - On Siemens SVC Plus.
- Mapping of MMCC HVDC/STATCOM modelling similarities/differences.
    - Evaluated MMCC STATCOM modelling approach assumed directly transferable to the (generic) MMCC HVDC model.
- Time domain (EMT like) simulations of the harmonic stability phenomena in OWPPs, employing detailed models of the relevant PEDs, including the switching devices.
    - HVAC and HVDC grid connected OWPPs.
    - Application of the total inter-harmonic distortion (TIHD) index.
        - Found useful when assessing the results of a vast range of time domain simulation study cases.
- Correlate time and frequency domain methods for harmonic stability studies in OWPPs.
    - HVAC and HVDC grid connected OWPPs.
    - Development of methods of modelling the passive components in the OWPPs, which are applicable to both the frequency and time domain, such as the export cable, which is discussed in Chapter 11.
- Development of a best practice procedure to evaluate the harmonic stability in OWPPs.
    - Applicable to OWPPs with and without PEDs in the transmission system.

14.4.1 Commercial Contributions

The more specific contributions to DEWP are by the author considered to be:

- Development and strengthening of DEWP's in-house competencies with regard to the electrical system modelling and analysis of large OWPPs employing PEDs.
  - Enables DEWP to get the right information for e.g. the HVDC system in due time during the design of an OWPP, which will potentially lead to lowering the risks in each project.
  - Enables DEWP to provide relevant input during the grid code compliance process of an OWPP.
  - The author participated in negotiation meetings with HVDC vendors during the research period. The knowledge obtained during the state-of-the-art review enabled DEWP to ask for more detailed information about the HVDC products.
- Establishment and initialisation of a long term CRADA between DEWP and NREL.
  - PhD student Lorenzo Zeni, DEWP and DTU, continued this good research collaboration with NREL during his stay a few months after the author's stay ended.
  - The collaboration is deemed highly valuable by DEWP and there is an interest in continuing this success by sending future PhD students to NREL.
- Generic model development of the following commercial PEDs:
  - ABB's SVC Light (i.e. the CGI).
  - Siemens's SVC Plus.
  - A commercial multi-megawatt sized type 4 WTG.
  - ABB's HVDC Light generation 4.
- Validation of the following commercial PEDs using measurement data:
  - ABB's SVC Light.
  - Siemens's SVC Plus.
  - A commercial type 4 WTG.
- Evaluation of the simplified frequency domain method used by the company in the harmonic stability evaluation.
  - Expanded the evaluation to HVDC grid connected OWPPs.
- Specification of a best practice, which can be applied in the harmonic stability evaluation in DEWPs OWPPs.
  - The validated generic models of the PED can be used in the early evaluations prior to the selection/procurement of the PEDs, where the final models typically will be provided by the PED supplier or by a third party, responsible for the modelling.

14.4.2 Commercialization of the Research Project

The PhD project can be categorised as an enabling process [210], as it aids DEWP in the design of OWPPs. The findings enable the design and operation of the OWPP to become more efficient, profitable and reliable. Seen from an operational strategy point of view, the project adds value creation to DEWP in the following way [211]:

- **Quality**: OWPPs will conform in the desired way (i.e. no/or minimized risks of OWPP shutdown due harmonic instability issues), as the tools for accessing the stability will be provided by the project.
- **Speed**: By having reliable and well-defined methods to assess the harmonic stability will eventually lower the lead-time of the design of the OWPP.
- **Dependability**: By having standard ways to assess the stability of the OWPP, it becomes more straightforward to make a realistic time-plan for the OWPP design and therefore increase the dependability.

- **Flexibility**: By having standardised stability evaluation methods, it becomes more straightforward to redo the harmonic stability evaluation in case of change in structure of the OWPP.
- **Cost/revenue:** The construction cost of the OWPP is lowered as the risk of expensive retrofits is lowered. The increased availability of the OWPP will have a significant impact on the revenue, especially for Gigawatt sized OWPPs.

The author will continue working at DEWP after completion of the PhD project. The knowledge and methods obtained within the project will be directly transferred into one of DEWP's on-going HVDC grid connected OWPP projects.

14.4.3 Knowledge Dissemination

The main channels for knowledge and finding dissemination include:

- Collaboration with other on-going PhD projects within DEWP.
    - Five joints conference papers were published, where the author had the main responsibility for four of these, as listed in section 14.5.
    - The PhD students have held two R&D workshops yearly, where colleagues and relevant people from academia (e.g. PhD supervisors and master students at DEWP) were invited.
    - The conference papers were all presented at their respective venues (except the Cigré Paris session papers, due to the format of the conference).
- The author has supervised a master thesis project at Aalborg University, sharing the knowledge obtained within this project.
- As previously mentioned, the author participated in negotiation meetings with HVDC vendors during the research period. The knowledge obtained during the state-of-the-art review enabled DEWP to ask for more detailed information about the vendors' products.
- A business report has been written.
    - A requirement in order to achieve the Industrial PhD.
    - Counts toward knowledge sharing of 7.5 ECTS.
    - Is included in the material submitted to the Doctoral School and the assessment committee.
- The author provided information to the colleagues at NREL regarding the harmonic stability challenges in DEWP's OWPP projects.

14.5 Publications

Both journal and conference papers have been prepared as outlined in the following.

Table 14-1 Published papers.

J. Glasdam, “Harmonics in Offshore Wind Power Plants”, book, Springer Thesis Recognizing Outstanding Ph.D. Research, 2016
J. Glasdam, C. L. Bak, and J. Hjerrild, "Transient studies in large offshore wind farms employing detailed circuit breaker representation," Energies, vol. 5, no. 7, pp. 2214--2231, 2012. (Published).
J. Glasdam, C.L. Bak, J. Hjerrild, A. Borghetti, F. Napolitano, C.A. Nucci, M. Paolone, “Vacuum Circuit Breaker Modelling For Assessment of Transient Recovery Voltages Under Various Network Configurations”, Electric Power Systems Research, (submitted).
J. Glasdam, J. Hjerrild, L. H. Kocewiak, and C. L. Bak, L. Zeni, "Comparison Of Field Measurements And EMT Simulation Results On A Multi-Level Statcom For Grid Integration Of London Array Wind Farm," In *Cigré Paris Session, 2014*, P. B4_206_2014, (Published).
J. Glasdam, J. Hjerrild, L. H. Kocewiak, and C. L. Bak, "Review on multi-level voltage source converter based HVDC technologies for grid connection of large offshore wind farms," in *Power System Technology (POWERCON), 2012 IEEE International Conference on*, 2012, pp. 1--6. (Published).
J. Glasdam, C. L. Bak, V. Gevorgian, R. Wallen, J. Hjerrild, and Ł. Kocewiak, "Characterization of a Power Electronic Grid Simulator for Wind Turbine Generator Compliance Testing," in *The 13th International Workshop on Large-Scale Integration of Wind Power into Power Systems as well as Transmission Networks for Offshore Wind Farms*, Berlin, 2014, (Published).
L. Zeni, J. Glasdam, B. Hesselbæk, T. Lund, P.E. Sørensen, A.D. Hansen, P.C. Kjær, “Coordinated System Services From Offshore Wind Power Plants Connected Through HVDC Networks”, *CIGRÉ PARIS SESSION*, 2014, p. C1_212_2014, (published).
J. Glasdam, C. L. Bak, J. Hjerrild, and Ł. Kocewiak, “Control System interaction in the VSC-HVDC Grid Connected Offshore Wind Power Plant”, *CIGRÉ Lund symposium*, *2015,* (accepted).
J. Glasdam, L. Zeni, M. Grynning , C.L. Bak, J. Hjerrild, P.E. Sørensen, A.D. Hansen, P.C Kjær, M. Blanke, K. Andersen, T.S. Sørensen, B. Hesselbæk, "HVDC Connected Offshore Wind Power Plants: Review and Outlook of Current Research," in *Proc. of the 12th International Workshop on Large-Scale Integration of Wind Power into Power Systems as well as on Transmission Networks for Offshore Wind Power Plants*, London, 2013, (Published).
J. Glasdam, L. Zeni, C. L. Bak, J. Hjerrild, B. Hesselbæk, P. E. Sørensen, A. D. Hansen, and P. C. Kjær, "An assessment of converter modelling needs for offshore wind power plants connected via VSC-HVDC networks," in *Proc. of the 12th International Workshop on Large-Scale Integration of Wind Power into Power Systems as well as on Transmission Networks for Offshore Wind Power Plants*, London, 2013, (Published).

This present report combined with the above listed scientific papers has been submitted for assessment in partial fulfillment of the PhD degree. The scientific papers are not included in this version due to copyright issues. Detailed publication information is provided above and the interested reader is referred to the original published papers. As part of the assessment, co-author statements have been made available to the assessment committee and are also available at the Faculty of Engineering and Science, Aalborg University.

14.6 Future Work

The one month measurement campaign at London Array OWPP (Chapter 5) resulted in approximately 11 TB of measurement data. The measurement data has been successfully used in the development and evaluation of a generic model of the MMCC based STATCOM. The high quality measurement can in a future work be used to make a statistical analysis of the harmonics generated by the STATCOM for different operating points, for various OWPP power production levels and for the harmonics relationship to the power system's fundamental frequency. This will provide further knowledge of the harmonic characteristics of the MMCC STATCOM.

The application of active filtering as a mean to reduce to OWPP's susceptibility to the harmonic instability phenomena has successfully been demonstrated taking into consideration the BRF, which is the commonly applied method to improve the harmonic stability in real-life OWPPs. More appropriate means of improving the stability using active control methods are available in the literature. It was decided in this project to focus on the harmonic stability evaluation primarily using commercially applied active filtering. Future work using other types of harmonic stability filtering in OWPPs is considered valuable. The application of the active filtering as a mean to improve the harmonic stability in OWPPs was done using BRFs in the WTGs. It is sensible to assess whether it is more suitable to implement the active filtering in e.g. the offshore HVDC station, centralising the mitigation mean.

Typically, active filtering is used in the direct chain of the WTG's current control system, as described in Chapter 10. Hence, the active filtering might impede the dynamic response of the WTG during e.g. faults. Having validated generic models of the WTG (without active harmonic filtering) during faults enables the researcher to evaluate the active filters impact by simply adding the active filtering into the already validated model and compare the results. This is suggested for future work due to time considerations.

Additional harmonic controllers can be implemented in the rotating reference frame using resonant controllers or in nested rotating frames, as described in Chapter 10. The resonant controllers are only affecting the response in a narrow frequency band around the frequency at which they compensate and would ideally not be influencing the converter's dynamics and stability. A harmonic stability evaluation with the application of harmonic filtering in the WTGs in OWPPs with PEDs in the transmission system is suggested as future work.

The inherent background harmonics in the HVAC grid connected OWPP have been omitted in the time domain model for simplicity. The inclusion would have added to the overall harmonic distortion but it is in this work considered not to have an impact of the occurrence of instability. This simplification of omitting the influence of the background harmonics in the harmonic stability evaluation in the time domain is proposed for future work.

The harmonic stability evaluation for an HVDC grid connected OWPP in section 12.3, was done taken the aggregated WTG as the source in the calculation. The procedure is essentially identical for when the HVDC system is taken as the source in the analysis and is proposed as future work.

The harmonic stability evaluation in an HVAC grid connected OWPP with a STATCOM situated at the grid connection point was presented in section 12.4. The study was only carried out in the time

domain. Future work is suggested to more carefully correlate the simulation results with the outcome of a frequency domain analysis.

The harmonic stability evaluation taken into consideration London Array OWPP was made for only one of the four OWPP sections in Figure 5-2 on page 59. Future work could include the possible effect of the remaining three OWPP sections.

14.7 Chapter Summary

The main scope of the research project has been achieved as the harmonic stability assessment method used by DEWP among others has been evaluated against time domain simulation results using validated, generic models of the considered PEDs, including the switching devices. Furthermore, a recommendation for a best practice procedure for the harmonic stability evaluation in OWPPs is proposed, based on the findings of this research project, described in Chapter 13.

Reference List

[1] L. Kocewiak, J. Hjerrild og C. Bak, »Software Development for Harmonic and Transient Measurements in Wind Farms,« *IEEE Transactions on Instrumentation and Measurement,* 2011.

[2] L. Sainz, J. J. Mesas, R. Teodorescu og Pedro Rodriguez, »Deterministic and Stochastic Study of Wind Farm Harmonic Currents,« *IEEE TRANSACTIONS ON ENERGY CONVERSION,* årg. 25, pp. 1071-1080, 2010.

[3] V. Akhmatov og P. B. Eriksen, »A large wind power system in almost island operation—A Danish case study,« *Power Systems, IEEE Transactions on,* årg. 22, nr. 3, pp. 937--943, 2007.

[4] The World Wind Energy Association , »2014 Half-year report,« 2014.

[5] REN 21, »GLOBAL STATUS REPORT 2014,« 2014.

[6] V. Pappala, S. Singh, M. Wilch og I. Erlich, »Reactive power management in offshore wind farms by adaptive PSO,« i *Intelligent Systems Applications to Power Systems, 2007. ISAP 2007. International Conference on*, 2007.

[7] P. Brogan, »The Stability of Multiple, high power, active front end voltage sourced converters when connected to wind farm collector systems,« i *Proc. 2010 EPEC*, 2010.

[8] M. Liserre, R. Teodorescu og F. Blaabjerg, »Stability of photovoltaic and wind turbine grid-connected inverters for a large set of grid impedance values,« *Power Electronics, IEEE Transactions on,* årg. 21, nr. 1, pp. 263--272, 2006.

[9] J. Sun, »Impedance-based stability criterion for grid-connected inverters,« *Power Electronics, IEEE Transactions on,* årg. 26, nr. 11, pp. 3075--3078, 2011.

[10] M. Mohseni og S. M. Islam, »Comparing technical connection requirements for large wind power plants,« i *Power and Energy Society General Meeting, 2011 IEEE*, 2011.

[11] A. L'Abbate et. al., »The role of facts and HVDC in the future paneuropean transmission system development,« i *AC and DC Power Transmission, 2010. ACDC. 9th IET International Conference on*, 2010.

[12] J. Glasdam, J. Hjerrild, L. H. Kocewiak, C. L. Bak og L. Zeni, »Comparison of Field Measurements and EMT Simulation Results on a Multi-Level STATCOM for Grid Integration of London Array Wind Farm,« i *Cigré Paris Session*, 2014.

[13] L. Kocewiak, C. Bak og J. Hjerrild, »Harmonic Aspects of Offshore Wind Farms,« 2010.

[14] W. Wiechowski og P. B. Eriksen, »Selected studies on offshore wind farm cable connections-challenges and experience of the Danish TSO,« i *Power and Energy Society General Meeting-Conversion and Delivery of Electrical Energy in the 21st Century, 2008 IEEE*, 2008.

[15] K. Xiangyu og J. Hongjie, »Techno-Economic Analysis of SVC-HVDC Transmission System for Offshore Wind,« i *Power and Energy Engineering Conference (APPEEC), 2011 Asia-Pacific*, 2011.

[16] J. Glasdam, L. Zeni, M. Grynning, C. L. Bak, J. Hjerrild, P. E. Sørensen, A. D. Hansen, P. C. B. M. Kjær, K. Andersen, T. Sørensen og B. Hesselbæk, »HVDC Connected Offshore Wind Power Plants: Review and Outlook of Current Research,« i *Proc. of the 12th International Workshop on Large-Scale Integration of Wind Power into Power Systems as well as on Transmission*

Networks for Offshore Wind Power Plants, London, 2013.

[17] J. Glasdam, J. Hjerrild, L. H. Kocewiak og C. L. Bak, »Review on multi-level voltage source converter based HVDC technologies for grid connection of large offshore wind farms,« i *Power System Technology (POWERCON), 2012 IEEE International Conference on*, 2012.

[18] S. K. Chaudhary, R. Teodorescu, P. Rodriguez, P. C. Kjaer og A. M. Gole, »Negative sequence current control in wind power plants with VSC-HVDC connection,« *Sustainable Energy, IEEE Transactions on,* årg. 3, nr. 3, pp. 535--544, 2012.

[19] S. K. Chaudhary, »Control and Protection of Wind Power Plants with VSC-HVDC Connection,« Aalborg, Denmark, 2011.

[20] L. H. Kocewiak, J. Hjerrild og C. L. Bak, »Harmonic models of a back-to-back converter in large offshore wind farms compared with measurement data,« i *Nordic Wind Power Conference (NWPC'2009)*, 2009.

[21] Ł. H. Kocewiak, J. Hjerrild og C. Leth Bak, »Wind turbine converter control interaction with complex wind farm systems,« *IET Renewable Power Generation,* årg. 7, nr. 4, November 2013.

[22] The Crown Estate, »The Crown Estate Round 3 Offshore Wind Farm Connection Study Version 1.0,« 2008.

[23] H. Knaak, »Modular multilevel converters and HVDC/FACTS: A success story,« i *Power Electronics and Applications (EPE 2011), Proceedings of the 2011-14th European Conference on*, 2011.

[24] B. Jacobson, Y. Jiang-Hafner, P. Rey, G. Asplund, M. Jeroense, A. Gustafsson og M. Bergkvist, »HVDC with voltage source converters and extruded cables for up to +/-300 kV and 1000 MW,« i *Cigre session*, 2006.

[25] B. Jacobson, P. Karlsson, G. Asplund, L. Harnefors og T. Jonsson, »VSC-HVDC transmission with cascaded two-level converters,« *CIGRÉ SC B4 Session 2010,* 2010.

[26] K. Friedrich, »Modern HVDC PLUS application of VSC in Modular Multilevel Converter topology,« i *Industrial Electronics (ISIE), 2010 IEEE International Symposium on*, 2010.

[27] G. Mondal, R. Critchley, F. Hassan og W. Crookes, »Design and simulation of a modular multi-level converter for MVDC application,« i *Industrial Electronics (ISIE), 2011 IEEE International Symposium on*, 2011.

[28] R. Whitehouse, C. Oates, J. Maneiro og N. MacLeod, »A new simulator laboratory for research and development of VSC HVDC topologies and control algorithms,« i *AC and DC Power Transmission, 2010. ACDC. 9th IET International Conference on*, 2010.

[29] U. Gnanarathna, A. Gole og R. Jayasinghe, »Efficient modeling of modular multilevel HVDC converters (MMC) on electromagnetic transient simulation programs,« *Power Delivery, IEEE Transactions on,* årg. 26, nr. 1, pp. 316--324, 2011.

[30] C. Oates og C. Davidson, »A comparison of two methods of estimating losses in the Modular Multi-Level Converter,« i *Power Electronics and Applications (EPE 2011), Proceedings of the 2011-14th European Conference on*, 2011.

[31] T. Nakajima og S. Irokawa, »A control system for HVDC transmission by voltage sourced converters,« i *Power Engineering Society Summer Meeting, 1999. IEEE*, 1999.

[32] J. Kreusel og D. Retzmann, »Integrated AC/DC Transmission Systems--Benefits of Power Electronics for Security and Sustainability of Power Supply,« i *Power System Computation*

Conference, 2008.

[33] H. Dong og M. Yuan, »The Study of Control Strategy for VSC-HVDC Applied in Offshore Wind Farm and Grid Connection,« i *Power and Energy Engineering Conference (APPEEC), 2011 Asia-Pacific*, 2011.

[34] S. Ruihua, Z. Chao, L. Ruomei og Z. Xiaoxin, »VSCs based HVDC and its control strategy,« i *Transmission and Distribution Conference and Exhibition: Asia and Pacific, 2005 IEEE/PES*, 2005.

[35] L. Xu, L. Yao og C. Sasse, »Grid integration of large DFIG-based wind farms using VSC transmission,« *Power Systems, IEEE Transactions on,* årg. 22, nr. 3, pp. 976--984, 2007.

[36] A. Bodin, »HVDC Light a preferable power transmission system for renewable energies,« i *Energetics (IYCE), Proceedings of the 2011 3rd International Youth Conference on*, 2011.

[37] X. Chen, W. Lin, H. Sun, J. Wen, N. Li og L. Yao, »LCC based MTDC for grid integration of large onshore wind farms in Northwest China,« i *Power and Energy Society General Meeting, 2011 IEEE*, 2011.

[38] S. Bozhko, R. Li, R. Blasco-Gimenez, G. Asher, J. Clare, L. Yao og C. Sasse, »STATCOM-controlled HVDC power transmission for large offshore wind farms: engineering issues,« i *IEEE Industrial Electronics, IECON 2006-32nd Annual Conference on*, 2006.

[39] N. Flourentzou, V. Agelidis og G. Demetriades, »VSC-based HVDC power transmission systems: An overview,« *Power Electronics, IEEE Transactions on,* årg. 24, nr. 3, pp. 592--602, 2009.

[40] B. Gemmell, J. Dorn, D. Retzmann og D. Soerangr, »Prospects of multilevel VSC technologies for power transmission,« i *Transmission and Distribution Conference and Exposition, 2008. IEEE/PES*, 2008.

[41] ABB, It's time to connect, 7 red., 2013.

[42] H.-P. Nee og L. Ängquist, »Perspectives on Power Electronics and Grid Solutions for Offshore Wind Farms,« 2010.

[43] M. Pereira, D. Retzmann, J. Lottes, M. Wiesinger og G. Wong, »SVC PLUS: An MMC STATCOM for network and grid access applications,« i *PowerTech, 2011 IEEE Trondheim*, 2011.

[44] H. K. Tyll og F. Schettler, »Historical overview on dynamic reactive power compensation solutions from the begin of AC power transmission towards present applications,« i *IEEE/PES Power Systems Conference and Exposition - PSCE'09*, Seattle, 2009.

[45] A. Adamczyk, R. Teodorescu, R. Mukerjee og P. Rodriguez, »Overview of FACTS devices for wind power plants directly connected to the transmission network,« i *Industrial Electronics (ISIE), 2010 IEEE International Symposium on*, 2010.

[46] P. Maibach, J. Wernli, P. Jones og M. Obad, »STATCOM technology for wind parks to meet grid code requirements,« i *Proceedings of EWEC*, 2007.

[47] I. Erlich og F. Shewarega, »Insert Impact of Large-Scale Wind Power Generation on the Dynamic Behaviour of Intrerconnected Systems,« i *iREP Symposium*, 2007.

[48] E. Camm, M. Behnke, O. Bolado, M. Bollen, M. Bradt, C. Brooks, W. Dilling, M. Edds, W. Hejdak, D. Houseman, S. Klein, F. Li, J. Li, P. Maibach, T. Nicolai, J. Patino, S. Pasupulati, N. Samaan, S. Saylors, T. Siebert og T. Smith, »Reactive power compensation for wind power plants,« i *Power Energy Society General Meeting, 2009. PES '09. IEEE*, 2009.

[49] T. Ackermann, Wind power in power systems, Wiley, 2005.

[50] J. Lai og F. Peng, »Multilevel converters-a new breed of power converters,« *Industry Applications, IEEE Transactions on,* årg. 32, nr. 3, pp. 509--517, 1996.

[51] K. R. Padiyar, Facts controllers in power transmission and distribution, New Age International (P) Ltd., Publishers, 207.

[52] C. Davidson og G. de Préville, »The future of high power electronics in transmission and distribution power systems,« i *Power Electronics and Applications, 2009. EPE'09. 13th European Conference on*, 2009.

[53] R. Knight, D. Young og D. Trainer, »Relocatable GTO-based Static-Var Compensator for NGCSubstations,« i *CIGRE Session*, Paris, 1998.

[54] A. Lesnicar og R. Marquardt, »An innovative modular multilevel converter topology suitable for a wide power range,« i *Power Tech Conference Proceedings, 2003 IEEE Bologna*, 2003.

[55] A. Scarfone, B. Oberlin, J. Di Luca Jr, D. Hanson og C. Horwill, »A+/-150 MVAr STATCOM for Northeast Utilities' Glenbrook substation,« i *Power Engineering Society General Meeting, 2003, IEEE*, 2003.

[56] A. Shafiu, A. Hernandez, F. Schettler, J. Finn og E. Jorgensen, »Harmonic studies for offshore windfarms,« i *AC and DC Power Transmission, 2010. ACDC. 9th IET International Conference on*, 2010.

[57] D. G. Holmes og T. A. Lipo, Pulse Width Modulation for Power Converters: Principles and Practice, IEEE Press, 2003.

[58] L. Kocewiak, »Harmonics in large offshore wind farms,« Aalborg, 2012.

[59] L. Harnefors, M. Bongiorno og S. Lundberg, »Stability analysis of converter-grid interaction using the converter input admittance,« i *Power Electronics and Applications, 2007 European Conference on*, 2007.

[60] X. Chen og J. Sun, »Characterization of inverter-grid interactions using a hardware-in-the-loop system test-bed,« i *Power Electronics and ECCE Asia (ICPE \& ECCE), 2011 IEEE 8th International Conference on*, 2011.

[61] J. Enslin, W. Hulshorst, A. Atmadji, P. Heskes, A. Kotsopoulos, J. Cobben og P. Van der Sluijs, »Harmonic interaction between large numbers of photovoltaic inverters and the distribution network,« i *Power Tech Conference Proceedings, 2003 IEEE Bologna*, 2003.

[62] M. Cespedes og J. Sun, »Online grid impedance identification for adaptive control of grid-connected inverters,« i *Energy Conversion Congress and Exposition (ECCE), 2012 IEEE*, 2012.

[63] X. Wang, F. Blaabjerg og Z. Chen, »Autonomous Control of Inverter-Interfaced Distributed Generation Units for Harmonic Current Filtering and Resonance Damping in an Islanded Microgrid,« *IEEE Transactions on Industry Applications,* 2014.

[64] E. Mollerstedt og B. Bernhardsson, »Out of control because of harmonics-an analysis of the harmonic response of an inverter locomotive,« *Control Systems Magazine, IEEE,* årg. 20, nr. 4, pp. 70--81, 2000.

[65] E. Möllerstedt, »Dynamic analysis of harmonics in electrical systems,« 2000.

[66] ABB, 12 12 2014. [Online]. Available: http://www.abb.com/product/seitp322/512833dd2f0c8709c12576bf0042b28f.aspx?productLanguage=dk&country=DK.

[67] N. Watson og J. Arrillaga, Power System Harmonics, Wiley and Sons, 2003.

[68] N. Watson og J. Arrillaga, Power Systems Electromagnetic Transients Simulation, 1st red., IET Power and Energy Series 39, 2003.

[69] A. Kopta, M. Rahimo, U. Schlapbach, R. Schnell og D. Schneider, »High Voltage SPT+ HiPak modules rated at 4500V,« *PCIM, Nürnberg,* 2007.

[70] S. Allebrod, R. Hamerski og R. Marquardt, »New transformerless, scalable modular multilevel converters for HVDC-transmission,« i *Power Electronics Specialists Conference, 2008. PESC 2008. IEEE*, 2008.

[71] A. Nabae, I. Takahashi og H. Akagi, »A new neutral-point-clamped PWM inverter,« *Industry Applications, IEEE Transactions on,* nr. 5, pp. 518--523, 1981.

[72] S. Dodds, B. Railing, K. Akman, B. Jacobson, T. Worzyk og B. Nielsson, »HVDC VSC (HVDC light) transmission – operating experiences,« i *Cigre session*, 2010.

[73] T. Bruckner og S. Bemet, »Loss balancing in three-level voltage source inverters applying active NPC switches,« i *Power Electronics Specialists Conference, PESC. 2001 IEEE 32nd Annual*, 2001.

[74] T. Bruckner, S. Bernet og H. Guldner, »The active NPC converter and its loss-balancing control,« *Industrial Electronics, IEEE Transactions on,* årg. 52, nr. 3, pp. 855--868, 2005.

[75] G. Asplund, Y. J. Häfner, J. Lindberg, P. Lundberg, J. Svensson og R. Pålsson, Electric power converter, US Patent 7,321,500, 2008.

[76] J. Tibola, H. Pinheiro og R. de Camargo, »Closed loop selective harmonic elimination applied to a grid connected PWM converter with LCL filter,« i *Power Electronics Conference (COBEP), 2011 Brazilian*, 2011.

[77] G. Adam, S. Finney, A. Massoud og B. Williams, »Capacitor balance issues of the diode-clamped multilevel inverter operated in a quasi two-state mode,« *Industrial Electronics, IEEE Transactions on,* årg. 55, nr. 8, pp. 3088--3099, 2008.

[78] U. Gnanarathna, S. Chaudhary, A. Gole og R. Teodorescu, »Modular multi-level converter based HVDC system for grid connection of offshore wind power plant,« i *AC and DC Power Transmission, 2010. ACDC. 9th IET International Conference on*, 2010.

[79] J. Pou, R. Pindado og D. Boroyevich, »Voltage-balance limits in four-level diode-clamped converters with passive front ends,« *Industrial Electronics, IEEE Transactions on,* årg. 52, nr. 1, pp. 190--196, 2005.

[80] G. Adam, B. Alajmi, K. Ahmed, S. Finney og B. Williams, »New flying capacitor multilevel converter,« i *Industrial Electronics (ISIE), 2011 IEEE International Symposium on*, 2011.

[81] H. Akagi, »Classification, terminology, and application of the modular multilevel cascade converter (MMCC),« *Power Electronics, IEEE Transactions on,* årg. 26, nr. 11, pp. 3119--3130, 2011.

[82] Q. Tu, Z. Xu, H. Huang og J. Zhang, »Parameter design principle of the arm inductor in modular multilevel converter based HVDC,« i *Power System Technology (POWERCON), 2010 International Conference on*, 2010.

[83] J. Dorn, H. Huang og D. Retzmann, »A new Multilevel Voltage-Sourced Converter Topology for HVDC Applications,« i *CIGRE B4-304*, 2008.

[84] C. Davidson og D. Trainer, »Innovative concepts for hybrid multi-level converters for HVDC

power transmission,« i *AC and DC Power Transmission, 2010. ACDC. 9th IET International Conference on*, 2010.

[85] Y. Zhang, G. Adam, T. Lim, S. Finney og B. Williams, »Voltage source converter in high voltage applications: Multilevel versus two-level converters,« i *AC and DC Power Transmission, 2010. ACDC. 9th IET International Conference on*, 2010.

[86] S. Rohner, S. Bernet, M. Hiller og R. Sommer, »Analysis and simulation of a 6 kV, 6 MVA modular multilevel converter,« i *Industrial Electronics, 2009. IECON'09. 35th Annual Conference of IEEE*, 2009.

[87] Q. Tu, Z. Xu og J. Zhang, »Circulating current suppressing controller in modular multilevel converter,« i *IECON 2010-36th Annual Conference on IEEE Industrial Electronics Society*, 2010.

[88] Q. Tu, Z. Xu og L. Xu, »Reduced switching-frequency modulation and circulating current suppression for modular multilevel converters,« *Power Delivery, IEEE Transactions on,* årg. 26, nr. 3, pp. 2009--2017, 2011.

[89] A. Antonopoulos, L. Angquist og H. Nee, »On dynamics and voltage control of the modular multilevel converter,« i *Power Electronics and Applications, 2009. EPE'09. 13th European Conference on*, 2009.

[90] M. Hagiwara, R. Maeda og H. Akagi, »Control and analysis of the modular multilevel cascade converter based on double-star chopper-cells (MMCC-DSCC),« *Power Electronics, IEEE Transactions on,* årg. 26, nr. 6, pp. 1649--1658, 2011.

[91] Dommaschk et. al., Device for converting an electric current, U.S. Patent 0,118,578, 2010.

[92] L. Harnefors og J. B., Power converter with multi-level voltage output and harmonics filter, U.S. Patent 0,261,598,, 2011.

[93] J. A. Houldsworth og D. A. Grant, »The use of harmonic distortion to increase the output voltage of a three-phase PWM inverter,« *Industry Applications, IEEE Transactions on,* nr. 5, pp. 1224--1228, 1984.

[94] R. Feldman, M. Tomasini, J. Clare, P. Wheeler, D. Trainer og R. Whitehouse, »A hybrid voltage source converter arrangement for HVDC power transmission and reactive power compensation,« i *Power Electronics, Machines and Drives (PEMD 2010), 5th IET International Conference on*, 2010.

[95] G. Adam, S. Finney, B. Williams, D. Trainer, C. Oates og D. Critchley, »Network fault tolerant voltage-source-converters for high-voltage applications,« i *AC and DC Power Transmission, 2010. ACDC. 9th IET International Conference on*, 2010.

[96] R. Feldman, M. Tomasini, J. Clare, P. Wheeler, D. Trainer og R. Whitehouse, »A low loss modular multilevel voltage source converter for HVDC power transmission and reactive power compensation,« i *AC and DC Power Transmission, 2010. ACDC. 9th IET International Conference on*, 2010.

[97] A. Cross, D. Trainer og R. Crookes, »Chain-link based HVDC Voltage Source Converter using current injection,« i *AC and DC Power Transmission, 2010. ACDC. 9th IET International Conference on*, 2010.

[98] M. Merlin, T. Green, P. Mitcheson, D. Trainer, D. Critchley og R. Crookes, »A new hybrid multi-level Voltage-Source Converter with DC fault blocking capability,« i *AC and DC Power Transmission, 2010. ACDC. 9th IET International Conference on*, 2010.

[99] J. Häfner og B. Jacobson, » Proactive Hybrid HVDC Breakers – A Key Innovation for Reliable

HVDC grids,« i *CIGRE Symposium, Bologna, Italy*, 2011.

[100] M. Hagiwara, R. Maeda og H. Akagi, »Negative-Sequence Reactive-Power Control by a PWM STATCOM Based on a Modular Multilevel Cascade Converter (MMCC-SDBC),« *Industry Applications, IEEE Transactions on,* årg. 48, nr. 2, pp. 720--729, 2012.

[101] R. Betz, T. Summers og T. Furney, »Symmetry compensation using a H-bridge multilevel STATCOM with zero sequence injection,« i *Industry Applications Conference, 2006. 41st IAS Annual Meeting. Conference Record of the 2006 IEEE*, 2006.

[102] J. Glasdam, L. Zeni, C. L. Bak, J. Hjerrild, P. E. Sørensen, A. D. Hansen og P. C. Kjær, »An assessment of converter modelling needs for offshore wind power plants connected via VSC-HVDC networks,« i *Proc. of the 12th International Workshop on Large-Scale Integration of Wind Power into Power Systems as well as on Transmission Networks for Offshore Wind Power Plants*, London, 2013.

[103] K. Strunz og E. Carlson, »Nested fast and simultaneous solution for time-domain simulation of integrative power-electric and electronic systems,« *Power Delivery, IEEE Transactions on,* årg. 22, nr. 1, pp. 277--287, 2007.

[104] H. Saad, J. Peralta, S. Dennetière, J. Mahseredjian, J. Jatskevich, J. Martinez, A. Davoudi, M. Saeedifard, V. Sood, X. Wang og . others, »Dynamic Averaged and Simplified Models for MMC-Based HVDC Transmission Systems,« *IEEE TRANSACTIONS ON POWER DELIVERY,* årg. 28, nr. 3, p. 1723, 2013.

[105] J. Xu, C. Zhao, W. Liu og C. Guo, »Accelerated Model of Modular Multilevel Converters in PSCAD/EMTDC,« *IEEE TRANSACTIONS ON POWER DELIVERY,* årg. 28, nr. 1, pp. 129-136, January 2013.

[106] C. K. Alexander og M. N. O. Sadiku, Fundamentals of Electric Circuits, 3 red., McGraw-Hill Higher Education, 2005.

[107] A. G. M. Strollo, »A new IGBT circuit model for SPICE simulation,« *in Proc. Power Electron. Specialists Conf.,* årg. 1, p. 133–138, Jun 1997.

[108] J. Peralta, H. Saad, S. Dennetière, J. Mahseredjian og S. Nguefeu, »Detailed and averaged models for a 401-level MMC--HVDC system,« *Power Delivery, IEEE Transactions on,* årg. 27, nr. 3, pp. 1501--1508, 2012.

[109] A. Gole, A. Keri, C. Kwankpa, E. Gunther, H. Dommel, I. Hassan, J. Marti, J. Martinez, K. Fehrle, L. Tang og . others, »Guidelines for modeling power electronics in electric power engineering applications,« *Power Delivery, IEEE Transactions on,* årg. 12, nr. 1, pp. 505--514, 1997.

[110] H. W. Dommel, »Digital computer solution of electromagnetic transients in single-and multiphase networks,« *Power Apparatus and Systems, IEEE Transactions on,* nr. 4, pp. 388--399, 1969.

[111] H. W. Dommel, EMTP Theory Book, Portland: Bonneville Power Administration, 1996.

[112] H. W. Dommel, »Nonlinear and time-varying elements in digital simulation of electromagnetic transients,« *Power Apparatus and Systems, IEEE Transactions on,* nr. 6, pp. 2561--2567, 1971.

[113] R. Jain, »Some *A*-stable methods for stiff ordinary differential equations,« *Mathematics of Computation,* årg. 26, nr. 117, pp. 71--77, 1972.

[114] Manitoba HVDC Research Center, EMTDC Transient Analysis for PSCAD Power System Simulation, 2010.

[115] J. Glasdam, C. L. Bak og J. Hjerrild, »Transient studies in large offshore wind farms employing detailed circuit breaker representation,« *Energies,* årg. 5, nr. 7, pp. 2214--2231, 2012.

[116] KPMG, »Offshore Transmission: An Investor Perspective,« 2012.

[117] London Array Limited, February 2012. [Online]. Available: http://www.londonarray.com/.

[118] M. Pereira, M. Pieschel og R. Stoeber, »Prospects of the new SVC with Modular Multilevel Voltage Source Converter,« i *CIGRE Colloquium, October*, 2011.

[119] L. Christensen, M. Ulletved, P. Sørensen, T. Sørensen, T. Olsen, H. Nielsen, P. Sørensen og O. Holmstrøm, »GPS synchronized high voltage measuring system,« i *Nordic Wind Power Conference, nov.*, 2007.

[120] Powertek, December 2013. [Online]. Available: http://www.powertekuk.com/cwt.htm.

[121] S. Sirisukprasert, A. Huang og J. Lai, »Modeling, analysis and control of cascaded-multilevel converter-based STATCOM,« i *Power Engineering Society General Meeting, 2003, IEEE*, 2003.

[122] J. Kumar, B. Das og P. Agarwal, »Modeling of 11-Level Cascade Multilevel STATCOM,« *International Journal of Recent Trends in Engineering,* årg. 2, nr. 5, 2009.

[123] T. Yeh, H. Jhu og H. Sung, »Modeling and control of three-phase multilevel inverter-based STATCOM,« i *Power Electronics for Distributed Generation Systems (PEDG), 2010 2nd IEEE International Symposium on*, 2010.

[124] R. Teodorescu, M. Liserre og P. Rodriguez, Grid converters for photovoltaic and wind power systems, årg. 29, John Wiley & Sons, 2011.

[125] A. Timbus, M. Liserre, R. Teodorescu, P. Rodriguez og F. Blaabjerg, »Evaluation of current controllers for distributed power generation systems,« *Power Electronics, IEEE Transactions on,* årg. 24, nr. 3, pp. 654--664, 2009.

[126] M. Hagiwara og H. Akagi, »Control and experiment of pulsewidth-modulated modular multilevel converters,« *Power Electronics, IEEE Transactions on,* årg. 24, nr. 7, pp. 1737--1746, 2009.

[127] G. Asplund, »Method for controlling a voltage source converter and a voltage converting apparatus«. US Patent 20,100,328,977, 30 December 2010.

[128] L. G. Franquelo, J. Rodriguez, J. I. Leon, S. Kouro, R. Portillo og M. A. Prats, »The age of multilevel converters arrives,« *Industrial Electronics Magazine, IEEE,* årg. 2, nr. 2, pp. 28--39, 2008.

[129] J. Rodriguez, J.-S. Lai og F. Z. Peng, »Multilevel inverters: a survey of topologies, controls, and applications,« *Industrial Electronics, IEEE Transactions on,* årg. 49, nr. 4, pp. 724--738, 2002.

[130] L. M. Tolbert og T. G. Habetler, »Novel multilevel inverter carrier-based PWM method,« *Industry Applications, IEEE Transactions on,* årg. 35, nr. 5, pp. 1098--1107, 1999.

[131] Energinet DK, »Wind Turbines Connected to Grids With Voltages Above 100 kV,« 2004.

[132] National Grid, »The Grid Code, National Grid Electricity Transmission plc,« 2010.

[133] International Electrotechnical Commission, EC 61000-21, Wind turbine generator systems – Part 21: Measurement and assessment of power quality characteristics of grid connected wind turbines, 2001.

[134] CIC Research, May 2014. [Online]. Available: http://www.cic-research.com/Merchant2/merchant.mvc?Screen=PROD&Store_Code=CR&Product_Code=DP

20-10K.

[135] Power Electronic Measurements, May 2014. [Online]. Available: http://www.pemuk.com/products/rct-industrial-sensor/rcti.aspx.

[136] National Instrument, May 2014. [Online]. Available: http://sine.ni.com/ds/app/doc/p/id/ds-179/lang/da.

[137] National Instrument, May 2014. [Online]. Available: http://sine.ni.com/nips/cds/view/p/lang/da/nid/208796.

[138] J. Glasdam, C. L. Bak, V. Gevorgian, J. Hjerrild og Ł. Kocewiak, »Characterization of a Power Electronic Grid Simulator for Wind Turbine Generator Compliance Testing,« i *The 13th International Workshop on Large-Scale Integration of Wind Power into Power Systems as well as Transmission Networks for Offshore Wind Farms*, Berlin, 2014.

[139] P. B. Brogan, E. Grondahl, R. Jones og H. Stiesdal, »Power converters,« *US Patent 7,372,174,* May 2008.

[140] International Electrotechnical Commission, IEC 61400-27 - Electrical simulation models for wind power generation Wind Turbines, 1st red., 2012.

[141] P. Delarue, A. Bouscayrol, A. Tounzi, X. Guillaud og G. Lancigu, »Modelling, control and simulation of an overall wind energy conversion system,« *Renewable Energy,* årg. 28, nr. 8, pp. 1169--1185, 2003.

[142] J. Slootweg, H. Polinder og W. Kling, »Representing wind turbine electrical generating systems in fundamental frequency simulations,« *Energy conversion, IEEE transactions on,* årg. 18, nr. 4, pp. 516--524, 2003.

[143] D. J. Trudnowski, A. Gentile, J. M. Khan og E. M. Petritz, »Fixed-speed wind-generator and wind-park modeling for transient stability studies,« *Power Systems, IEEE Transactions on,* årg. 19, nr. 4, pp. 1911--1917, 2004.

[144] M. P. Kazmierkowski og L. Malesani, »Current control techniques for three-phase voltage-source PWM converters: a survey,« *Industrial Electronics, IEEE Transactions on,* årg. 45, nr. 5, pp. 691--703, 1998.

[145] A. Tripathi og P. C. Sen, »Comparative analysis of fixed and sinusoidal band hysteresis current controllers for voltage source inverters,« *Industrial Electronics, IEEE Transactions on,* årg. 39, nr. 1, pp. 63--73, 1992.

[146] D. N. Zmood, D. G. Holmes og G. H. Bode, »Frequency-domain analysis of three-phase linear current regulators,« *Industry Applications, IEEE Transactions on,* årg. 37, nr. 2, pp. 601--610, 2001.

[147] H.-s. Song og K. Nam, »Dual current control scheme for PWM converter under unbalanced input voltage conditions,« *Industrial Electronics, IEEE Transactions on,* årg. 46, nr. 5, pp. 953--959, 1999.

[148] P. Rioual, H. Pouliquen og J.-P. Louis, »Regulation of a PWM rectifier in the unbalanced network state using a generalized model,« *Power Electronics, IEEE Transactions on,* årg. 11, nr. 3, pp. 495--502, 1996.

[149] G. Saccomando og J. Svensson, »Transient operation of grid-connected voltage source converter under unbalanced voltage conditions,« i *Industry Applications Conference, 2001. Thirty-Sixth IAS Annual Meeting. Conference Record of the 2001 IEEE*, 2001.

[150] R. Nelson, H. Ma og N. Goldenbaum, »Fault ride-through capabilities of siemens full-converter wind turbines,« i *Power and Energy Society General Meeting, 2011 IEEE*, 2011.

[151] D. Roiu, R. I. Bojoi, L. R. Limongi og A. Tenconi, »New stationary frame control scheme for three-phase PWM rectifiers under unbalanced voltage dips conditions,« *Industry Applications, IEEE Transactions on,* årg. 46, nr. 1, pp. 268--277, 2010.

[152] L. Xu, B. R. Andersen og P. Cartwright, »VSC transmission operating under unbalanced AC conditions-analysis and control design,« *Power Delivery, IEEE Transactions on,* årg. 20, nr. 1, pp. 427--434, 2005.

[153] H. Akagi, E. H. Watanabe og M. Aredes, Instantaneous power theory and applications to power conditioning, årg. 31, John Wiley & Sons, 2007.

[154] J. Svensson og M. Lindgren, »Influence of nonlinearities on the frequency response of a grid-connected vector-controlled VSC,« *Industrial Electronics, IEEE Transactions on,* årg. 46, nr. 2, pp. 319--324, 1999.

[155] N. Bao, Q. Chen og T. Jiang, »Modelling and identification of a wind turbine system,« *Wind Engineering,* årg. 20, nr. 4, pp. 203--218, 1996.

[156] A. Dadone, L. Dambrosio og B. Fortunato, »One step ahead adaptive control technique for wind systems,« *Energy conversion and management,* årg. 39, nr. 5, pp. 399--413, 1998.

[157] Y. Coughlan, P. Smith, A. Mullane og M. O'Malley, »Wind turbine modelling for power system stability analysis—a system operator perspective,« *Power Systems, IEEE Transactions on,* årg. 22, nr. 3, pp. 929--936, 2007.

[158] EirGrid, December 2014. [Online]. Available: http://www.eirgrid.com/customers/gridconnections/generatorconnections/winddynamic modelling/.

[159] G. Rogdakis, R. Garcia-Valle og I. Arana, »Transient Model Validation of Fixed-Speed Induction Generator Using Wind Farm Measurements,« *Power Systems, IEEE Transactions on,* årg. 27, nr. 1, pp. 564--571, 2012.

[160] N. P. Strachan og D. Jovcic, »Stability of a variable-speed permanent magnet wind generator with weak AC grids,« *Power Delivery, IEEE Transactions on,* årg. 25, nr. 4, pp. 2779--2788, 2010.

[161] J. N. Nielsen, V. Akhmatov, J. Thisted, E. Grøndahl, P. Egedal, M. N. Frydensbjerg og K. H. Jensen, »Modelling and fault-ride-trough tests of Siemens Wind Power 3.6 MW variable-speed wind turbines,« *Wind Engineering,* årg. 31, nr. 6, pp. 441--452, 2007.

[162] A. A. A. Radwan og Y. A.-R. I. Mohamed, »Analysis and active-impedance-based stabilization of voltage-source-rectifier loads in grid-connected and isolated microgrid applications,« *IEEE TRANSACTIONS ON SUSTAINABLE ENERGY,* årg. 4, nr. 3, pp. 563--576, 2013.

[163] L. Harnefors, »Analysis of subsynchronous torsional interaction with power electronic converters,« *Power Systems, IEEE Transactions on,* årg. 22, nr. 1, pp. 305--313, 2007.

[164] S. Vesti, T. Suntio, J. Oliver, R. Prieto og J. Cobos, »Impedance-based stability and transient-performance assessment applying maximum peak criteria,« *Power Electronics, IEEE Transactions on,* årg. 28, nr. 5, pp. 2099--2104, 2013.

[165] A. A. A. Radwan og Y.-R. Mohamed, »Linear active stabilization of converter-dominated DC microgrids,« *Smart Grid, IEEE Transactions on,* årg. 3, nr. 1, pp. 203--216, 2012.

[166] X. Feng, J. Liu og F. C. Lee, »Impedance specifications for stable DC distributed power systems,« *Power Electronics, IEEE Transactions on,* årg. 17, nr. 2, pp. 157--162, 2002.

[167] S. D. Sudhoff, S. F. Glover, P. T. Lamm, D. H. Schmucker og D. Delisle, »Admittance space stability analysis of power electronic systems,« *Aerospace and Electronic Systems, IEEE Transactions on,* årg. 36, nr. 3, pp. 965--973, 2000.

[168] C. M. Wildrick, F. C. Lee, B. H. Cho og B. Choi, »A method of defining the load impedance specification for a stable distributed power system,« *IEEE Transactions on Power Electronics,* årg. 10, nr. 3, pp. 280--285, 1995.

[169] B. Choi, D. Kim, D. Lee, S. Choi og S. JIAN, »Analysis of input filter interactions in switching power converters,« *IEEE transactions on power electronics,* årg. 22, nr. 2, pp. 452--460, 2007.

[170] A. Emadi, A. Khaligh, C. H. Rivetta og G. A. Williamson, »Constant power loads and negative impedance instability in automotive systems: definition, modeling, stability, and control of power electronic converters and motor drives,« *Vehicular Technology, IEEE Transactions on,* årg. 55, nr. 4, pp. 1112--1125, 2006.

[171] J. Sun, »Small-signal methods for AC distributed power systems--a review,« *Power Electronics, IEEE Transactions on,* årg. 24, nr. 11, pp. 2545--2554, 2009.

[172] R. D. Middlebrook, »Input filter considerations in design and applications of switching regulators,« i *Proc. IEEE Ind. Appl. Soc. Annu. Meeting*, 1976.

[173] L. Harnefors, M. Bongiorno og S. Lundberg, »Input-admittance calculation and shaping for controlled voltage-source converters,« *Industrial Electronics, IEEE Transactions on,* årg. 54, nr. 6, pp. 3323--3334, 2007.

[174] K. Ogata og Y. Yang, »Modern control engineering,« 1970.

[175] O. J. Smith, »A controller to overcome dead time,« *ISA Journal,* årg. 6, nr. 2, pp. 28--33, 1959.

[176] M. H. Bierhoff og F. W. Fuchs, »Active damping for three-phase PWM rectifiers with high-order line-side filters,« *Industrial Electronics, IEEE Transactions on,* årg. 56, nr. 2, pp. 371--379, 2009.

[177] L. Harnefors og H.-P. Nee, »Model-based current control of AC machines using the internal model control method,« *Industry Applications, IEEE Transactions on,* årg. 34, nr. 1, pp. 133--141, 1998.

[178] M. Jasinski, »Direct power and torque control of AC/DC/AC converter-fed induction motor drives,« *Faculty of Electrical Engineering, PhD. Thesis, Warsaw University of Technology,* 2005.

[179] L. H. Kocewiak, J. Hjerrild og C. L. Bak, »Wind Turbine Control Impact on Stability of Wind Farms Based on Real-Life Systems Analysis,« *EWEA 2012.*

[180] P. Brogan og N. Goldenbaum, »Harmonic model of the network bridge power converter for wind farm harmonic studies,« i *12th International Workshop on Large-Scale Integration of Wind Power into Power Systems as well as on Transmission Networks for Offshore Wind Power Plants*, London, 2013.

[181] P. Dang, T. Ellinger og J. Petzoldt, »Dynamic Interaction Analysis of APF Systems,« *Industrial Electronics, IEEE Transactions on ,* årg. 61, nr. 9, pp. 4467-4473, Sept 2014.

[182] X. Wang, F. Blaabjerg, M. Liserre, Z. Chen, J. He og Y. Li, »An active damper for stabilizing power electronics-based AC systems,« i *Applied Power Electronics Conference and Exposition (APEC), 2013 Twenty-Eighth Annual IEEE*, 2013.

[183] D. Basic, V. Ramsden og P. Muttik, »Selective compensation of cycloconverter harmonics and interharmonics by using a hybrid power filter system,« i *Power Electronics Specialists Conference, 2000. PESC 00. 2000 IEEE 31st Annual*, 2000.

[184] P. Brogan og R. Yacamini, »Stability of selective harmonic active filters,« i *Power Electronics and Variable Speed Drives, 2000. Eighth International Conference on (IEE Conf. Publ. No. 475)*, 2000.

[185] V. Blasko og V. Kaura, »A new mathematical model and control of a three-phase AC-DC voltage source converter,« *Power Electronics, IEEE Transactions on,* årg. 12, nr. 1, pp. 116--123, 1997.

[186] G. Franklin, J. Powell og M. Workman, Digital control of dynamic systems, 3rd red., Prentice-Hall, 2006.

[187] T. Kugelstadt, »Active filter design techniques,« *Op amps for everyone: design reference,* pp. 271--281, 2008.

[188] Z. Emin, F. Ghassemi og J. Price, »Harmonic performance requirements of an HVDC connection; network owner perspective,« i *AC and DC Power Transmission, 2010. ACDC. 9th IET International Conference on*, 2010.

[189] B. Gustavsen og A. Semlyen, »Rational approximation of frequency domain responses by vector fitting,« *Power Delivery, IEEE Transactions on,* årg. 14, nr. 3, pp. 1052--1061, 1999.

[190] J. Bowles, »AC System and Transformer Representation for HV-DC Transmission Studies,« *Power Apparatus and Systems, IEEE Transactions on,* nr. 7, pp. 1603--1609, 1970.

[191] N. G. Hingorani og M. F. Burbery, »Simulation of AC system impedance in HVDC system studies,« *Power Apparatus and Systems, IEEE Transactions on,* nr. 5, pp. 820--828, 1970.

[192] N. Watson, »Frequency-dependent A.C. system equivalents for harmonic studies and transient convertor simulation,« New Zealand, 1987.

[193] A. Morched, B. Gustavsen og M. Tartibi, »A universal model for accurate calculation of electromagnetic transients on overhead lines and underground cables,« *Power Delivery, IEEE Transactions on,* årg. 14, nr. 3, pp. 1032--1038, 1999.

[194] B. Gustavsen, J. Martinez og D. Durbak, »Parameter determination for modeling system transients-Part II: Insulated cables,« *Power Delivery, IEEE Transactions on,* årg. 20, nr. 3, pp. 2045--2050, 2005.

[195] B. Gustavsen og H. J. De Silva, »Inclusion of Rational Models in an Electromagnetic Transients Program: Y-Parameters, Z-Parameters, S-Parameters, Transfer Functions,« *Power Delivery, IEEE Transactions on,* årg. 28, nr. 2, pp. 1164--1174, 2013.

[196] D. Deschrijver, M. Mrozowski, T. Dhaene og D. De Zutter, »Macromodeling of multiport systems using a fast implementation of the vector fitting method,« *Microwave and Wireless Components Letters, IEEE,* årg. 18, nr. 6, pp. 383--385, 2008.

[197] B. Gustavsen og O. Mo, »Interfacing convolution based linear models to an electromagnetic transients program,« i *Proc. Int. Conf. Power Systems Transients*, 2007.

[198] K. Kurokawa, »Power waves and the scattering matrix,« *Microwave Theory and Techniques, IEEE Transactions on,* årg. 13, nr. 2, pp. 194--202, 1965.

[199] Z. Zhongyuan, L. Fangcheng og L. Guishu, »A high-frequency circuit model of a potential transformer for the very fast transient simulation in GIS,« *Power Delivery, IEEE Transactions*

on, årg. 23, nr. 4, pp. 1995--1999, 2008.

[200] A. C. Lima, B. Gustavsen og A. B. Fernandes, »Inaccuracies in network realization of rational models due to finite precision of RLC branches,« i *Int. conf. on Power Syst. Transients, IPST*, 2007.

[201] N. Tleis, Power Systems Modelling and Fault Analysis, Newnes, 2008.

[202] International Electrotechnical Commission, IEC 60287-1-1 - Electric cables - Calculation of the current rating - Part 1-1 Current rating equations (100 % load factor) and calculation of losses - General, 2006.

[203] M. Garcia-Gracia, M. P. Comech, J. Sallan og A. Llombart, »Modelling wind farms for grid disturbance studies,« *Renewable energy,* årg. 33, nr. 9, pp. 2109--2121, 2008.

[204] L. Fernandez, C. Garcia, J. Saenz og F. Jurado, »Equivalent models of wind farms by using aggregated wind turbines and equivalent winds,« *Energy conversion and management,* årg. 50, nr. 3, pp. 691--704, 2009.

[205] U. S. Gudmundsdottir, Modelling of long High Voltage AC Cables in the Transmission System, Department of Energy Technology, Aalborg University, 2010.

[206] F. J. Harris, »On the use of windows for harmonic analysis with the discrete Fourier transform,« *Proceedings of the IEEE,* årg. 66, nr. 1, pp. 51--83, 1978.

[207] International Electrotechnical Commission, IEC 61000-4-7, Testing and measurement techniques—General guide on harmonics and interharmonics measurements and instrumentation, for power supply systems and equipment connected thereto, 2002.

[208] Cigré WG B4-57, »Guide for the Development of Models for HVDC Converters in a HVDC Grid,« Paris, 2014.

[209] J. Slootweg, H. Polinder og W. Kling, »Initialization of wind turbine models in power system dynamics simulations,« i *Power Tech Proceedings, 2001 IEEE Porto*, 2001.

[210] Business Today, May 2010. [Online]. Available: http://businesstoday.intoday.in/story/how-innovation-really-works/1/5598.html. [Senest hentet eller vist den 12 12 14].

[211] W. J. Stevenson og M. Hojati, Operations management, årg. 8, McGraw-Hill/Irwin Boston, 2007.

About the Author

Dr. Jakob Glasdam was born in Denmark, 1984. He received his B.Sc. degree from Southern University of Denmark in 2009, M.Sc. and Ph.D. from Aalborg University, Denmark, in 2011 and 2015, respectively. All degrees are within electrical and electronic engineering.

Dr. Glasdam received an award for his master thesis from the Energy Sponsor Programme in Denmark for his excellent work for: “Demonstrating marvellous academic skills, extraordinary engagement and solid work reflecting innovative thinking”.

Dr. Glasdam was awarded the Ph.D. degree with the designation “he is an excellent researcher”. The Ph.D. research has subsequently been published as a book in "Springer Theses - Recognizing Outstanding Ph.D. Research".

Dr. Glasdam was employed at DONG Energy Wind Power from 2011 to 2015, first working on his PhD and since as an offshore wind power plant grid connection engineer. His main tasks as a grid connection engineer was the system design and studies for a German offshore wind power plant (OWPP) employing a high voltage direct current transmission system.

Dr. Glasdam is from 2016 working as a senior engineer in the grid-planning department at Energinet.dk.

He is specialized within the field of dynamic and harmonic studies in power systems and OWPPs employing power electronic devices in the transmission system.